UNIVERSITY OF LIVERPOOL

Investigating the Safety and Efficacy of Regenerative Medicine Therapies in Mouse Models of Kidney Disease

Thesis submitted in accordance with the requirements of the University of Liverpool for the degree of Doctor in Philosophy

by Lauren Nicolle Scarfe

June 2017

ABSTRACT

Investigating the Safety and Efficacy of Regenerative Medicine Therapies in Mouse Models of Kidney Disease, by Lauren Scarfe

Acute kidney injury (AKI) and chronic kidney disease (CKD) are serious health problems with high morbidity and mortality. There are currently no specific treatments available to patients with AKI or CKD, and many patients require renal replacement therapy to survive. Cell-based regenerative medicine therapies have shown potential for treating AKI and CKD in preclinical models, however conventional methods of measuring kidney function and tracking exogenously administered cells are not ideal. Novel imaging-based methods provide an alternative approach, allowing kidney function and cell biodistribution to be monitored longitudinally, without sacrificing many animals at multiple time points. The work in this thesis aimed to evaluate the use of two novel methods for assessing kidney function in mice, and apply them in the assessment of cell therapy efficacy in two preclinical models of kidney disease. Furthermore, preclinical imaging approaches were used to track cell biodistribution *in vivo*, in order to gain insights into the mechanism of action of cell therapy, and long-term safety.

Two novel methods of measuring kidney function were assessed: 1) transcutaneous measurement of FITC-sinistrin clearance, and 2) photoacoustic imaging of IRDye clearance kinetics. The transcutaneous measurement of FITC-sinistrin clearance was found to be a superior method of measuring kidney function in mice, correlating more strongly with histological assessment of structural damage compared with traditional biochemical techniques in the adriamycin model of CKD, and the ischemia-reperfusion model of AKI. Photoacoustic imaging of IRDye clearance kinetics was also found to correlate better with histology in the adriamycin model, however the transcutaneous method was preferred for subsequent studies due to practical considerations including shorter anaesthesia time, higher throughput data collection, and ease of data handling.

The efficacy of human kidney-derived cells (hKCs) was assessed following early and late administration in the adriamycin model. It was found that the hKCs induced a trend towards improved kidney function when administered on day one, but there was no effect when treatment was delayed until day 15, after overt proteinuria was established. Furthermore, bioluminescence imaging of luciferase^{+} hKCs demonstrated that intravenously administered hKCs remained trapped in the lungs, where they promptly died and did not migrate to the kidneys. These results support a paracrine/endocrine mechanism of action of cell therapy,

and suggest that efficacy may be absent or diminished when treatment is administered later in the course of the disease.

The efficacy of hKCs was also assessed in the ischemia-reperfusion model, and was compared with human mesenchymal stromal cells derived from either bone marrow or the umbilical cord. These results were unexpected, as it was found that none of the cell types tested had any effect on kidney structure or function, and furthermore, the cells did not die in the lungs within 24h of administration. These results may allude to a potential role of cell death in the mechanism of action of cell therapy, however this requires a great deal of further investigation.

Finally, preclinical imaging techniques were used to optimise an intracardiac method of cell administration, and to compare the short- and long-term biodistribution of cells following intravenous and intracardiac administration. Intracardiac administration was shown to deliver cells to all organs of the body, including the kidney, and a multi-modal imaging approach enabled whole-body imaging of live cells by bioluminescence imaging, in conjunction with detailed organ-specific imaging of intra-organ biodistribution with magnetic resonance imaging. Longitudinal bioluminescence imaging demonstrated the effect of route of administration on tumour development, with intracardiac administration leading to more aggressive tumour development compared with intravenous administration. These results highlight the value of preclinical imaging in the assessment of regenerative medicine therapies, and show the importance of longitudinal monitoring of the safety of a cell therapy.

Overall, the results of this thesis demonstrate the use of novel imaging-based methods of assessing kidney function and cell biodistribution in preclinical assessment of the safety and efficacy of cell-based regenerative medicine therapies. These minimally-invasive methods are more reliable than traditional analyses, and allow individual animals' responses to be monitored over time, thus reducing the number of animals required for such experiments.

ACKNOWLEDGEMENTS

First and foremost, I would like to thank my supervisors, Bettina Wilm and Trish Murray, as I most certainly would not be here without them. Trish first inspired my interest in regenerative medicine with a lecture on stem cells in the first year of my Bachelor's degree, and following a summer project, Bettina was the first person to suggest that I should pursue a PhD and encouraged me to apply. They have given me a great deal of support and advice throughout the past few years, and provided me with many opportunities to expand my scientific skills and confidence. Both Bettina and Trish have been wonderful mentors over the years, and I have learnt so much from them, for which I will always be grateful.

I would like to thank all members of the stem cell group, particularly Sumaya, Michela, Ilaria, Kelly, Jack, Arthur, and Sumita, who have been lovely colleagues and friends over the years. I have also been very lucky to work on a highly multidisciplinary project, and would like to thank the UK Regenerative Medicine Platform, and also NephroTools, for the opportunity to meet lots of different people, and attend and present at many conferences and workshops. In particular, the opportunity to present my research on so many occasions has been very valuable to me, and I am no longer terrified of public speaking!

I would like to thank Aleksandra Rak-Raszewska, who set up the adriamycin model before I began my PhD, and gave me a crash course in everything I needed to know to get started! I would also like to thank the Vanderbilt Mouse Kidney Injury Workshop in Nashville, Tennessee, for providing me with the surgical skills required to set up the IRI model in Liverpool, and Mark deCaestecker and Nataliya Skrypnyk (Vanderbilt University, Nashville) for continued support and advice during optimisation studies. Thanks also to Adrian Woolf (University of Manchester) and Lorenzo Ressel for their expert eyes in histological scoring of kidney injury. I would like to thank everyone in the BSU for their animal care and advice, and particularly Edyta Kijak, who provided excellent assistance with my surgeries, and has become a wonderful friend. I'll miss IRI surgeries listening to cheesy music and Edyta's constant chatter!

My research has been heavily reliant on my colleagues to culture and prepare cells for me to administer to the animals, for which I would like to thank Ilaria Santeramo, Arthur Taylor, Jack Sharkey. In addition to cell preparation, they were also on hand to help with various aspects of my experimental work. Ilaria helped out with dissections for the experiments in Chapter 4, and Arthur was essential for MR imaging in Chapter 6. Jack has worked alongside

me in many studies throughout my PhD, particularly with MSOT imaging in Chapter 3 and optimisation of the US-IC injections in Chapter 6.

I would like to thank everyone who has provided me with support and advice in using the transcutaneous device: Aleksandra, for teaching me how to use it, Stefania Geraci and Norbert Gretz (University of Heidelberg) for help with analysis in the early days, and Daniel Schock-Kusch and Dzmitry Stsepankou (MediBeacon, Germany), for continued support and helpful tips. I would also like to thank Tim Devling, Neal Burton, and Thomas Sardella from iThera Medical, who taught me how to use the MSOT and have provided continued help and troubleshooting over the years. Many thanks also to Carmel Horan and Adrian Thomson (University of Edinburgh) for getting Jack and I started with US-IC injections, and to Marta García-Fiñana for statistical advice over the years. Importantly, Chapter 3 consists of a published paper and I would like to acknowledge those who performed certain analyses: Jiaguo Huang (University of Heidelberg) for carrying out plasma protein binding analysis, Darsy Darssan and Marta García-Fiñana (UoL) for carrying out statistical analyses, Neal Burton (iThera Medical) for producing the temporal colour map, David Mason (UoL) for help with quantifying renal fibrosis, and all senior authors for helpful feedback and guidance during writing and publication.

Next, I would like to thank my Masters students, Cai Astley and Lydia Beeken. Cai worked on the studies assessing the tumour formation of mMSCs following IV and IC administration, and helped with bioluminescence imaging and performed the Prussian Blue staining of iron. Lydia worked on optimising staining protocols for tissues from the IRI model, and also carried out the isolectin staining of blood vessels in the brain. Cai and Lydia were both very helpful in the lab, and great guinea pigs for me to practice my teaching skills on!

I feel it is important to express my sincere gratitude towards the animals used throughout my PhD. My research has consisted entirely of animal work, and as such a large number of mice have been sacrificed. Carrying out animal work is never an easy task, and I can only hope that I have conducted my research with the utmost care and respect, and that this work eventually informs the development of a therapy that can be used to improve, and maybe even save, the lives of some patients with AKI and CKD.

Finally, I would like to thank my friends and family, particularly my Mum, Shirley, and my best friend, Anna. You've supported me since the very beginning and never doubted that I could do this. It's been a particularly tough year, and I couldn't have done it without you.

CONTENTS

Abstract ..... **i**
Acknowledgements ..... **iii**
Contents ..... **v**
List of Figures ..... **viii**
List of Tables ..... **x**
List of Supplementary Videos ..... **xi**
Abbreviations ..... **xii**

CHAPTER 1: Introduction **1**
1.1 The Kidney: Structure and Function **2**
1.1.1 The Structure of the Kidney and Urine Production **2**
1.1.2 Additional Functions of the Kidney **6**
1.2 Acute Kidney Injury and Chronic Kidney Disease: A Global Problem **7**
1.2.1 Acute Kidney Injury **7**
1.2.2 Chronic Kidney Disease **9**
1.2.3 The Relationship Between AKI and CKD **10**
1.2.4 Current Treatment Options **11**
1.3 Regenerative Medicine Therapies **12**
1.4 Animal Models of Kidney Disease and Preclinical Studies of RMT Efficacy **15**
1.4.1 Models of Acute Kidney Injury **16**
1.4.2 Models of Chronic Kidney Disease **24**
1.4.3 Benefits and Limitations of Animal Models **30**
1.5 Traditional and Novel Measures of Assessing Kidney Function *in vivo* **31**
1.5.1 Traditional Measures of Kidney Function **31**
1.5.1 Novel Measures of Kidney Function **32**
1.6 Preclinical Imaging in Regenerative Medicine Research **34**
1.7 Summary and Thesis Aims **38**

CHAPTER 2: General Methods **39**
2.1 Kidney Injury Models and *in vivo* Measures of Kidney Function **40**
2.2 Analysis of Kidney Injury **45**
2.3 Cell Therapy: Administration and Tracking **48**
2.4 Statistical Analyses **56**

CHAPTER 3: Characterising the adriamycin mouse model of chronic kidney disease, and minimally-invasive methods of assessing kidney function *in vivo* **57**
3.1 Abstract **58**
3.2 Introduction **58**
3.3 Materials and Methods **60**
3.4 Results **64**
3.4.1 The half-life of transcutaneously measured FITC-sinistrin becomes significantly increased over the course of ADR-induced nephropathy 64

3.4.2 The passage of IRDye through the kidney measured using MSOT is delayed in ADR mice 67
3.4.3 Minimally invasively measured clearance kinetics of sinistrin and IRDye show a strong correlation with glomerular histological damage 69
3.5 Discussion **71**
3.6 Acknowledgements **75**
3.7 Author Contribution Statement **75**
3.8 Competing Financial Interests **75**
3.9 Supplementary Figures and Tables **76**

CHAPTER 4: Assessing the efficacy of human kidney-derived cells for ameliorating acute and chronic kidney disease **85**
4.1 Introduction **86**
4.2 Experimental Design **90**
4.3 Results **92**
4.3.1 Acute Study **92**
4.3.1.1 Morbidity and Mortality **92**
4.3.1.2 *In vivo* Cell Tracking **92**
4.3.1.3 Kidney Function **93**
4.3.1.4 Histology **93**
4.3.2 Chronic Study **95**
4.3.2.1 Morbidity and Mortality **95**
4.3.2.2 Initial Assessment of Kidney Injury and Grouping **95**
4.3.2.3 Longitudinal Assessment of Kidney Function **97**
4.3.2.4 *In vivo* Cell Tracking **101**
4.3.2.5 Histology **102**
4.4 Discussion **102**
4.5 Supplementary Tables **110**

CHAPTER 5: Assessing the efficacy of human kidney-derived and mesenchymal cells in a mouse model of ischemia-reperfusion injury **113**
5.1 Introduction **114**
5.2 Experimental Design **117**
5.3 Results **119**
5.3.1 Optimising the IRI Model **119**
5.3.1.1 Bilateral Ischemia Pilot Study **119**
5.3.1.2 Unilateral Ischemia with Contralateral Nx Pilot Study **122**
5.3.1.3 Finalising the Ischemia Time in the Unilateral Ischemia with Contralateral Nx Model **127**
5.3.2 Assessing the Efficacy of Human Cells in the IRI Model **132**
5.3.2.1 Four-day study **132**
5.3.2.2 One-day study **132**
5.4 Discussion **134**

5.5 Supplementary Figures and Tables **143**

CHAPTER 6: Preclinical imaging approaches for assessing the short- and long-term biodistribution of stem cells following intracardiac or intravenous administration to mice **147**

6.1 Introduction **148**

6.2 Experimental Design **152**

6.3 Results **153**

6.3.1 Optimising Intracardiac Cell Administration **153**

6.3.2 Comparing the Biodistribution of Mouse and Human Cells Following IV and IC Administration Routes **155**

6.3.3 Quantification of Labelled Cells in the Kidneys using Bioluminescence and Histology **155**

6.3.4 MR Imaging to Track Cell Biodistribution Within the Kidneys and Brain at Higher Spatial Resolution **160**

6.3.5 Longitudinal MRI/BLI Tracking of Labelled Cells **162**

6.3.7 Comparison of Administration Route on the Long-Term Biodistribution of mMSCs **164**

6.3.7.1 Analysis of MSC-derived tumours **168**

6.3.7.2 Comparison of tumour-forming potential based on genetic background and immune status of mice **170**

6.4 Discussion **172**

6.5 Supplementary Table **178**

CHAPTER 7: Final discussion and summary **179**

List of References **192**

LIST OF FIGURES

Figure 1.1: Schematic representation of the structure of the nephron and glomerulus **3**
Figure 1.2: Diagram explaining the relationship between AKI, CKD, and ESRD **10**
Figure 1.3: Kidney transplants in the UK **12**
Figure 1.4: Approximate number of publications reporting on the efficacy of stem cell therapies in animal models of kidney disease up to 2016 ..... **15**
Figure 1.5: Summary of the characteristics of the progression of adriamycin nephropathy in mice **27**
Figure 2.1: Ischemia reperfusion injury **42**
Figure 2.2: Transcutaneous assessment of FITC-sinistrin clearance **43**
Figure 2.3: Tubular injury scoring **49**
Figure 2.4: Ultrasound-guided intracardiac administration of cells **51**
Figure 2.5: Unsuccessful IC injections **52**
Figure 3.1: Assessment of body weight change and urinary albumin excretion during the study **65**
Figure 3.2: Transcutaneous assessment of FITC-sinistrin clearance over time **66**
Figure 3.3: MSOT imaging of IRDye clearance kinetics **68**
Figure 3.4: Histological evaluation and quantification of glomerulosclerosis and fibrosis ... **70**
Figure 3.5: Correlation graphs between % abnormal glomeruli and minimally invasive methods of measuring kidney function **72**
Supplementary Figure S3.1: Additional body weight, urinary albumin, BUN and SCr data.. **76**
Supplementary Figure S3.2: Additional PSR and Masson's Trichrome images of renal injury **77**
Supplementary Figure S3.3: Sample graph depicting FITC-sinistrin emission data **78**
Supplementary Figure S3.4: Absorption and emission spectrum scan of IRDye **78**
Figure 4.1: Experimental Design Schematics **91**
Figure 4.2: Mean body weight change of mice in the acute study **93**
Figure 4.3: Bioluminescence imaging of ZsGreen^{+}/Luciferase^{+} hKC biodistribution *in vivo* and *ex vivo* **94**
Figure 4.4: Mean urinary albumin of mice in the acute study **95**
Figure 4.5: Mean body weight change of mice in the chronic study **96**
Figure 4.6: Pre-treatment assessment of kidney injury **97**
Figure 4.7: Longitudinal assessment of kidney function **100**
Figure 4.8: Bioluminescence imaging of ZsGreen^{+}/Luciferase^{+} hKC biodistribution *in vivo* and *ex vivo* **103**
Figure 4.9: Histological evaluation of glomerulosclerosis **104**
Figure 5.1: Pilot bilateral IRI model – renal injury analyses **120**
Figure 5.2: Urine biochemistry and problems collecting urine **123**
Figure 5.3: Pilot unilateral with nephrectomy IRI model – renal injury analyses **124**
Figure 5.4: Highlighting the importance of careful temperature control **125**
Figure 5.5: Repeated baseline measurements of FITC-sinistrin half-life **126**
Figure 5.6: Characterisation of the renal injury induced by 31 min unilateral ischemia with contralateral nephrectomy **128**
Figure 5.7: Expression of tissue biomarkers of injury and repair in IRI and sham mice **130**

Figure 5.8: Correlation of three measures of kidney function (FITC-sinistrin clearance, SCr, BUN) with histological evaluation of tubular injury **131**
Figure 5.9: Efficacy of different types of human cells in the IRI model **133**
Figure 5.10: Expression of tissue biomarkers of injury and repair following cell therapy .. **134**
Figure 5.11: Short-term cell tracking and efficacy of hKCs **135**
Supplementary Figure S5.1: Example FITC-sinstrin clearance curves **145**
Figure 6.1: Biodistribution of cells following intravenous or intracardiac administration of various cell types **156**
Figure 6.2: Tissue biodistribution of mKSCs following intravenous or intracardiac administration **157**
Figure 6.3: Quantification of ZsGreen^{+} mKSCs in kidneys and correlation with BLI **158**
Figure 6.4: *In vivo* and *ex vivo* tracking of ZsGreen^{+}/Luciferase^{+}/SPION^{+} mMSCs in the kidneys and brain following IC or IV administration **161**
Figure 6.5: Multi-modal imaging of ZsGreen^{+}/luciferase^{+}/SPION^{+} mMSCs in the kidneys for 48h following IC administration **163**
Figure 6.6: Longitudinal cell tracking following IV-administration of mMSCs **165**
Figure 6.7: Longitudinal cell tracking following IC-administration of mMSCs **167**
Figure 6.8. Analysis of mMSC tumours formed 30 days after IC administration **169**
Figure 6.9: Fluorescence Activated Cell Sorting (FACS) analysis of bone marrow **170**
Figure 6.10: Comparison of tumour-formation potential in different mouse strains **171**
Figure 7.1: Comparison of the mean (actual or estimated from graph) SCr and BUN **186**

LIST OF TABLES

Table 1.1: The stages of AKI **8**
Table 1.2: The stages of CKD **9**
Table 1.3: Summary of studies assessing the efficacy of cell therapy in the IRI model..... **19**
Table 1.4: Summary of the advantages and disadvantages of the most commonly used imaging modalities in preclinical research **35**
Table 2.1: Data acquisition details for MR imaging **54**
Table 3.1: Statistical mixed-effects models describing urinary albumin and FITC-sinistrin half-life over time **67**
Table 3.2: Table summarising the associations in the ADR group between % abnormal glomeruli and the four biomarkers **73**
Supplementary Table S3.1A: Table summarising the individual values of all longitudinal parameters **79**
Supplementary Table S3.1B: Table summarising the individual values of all end-point analyses **80**
Table 3.2: Table summarising the statistical analyses used to detect significant differences between ADR and CTRL at week 5 ..... **81**
Supplementary Table S3.3: Table summarising the results of the mixed-design ANOVA models **81**
Supplementary Table S3.4: IRDye protein plasma binding analysis **82**
Supplementary Table S3.5: Multiple regression models of the association between abnormal glomeruli and various other parameters **83**
Table 4.1: Summary of published studies assessing the efficacy of hKCs in animal models of kidney injury **88**
Table 4.2: Pre-treatment evaluation of kidney function (sorted by increasing urinary albumin values **98**
Table 4.3: Assignment of animals to a cell therapy or control treatment group **99**
Table 4.4: Histological evaluation of glomerulosclerosis **106**
Supplementary Table S4.1: Acute study: individual urinary albumin values **110**
Supplementary Table S4.1: Chronic study: individual urinary albumin and FITC-sinistrin half-life values **111**
Supplementary Table S4.3: Tukey Pairwise Comparisons **112**
Table 5.1: Table summarising the various approaches to the IRI model **115**
Table 5.2: Pilot bilateral IRI model – renal injury analyses **121**
Table 5.3: Urine volumes produced throughout a typical experiment **122**
Table 5.3: Pilot unilateral IRI model – renal injury analyses **125**
Table 5.3: 31 min IRI vs sham – renal injury analyses **129**
Supplementary Table S5.1: Tukey pairwise comparisons – characterisation of 31 min ischemia **143**
Supplementary Table S5.2: Tukey pairwise comparisons – efficacy of hKCs **144**
Table 6.1: Table of different bioluminescence scales used **153**
Table 6.2: Bioluminescence signal quantification **168**
Supplementary Table S6.1: Tukey pairwise comparisons **178**
Figure 7.1: Comparison of the mean (actual or estimated from graph) SCr and BUN **186**

LIST OF SUPPLEMENTARY MOVIES

Supplementary Movie S3.1: Clearance of IRDye through the kidney of an ADR-injured mouse at week 5 ..... **84**
https://www.dropbox.com/s/6ygm83f9m9sc1xi/C4.2%20Injection%20Scan.avi?dl=0
Supplementary Movie S3.2: Clearance of IRDye through the kidney of a CTRL mouse at week 5 ..... **84**
https://www.dropbox.com/s/6ygm83f9m9sc1xi/C4.2%20Injection%20Scan.avi?dl=0

LIST OF ABBREVIATIONS

α-SMA	α-smooth muscle actin
ACE	angiotensin converting enzyme
ADR	adriamycin
AKI	acute kidney injury
Alb:Cr	albumin to creatinine ratio
ALI	acute lung injury
ANOVA	analysis of variance
ARF	acute renal failure
ASC	adult stem cell
ATP	adenosine triphosphate
BLI	bioluminescence imaging
BSA	bovine serum albumin
BUN	blood urea nitrogen
BW	body weight
CA	carotid artery
CDDP	*cis*-diamminedichloroplatinum (II)
CKD	chronic kidney disease
CLP	caecal ligation and puncture
CP	cisplatin
CTRL	control
d	day
DAMPs	damage-associated molecular patterns
DAPI	4',6-diamidino-2-phenylindole
DBA	dolichos biflorus agglutinin
dH_2O	distilled water
DMSO	dimethyl sulphoxide
DN	diabetic nephropathy
ECD	expanded criteria donor
ELISA	enzyme-linked immunosorbent assay
EM	electron microscopy
ESC	embryonic stem cell
ESRD	end-stage renal disease
FasL	fas ligand
FITC	fluorescein isothiocyanate
FOV	field of view
FSGS	focal segmental glomerulosclerosis
GBM	glomerular basement membrane
GFP	green fluorescent protein
GFR	glomerular filtration rate

GvHD	graft-versus-host disease
H	hour
H&E	haematoxylin & eosin
hBM-MSC	human bone marrow-derived mesenchymal stem/stromal cell
HIFs	hypoxia inducible factors
HIV	human immunodeficiency virus
hKCs	human kidney-derived cells
HLA	human leukocyte antigen
HSC	haematopoeitic stem cell
hUC-MSC	human umbilical cord-derived mesenchymal stem/stromal cell
IC	Intracardiac
ICG	indocyanine green
IF	immunofluorescence
IL	Interleukin
iPSC	induced pluripotent stem cell
IRDye	IRDye 800CW carboxylate
iRFP	infrared fluorescent protein
IRI	ischemia-reperfusion injury
ISOM	inner stripe of the outer medulla
ITM	institute of translational medicine
IV	intravenous
IVC	individually ventilated cage
KIM-1	kidney injury molecule-1
LED	light emitting diode
LME	linear mixed effects model
LPS	lipopolysaccharide
LTA	lotus tetragonolobus agglutinin
MCP-1	monocyte chemotactic protein-1
min	minute
mKSCs	mouse kidney stem cells
mMSCs	mouse mesenchymal stem/stromal cells
MOI	multiplicipty of infection
MR	magnetic resonance
MRI	magnetic resonance imaging
ms	millisecond
MSC	mesenchymal stem/stromal cell
MSOT	multispectral optoacoustic tomography
NaCl	sodium chloride
NF-κB	nuclear factor-kappa B
NGAL	neutrophil gelatinase-associated lipocalin
NGS	normal goat serum
NIR	near infrared

NK	natural killer
NOD	non-obese diabetic
Nx	nephrectomy
OCT	optimal cutting temperature
OSOM	outer stripe of the outer medulla
p	photon
PAS	periodic acid-schiff
PBS	phosphate-buffered saline
PDX	podocalyxin
PET	positron emission tomography
PPB	plasma protein binding
PSC	pluripotent stem cell
PSR	picro-sirius red
qRT-PCR	quantitative reverse transcriptase polymerase chain reaction
RB	rhabdomyolysis
RMT	regenerative medicine therapies
ROI	region of interest
ROS	reactive oxygen species
RRT	renal replacement therapy
s	second
SC	subcutaneous
SCID	severe combined immunodeficient
SCr	serum creatinine
SDS	sodium dodecyl sulphate
SE	standard error
SPECT	single photon emission computed tomography
SPION	superparamagnetic iron oxide nanoparticle
sr	steradian
STZ	streptoxotocin
TA	transcutaneous assessment (of FITC-sinistrin clearance)
TGF-β	transforming growth factor-β
TLR	toll-like receptor
TNF-α	tumour necrosis factor alpha
Tregs	regulatory T cells
UCr	urinary creatinine
UoL	university of liverpool
UTO	urinary tract obstruction
UUO	unilateral ureteric obstruction
VCAM-1	vascular cell adhesion molecule-1
VEGF	vascular endothelial growth factor

CHAPTER 1

Introduction

1.1 The Kidney: Structure and Function

The kidneys perform various functions in the body and are essential organs for life. The primary function of the kidneys is to act as a filter for the blood; removing waste products and excreting them from the body via urine, in addition to maintaining the volume, pH, and ion homeostasis of blood. When the kidneys do not function correctly, waste products and fluid build up in the body, and abnormal pH and electrolyte levels interfere with the function of various other organs of the body, and thus kidney dysfunction can be fatal.

1.1.1 The Structure of the Kidney and Urine Production[1]

Kidneys exist in pairs, and are located by the posterior abdominal wall, with the left kidney having a slightly higher position in the body than the right. The kidney is enclosed in a fibrous capsule, and surrounded by a protective layer of perirenal fat. The kidneys are supplied by the renal arteries, which branch off from the abdominal aorta. Together, the kidneys receive approximately 20% of the cardiac output[3]. The nephron (Fig. 1.1) is the functional unit of the kidney: there are typically one million nephrons in each human kidney, although this varies considerably between individuals, from just 250,000 to over 2.5 million nephrons per kidney, and this is strongly correlated with birth weight[4]. Each nephron comprises a renal corpuscle, consisting of a glomerulus and Bowman's capsule, and a renal tubule, consisting of a proximal tubule (straight and convoluted portions), the loop of Henle, and a distal tubule (straight and convoluted portions), which empties into a collecting duct.

The parenchyma of the kidney is divided into the cortex and the medulla: the nephron begins with the renal corpuscle and the proximal tubule located in the cortex, the loop of Henle then dips into the medulla, and the distal tubule returns the nephron back to the cortex. The human kidney contains multiple renal pyramids within the medulla, whereas the kidney of small mammals, such as the mouse, only has one renal pyramid[5]. The medulla can be divided into an outer and inner zone, and the outer zone can be further divided into an outer and inner stripe. The outer stripe of the outer medulla (OSOM) contains the straight portions of the proximal and distal tubules, the thick ascending limb of the loop of Henle, and the collecting ducts. The inner stripe of the outer medulla (ISOM) contains the thick ascending limb and the thin descending limb of the loop of Henle, and the collecting ducts.

[1] Two book chapters, Halgrimsson *et al.,* (2003) and McBride *et al.,* (2016), provided the information for this section, unless otherwise referenced

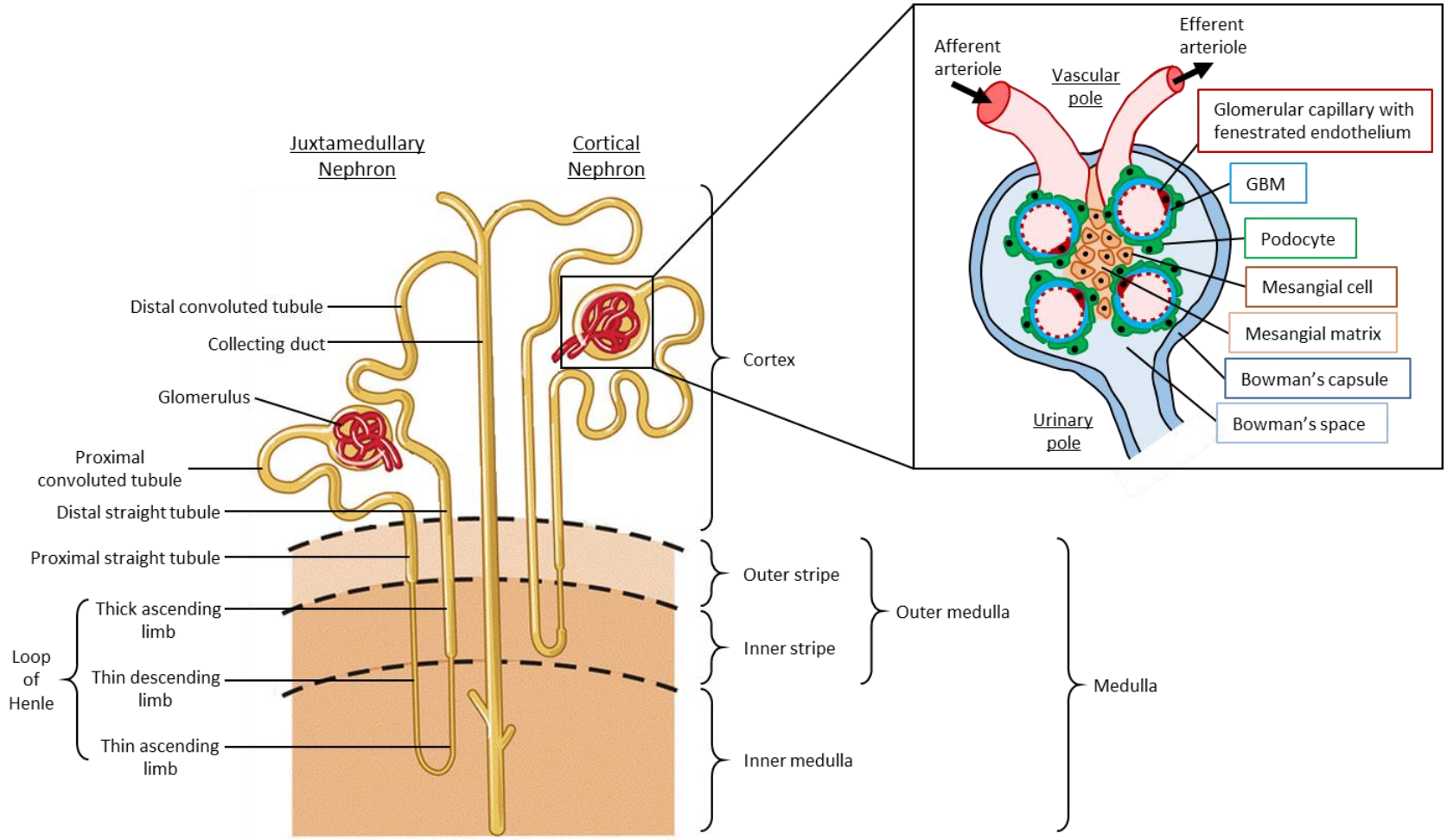

Figure 1.1: Schematic representation of the structure of the nephron and glomerulus. *Adapted from McBride (2016).*

The inner medulla contains the thin ascending and descending limbs of the loop of Henle and larger collecting ducts which empty into the renal pelvis.

Two types of nephrons exist, classified according to their starting location and length of the tubules. Cortical nephrons are the most abundant, making up approximately 85% of all nephrons. The glomeruli of cortical nephrons are located in the outer portion of the cortex and have shorter loops of Henle, generally extending only to the ISOM. Juxtamedullary nephrons have glomeruli located in the inner cortex, close to the border between the cortex and medulla, and tend to have much longer tubules, with the loop of Henle extending deep into the inner medulla.

The Renal Corpuscle

The renal corpuscle is comprised of the glomerulus and the Bowman's capsule, which is continuous with the proximal tubule and surrounds the glomerulus. The space between these two structures is known as the Bowman's space. The glomerulus is a tightly packed tuft of capillaries which selectively filters components of the blood through its filtration barrier, to produce an ultrafiltrate. The filtration barrier is comprised of[1,6]:

1) Highly fenestrated endothelial cells of the glomerular capillaries, which serve as a size-specific barrier to cells and large macromolecules within the blood, only permitting the filtration of water and small molecules through the fenestrations.
2) The glomerular basement membrane (GBM), which consists of type IV collagen, fibronectin, laminin, and proteoglycans. The GBM provides structural support to the glomerulus and protects the filtration barrier from the hydrostatic pressure generated within the glomerular capillaries.
3) Podocytes, which are highly specialised epithelial cells formed from the visceral layer of the Bowman's capsule, form the final component of the filtration barrier. Podocytes have a large cell body and extend long cytoplasmic processes which wrap around the glomerular capillaries. These lead to secondary processes called pedicels, which interdigitate with the pedicels of adjacent podocytes, forming a network of narrow filtration slits between the glomerular capillaries and the Bowman's space. The filtration slits are bridged by the slit diaphragm, which is a filamentous, porous sheet that serves as an additional size-specific barrier to macromolecules.

Additionally, the renal corpuscle also contains mesangial cells, located between the capillary loops and around the vascular pole. Mesangial cells and their associated mesangial matrix

provide structural support to the GBM, and also function to phagocytose any macromolecules trapped within the GBM.

Blood enters the kidney via the renal artery, which branches to form the afferent arteriole that enters the glomerulus at the vascular pole of the renal corpuscle, and leaves the glomerulus via the efferent arteriole. The hydrostatic pressure from blood flowing through the glomerular capillaries forces water and small solutes, such as amino acids, salts, urea, creatinine, and glucose, out of the plasma. In addition to filtering based on the size of molecules, the glomerular filtration barrier also selects molecules based on charge. Many components of the filtration barrier are negatively charged, and this therefore prevents negatively charged molecules, such as plasma proteins, from crossing the barrier. Importantly, while large proteins such as albumin are generally blocked by the filtration barrier, approximately 0.06% of plasma albumin manages to pass through the filtration barrier, owing to the flexibility and ellipsoid shape of the albumin molecule enabling it to slide through the filtration slits[7]. The majority of the filtered albumin is then reabsorbed, predominantly by the proximal tubule, resulting in very low albumin excretion in the urine of healthy individuals. The resulting ultrafiltrate is forced into the Bowman's space and then passes through to the proximal tubule at the urinary pole of the renal corpuscle.

The Proximal Tubule

The proximal tubule is responsible for reabsorption of proteins, amino acids, and glucose, and most of the reabsorption of water and salts from the ultrafiltrate produced in the renal corpuscle. Nitrogenous waste products, including urea and creatinine, are not reabsorbed at any point throughout the tubules, and remain in the filtrate. Cells of the proximal tubule are highly adapted for reabsorption, with a dense brush border of microvilli on the apical surface of tall tubular cells, which greatly increase the surface area available for reabsorption. The proximal tubule reabsorbs around 50 – 60% of the water and solutes filtered by the glomerulus[8]. The proximal tubule consists of a convoluted and a straight portion, and there is significant morphological variation throughout the tubule, and as such it can be divided into three segments, S1, S2, and S3. The S1 and S2 segments have greater rates of water and solute reabsorption, whilst the S3 segment establishes high solute concentration gradients[8]. Further along the proximal tubule, the cells become shorter in height and the brush border diminishes, eventually leading from the straight portion of the proximal tubule, to the loop of Henle.

The Loop of Henle

The loop of Henle consists of three distinct portions, the thin descending limb, the thin ascending limb, and the thick ascending limb, all of which are surrounded by an extensive vascular network, the vasa recta. The loop of Henle provides a 'counter-current multiplier' function, the purpose of which is to modify the water and solute content of the ultrafiltrate to produce a concentrated urine. The cells of the different portions of the loop have differing permeability to water and salts, thus creating an osmotic gradient in the renal medulla. The thin descending limb is freely permeable to water and salts, allowing water to passively diffuse by osmosis into the interstitial space, while sodium chloride (NaCl) and urea diffuse from the blood in the vasa recta into the lumen of the loop. The thin ascending limb is permeable to salts but impermeable to water, and the thick ascending limb is impermeable to water, and actively transports NaCl from the filtrate.

The Distal Tubule

Like the proximal tubule, the distal tubule is divided into a straight and a convoluted portion. The straight distal tubule is continuous with the thick ascending limb of the loop of Henle and also functions to actively pump NaCl out of the lumen of the tubule, whilst remaining impermeable to water. The distal tubule travels from the medulla back to the cortex and transitions from a straight tubule to the convoluted tubule. The convoluted distal tubule is responsible for removing any remaining sodium, and actively secretes hydrogen and potassium ions into the filtrate.

Following glomerular filtration and tubular modification of water and solute content, the resulting product is a concentrated urine, containing nitrogenous waste products and excess water. Urine is transported from the distal tubule, via a collecting tubule, to the collecting duct.

The Collecting Duct

The collecting duct is the final portion of the nephron, and serves multiple collecting tubules in the surrounding area. The collecting duct then delivers the urine to the renal pelvis, which is continuous with the ureter, and transports urine into the bladder.

1.1.2 Additional Functions of the Kidney

The kidney is also involved in maintaining homeostasis across the whole body. The regulation of electrolyte concentrations and acid-base balance is achieved by removing Na^+, Cl^-, and

bicarbonate from the filtrate, and secreting H^+ and K^+ into the filtrate. The kidney also participates in the renin-angiotensin-aldosterone system in order to regulate extracellular fluid volume and sodium and water balance, thus regulating blood pressure. Renin is secreted by juxtaglomerular cells in the kidney in response to various factors, including hydrostatic pressure in the afferent arterioles of the glomeruli, angiotensin II levels, and sodium concentration in the macula densa. Renin is an enzyme which cleaves angiotensinogen, produced by the liver, forming angiotensin I. Angiotensin-converting-enzyme (ACE) then converts angiotensin I to angiotensin II. There are two subtypes of receptor which angiotensin II acts upon, each with opposing roles. In addition to various other roles, activation of type I receptors leads to systemic and renal vasodilation, thus decreasing blood pressure, and activation of type II receptors leads to systemic and renal vasoconstriction, thus increasing blood pressure[9].

As such, the kidney is a vital organ involved in various important aspects of whole-body homeostasis. Dysfunction of the kidney is therefore a serious health problem which reduces the quality of life of an individual and can lead to death.

1.2 Acute Kidney Injury and Chronic Kidney Disease: A Global Problem

1.2.1 Acute Kidney Injury

Kidney disease constitutes a serious health problem worldwide, with high costs for both the patient and the economy. Acute kidney injury (AKI) is defined as a rapid decline in kidney function over hours or days; resulting in a systemic accumulation of waste products such as creatinine and urea[10]. AKI is a common complication in hospitalised patients; affecting around 20% of adults and 30% of children worldwide[11], with risk factors including older age, underlying chronic kidney disease (CKD), and pre-existing conditions such as cardiovascular disease and diabetes mellitus[12]. AKI can arise from a wide range of aetiologies, predominantly ischemia[13,14], drug toxicity[15-18], or sepsis[19,20], and can range in severity from mild changes in kidney function to severe impairment of function requiring renal replacement therapy (RRT). AKI is associated with high morbidity and mortality: approximately 1 - 2% of AKI patients require RRT, and of those, 40 - 60% do not survive[21]. Previously, the term acute renal failure (ARF) was used to describe the acute loss of kidney function, however as the understanding of the syndrome increased, it became apparent that even mild changes in serum creatinine were associated with mortality[22]. As such, the term AKI was developed in order to reflect the wide spectrum of injury possible.

Until relatively recently, there was a lack of standardisation for the characterisation and definition of AKI, with more than 35 different definitions used in AKI diagnosis[23]. The requirement for standardisation in staging AKI led to the development of the RIFLE criteria by the Acute Kidney Injury Network[24]. RIFLE is an acronym reflecting the increasing severity stages of kidney injury: **R**isk, **I**njury, **F**ailure; and the potential outcomes: **L**oss and **E**nd-Stage Renal Disease (ESRD). This system was further refined to include patients with mild changes in serum creatinine of just 0.3mg/dL and above, and to exclude the 'L' and 'E' outcomes[25], and thus a three-stage classification system was developed[25,26] (Table 1.1).

Table 1.1: The stages of AKI. *Table adapted from Kidney Disease: Improving Global Outcomes (KDIGO) Clinical Practice Guideline for Acute Kidney Injury.*

Stage	Serum Creatinine	Urine Output
1	1.5 – 1.9 times baseline OR ≥ 0.3 mg/dL	< 0.5ml/kg/h for 6 – 12h
2	2.0 – 2.9 times baseline	< 0.5ml/kg/h for ≥ 12h
3	3.0 times baseline OR ≥ 4.0 mg/dL OR initiation of RRT	< 0.3 ml/kg/h for ≥ 24h OR anuria for ≥ 12h

The tubules are the predominant site of injury in AKI, and while there are some differences in the pathophysiology depending on the aetiology of AKI, common histopathological findings include a loss of the brush border on proximal tubules, detachment of tubular epithelial cells, sloughing of cells and cellular debris into the lumen of tubules, and the formation of casts within tubules[13,27]. The proximal tubule is the most sensitive part of the tubule to injury for two main reasons. 1) During ischemia, cells of the proximal tubule cannot efficiently use glycolysis for adenosine triphosphate (ATP) production, and as such are highly sensitive to ischemia; 2) the majority of tubular reabsorption takes place in the proximal tubule, so toxins filtered by the glomerulus will affect proximal tubular cells the most[28]. However, the kidney has a remarkable capacity for regeneration following an episode of AKI. Surviving tubular cells dedifferentiate to a progenitor-like state, migrate along the basement membrane of the denuded tubule, where they then proliferate and re-differentiate to replace lost tubular cells[13,28,29]. However, AKI is often associated with maladaptive repair, in which the resolution of kidney injury and functional recovery are incomplete, leading to persistent and progressive loss of kidney function. Maladaptive repair following AKI is more

common with increasing age, chronic insults to the kidney, and other co-morbidities, and is characterised by tubular loss, fibrosis, glomerulosclerosis, chronic inflammation, and vascular rarefaction[30].

1.2.2 Chronic Kidney Disease

Chronic kidney disease is defined as an abnormality of kidney structure and/or function, which persists for more than three months[31]. CKD is an increasingly common problem worldwide, with an estimated prevalence of 11 - 13% of the global population[32]. The aetiology of CKD in adults is often multi-factorial, with risk factors including diabetes[33], hypertension[34,35], obesity[34,36], older age[37], and a previous episode of AKI[38], in addition to various other factors including gender, ethnicity, and socio-economic status[39]. Conversely, CKD in children and young adults under around 25 years tends to arise from primary renal disease of genetic origin[40,41].

CKD is primarily classified based on the estimation of glomerular filtration rate (GFR)[31] (Table 1.2). There are no specific treatments for CKD. The progression of CKD to more advanced stages is currently only controlled by general lifestyle management, such as controlling blood pressure, having a good diet, and regular exercise[31]. When patients reach stage 5, they are deemed to be in renal failure, and are put on RRT in the form of dialysis, or ultimately, a kidney transplant.

Table 1.2: The stages of CKD. *Table adapted from Kidney Disease: Improving Global Outcomes (KDIGO) CKD Work Group. Clinical Practice Guideline for the Evaluation and Management of Chronic Kidney Disease.*

Stage	GFR (ml/min/1.73m^2)	Description	
1	> 90	Normal kidney function	Only classed as CKD in the presence of other evidence of kidney damage
2	60 - 89	Mildly reduced kidney function	*e.g*. albuminuria, histological/structural abnormalities
3a	45 – 59	Moderately reduced kidney function	
3b	30 - 44		
4	15 - 29	Severely reduced kidney function	
5	< 15	Kidney failure (ESRD)	

1.2.3 The relationship between AKI and CKD

Previously, it was thought that AKI and CKD were entirely separate conditions[38], and moreover, that AKI was a transient condition, whereby patients who survived AKI recovered fully and suffered no long-term consequences[42]. However, functional recovery is generally assessed by serum creatinine (SCr) levels, which is an insensitive biomarker[43,44], and there is now evidence showing that in fact many patients never fully return to pre-injury kidney function levels[45]. Furthermore, a single episode of AKI may predispose patients to subsequent CKD[38,46 47,48] or may even lead directly to ESRD[49]. The severity of AKI predicts progression to CKD, with patients who require dialysis being over 5,000 times more likely to progress to CKD than patients with less severe AKI[46]. In fact, it is now understood that AKI and CKD are closely interlinked conditions and each condition is a risk factor for the other: patients who have suffered AKI are at higher risk of developing CKD and ESRD than patients without AKI; patients with underlying CKD have a higher risk of suffering an episode of AKI, and such patients are less likely to recover from AKI and the underlying CKD may be exacerbated[38] (Fig. 1.2). Despite improved understanding of the links between AKI and CKD, the transition from AKI to CKD is poorly understood.

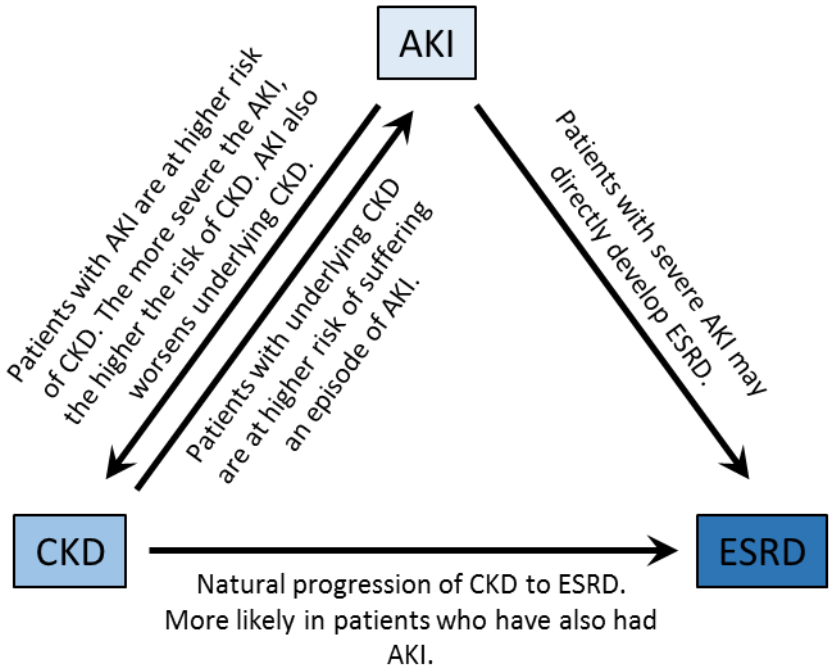

Figure 1.2: Diagram explaining the relationship between AKI, CKD, and ESRD.

1.2.4 Current Treatment Options

There are currently no specific treatments for AKI or CKD, and despite research efforts into different therapeutic interventions for reducing the severity of AKI[50], none have yet been approved for use in the clinic. Treatments for AKI patients primarily remain at simply controlling blood pressure, avoiding nephrotoxins, and providing RRT[26]. RRT is required for patients with severe AKI, and for CKD patients whose kidney disease progresses to stage 5, placing them in end stage renal disease. While dialysis is effective at performing filtration and elimination of waste products, it does not perform other important functions of the kidney, such as hormone regulation and the production of vitamin D[51]. Additionally, dialysis is cumbersome for the patient, often requiring multiple hospital visits every week for haemodialysis, or daily dialysis at home for peritoneal dialysis[52], and can be associated with various side-effects including fatigue, low blood pressure, sepsis, and peritonitis[53]. As such, dialysis is a relatively short-term solution, and while this is sufficient for sustaining AKI patients until kidney function improves, a kidney transplant is ultimately required for patients with ESRD. The number of patients registered in the UK as waiting for a kidney transplant has declined slightly in recent years[54] (Fig. 1.3), however the number of donor kidneys available for transplant still does not come close to meeting the demand. In 2015/16, there were 5,275 patients registered in the UK as waiting for a kidney transplant, but only 3,263 kidney transplants were performed in the same time period. The gap between the number of donor kidneys required and those available for transplant is even greater in the United States[55].

The problem with the lack of donor kidneys has been partially addressed by the introduction of expanded criteria donors (ECD), whereby high-risk donors that previously would have been deemed unsuitable for kidney donation are now accepted. ECDs are classed as donors over the age of 60, or those aged 50 – 59 with two of the following medical risk factors: a history of hypertension, a serum creatinine value greater than 1.5 mg/dL, or a cerebrovascular accident (stroke) as the cause of death[56]. It is recommended that ECD kidneys are preferentially transplanted to patients with a high risk of mortality on dialysis, and are unlikely to survive long enough to receive a standard kidney[56]. However, ECD kidneys are reported to have lower long-term graft survival than standard kidneys[57-59], and despite the additional kidneys available for transplant, there are still not enough donor kidneys to meet the demand, and many patients die while waiting for a transplant[54,55].

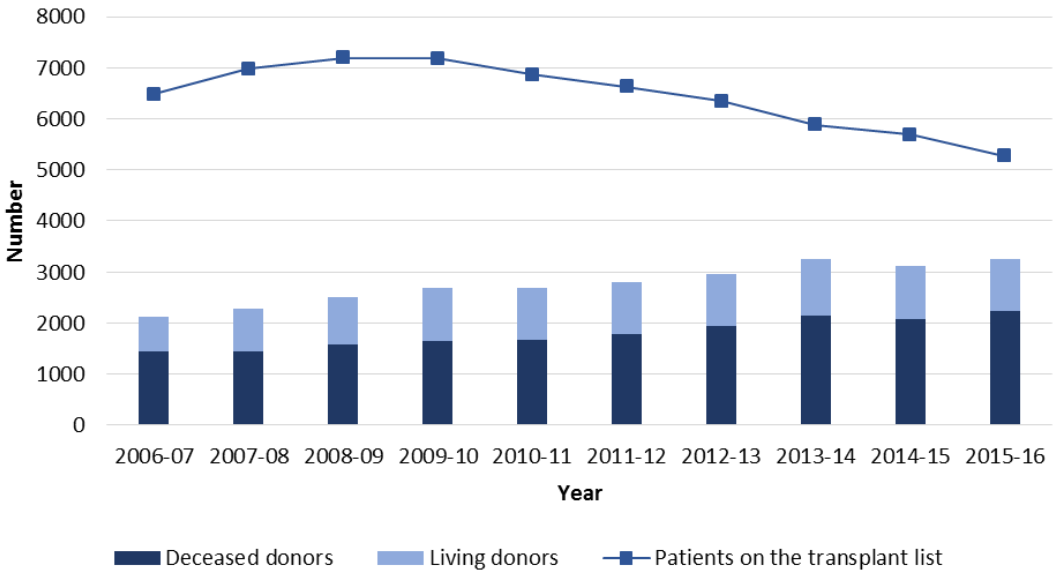

Figure 1.3: Kidney transplants in the UK. Data obtained from the NHS Blood and Transplant Organ Donation and Transplantation Activity Reports in the years from 2006/07 – 2015/16.

There is therefore an urgent need for new therapies to treat kidney disease: to reduce the initial severity of AKI, to improve recovery following an episode of AKI, to reduce the risk of developing CKD following an episode of AKI, and to slow down the progression of CKD to ESRD. Regenerative medicine therapies (RMT) may provide a new therapeutic strategy for treating kidney diseases.

1.3 Regenerative Medicine Therapies

RMTs encompass a broad range of advanced therapy medicinal products, including cell therapy, gene therapy, and tissue engineering[60]. This thesis will focus on the use of cell-based therapies for ameliorating kidney disease.

Stem cells are rare cells within tissues that have an unlimited capacity for self-renewal and can differentiate to form mature cells of the body[61,62]. There are many different types of stem cells, but can be broadly categorised into pluripotent stem cells (PSCs) and adult stem cells (ASCs). PSCs are immature cells capable of differentiation to form the three embryonic germ layers: endoderm, mesoderm, and ectoderm. They can be isolated from the inner cell mass of embryos (embryonic stem cells, ESCs)[63-65], or can be generated by reprogramming terminally differentiated somatic cells back to a pluripotent state (induced pluripotent stem cells, iPSC) by the viral introduction of four transcription factors; Oct3/4, Sox2, c-Myc, and

Klf4: the 'Yamanaka factors'[66,67]. As iPSCs are derived from somatic cells, they circumvent many of the ethical issues surrounding the isolation of ESCs from embryos, and are not subject to the same legal regulations as ESCs.

On the other hand, ASCs are multipotent or unipotent stem cells, and as such are more limited in the cell types that they can form. One of the most well-studied ASCs is the haematopoietic stem cell (HSC), which is found in the bone marrow and in cord blood. HSCs are responsible for forming all types of blood cells in the circulation[68-70], and the potency of HSCs is such that it is possible to completely replenish the haematolymphoid system in a lethally-irradiated mouse with just a single HSC[70]. HSC transplants are now commonly used in the clinic for treating a range of haematological disorders, including blood malignancies such as leukaemia and lymphoma, and non-malignant disorders such as sickle cell anaemia, Fanconi anaemia, and auto-immune disorders[71,72].

In addition to HSCs, the bone marrow also contains mesenchymal stem/stromal cells (MSCs), which are multipotent cells that form components of the skeletal system: bone, cartilage, fat, and the supporting stroma[73,74]. MSCs are a highly heterogenous cell population, consisting of both true stem cells, with an unlimited capacity for self-renewal, in addition to multipotent stromal cells, capable of forming multiple cell types, but not unlimited self-renewal. As such, the International Society for Cellular Therapy suggested in 2005 that the term 'mesenchymal stem cell' should be restricted only to the subset of these cells which display true stem cell properties, whilst the term 'multipotent mesenchymal stromal cell' should be used for describing the unfractionated, heterogenous cell population[75]. The acronym 'MSC' is still used to describe both subsets of cells; in this thesis it is intended to describe mesenchymal stromal cells. There is no unique phenotypic marker by which to characterise MSCs. Rather, cells must meet the minimum criteria set out by the International Society for Cellular Therapy in order to be defined as MSCs: 1) they must adhere to plastic in culture; 2) they must express the markers CD73, CD90, and CD105 (≥ 95% positive); 3) they must not express the haematopoietic markers CD11b, CD14, CD19, CD34, CD45, CD79α, and HLA-DR (≤ 2% positive); 4) finally, they must be able to differentiate to form osteoblasts, chondrocytes, and adipocytes[76]. Since their discovery in the bone marrow in the early 1970s[77], MSCs have also been identified in various other tissue types, including umbilical cord blood[78], umbilical cord Wharton's jelly[79], adipose tissue[80], and placenta[81], in addition to most other organs in the body[82], however bone marrow-derived MSCs remain the most commonly used MSCs in research[74].

In addition to forming mesodermal tissues, MSCs have been reported to potentially transdifferentiate to form tissues of the ectoderm (epithelial cells and neural cells) and endoderm (lung, muscle, and gut cells) lineages[74] although this remains controversial. Regardless of whether or not MSCs are able to transdifferentiate, their potential application in regenerative medicine for a wide range of ailments predominantly arises from their immunomodulatory properties, rather than their 'stemness'. The pathogenesis of many diseases, including those of the kidney, have a strong immunological component, and MSCs potentially have a beneficial effect through their ability to modulate various components of the innate and adaptive immune systems, including T cells, B cells, regulatory T cells (Tregs), dendritic cells, natural killer (NK) cells, and inflammatory cytokines, to promote an anti-inflammatory environment[83]. Additionally, MSCs express low levels of human leukocyte antigen (HLA) class I molecules, and do not express HLA class II molecules[84]. As such, allogeneic MSCs are not recognised as foreign cells when transplanted to a recipient: they are 'immunoprivileged', making them very attractive cell types for regenerative medicine. Consequently, MSCs are now being widely investigated in clinical trials for the treatment of graft-versus-host disease (GvHD), a common but life-threatening immunological complication of HSC transplantation, where immunocompetent donor cells attack host tissues. MSC therapy can be administered to patients with severe GvHD who do not respond to standard corticosteroid treatment[85,86]. The beneficial effect of MSC treatment for severe GvHD is striking: LeBlanc, *et al*., who first reported the use of MSCs for GvHD, stated that of the 25 patients they had encountered with grade IV acute GvHD, the only patient who was still alive was the child who received MSC infusions; the 24 patients who did not receive MSC therapy all died within 6 months of HSC transplantation[87].

However, despite vast quantities of preclinical research into the use of stem cells to treat many different diseases, and some promising results from clinical trials, very little progress has been achieved in translating such therapies to fully-approved products available to patients. Currently, there are only three stem cell therapies approved for use in Europe: haematopoetic stem cells for the treatment of blood cancers and other blood disorders, skin biopsies (containing epidermal stem cells) for the generation of skin grafts for burn patients, and limbal stem cells to restore the sight of patients with corneal damage[88]. Inadequate data on the safety of cell-based therapies is a major obstacle in the clinical translation of therapies[89-92].

1.4 Animal Models of Kidney Disease and Preclinical Studies of RMT Efficacy

AKI and CKD in humans can arise from many different aetiologies; ranging from clinical complications in hospitalised patients such as ischemia or sepsis, to a predisposition to developing disease resulting from a person's genetic make-up or lifestyle (*i.e.* obesity leading to type 2 diabetes). There are many different models of kidney disease in experimental animals, including both experimentally-induced diseases and spontaneously-developing disease in genetically modified animals[93,94], reflecting the wide range of aetiologies in humans. Models of kidney disease can be used for studying the pathophysiology of disease, the cellular and molecular mechanisms of the repair processes, and the efficacy of interventional therapies. In particular, preclinical research into the efficacy of stem cell therapies in experimental rodent models of kidney disease has increased rapidly in recent years (Fig. 1.4), with the majority of studies reporting beneficial effects of cell treatment in ameliorating kidney injury in experimental models.

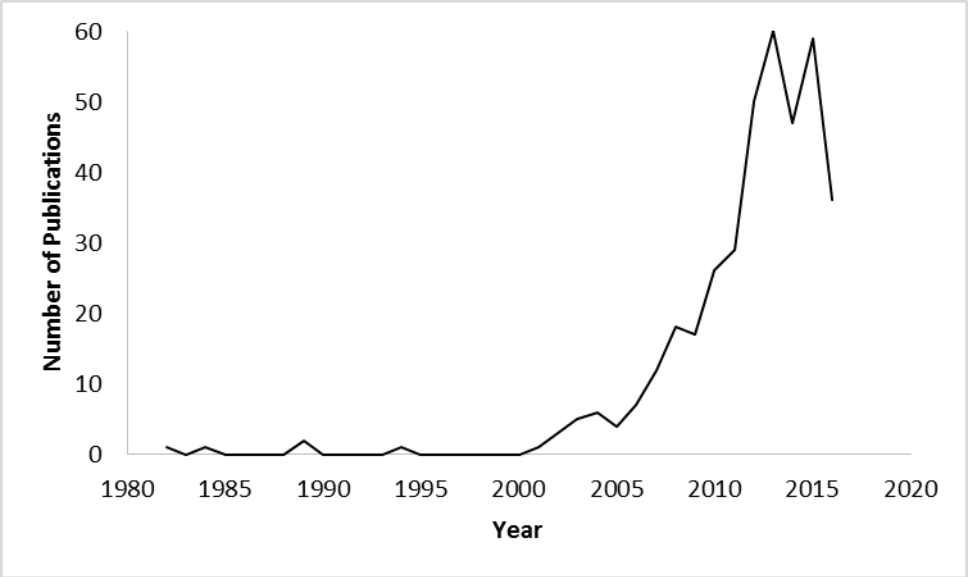

Figure 1.4: Approximate number of publications reporting on the efficacy of stem cell therapies in animal models of kidney disease up to 2016. Scopus search on 16/03/17 using the search terms: (TITLE-ABS-KEY ("stem cell") AND TITLE-ABS-KEY ("kidney disease" OR "kidney injury" OR nephropathy OR AKI OR CKD) AND TITLE-ABS-KEY (treatment OR administration OR therapy OR ameliorates OR improves OR efficacy) AND TITLE-ABS-KEY ("mouse" OR "rat")) AND DOCTYPE (ar).

An appropriate animal model must be selected in order to develop effective stem cell therapies for treating kidney diseases. There are many different animal models available, each producing certain characteristics of kidney injury that may model different aspects of the human disease. It is therefore imperative to test new therapies in the most appropriate

model for the human disease for which the therapy is intended, *i.e.* ischemic kidney injury, chemotherapy toxicity, diabetic nephropathy, ESRD, *etc.*

The most common experimental rodent models used in RMT research are described below, with some brief details on the clinical relevance, method of inducing injury, and efficacy of cell therapies for each model. Mouse models of ischemia-reperfusion injury and adriamycin nephropathy are used in the experiments presented in this thesis, and as such more focus is placed on these models, with additional notes on their pathophysiology.

1.4.1 Models of Acute Kidney Injury

Ischemia-Reperfusion Injury

Ischemia is the most common cause of AKI in humans[95], and localised or global renal ischemia can occur following a range of causes, including cardiac surgery[96,97], sepsis[19,98], and kidney transplantation[99,100]. Owing to its clinical relevance, simplicity, and reproducibility, ischemia-reperfusion injury (IRI) is a popular experimental model of AKI. Inducing IRI in experimental animals involves surgically clamping the renal artery in rats, or both the renal artery and vein in mice (ischemia), and the subsequent release of the clamp; restoring blood flow to the kidney (reperfusion). A more detailed description of the experimental model is provided in Chapter 5.

The proximal tubules are particularly sensitive to ischemia due to the low baseline oxygenation levels of the outer medulla under normal circumstances[30,101], and an inability to use glycolytic respiration in anoxic conditions[28]. Renal ischemia leads to a loss of tubular epithelial cell polarity, disruption of cytoskeletal integrity, loss of the proximal tubule brush border, and mislocation of cell adhesion molecules and membrane proteins soon after the onset of injury. This is followed by apoptosis and necrosis of tubular cells, and, due to inadequate cell adhesion, both viable and non-viable cells slough off from the basement membrane into the lumen of the tubule. Cellular debris builds up in the tubule lumen and complexes with proteins to form tubular casts, causing a physical obstruction and increased intratubular pressure[13]. The function of the injured, obstructed proximal tubule is therefore compromised, causing impaired solute reabsorption. Increased solute concentration in the distal tubule is detected by the macula densa, causing tubulo-glomerular feedback signals which result in a decrease in the afferent arteriole blood pressure and subsequent reduction in GFR[13]. In most cases, regeneration occurs to repair damaged tubules, as described previously in '*1.2.1 Acute Kidney Injury'.*

The molecular pathophysiology of ischemic kidney injury in response to vascular endothelial cell and tubular epithelial cell damage is highly complicated, involving the interaction of various chemokines/cytokines and inflammatory cells. In cases of prolonged ischemia, anaerobic metabolism results in a decreased in cellular pH, depletion of ATP, and an accumulation of lactate. Subsequent reperfusion, whilst restoring cellular oxygen levels and physiological pH, causes an influx of reactive oxygen species (ROS) and nitric oxide, resulting in oxidative stress and damaging the endothelial cells of the renal microvasculature[102,103]. This in turn leads to a breakdown in the glycocalyx, disruption of the actin cytoskeleton, and loss of endothelial cell-cell contacts and barrier function, resulting in increased microvascular permeability and leakage of fluid into the interstitium (oedema)[13]. The damaged endothelial cells also increase their expression of cell adhesion molecules, resulting in endothelium-leukocyte interactions, and leading to the activation and recruitment of further leukocytes, production of inflammatory cytokines, and the development of a pro-inflammatory state[13].

The pathophysiology of renal ischemic injury has a strong immunological component, comprising both the innate and adaptive arms of the immune system. The immune response is activated early after the induction of injury, following the release of pro-inflammatory damage-associated molecular patterns (DAMPs) from cells damaged by hypoxia, and the upregulation of hypoxia inducible factors (HIFs), cell adhesion molecules, pro-inflammatory cytokines, and upregulation of toll-like receptors (TLRs) on tubular epithelial cells[104,105]. These factors promote the rapid infiltration of macrophages, lymphocytes, dendritic cells, and neutrophils. Cells of the innate immune system predominate in the early phase of injury, whereas lymphocytes of the adaptive immune system are recruited several hours after injury, and are the most common immune cells throughout the later phase of injury[13,105]. Macrophages are key components of both injury and repair following renal IRI. Macrophages can be broadly categorised into two types: classically-activated M1 macrophages produce pro-inflammatory cytokines and are involved in defence against infection and tumours, whereas alternatively-activated M2-spectrum macrophages have an anti-inflammatory role and are involved in regulating tissue repair[106]. Pro-inflammatory M1 macrophages predominate in the initial phase of kidney injury, and depletion of macrophages prior to inducing renal ischemia protects the kidney from injury, demonstrating that the initial influx of macrophages into the kidney acts to promote damage. Conversely, macrophages are mainly polarised to an anti-inflammatory M2 phenotype during the later repair phase, and depletion of macrophages 3 – 5 days after ischemia (during the repair phase) exacerbates injury[107]. Macrophages can be activated by a wide range of stimuli, and thus change their

phenotype in response to the local microenvironment. Macrophages stimulated to an M1 phenotype *in vitro* and administered to mice during the repair phase are able to switch to a M2 phenotype to help promote tissue repair[107].

Because of its popularity as an experimental model of AKI, the IRI model has been used in a vast number of studies assessing the efficacy of RMTs. Table 1.3 summarises just some of these studies, with more focus placed on reports published in recent years.

Collectively, these studies demonstrate that various different cell types have the capacity to ameliorate structural and functional injury, as shown by reduced SCr, blood urea nitrogen (BUN), and histopathological tubular injury scores. Many studies show that cell therapy leads to significantly increased proliferation and reduced apoptosis of tubular cells[108-121]. This is achieved by modulating the immune response to injury, by downregulating the expression of pro-inflammatory cytokines such as interleukin (IL)-1β, IL-6, and tumour necrosis factor-alpha (TNF-α)[108,112-116,118,121,122] and upregulating anti-inflammatory cytokines such as IL-10 and IL-4[108,112,115,116,118,119,121,122]. Immune cell infiltration to the post-ischemic kidney is attenuated, with a decrease in total macrophage infiltration[108,110,114,118,122] but an increase in the proportion of anti-inflammatory M2-polarised macrophages[122]. Moreover, oxidative stress is reduced by increasing levels of antioxidant enzymes, such as glutathione reductase, glutathione peroxidase, and heme oxygenase-1[108,111,115,121]. Altogether, these effects act to limit the damage caused by inflammation and oxidative stress, thereby limiting tubular cell damage and preserving renal function.

Most efficacy studies have been carried out with MSCs (of various sources, generally bone marrow-derived) and following intravenous administration. Other cell types and administration routes have also been investigated, however it is still unclear as to which is the best cell type and administration route to achieve maximum efficacy.

Table 1.3: Summary of studies assessing the efficacy of cell therapies in the IRI model. h, human; m, mouse; r, rat; AD, adipose-derived; ASCs, adipose stem cells; BM, bone marrow-derived; CM, conditioned media; EPC, endothelial progenitor cell; ERC, endometrial regenerative cell; EV, extracellular vesicles; EX, exosomes; FKCs, fetal kidney cells; Gl, glomerular; iPSC, induced pluripotent stem cell; KC, kidney cell; MSC, mesenchymal stem cell; RPC, renal progenitor cell; SVF, stromal vascular fraction; UC, umbilical cord; UCB, umbilical cord blood; WJ, Wharton's jelly; CA, carotid artery; IP, intraperitoneal; IR, intra-renal; JV, jugular vein; RA, renal artery; RC, renal capsule; RP, renal parenchyma; SRA, suprarenal aorta; ND, not determined

	Reference	Cell type & source	Cell dose	Route and timing of administration	IRI model & ischemia time	Functional & structural improvement	Increased proliferation	Decreased apoptosis	Decreased pro-inflammatory cytokines	Increased anti-inflammatory cytokines	Decreased immune cell infiltration	Decreased oxidative stress markers	Summary of Key Findings
Bone marrow-derived cells	Ornellas *et al.,* (2017)	rBM-MCs	1.0 x10^6	JV; 1h	rat bilateral 60 min	✓	✓	✓	✓	✓	✓	✓	rBM-MCs ameliorated functional and structural injury, with increased proliferation and decreased apoptosis of tubular cells. BM-MCs modulated expression of cytokines and antioxidant mediators.
	Cai *et al.,* (2014)	rBM-MSCs	up to 1.0 x10^6	IV vs CA vs RA; 0h	rat unilateral w/ Nx 45 min	✓	ND	ND	ND	ND	ND	ND	RA administration was found to be superior to IV and CA, but the beneficial effects diminished with increasing cell doses, due to occlusion of glomerular capillaries by rBM-MSCs and subsequent decreased blood flow to the kidney
	Zhou *et al.,* (2013)	rBM-MSCs	up to 5.0 x10^6	IV vs RA; 0h	rat unilateral w/ Nx 60 min	✓	✓	ND	ND	ND	ND	✓	rBM-MSCs ameliorated functional and structural injury, promoted tubular cell proliferation, and restored tissue antioxidant enzyme levels independent of dose or route of administration.

Bone marrow-derived cells	Togel *et al.,* (2009)	rBM-MSCs	up to 5.0 $\times 10^6$ per kg BW	SRA; 0h	rat bilateral 58, 40, or 35 min	✓	ND	ND	ND	ND	ND	ND	rBM-MSCs improved renal function recovery in the short-term, and preserved long-term renal function at 3 months, independent of cell dose. Autologous rBM-MSCs had greater efficacy than allogeneic cells at comparable doses. VEGF is an important mediator in renal protection of rBM-MSCs. No long-term adverse effects were observed.
	Semedo *et al.,* (2009)	rBM-MSCs	2.0 $x10^5$	IV; 6h	rat bilateral 60 min	✓	✓	✓	✓	✓	ND	ND	rBM-MSCs ameliorated functional and structural injury, and increased proliferation. rBM-MSCs polarised the immune response towards a Th2 profile (decreased pro-inflammatory cytokines and increase anti-inflammatory cytokines)
	Wise *et al.,* (2014)	hBM-MSC	1.0 $x10^6$	IV; 0h	mouse unilateral 40 min / bilateral 25 min	✓	✓	ND	ND	ND	ND	ND	hBM-MSCs ameliorated injury and increased tubular cell proliferation. IV-administered hBM-MSCs homed to injured kidneys (either via lungs or directly). MSCs induced M2 Mϕ polarisation *(in vitro)*.
	Xing *et al.,* (2014)	mBM-MSCs *vs* CM	2.0 $x10^6$	IV; day 1	mouse unilateral 30 min / bilateral 28 min	✓	✓	✓	ND	ND	✓	ND	mBM-MSCs, but not CM, attenuated functional and structural renal injury, increased tubular cell proliferation, decreased tubular cell apoptosis, and decreased Mϕ infiltration. Daily high-dose administration of CM still had no effect.
Adipose tissue-derived cells	Zhou *et al.,* (2017)	hAD-MSCs *vs* hAD-SVF	2.0 $x10^6$	RP; 0h	rat unilateral 45 min	✓	✓	✓	✓	✗	ND	ND	Both hAD-MSCs and hAD-SVF cell therapies ameliorated functional and structural injury, with no differences between the two cell types. Cytokine modulation, increased proliferation, decreased apoptosis, and decreased microvascular rarefaction were observed following cell therapy

Adipose tissue-derived cells	Sheashaa *et al.*, (2016)	rAD-MSCs	1.0 x10^6	IV; 4h	rat unilateral w/ Nx 45 min	✓	ND	ND	ND	ND	ND	✓	rAD-MSCs ameliorated functional and structural injury, with attenuated oxidative stress
	Lin *et al.*, (2016)	rAD-MSCs *vs* rAD-MSC-EX *vs* combination of cells + EX	1.2 x10^6	IV; 3h	rat bilateral 60 min	✓	ND	✓	✓	ND	✓	✓	rAD-MSCs and rAD-MSC-EX both ameliorated functional and structural injury, but a combination therapy of both cells and EXs had greater efficacy than either therapy alone. Combination therapy led to greatest reduction in markers of inflammation, apoptosis, and oxidative stress.
	Donizetti-Oliveira *et al.*, (2012)	mASCs	2.0 x 10^5	IP; 4h or 6 weeks	mouse unilateral 60 min	✓	✓	ND	✓	✓	ND	ND	ASCs improved kidney histology by reducing inflammation and hypoxia, without migrating to kidneys. Late administration (week 6) of ASCs improved renal fibrosis at week 10.
	Chen *et al.*, (2011)	rAD-MSCs	(3x) 1.0 x10^6	IR; 0h & IV; 6h, 24h	rat bilateral 60 min	✓	ND	✓	✓	✓	ND	✓	rAD-MSCs ameliorated functional and structural injury by decreasing inflammation, oxidative stress, and apoptosis.
Umbilical cord related cells	Liang *et al.*, (2015)	hWJ-EPCs	5.0 x10^5	RC;0h	mouse unilateral w/ Nx 40 min	✓	ND	✓	✓	ND	ND	✓	hWJ-EPCs ameliorated functional and structural injury, with increased proliferation and decreased apoptosis of tubular cells, decreased ROS production, microvascular rarefaction, and fibrosis.
	Jang *et al.*, (2014)	hUCB-MSCs	up to 3.0 x10^6	IP or IV; -24h & 0h	mouse bilateral 27 min	✓	ND	ND	✘	✘	✓	ND	hUCB-MSCs could attenuate early functional and structural renal damage, and VEGF production had a role in efficacy. Injection route and dose did not affect efficacy.
	Li *et al.*, (2013)	hUC-MSCs	2.0 x10^6	IV; 24h	mouse bilateral 30 min	✓	✓	✓	✓	✓	✓	ND	hUC-MSCs ameliorated functional and structural injury, with increased proliferation and decreased apoptosis of tubular cells. hUC-MSCs modulated cytokine expression, decreased Mϕ infiltration, and promoted M2 polarisation *(in vitro)*.

Kidney-derived cells	Gupta *et al.,* (2015)	rFKCs *vs* CM	2.0 x10^6	IV; 24h cells or 24h, 48h, 72h CM	rat bilateral 45 min	✓	✓	✓	✓	✓	ND	✓	FKCs ameliorated functional and structural injury, with increased proliferation and decreased apoptosis of tubular cells, modulation of cytokine expression, and upregulation of antioxidant enzyme expression. CM had no effect on functional injury.
	Ranghino *et al.,* (2017)	hGl-MSCs *vs* hGl-MSC-EV *vs* hKCs *vs* hKC-EV	1.0 x10^6 cells or 230-480 x10^6 EVs	IV; 0h	mouse unilateral w/ Nx 35 min	✓	✓	✘	ND	ND	ND	ND	hGl-MSCs and hKCs ameliorated functional and structural injury, but hGl-MSCs had greater efficacy with increased tubular cell proliferation. EVs from hGl-MSCs had similar efficacy to the cells, but EVs from hKCs had no effect.
iPSCs	Li *et al.,* (2015)	miPSC-RPCs in hydrogel	1.0 x10^5	RP; 0h	rat unilateral w/ Nx 45 min	✓	✓	✓	ND	✓	ND	ND	iPSC-RPCs ameliorated functional and structural injury, with increased proliferation and decreased apoptosis of tubular cells. iPSC-RPCs formed tubular structures *in vivo*.
	Toyohara *et al.,* (2015)	hiPSC-RPC *vs* CM	1.5 x10^6	RP *vs* SC; 0h; or 200µl CM IP daily	mouse unilateral w/ Nx 40 min	✓	ND	ND	ND	ND	ND	ND	hiPSC-RPCs administered RP integrated into the kidney and generated tubular structures, but did not improve kidney injury, whereas cells administered SC did not integrate, but improved functional and structural injury. Only OSR1$^+$SIX2$^+$ cells had a beneficial effect.

Cisplatin

Many different drugs are known to be toxic to the kidney[123], and in one multi-national, multi-centre study, drugs were implicated in 19% of all cases of AKI[124]. One of the most common nephrotoxicants is cisplatin (also known as cisplatinum or *cis*-diamminedichloroplatinum(II) (CDDP)). Cisplatin is a common chemotherapeutic drug used to treat a wide range of solid cancers, however the main clinical side-effect and dose-limiting factor of cisplatin in patients is nephrotoxicity[125]. Cisplatin nephrotoxicity is very common: around one-third of patients treated with a single dose of cisplatin develop AKI, and the risk of AKI increases with subsequent doses[126]. Cisplatin nephropathy is very simple and inexpensive to model in rodents, most commonly requiring a single intraperitoneal injection of 5 mg/kg in rats[127], or up to 25 mg/kg in mice[93,128]. However, this single-dose model does not accurately reflect the clinical dosing regimen whereby multiple doses would be administered. A recent report described an alternative model of cisplatin nephrotoxicity, using multiple low doses of cisplatin to induce a kidney injury in mice which more closely replicates the injury in humans[129]. Due to its clinical relevance, cisplatin is a commonly used model of AKI for studying the efficacy of RMTs. A great number of studies have been published reporting beneficial effects of various cell types in rodent models of cisplatin nephropathy, including MSCs derived from bone marrow[130-132], adipose tissue[132,133], or amniotic fluid[132], kidney-derived cells[134], and iPSC-derived renal progenitor cells[135].

Sepsis

Sepsis, a systemic reaction to overwhelming infection, is a common complication in hospitalised patients, affecting almost 30% of patients in intensive care[136]. Sepsis can both contribute to, and result from, AKI, with one report stating that 28% of AKI patients had sepsis prior to developing AKI, and 40% of AKI patients became septic soon after their AKI diagnosis[137]. There are three main experimental models of sepsis: 1) infusion of lipopolysaccharide (LPS), which models the role of endotoxin in human sepsis; 2) infusion of a single pathogen, which allows reproducible infection for studying pathogen-specific infection; 3) caecal ligation and puncture (CLP), which models polymicrobial sepsis, and is more clinically relevant and the most widely used animal model of sepsis[138]. Very little research has been published on the effects of stem cell therapy for treating sepsis-associated AKI, however Luo and colleagues recently reported some promising results, showing that intravenous MSC infusion 3h after CLP surgery improved kidney function at 24h and reduced mortality[139].

Rhabdomyolysis

Rhabdomyolysis is a condition in which skeletal muscle rapidly breaks down, releasing electrolytes, myoglobin, and enzymes such as creatine kinase, lactate dehydrogenase, and aldolase into the bloodstream[140]. The most common causes of rhabdomyolysis in adults are trauma (e.g. crush injury) and alcohol/drug abuse, whilst in children the main causes are infection and congenital disorders[141,142]. AKI is a major complication of rhabdomyolysis, occurring in around 24% of patients. Kidney damage occurs as a result of renal vasoconstriction, toxicity of released myoglobin on kidney tubular cells, and myoglobin-protein complexes leading to tubular obstruction[140]. Rhabdomyolysis is modelled in rodents by a deep intramuscular injection of 8 – 10 mg/kg 50% glycerol[143], distributing the dose equally between both hind limbs. Various stem cell therapies have shown promise in rodent models of rhabdomyolysis, including MSCs[144-146], kidney-derived cells[147-149], and interestingly, liver-derived stem cells[150]. Notably, the $CD133^+$ human kidney-derived cells utilised in many of the experiments described in this thesis were first tested for therapeutic efficacy in rodent models of rhabdomyolysis[148,151].

1.4.2 Models of Chronic Kidney Disease

Adriamycin Nephropathy

Adriamycin (ADR) (doxorubicin) is an anthracycline antibiotic capable of DNA intercalation, leading to DNA double strand breaks and subsequent apoptosis of cells[152]. As such, ADR has potent anti-tumour activity, and is commonly used clinically as a chemotherapeutic agent to treat various types of cancer[152,153]. The most potent side-effect of ADR in the clinic is cardiotoxicity[154], however it is also nephrotoxic, and patients' renal function must be closely monitored during chemotherapy to reduce the risk of AKI[153]. The mechanism by which ADR induces renal damage is poorly understood, but it is thought to be related to the generation of ROS following the reduction of ADR to semiquinone[155-158]. ADR is directly toxic to glomerular epithelial cells[159], and clipping the renal artery during ADR administration can protect the kidney from ADR nephropathy[160]. ADR causes a breakdown of the glomerular filtration barrier by initiating podocyte dysfunction and loss, and therefore disrupting the integrity of the slit diaphragm[161,162], and downregulating proteoglycan synthesis, leading to an 80% reduction in the thickness of the glycocalyx and causing a loss of charge- and size-selectivity of the GFB[163]. As a result, large proteins are able to pass through the disrupted GFB into the tubules. The abnormal presence of proteins in tubules is intrinsically toxic to the kidney[164], due to the subsequent reabsorption of proteins by proximal tubular cells, leading

to an upregulation of inflammatory mediators[165]. This therefore leads to interstitial inflammation and subsequent tubular cell dysfunction and atrophy[165,166]. When tubular protein load exceeds the reabsorption capacity of the tubules, protein is excreted into urine (proteinuria), and proteins complex with sloughed cellular debris, depositing proteinaceous casts within tubules.

Experimentally, a single intravenous administration of ADR is sufficient to induce a progressive chronic kidney injury in rodents which closely resembles the human disease, focal segmental glomerulosclerosis (FSGS)[167,168]. ADR has a very narrow 'therapeutic' window, with doses just 0.5 mg above or below the optimum dose resulting in fatal toxicity or failure to develop injury, respectively[169]. As such, the dose of ADR must be carefully optimised for the species, strain, sex, and immune-status of the animal, in addition to the batch of ADR. ADR susceptibility has been shown to be determined by a single gene locus on chromosome 16, with recessive inheritance[170]. As a result, BALB/c mice are highly susceptible to ADR nephropathy, whereas C57BL/6 mice are highly resistant[163,171]. Furthermore, immunodeficient mice, such as severe combined immunodeficient (SCID) mice are more susceptible to ADR than their immunocompetent BALB/c counterparts, requiring half the dose to induce similar levels of injury: 5.3 mg/kg for male BALB/c SCID mice, compared with around 10 mg/kg for male BALB/c mice[169,171,172].

ADR nephropathy in rodents is primarily characterised by persistent overt proteinuria and glomerular sclerosis (Fig. 1.5). Injury progression is faster in mice[171] than in rats[167]. In mice, the onset of glomerular sclerosis is evident from week 4, with expansion of the mesangium and collapse of the glomerular tuft, leading to extensive focal and global sclerosis by week six. Further histopathological features include an initial phase of increased glomerular size and hypercellularity, followed by a decrease in glomerular size and hypocellularity from week four; tubular atrophy, involving a decrease in tubular epithelial cell height and loss of the brush border; proteinaceous casts within dilated tubules; and interstitial expansion, inflammation, and fibrosis[171,172]. Ultrastructural changes detected by electron microscopy (EM) predominantly involve podocyte foot process effacement and fusion within two weeks, leading to the loss of foot processes and denudement of the glomerular basement by week six[171,172]. Typically, mice lose a lot of body weight within the first one to two weeks, losing up to 30% of the starting body weight[171], but gradually gain weight from week two onwards.

The Harris group in Sydney, Australia, have carried out extensive studies investigating the role of the immune system in the progression of ADR nephropathy in mice. They have

demonstrated that the progression of injury following ADR administration has an important immunological component, with prominent tubulointerstitial infiltration of $CD4^+$ T cells, $CD8^+$ T cells, and macrophages during injury[171]. Subsequently, the group have shown that while $CD4^+$ T cells exert a protective effect in ADR nephropathy[173], $CD8^+$ T cells are involved in aggravating injury[174]. SCID mice, which lack T and B cells but have functioning macrophages and NK cells[175], are more susceptible to ADR nephropathy[172], suggesting a role of macrophages and/or NK cells in the development of renal injury. NK cells were shown to have little effect in the development of renal injury[176], whereas macrophages played a key role in the pathogenesis of ADR nephropathy[177,178]. Moreover, inflammatory cytokines play a major role in the development of ADR nephropathy. Early work by the Harris group showed that ADR nephropathy led to significantly increased activation of the nuclear factor-kappa B (NF-κB) family of transcription factors, which mediated infiltration of inflammatory cells into the cortex of ADR injured rats, and inhibition of NF-κB resulted in amelioration of renal injury[179].

The majority of studies assessing the efficacy of cell therapies using the adriamycin model have been carried out using MSCs in rat models, and report somewhat conflicting results. Guo *et al*., (2014) and Anan *et al*., (2016) both report beneficial effects of MSCs on kidney function and structure following ADR administration, as assessed by serum biochemistry and histology, respectively[180,181]. Conversely, Zoja et al., (2012), Sarhan et al., (2014), and Magnasco et al., (2008) all describe improvements in glomerulosclerosis, but not in functional biomarkers[182-184]. Very few publications report the efficacy of cell-based therapies in mouse models of adriamycin nephropathy, however a study published by Ronconi *et al*. in 2009 is of importance to this thesis. Ronconi and colleagues isolated a population of endogenous renal progenitor cells and, using a mouse model of adriamycin nephropathy, demonstrated the ability of these cells to integrate into the injured kidney and regenerate damaged podocytes following intravenous administration, leading to improved kidney function and reduced structural damage[185].

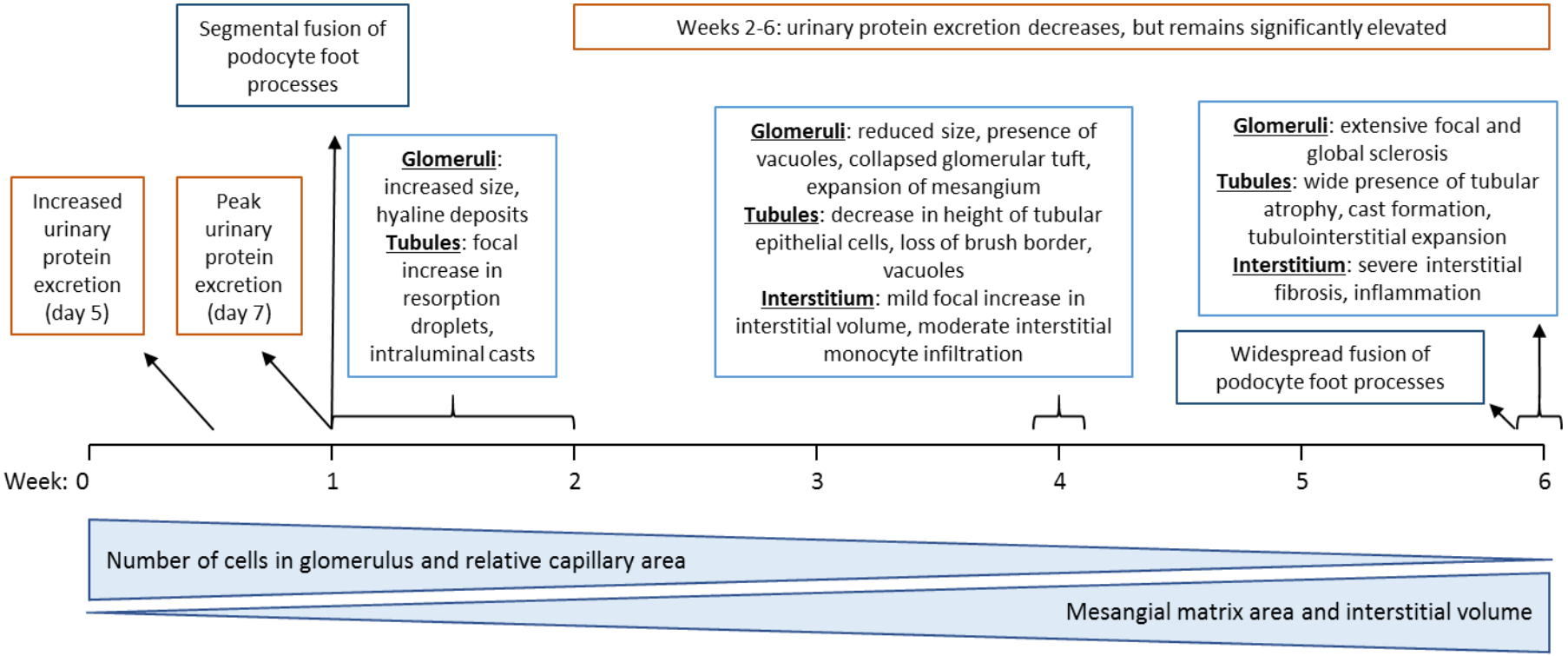

Figure 1.5: Summary of the characteristics of the progression of adriamycin nephropathy in mice, as described by Wang *et al*. (2000).

Unilateral Ureteric Obstruction

Congenital urinary tract obstruction (UTO) is the leading known cause of CKD in children[186,187], and can reduce nephron number and impair kidney growth and development depending on the severity, duration, and timing of obstruction. Unilateral ureteric obstruction (UUO) is a very commonly used experimental model, not only for studying the pathogenesis of UTOs in children, but also as a generic model of the development of renal fibrosis in CKD[188,189]. The progressive accumulation of interstitial fibrosis is a common final pathway in CKD of all etiologies[188]. The UUO model is highly predictable and reproducible in the development of renal fibrosis, in addition to being a very fast, high-throughput model[188,189], making it ideal for studying the mechanisms of fibrosis development in addition to preventative therapies. The UUO model can either be irreversible or reversible. Both models require surgery and involve either clamping[190] or ligation[191] of the ureter, leading to hydronephrosis and renal fibrosis. In the reversible model, following a period of obstruction, the clamp is removed[190] or the ligated ureter is re-anastamosed to the bladder[191], allowing the kidney to decompress and undergo repair and remodelling. For RMT studies, the irreversible model is most frequently used in order to assess the effect of cell therapy on the development of renal fibrosis. Results have shown that MSCs ameliorate renal fibrosis following obstruction, both when administered at the time of obstruction[192,193] and following seven days of obstruction[194].

Diabetic Nephropathy

Diabetes mellitus is the leading known cause of ESRD[195] and is a major problem for public health: the estimated worldwide prevalence of diabetes was 285 million in 2010, and is forecast to rise to 439 million by 2030[196]. CKD, diabetes, and cardiovascular disease are a triad of diseases that often occur together, due to complex interactions between the diseases and shared risk factors, leading to high mortality levels[33]. There are two types of diabetes: Type I (insulin-dependent) results from the autoimmune destruction of islet β-cells in the pancreas[197], whereas type II (non-insulin dependent) is characterised by hyperglycaemia and insulin resistance and is predominantly caused by a combination of genetics and lifestyle factors, such as obesity, smoking, and alcohol consumption[198]. Diabetic nephropathy (DN) occurs, at least in part, due to persistent hyperglycaemia and hyperfiltration, and is characterised by proteinuria, thickening of the glomerular basement membrane, expansion of the mesangial matrix, and progressive glomerulosclerosis[199,200]. Due to their different etiologies, type I and II diabetes are modelled separately in animals.

Type I diabetes is most commonly modelled either by administration of streptozotocin (STZ), an antibiotic that is toxic to the pancreatic β-cells[201], or by the non-obese diabetic (NOD) mouse, which develops a spontaneous destruction of pancreatic β-cells at around five months of age[201]. Type II diabetes can be modelled simply with a high fat diet, which induces obesity and insulin resistance in C57BL/6 mice[201]. However, type II diabetes is most commonly modelled by obese genetic mutant mice, such as *db/db*, *ob/ob*, the Agouti mutation, and the New Zealand Obese mouse[201], and new genetic mouse models of DN are continually developing in an attempt to more closely resemble the human disease[202-204].

MSCs have shown great promise in various models of DN, with decreased blood glucose levels reported in the majority of studies, and improved β-cell function and morphology reported in some studies, in addition to improved kidney function and histology[205]. Ezquer *et al.,* (2008) showed that MSCs administered to STZ mice after the widespread destruction of pancreatic β-cells resulted in decreased blood glucose levels within one week of MSC administration, reaching normal levels after one month[206]. Additionally, MSC therapy significantly increased the number of pancreatic islet cells and prevented the progression to nephropathy. A recent study described similar beneficial effects of BM-MSCs and conditioned media in both an STZ model of type I diabetes and a high-fat diet model of type II diabetes[207], supporting a paracrine role of MSC therapy in both DN models. The amelioration of kidney injury was characterised by a decrease in the infiltration of bone marrow-derived cells and macrophages and downregulation of pro-inflammatory cytokine expression.

Subtotal Nephrectomy

Rather than attempting to recapitulate the causes of kidney disease in rodent models, the outcome of the disease can instead be modelled. Loss of renal mass (loss of nephrons) and progressive loss of renal function is an inevitable outcome in CKD[208], regardless of the initiating cause. Moreover, low birth weight is associated with reduced nephron number, and is a risk factor for CKD in later life[39,209]; nephrectomy for the removal of renal tumours increases the risk of CKD[210]; and living kidney donation halves the donor's renal mass, with currently unproven long-term consequences[211]. In the experimental model of subtotal nephrectomy (also known as partial or 5/6 nephrectomy, or the remnant kidney model), a proportion of the total renal mass (often five-sixths) is surgically removed by unilateral nephrectomy and removal of the poles of the remaining kidney, either by ligation or ablation[93]. The proportion of renal tissue removed closely correlates with the rate of

progression to renal failure[93]. Rats are most frequently used in this model, where removal of renal mass induces progressive CKD, featuring arterial hypertension, proteinuria, and glomerular sclerosis[212]. Mice can also be used, but susceptibility is strain-dependent: CD1 mice are very susceptible to renal mass reduction, developing CKD within four weeks, and while C57BL/6 mice are highly resistant[213,214], increasing their blood pressure with administration of angiotensin II heightens their susceptibility[214]. MSCs have been shown to improve functional and histopathological damage in models of subtotal nephrectomy[215-219]. An interesting study used two subtotal nephrectomy models (5/6 and 2/3) to simulate different stages of renal failure in order to assess the effect of timing on the efficacy of cell therapy[219]. MSC therapy improved kidney function and structure in both models, however the effect was greater in the 2/3 nephrectomy model, indicating that treatment is less effective when renal failure is more advanced.

1.4.3 Benefits and Limitations of Animal Models

The benefits of modelling human disease in animals are clear: studying experimental animals allows us to understand the pathology and progression of disease in a whole-body system, and the beneficial and adverse effects of therapeutic intervention in a strictly controlled environment with appropriate controls; tasks that are limited in *in vitro* models, and clearly impossible in humans.

However, there are many limitations of animal models that must be considered. AKI and CKD are highly complex, multi-factorial diseases in humans, meaning that animal models of single-cause AKI/CKD do not faithfully recapitulate the human diseases[220-222]. Moreover, experimental models are most often carried out in young, otherwise healthy animals, and typically in inbred male animals[221,222]. This is clearly not representative of the patient population, who are first of all, genetically diverse and both male and female, and typically present with co-morbidities such as hypertension, obesity, and diabetes, and are of advanced age. An example of the gap between human disease and experimental models is the complex systemic disease, diabetes, which features complications such as cardiovascular disease, neuropathy, retinopathy, in addition to nephropathy[223]. While some of the early changes of diabetic nephropathy can be modelled in animals, such as glomerular hyperfiltration, albuminuria, and some histopathological changes, the development of renal failure is absent, and it is unknown whether this is due to an inherent resistance to nephropathy in the models used, or if the models are simply not analysed at a late enough time point for renal failure to develop[201].

However, the simplicity of animal models can be seen as a benefit in some cases. The onset of disease is known in animal models, allowing researchers to study the full course of disease progression from start to finish. Furthermore, by only modelling certain aspects of disease we can dissect out specific features of human disease and study them without confounding factors, for example, bilateral nephrectomy does not model any clinical disease, but allows the study of the effects of renal failure, without confounding effects of ischemia or toxic drugs[224]. This allows the most promising candidate therapies to be identified, and they should then be tested in more complex disease models, which should factor in age and sex heterogeneity, in addition to co-morbidities, such as modelling AKI in diabetic mice[221,222].

1.5 Traditional and Novel Measures of Assessing Kidney Function *in vivo*

1.5.1 Traditional Measures of Kidney Function

A common feature of all experimental models of kidney injury is the use of serum biomarkers SCr and BUN to evaluate kidney function. SCr is also the key parameter used clinically to diagnose and stage the level of kidney injury. However, it is widely known that SCr and BUN are insensitive and non-specific measures of kidney function[43,225]. SCr and BUN levels can be affected by both renal and non-renal factors that are unrelated to kidney function or injury, such as age, gender, muscle mass, protein intake, infection, and hydration status[43]. It has been shown in mice that creatinine excretion has a substantial secretory component, accounting for up to 50% of creatinine excretion and therefore making creatinine measurements a poor evaluation of GFR[44]. Moreover, subtle damage to the kidney can be masked by the renal functional reserve[226,227]. As such, efforts have recently gone into the search for urine and serum biomarkers that are sensitive and specific to kidney injury. Notably, kidney injury molecule-1 (KIM-1), neutrophil gelatinase-associated lipocalin (NGAL), and IL-18 have been identified as biomarkers of early AKI that identify patients before the rise in SCr[43,228].

These novel urine and serum biomarkers are slowly becoming more commonly used in preclinical renal research, however the serial collection of urine and/or blood from experimental animals still presents a major problem. Prolonged housing in a metabolic cage for urine collection is highly stressful for animals[62,229], and the adverse effects are exacerbated in animals with poor health. Spot urine collection is less stressful, however animals with AKI often exhibit oliguria or anuria, adding further difficulties to the task of urine collection. Serial blood collection is stressful for the animal, risks tissue damage, is

technically difficult in small animals, and only yields a small volume of serum for analysis[230,231]. The alternative is therefore terminal blood collection, which yields large volumes of serum, but precludes longitudinal monitoring of individual animals and, if data at multiple time points is required, necessitates large animal numbers per experiment.

1.5.2 Novel Measures of Kidney Function

Transcutaneous Measurement of FITC-sinistrin Clearance

An alternative method of measuring kidney function in small animals is the transcutaneous assessment of fluorescein isothiocyanate (FITC)-sinistrin clearance[232,233]. The device comprises two light emitting diodes (LEDs), a photoreceptor, an internal memory, and is powered by a lithium battery which is connected to the device[234]. The device is affixed to the depilated skin of the animal with an adhesive patch, and the clearance of exogenously administered FITC-sinistrin is measured through the skin (see Chapter 2: Methods for a detailed description of the protocol). The LEDs emit light at 470nm to excite the FITC fluorophore, and the photoreceptor detects the excited light with a maximum sensitivity of 525nm[234]. A reading is taken approximately every second for the duration of the measurement, allowing a kinetic assessment of FITC-sinistrin clearance. Sinistrin is an ideal dye for assessing renal function as it is a small molecule that is quickly and exclusively filtered by the glomerulus, with no secretory component[232,235,236]. Sinistrin is an analogue of the clinically used inulin, but has the advantage of being water soluble, and thus the preparation of sinistrin does not require dialysis[235,236]. The transcutaneous device has been validated against traditional inulin clearance methods of measuring GFR in rats[237] and mice[234], and was found to be more sensitive than plasma clearance measurements[237]. The transcutaneous measurement has several advantages as a method of measuring kidney function in animals:

1. It is minimally invasive, and longitudinal measurements can be performed to monitor individual animals over time[238]
2. The device is affixed whilst animals are anaesthetised, but the measurement period occurs in conscious animals, thereby limiting any effects of anaesthesia on GFR[239,240]
3. It limits stress on animals[234], since they tolerate the device very well, can eat and move freely during the measurement period, and are only separated from cage-mates for a relatively short time during the measurement. Moreover, animals are anaesthetised during the most potentially stressful parts of the procedure (device attachment and intravenous administration of FITC-sinistrin)

4. It is repeatable, with an acceptable degree of variability in day-to-day measurements[238]
5. It does not require repeated blood measurements, unlike the method of measuring clearance kinetics of plasma FITC-inulin[241]

The transcutaneous measurement of kidney function has been applied in a range of preclinical renal studies. Cowley *et al.,* (2013) demonstrated the benefit of this method over traditional creatinine measurements, showing that the transcutaneous measurement could detect a significant decrease in GFR in Dahl salt sensitive rats within 14 days on a high salt diet, despite there being no changes in creatinine clearance[242]. This method has also been used to characterise the long-term changes in kidney function in a rat model of Type 2 diabetes[243], and to assess the effect of therapeutic intervention on kidney function in animal models of non-diabetic CKD[244], sepsis[245], and cisplatin-induced AKI[134]. Importantly, Santeramo *et al.* demonstrated the value of the transcutaneous measurement in its ability to monitor individual animals longitudinally in response to cell therapy, by assessing kidney function at baseline, after cisplatin-induced AKI prior to therapeutic intervention, and subsequently after cell administration[134]. Furthermore, this method of assessing kidney function is now being explored for clinical use[246,247].

Multispectral Optoacoustic Tomography

Another novel method of assessing kidney function is by photoacoustic imaging. IRDye 800CW carboxylate (from now, referred to only as IRDye) is a near infrared (NIR) dye that is excreted predominantly by the kidneys[248,249], and its clearance through the kidney can be directly imaged and quantified by photoacoustic imaging[248]. Photoacoustic imaging is a relatively new imaging technology which relies on the photoacoustic effect, that is, the production of sound waves from light[250], in order to produce images from within the body. A short pulse of non-ionising laser energy is applied to the animal, and the tissues of the body absorb this energy and convert some of it into heat. The rise in temperature causes thermoelastic expansion, and subsequent relaxation, resulting in an acoustic pressure wave which is detected as an ultrasound wave. Different tissues of the body will have different absorption, thermal, and elastic properties, and so the resulting ultrasound waves will reach the detector at different times and amplitudes depending on the depth and characteristics of their tissue of origin. A photoacoustic image can then be generated by reconstructing the detected acoustic signals, using their magnitude and arrival times at the detector to determine their location of origin[251,252]. Specifically, Multispectral Optoacoustic Tomography

(MSOT) is capable of imaging at multiple wavelengths, and signals can be spectrally unmixed to allow the identification of specific absorbers[253]. Furthermore, MSOT employs curved signal detectors which detect signals from multiple angles[254,255], enabling 3D reconstruction of anatomical images. MSOT is most frequently used to monitor tumours *in vivo*[256], however Taruttis *et al.,* (2012) have demonstrated its potential in dynamic imaging of kidney and liver function, by directly imaging the kinetics of IRDye and indocyanine green (ICG) in the respective organs[248]. This method of monitoring kidney function has the disadvantage that the animal is anaesthetised during the measurement, and as such GFR will be decreased[239,240], however an advantage is that the kidneys can be directly visualised during measurement. Photoacoustic imaging has a penetration depth of only around two to three centimetres[251,252], which is suitable for small rodents, but limits clinical use to superficial tissues, such as imaging certain tumours[257], vasculature[258], and inflammation[259]. As such, this method of monitoring kidney function is unlikely to be applied to human use, but still presents as a valuable new method in preclinical research.

1.6 Preclinical Imaging in Regenerative Medicine Research

Imaging technologies are becoming more widely used in scientific research and have many applications in regenerative medicine research. The most commonly used imaging modalities in preclinical research are bioluminescence imaging (BLI), fluorescence imaging, magnetic resonance imaging (MRI), positron emission tomography (PET), single photon emission computed tomography (SPECT), ultrasound, and more recently, photoacoustic imaging[89,260]. Each modality has distinct advantages and disadvantages (Table 1.4), and no single modality is ideal for all applications. Some imaging technologies used in preclinical research are also available in the clinic, making them attractive for clinical translation of new imaging protocols and other techniques. However, modalities that are exclusively restricted to preclinical use are still of great value in translational research, as they can provide information that would not be possible or feasible to gather otherwise.

Broadly speaking, imaging can provide three types of data that are important in regenerative medicine: anatomical structure, organ function, and/or cell tracking, depending on the modality chosen. Cell tracking is of particular interest in this thesis, as monitoring the biodistribution of cells is a key component of assessing the safety of a cell-based RMT. Monitoring organ function is also relevant to this thesis, however photoacoustic imaging for

assessing renal function was already discussed above, and thus will not be covered again in this section.

Table 1.4: Summary of the advantages and disadvantages of the most commonly used imaging modalities in preclinical research[89, 120]

Clinical/Preclinical Use	Imaging Modality	Advantages	Disadvantages
Preclinical use only	**Bioluminescence Imaging**	• Excellent sensitivity • Good temporal resolution • Safe	• Poor spatial resolution • Signal attenuation with greater imaging depths
	Fluorescence Imaging	• Good temporal resolution • Safe	• Poor sensitivity • Poor spatial resolution • Signal attenuation with greater imaging depths
Clinically available	**Magnetic Resonance Imaging**	• Excellent spatial resolution • Unlimited penetration depth • Safe	• Poor temporal resolution - whole body imaging not feasible.
	Nuclear Imaging (PET & SPECT)	• Excellent sensitivity • Good temporal resolution • Unlimited penetration depth • Can generate quantitative data from whole body scans.	• Poor spatial resolution • No anatomical information • Exposure to ionising radiation - safety concerns
	Ultrasound Imaging	• Can monitor renal perfusion with microbubble contrast agents • Safe	• Limited to structural, rather than molecular imaging
Currently only preclinical use, with clinical translation possible	**Photoacoustic Imaging**	• Excellent sensitivity • Good spatial and temporal resolution • Can generate quantitative data • Safe	• Limited penetration depth • Imaging lungs is not possible due to air spaces

Cell tracking is conventionally performed by the histological detection of labelled cells *ex vivo*[261]. However, this requires the sacrifice of multiple animals at many time points in order to study biodistribution over time, which does not allow the longitudinal evaluation of individual animals, is time consuming for the researcher, and the very large numbers of animals required for such experiments is against the principles of the 3Rs (Replacement, Reduction, Refinement)[262]. Moreover, histological detection of cells is most commonly performed by labelling cells with fluorescent cell membrane dyes, such as PKH26 or CM-DiI, prior to *in vivo* administration[147,148,185]. A major flaw of cell membrane dyes is that they readily transfer to host tissues both *in vitro* and *in vivo*[263], potentially resulting in false positive cell tracking. Conversely, preclinical imaging is minimally invasive, allowing individual animals' responses to be monitored over time, and by using reporter genes for cell tracking, it can be very specific and reliable. The two imaging modalities used for cell tracking in this thesis are discussed in more detail below.

Bioluminescence Imaging

BLI is an optical imaging modality commonly used for the *in vivo* tracking of cells in preclinical research[264]. BLI involves the detection of light which is generated following the oxidation of the substrate luciferin by the enzyme luciferase. For cell tracking experiments, the cells of interest are virally transduced to express luciferase prior to *in vivo* administration. The luciferase-expressing cells can then be detected *in vivo* following the administration of luciferin to the animals[264-266]. Mammalian tissues do not naturally emit light, resulting in very low background signals in BLI, giving very high signal-to-nose ratios and making BLI a very sensitive imaging modality[265]. However, the light emitted by luciferase is readily scattered and absorbed by overlying tissues, resulting in attenuation of the bioluminescent signal with greater depths. This leads to poor spatial resolution and penetration depth, and makes signal quantification somewhat unreliable[264]. BLI sensitivity decreases by approximately 10-fold for every centimetre of tissue[266], however this is not too much of a problem when imaging mice, as they can simply be turned over and imaged from another aspect. Luciferase is only expressed by live cells, and the luciferase gene is passed to daughter cells following cell division[266], making BLI useful for monitoring the survival and proliferation of transplanted cells. BLI has very good temporal resolution, with acquisition times ranging from one second to a couple of minutes, depending on the intensity of the signal. Moreover, most commercial systems allow up to five mice to be imaged at a time. This makes BLI a highly useful imaging modality for fast, high-throughput, whole-body imaging, suited to longitudinal stem cell tracking *in vivo*.

BLI has been used to track the homing of systemically administered luciferase$^+$ MSCs to the injured kidney following UUO[193] and IRI[109] surgery; to compare the biodistribution of cells following different administration routes[267]; and to validate the success of cell administration via a catheter threaded through the femoral artery to deliver cells specifically to the left kidney[268]. Furthermore, Gao and colleagues used BLI to monitor the longitudinal survival of MSC following administration to the renal parenchyma after bilateral IRI. The authors found that MSCs administered in a hydrogel had improved survival and longer retention in the kidney than MSCs administered in saline, and that this resulted in greater efficacy of MSCs, as shown by increased tubular cell proliferation and decreased apoptosis[269].

In addition to the kidney, BLI is used to track cell biodistribution and survival over time in a wide range of regenerative medicine applications, including myocardial infarction[270-273], liver injury[274,275], bone injuries[276-278], acute lung injury[279,280] angiogenesis[281], arthritis[282], and

GvHD[283]. Furthermore, longitudinal tumour monitoring is a common application of BLI, with many reports in cancer models[284-286], and with a specific focus of assessing the tumourigenicity of RMTs[287,288].

Magnetic Resonance Imaging

MRI is a very common imaging technology in the clinic, and is becoming more widely used in preclinical research. MRI uses a strong magnetic field to align the spin moments of hydrogen protons within the patient or animal's body relative to the magnetic field, and radiofrequency pulses to force these spins to higher energy levels. The spins relax when the radiofrequency pulse is removed, and release energy as they do so, which is then detected by radiofrequency coils, and can be reconstructed to produce images[289,290]. The longitudinal relaxation time is termed T_1 relaxation, and the transverse relaxation time is termed T_2 relaxation[290]. In T_1-weighted images, water appears dark and fat appears bright, whereas in T_2-weighted images, water appears bright and fat appears dark. This therefore results in the characteristic greyscale images, as different tissues in the body exhibit specific T_1 /T_2 relaxation times[290]. The main advantages of MRI are that it does not use ionising radiation and is therefore safe, and it has excellent spatial resolution with unlimited tissue penetration depth, allowing the generation of highly detailed images of organs[260]. However, MRI lacks sensitivity, and the temporal resolution is poor[260], meaning that whole body scanning at high resolution is not feasible, especially as only one animal can be imaged at a time.

Superparamagnetic iron oxide nanoparticles (SPIONs) are the agent most commonly used to track cells *in vivo*[291-293]. Reporter genes which generate MRI contrast such as ferritin, tyrosinase, or β-galactosidase, can also be used, however they have limited efficacy as cell tracking agents[294,295]. Reports have shown that following arterial administration, SPION-labelled MSCs can be detected in the cortex of the kidney, but not the medulla, and Prussian blue staining of iron deposits on kidney sections identified SPIONs exclusively in the glomeruli, thus validating the *in vivo* imaging data[296,297]. MRI is also widely used to track labelled stem cells in other regenerative medicine applications, most commonly in models of stroke[298-301] and spinal cord injury[302-304].

1.7 Summary and Thesis Aims

To summarise, the kidney is a vitally important organ, involved in waste removal and homeostasis. AKI and CKD are serious diseases associated with very high morbidity and mortality. There are currently no specific treatments aimed to treat AKI or slow down the progression of CKD, and current treatments are simply aimed at good clinical care, blood pressure management, and the provision of RRT when required. Regenerative medicine therapy is a promising solution and various cell types have been shown to ameliorate injury in many models of kidney injury. However, current methods of assessing kidney function and tracking administered cells *in vivo* are not without controversy. Preclinical imaging methods offer a more reliable method of assessing kidney function and tracking cells, but are currently not widely used.

The main aims of this thesis were to:

1. Assess the use of two novel methods of assessing kidney function in mice with kidney injury, the transcutaneous measurement of FITC-sinistrin, and photoacoustic imaging of IRDye clearance kinetics
2. Assess the efficacy of human kidney-derived cells in mouse models of acute and chronic kidney disease
3. Use preclinical imaging methods to track the biodistribution of cells *in vivo*, both to assess homing to the kidneys, and the long-term safety of cell therapy

CHAPTER 2

General Methods

All reagents and assays were purchased from Sigma Aldrich, UK, unless otherwise stated.

2.1 Kidney Injury Models and *in vivo* Measures of Kidney Function

BALB/c or BALB/c SCID mice were used for all kidney injury experiments. Animals were obtained from Charles River, UK, and were housed in individually ventilated cages (IVCs) under a 12h light/dark cycle, and were provided with standard food and water *ad libitum*. Animals were allowed one week after arrival to acclimate to the new surroundings before any experimental procedures began. All animal procedures were performed under a licence granted under the Animals (Scientific Procedures) Act 1986 and were approved by the University of Liverpool Animal Ethics Committee.

Adriamycin Kidney Injury Model

Female BALB/c SCID mice age 7-8 weeks were administered with 6.3mg/kg adriamycin (doxorubicin hydrochloride; Tocris Biosciences, UK, or TEVA, Israel) in 100µl (intravenous, IV). Uninjured control animals received 100µl 0.9% saline (IV). Body weight was monitored daily for two weeks, and twice weekly thereafter.

Ischemia-Reperfusion Injury Models

Male BALB/c mice age 8-10 weeks were anaesthetised with isoflurane and O_2, given 1mg/kg buprenorphine (subcutaneous, SC), 70µl 1:10 Baytril antibiotic (SC), and 0.5ml warmed saline (SC). The surgical site was shaved and sterilised with iodine and ethanol, ophthalmic ointment was applied to prevent corneal drying, and the mouse was transferred to a heat pad on the surgical table, and a rectal probe was inserted to monitor core body temperature. The mouse was placed in the prone position with the limbs taped down, and a surgical drape was placed over the animal. Once a surgical plane of anaesthesia had been established and core body temperature was at 37°C, the kidneys were palpated through the skin and two dorsal incisions were made in the skin over the region of the kidneys. The skin was bluntly dissected from the muscle, and a smaller incision was made in the muscle layer. Depending on the model required, the kidneys may have been clamped or removed (nephrectomy, Nx).

Two models of IRI were used in this thesis:

1. Bilateral ischemia: both kidneys clamped.
2. Unilateral ischemia with contralateral nephrectomy: right kidney removed, left kidney clamped

The nephrectomy was carried out by first displacing the adrenal gland from the kidney, using a sweeping motion with forceps. 4/0 silk suture was then tied around the renal artery, vein, and ureter with a double surgical knot. The kidney was removed by cutting distally to the knot. The stump was irrigated with sterile saline and returned to the abdominal cavity. The muscle layer was closed with a continuous suture using 7/0 absorbable suture material (Clinisorb), and the skin was closed with mattress sutures using 7/0 absorbable suture material (Clinisorb).

Renal ischemia was induced by first gently holding the kidney with atraumatic blunt forceps, and dissecting fat and connective tissue away from the renal pedicel. Small holes were made in the connective tissue either side of the renal artery and vein using forceps, and a vascular clamp (Schwartz Micro Serrefine sharp angled clamp, FST, Germany) was applied to the renal artery and vein using Schwartz clip applying forceps (Roboz, South Pointe Surgical Supply, Florida, USA). The timer was immediately started. The kidney was replaced back under the skin for the duration of clamping.

Successful ischemia was indicated by a uniform colour change from red to dark purple (Figure 2.1). If the kidney was not uniformly dark purple, this indicated that the clamping was not successful and the mouse was removed from further analyses. After the appropriate clamping time, the clamp was removed. Full reperfusion was confirmed by an immediate lightening of the colour of the kidney after removal of the clamp, leading to a return to the normal red colour after a few minutes. The muscle and skin layers were closed as described above. The mouse was recovered in a heat box, and then transferred to a clean home cage. Renal ischemia-reperfusion surgery was carried out using sterile techniques to minimise the risk of infection. Post-operative checks, including monitoring weight and checking sutures and hydration status, were performed daily for the duration of the studies.

Urine Collection

Urine was collected over 24h in metabolism cages (Tecniplast, Italy) for the adriamycin model, or over 5h (3pm - 8pm) using hydrophobic sand (LabSand; Datesand Ltd, UK) for the IRI model. Metabolism cages were not used for the IRI model due to project licence restrictions. Collected urine was centrifuged to remove any contaminants, and aliquots were stored at -20°C until analysis.

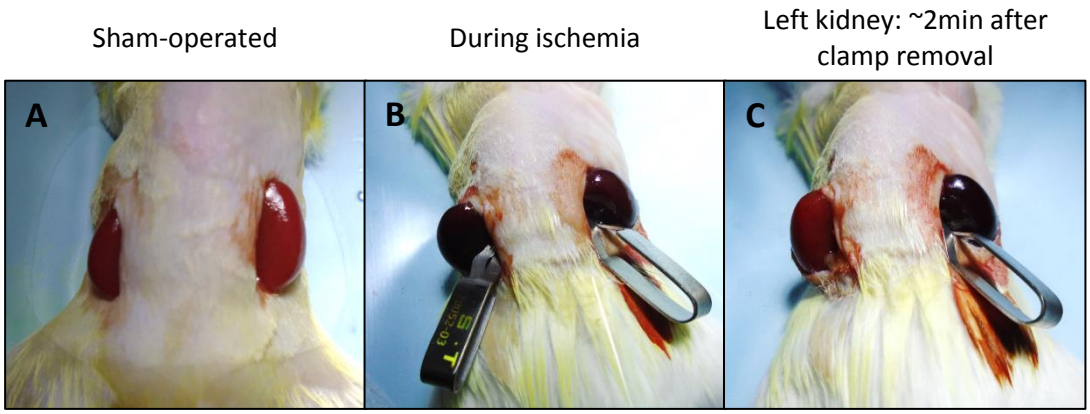

Figure 2.1: Ischemia Reperfusion Injury. Representative photographs showing the normal colour of kidneys (**A**), the colour change during ischemia (**B**), and the restoration of normal colour soon after removal of the clamp (**C**), indicating successful reperfusion.

Transcutaneous Assessment of FITC-sinistrin Clearance

Mice were anaesthetised with isoflurane and O_2, and positioned prone on a heat mat. A region of the fur on the right side of the back was removed using an electric shaver and depilatory cream (Veet for sensitive skin), which was left on for a maximum of three minutes. The transcutaneous device (NIC-Kidney; Mannheim Pharma & Diagnostics, Germany; Figure 2.2A)[234,237] was connected to a lithium battery, and attached to the shaved skin using double-sided black plaster (Mannheim Pharma & Diagnostics, Germany) which had been cut to size. The device was then secured in place with adhesive tape (Leukosilk, BSN Medical, Germany) wrapped around the abdomen of the mouse. After a period of one to three minutes to measure the background signals, 0.15mg/g body weight (BW) FITC-sinistrin (Fresenius-Kabi, Austria) was administered (IV). The mouse was recovered from the anaesthesia and transferred to a clean cage containing absorbent paper and some food pellets, and was monitored for 1h 30min (Figure 2.2B). The device was removed and the data read using MPD Lab software (Mannheim Pharma & Diagnostics, Germany). The half-life of the curve was analysed with a 3-compartment model using MPD Studio software (Mannheim Pharma & Diagnostics, Germany, Figure 2.2C)[305,306].

Multispectral Optoacoustic Tomography (MSOT) for assessing kidney function

Mice were anaesthetised with isoflurane and O_2, and placed on a nose cone on a heat mat. The abdomen was shaved using an electric shaver and a depilatory cream (Veet for sensitive skin), left on for a maximum of three minutes on the back, and two minutes on the stomach. A homemade catheter was prepared by using forceps to remove the tip from a 30G ½ inch needle, and inserting the cut end of the needle in to one end of 35cm fine bore catheter

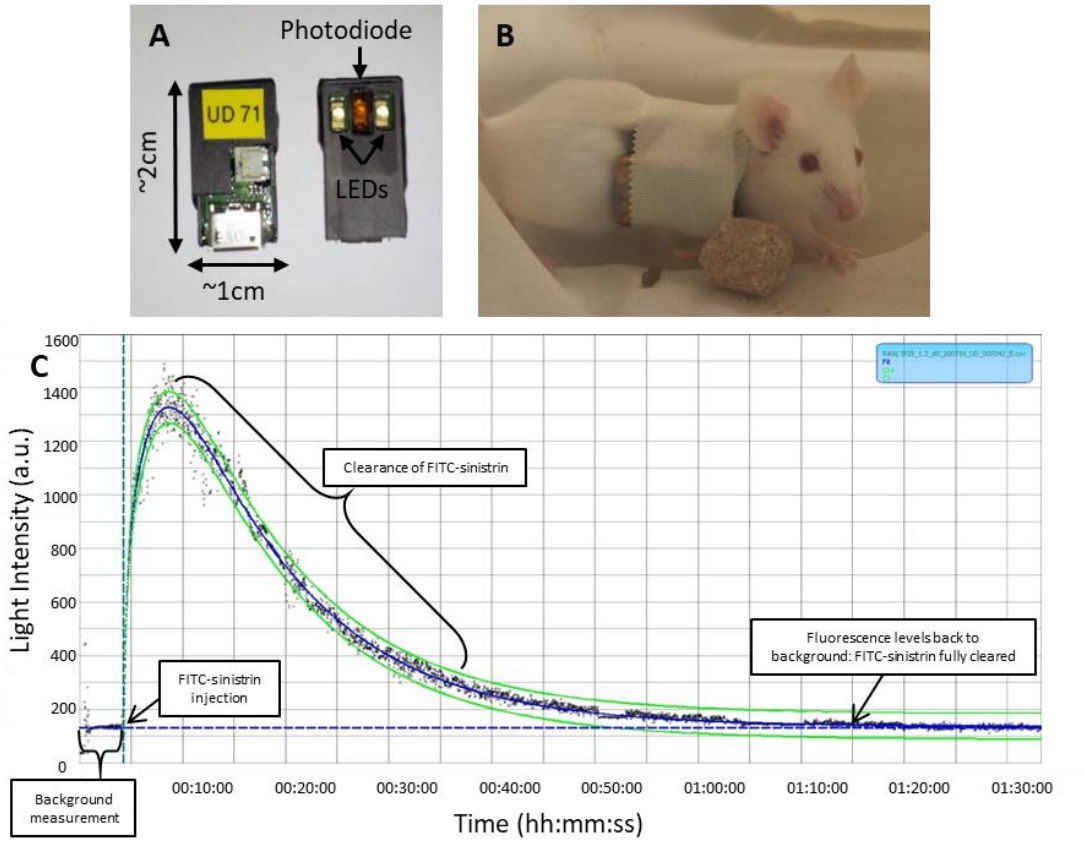

Figure 2.2: Transcutaneous assessment of FITC-sinistrin clearance. (**A**) Photograph of a transcutaneous device. (**B**) Photograph of a mouse during the measurement, showing that the mouse is conscious and alert, and tolerates the device well. (**C**) Representative FITC-sinistrin clearance curve from a healthy mouse. Black data points represent raw data, blue lines represent the 3-compartment fit, and green lines represent 95% confidence intervals.

tubing (inner diameter 0.28mm). A syringe containing sterile saline, attached to a 30G ½ inch needle, was then inserted into the other end of the tubing, and the tubing was flushed with saline before the free needle was inserted into the tail vein of the anaesthetised mouse. The mouse was transferred to the mouse holder, which was prepared according to standard MSOT protocols. The mouse was transferred to the MSOT scanner (inVision 256-TF, iThera Medical, Germany), and allowed to equilibrate to the temperature of the water for at least 10 min prior to image acquisition. The centre of one kidney was identified and a 0.1mm slice was imaged in the MSOT using a multispectral protocol (wavelengths: 700, 730, 760, 775, 785, 800, 850nm; frames per second: 10; averages: 20). 20nmol IRDye 800CW carboxylate (IRDye; LI-COR, Nebraska, USA) was administered in 200µl 0.9% saline via tail vein catheter 5 min after imaging began over a period of 10s. Mice were imaged for a further 25 min, to a total of 30 min. Mice were transferred to a heat box after imaging until fully recovered from the anaesthesia.

The data was reconstructed and signals from IRDye were resolved using multispectral processing. Regions of interest (ROI) were drawn around the cortex and papilla/pelvis (referred to only as pelvis) regions of the kidney. The difference in time between the mean peak pixel intensity in the cortex and the pelvis (T_{MAX} Delay) was calculated. Excretion half-life was calculated by fitting the exponential decay for the mean cortex pixel intensities.

Culling and Organ Collection

Mice were culled via a schedule one method; either by a rising concentration of CO_2 or by cervical dislocation. Blood was collected via cardiac puncture, and the needle was removed before expelling the blood from the syringe, to avoid haemolysis. Blood was collected into Eppendorf tubes, and allowed to clot at room temperature for several hours, before being repeatedly centrifuged at increasing speeds to collect serum. Aliquots of serum were made and stored at -20°C until analysis. Kidneys or other organs of interest were dissected from the mouse and fixed in 4% formaldehyde at 4°C for 24h. Kidneys were cut along the coronal or axial planes immediately after collection.

Paraffin-embedding and Sectioning

Fixed kidneys were washed in phosphate buffered saline (PBS) twice, and then transferred to 70% ethanol. Kidneys were processed in increasing concentrations of ethanol, then xylene, and finally molten paraffin wax (Tissue Processor TP1020, Leica, Germany), and then embedded in paraffin (Tissue Embedding Centre 1150, Leica, Germany). 5µm sections were cut using an automatic microtome (Microm HM 355S, Thermo Scientific, UK) on to glass slides (Superfrost Plus, Thermo Scientific, UK), and stored in an oven set at 36 - 40°C overnight to adhere the tissue to the slide. Slides were stored at room temperature until histological staining and analysis.

Freezing and Cryostat Sectioning

Fixed kidneys or other organs were washed in PBS twice, and soaked in 30% sucrose overnight, or until the tissue had sunk to the bottom of the tube. Tissues were then embedded in optimal cutting temperature (OCT) matrix (Cryomatrix, Thermo Scientific) and immersed in a bath of isopropanol cooled to a very low temperature with dry ice. Frozen tissues were stored at -20°C until cryosectioning, or -80°C for long term storage. 7µm sections were cut with a cryostat (HM 505, Microm, UK) on to glass slides (Superfrost Plus, Thermo Scientific, UK). Slides were stored at -20°C until analysis, or -80°C for long term storage.

2.2 Analysis of Kidney Injury

All serum and urine samples were thawed and centrifuged at 70-80,000 revolutions per minute (rpm) for 5 minutes prior to analysis.

Urinary Creatinine

Urinary creatinine (UCr) was measured using an in-house assay based on the Jaffe method[307]. 25µl standard or sample added to wells of a 96-well plate (Corning Costar 9018, Fisher Scientific, UK) in duplicate. 125µl reagent A added to all wells and plate was incubated at room temperature for 2 minutes. The reaction was stopped with 5µl reagent B. The plate was incubated on a plate shaker set at 500rpm for 10 minutes, and the plate was read at 490nm. The standard curve was plotted and the equation for the line of best fit was used to calculate the creatinine concentration in the unknown samples.

Creatinine standards: 1mg/ml creatinine stock. 400µg/ml top standard was prepared with a 2 in 3 dilution of the stock solution, and this was serially diluted to produce standards at the following concentrations: 400, 200, 100, 50, 25, 12.5, 6.25µg/ml.

Samples: 5µl urine was added in duplicate to all wells, and 20µl dH_2O added to all urine samples, to produce a 1:5 dilution.

Reagent A: 50ml 0.5M NaOH, 25ml 0.1M sodium phosphate dibasic, 29.5ml 0.56M Borax, 25ml sodium dodecyl sulphate (SDS), 45ml, picric acid, 5ml dimethyl sulphoxide (DMSO).

Reagent B: 5ml acetic acid, 1ml concentrated sulphuric acid, 44ml distilled water

Urinary Albumin

Urinary albumin was quantified with the mouse albumin enzyme-linked immunosorbent assay (ELISA) quantitation kit (Bethyl Laboratories, Texas, USA) according to manufacturer's instructions. A 1:1,000 dilution was required for baseline and control samples in the adriamycin model (female mice), and up to 1:1,000,000 dilution for samples from injured mice. A 1:10,000 dilution was required for all samples for the IRI model (male mice). The absorbance of the samples was read in a plate reader (FLUOstar Omega, BMG Labtech, Germany) at 450 nm immediately after the addition of the stop solution. The data was analysed using a four-parameter logistic fit (software from www.myassays.com). Albumin data was normalised to urine volume produced over 24h (mg/24h) or creatinine concentration (mg albumin: mg creatinine).

Urinary Kidney Injury Molecule-1

Urinary KIM-1 was quantified using Mouse TIM-1/KIM-1/HAVCR DuoSet and the DuoSet Ancillary Reagent Kit 2 (R&D Systems, UK), according to manufacturer's instructions. Samples were diluted 1:200 prior to analysis. The absorbance of the samples was read in a plate reader at 450 nm and 540 nm immediately after the addition of the stop solution. The reading at 540 nm was subtracted from that at 450 nm. The data was analysed by plotting a standard curve and the equation for the line of best fit was used to calculate the KIM-1 concentration in the unknown samples.

Serum Creatinine

SCr was quantified using the DetectX® Serum Creatinine Detection Kit (ArborAssays, Michigan, USA) according to manufacturer's instructions. Samples were assayed undiluted. The absorbance of the samples was read in a plate reader at 490 nm at 1 min and 30 min after the addition of the substrate. The reading at 1 min was subtracted from that at 30 min. The data was analysed by plotting a standard curve and the equation for the line of best fit was used to calculate the SCr concentration in the unknown samples.

Blood Urea Nitrogen

BUN was quantified using the QuantiChrom™ Urea Assay Kit (BioAssay Systems, California, USA) according to manufacturer's instructions. Samples were diluted 1:5 prior to analysis. The absorbance of the samples was read in a plate reader at 520 nm 20 min after the addition of the substrate. The data was analysed by plotting a standard curve and the equation for the line of best fit was used to calculate the BUN concentration in the unknown samples.

Histological Staining and Scoring

Picro-Sirius Red (PSR) Staining: Slides were de-waxed and hydrated in two changes of xylene (5 min each) and graded alcohols (100% through to 50% ethanol, then distilled water; 2 min each). Slides were stained in picro-sirius red solution (0.5g Sirius red F3B in 500ml saturated aqueous solution of picric acid) for one hour. Slides were washed in two changes of acidified water (5ml acetic acid in 1L distilled water), dehydrated in graded alcohols (50% through to 100% ethanol; 2 min each), cleared in two changes of xylene (5 min each) and mounted with a resinous medium (DPX Mountant).

Periodic Acid-Schiff (PAS) Staining (PAS staining kit 395B-1KT): Slides were de-waxed and hydrated in two changes of xylene (5 min each) and graded alcohols (100% through to 50%

ethanol, then distilled water; 2 min each). Slides were immersed in 0.01% periodic acid solution for 5 min and rinsed in several changed of distilled water. Slides were stained in Schiff's reagent for 15 min, and washed with running tap water for 5 min. Slides were counterstained with Gill's Haematoxylin No. 3 solution for 90s, and rinsed in running tap water until the water ran clear. Slides were finally dehydrated in graded alcohols (50% through to 100% ethanol; 2 min each), cleared in two changes of xylene (5 min each) and mounted with a resinous medium (DPX Mountant).

Masson's Trichrome Staining: Slides were de-waxed and hydrated in two changes of xylene (5 min each) and graded alcohols (100% through to 50% ethanol, then distilled water; 2 min each). Slides were stained in Weigert's haematoxylin working solution (equal parts solution A (1g haematoxylin in 100ml 95% ethanol) and solution B (4ml 29% ferric chloride, 1ml concentrated hydrochloric acid, 95ml distilled water)) for 10 min, rinsed in warm running tap water for 10 min, and then rinsed in distilled water. Slides were stained in Biebrich scarlet-acid fuschin solution (90ml 1% biebrich scarlet, 10ml 1% acid fuschin, 1ml glacial acetic acid) for 10 min, and then washed in distilled water. Slides were differentiated in phosphomolybdic-phosphotungstic acid solution (25ml 5% phosphomolybdic acid, 25ml 5% phosphotungstic acid) for 10-15 min, or until collagen was not red. Slides were directly transferred to aniline blue solution (2.5g aniline blue, 2ml acetic acid, 100ml distilled water) for 5-10 min, briefly rinsed in water, then immersed in 1% acetic acid solution for 2-5 min. Slides were washed in distilled water, then dehydrated quickly in 95%, then 100% ethanol. Slides were cleared in two changes of xylene (5 min each) and mounted with a resinous medium (DPX Mountant).

PSR-stained kidney sections from the adriamycin model were blindly scored for the percentage of glomerular damage by a qualified paediatric nephrologist, Professor Adrian Woolf, University of Manchester. All glomeruli were assessed, and were categorised as abnormal if the PSR staining extended beyond the confines of the mesangium, into the glomerular tufts. Additional features of injury included the adhesion of glomerular tufts to the Bowman's capsule, and the obliteration of capillary loops.

Fibrillar collagen within PSR-stained kidney sections was detected using polarised microscopy, and image analysis software (Fiji) was used to quantify the percentage of fibrosis.

PAS-stained kidney sections from the IRI model were blindly scored for tubular injury by a qualified veterinary pathologist, Dr Lorenzo Ressel, School of Veterinary Science, University

of Liverpool. 10 fields of view (FOV) within the OSOM and distal cortex at x200 magnification were scored 0-5 based on the degree of necrosis and cast formation: 0 = none, 1 = <10%, 2 = 11-25%, 3 = 26-45%, 4 = 46-75%, 5 = >76% (Figure 2.3). The overall score is the sum of the scores for the 10 FOVs. This method was adapted from Wang *et al.* (2005)[308].

Immunofluorescence on Frozen Tissue Sections

Immunostaining was performed within a humidified chamber. 7µm frozen tissue sections were removed from the freezer and allowed to thaw at room temperature for 10-15 minutes. The sections were washed three times with PBS, for 2-3 min each wash. Sections were permeabilised with 0.25% Triton-X 100 in PBS for 10 min at room temperature, and then washed three times in PBS. Each section on a slide was encircled with a hydrophobic pen, (PAP pen, Abcam) and then blocked with 2% bovine serum albumin (BSA) in PBS for 1h at room temperature. Primary antibodies (KIM-1: Goat polyclonal IgG, R&D Systems (AF1817-SP); Ki67: Rabbit polyclonal IgG, Abcam (ab16667)) were diluted 1:100 in 2% BSA in PBS, and sections were incubated with the primary antibody, or 2% BSA in PBS for the negative control, overnight at 4°C. The next day, sections were washed thoroughly three times with PBS, for 5 min each wash, and then incubated with the secondary antibodies (Alexa Fluorophores, Invitrogen) and 4',6-diamidino-2-phenylindole (DAPI), diluted to a working concentration of 100 µg/ml in 2% BSA in PBS, for 1h at room temperature. The secondary antibodies were applied to the negative control, to test the specificity of the secondary antibodies. Sections were washed three times with PBS, and once with distilled water, for 5 min each wash, mounted with antifade mounting media (Gelmount, Biomedia), and sealed with clear nail polish. Immunostained slides were stored at 4°C. Fluorescence images were acquired using a Leica DM2500 microscope with a Leica DFC350 FX camera (Leica, Germany).

Note that an irrelevant isotype antibody would have been the optimal control to ensure the specificity of the antibody to the antigen of interest.

2.3 Cell Therapy: Administration and Tracking

Cell Preparation and Administration

Mouse kidney stem cells (mKSCs)[309], mouse MSCs (mMSCs; D1 ORL UVA [D1](ATCC® CRL-12424™), ATCC, UK), human umbilical cord-derived MSCs (hUC-MSCs; provided by NHS Blood and Transplant) and human bone marrow-derived MSCs (hBM-MSCs; Lonza Walkersville Inc., UK) were cultured and prepared for *in vivo* administration by Dr Arthur Taylor, Institute of

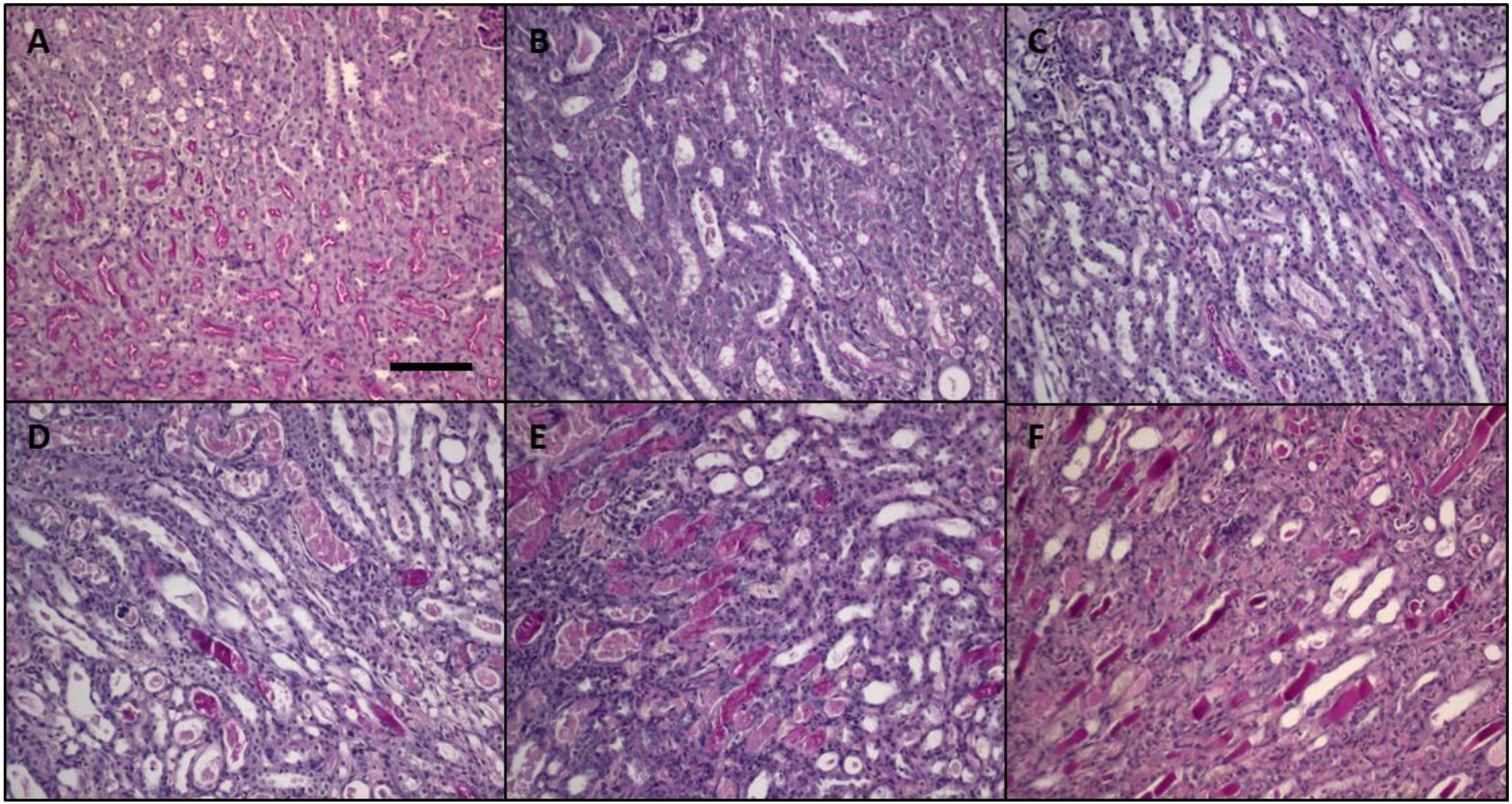

Figure 2.3: **Tubular injury scoring.** Representative images of tubular injury scoring by a veterinary pathologist: (**A**) 0 = none, (**B**) 1 = <10%, (**C**) 2 = 11-25%, (**D**) 3 = 26-45%, (**E**) 4 = 46-75%, (**F**) 5 = >76%. Images taken at 20x magnification, scale bar = 100µm

Translational Medicine (ITM), University of Liverpool (UoL). Human kidney-derived cells (hKCs)[134] were isolated from a human infant kidney donated from Alder Hey Children's Hospital, Liverpool, UK, and were cultured and prepared for *in vivo* administration by Dr Ilaria Santeramo, ITM, UoL. All cells were cultured at 37°C under a humidified atmosphere with 5% CO_2 as described perviously[134,309]. Average cell diameter was estimated by measuring the volume of a cell pellet in a packed cell volume (PCV) tube according to the manufacturer's instructions (Techno Plastic Products, Switzerland).

Prior to *in vivo* administration, mKSCs, mMSCs, hKSCs, and hBM-MSCs (only those used in Chapter 6) were transduced with a lentiviral vector encoding firefly luciferase and ZsGreen under control of the constitutive promoter EF1a, by Dr Arthur Taylor as previously described[310,311]. The mKSCs were infected with a multiplicity of infection (MOI) of 10, whereas all other cells where infected with an MOI of 5. In all cases, at least 90% of the cell population expressed the vector after transduction. SPIONs[291,293] for mMSC labelling were synthesised by Dr Michael Barrow, Department of Chemistry, UoL, and were incubated with cells at a labelling concentration of 25 µg/ml for 24h prior to *in vivo* administration. For *in vivo* administration, cells were trypsinised, pelleted, carefully resuspended in ice cold PBS and kept on ice until injection. Immediately prior to administration, cells were gently re-suspended using a pipette, and warmed slightly to room temperature before administration to the animal, using a 29G ½ inch insulin needle.

Ultrasound-Guided Intracardiac Injection

Mice were provided with 1mg/kg buprenorphine for pain relief prior to intracardiac injection. Mice were anaesthetised using isoflurane and O_2, and positioned supine on the heated ultrasound platform, with the limbs taped (Leukosilk, BSN Medical, Germany) in the extended position (Figure 2.4A). The chest was shaved using an electric shaver and a depilatory cream (Veet for sensitive skin), left on for a maximum of two minutes. The skin over the chest was held taut by a strip of tape placed over the abdomen, and swabs were placed either side of the mouse (Figure 2.4A, B, C). Ultrasound gel (ultrasoundgel.co.uk, UK) was placed liberally on the chest, making sure to avoid introducing bubbles. The heart was located by ultrasound (S-Sharp, Taiwan), with the transducer at a slight angle (approx. 30° counter-clockwise) (Figure 2.4B, C, F). The needle was then introduced in to the plane of imaging and tapped on the skin of the mouse several times, to confirm the needle stayed within the imaging plane, even when moved (Figure 2.4D, E). The needle was then gently inserted in to the heart, and visualisation of both the needle and the heart was confirmed (Figure 2.4G) before the cell

solution was slowly injected. The needle was then withdrawn from the heart in a smooth motion. The ultrasound gel was cleaned off the mouse and the mouse was recovered in a heat box. Mice were closely monitored for signs of adverse effects following the intracardiac injection. A successful injection could be observed by a change in contrast within the heart as the cell solution was administered (Figure 2.4H), and by bioluminescence imaging of luciferase^{+} cells (see Figure 2.5 for examples of unsuccessful IC injections).

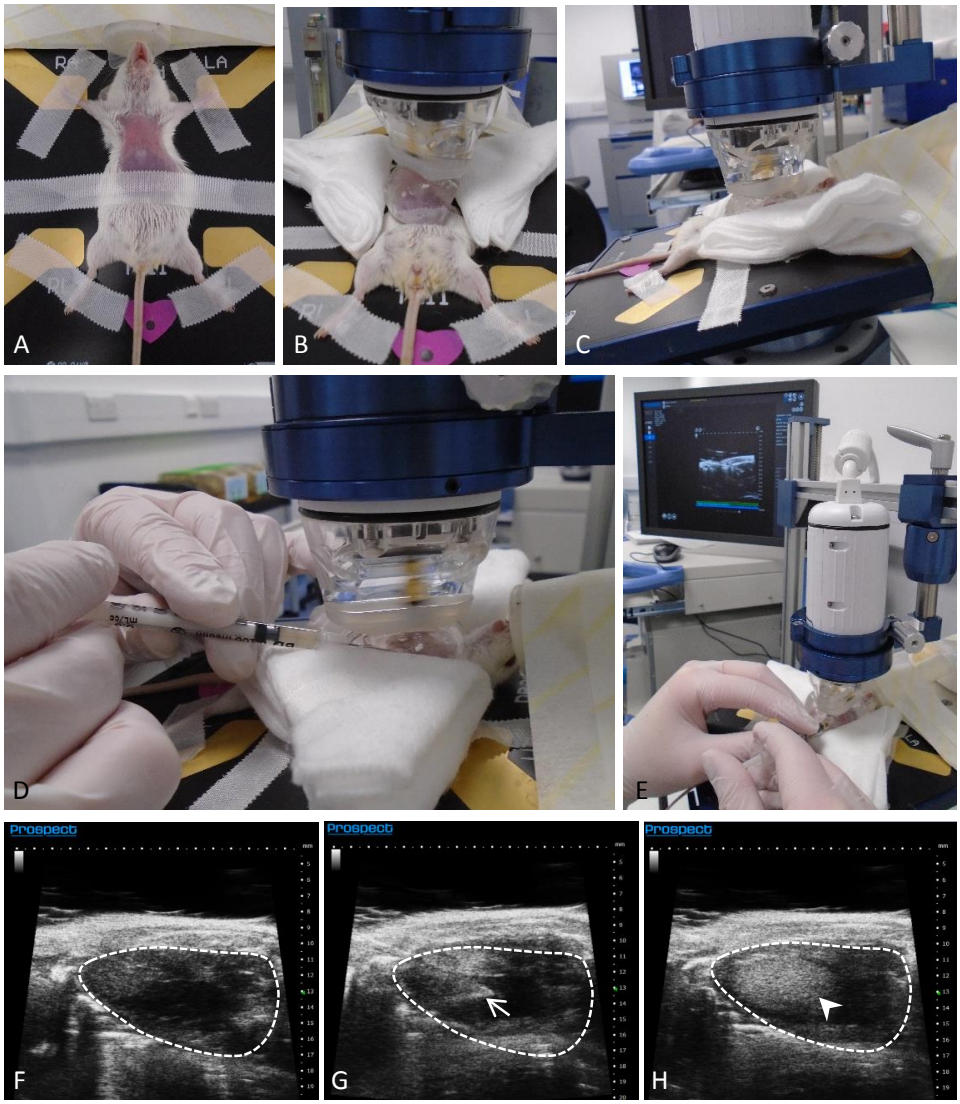

Figure 2.4: Ultrasound-guided intracardiac administration of cells. (**A**) Photograph of mouse set-up for ultrasound-guided intracardiac injection. (**B - C**) Photographs of the ultrasound transducer in place for heart imaging. (**D - E**) Photographs of position of needle for intracardiac injection. (**F - H**) Snapshot images of left cardiac ventricle, outlined with a dashed white line, before injection (**C**), during the injection, with the tip of the needle (arrow) in the left ventricle (**D**), and after injection of the cell solution (**E**), where the contrast within the left ventricle has changed (arrowhead), indicating a successful injection.

Bioluminescence Imaging

Mice were anaesthetised using isoflurane and O_2, and imaged in the IVIS Spectrum (Perkin Elmer, UK) 15 min after the administration of 150mg/kg BW luciferin (SC). Image acquisition was performed using automatic exposure settings, where the system automatically adjusted the exposure time, up to a pre-set maximum, in order to obtain a minimum of 3000 bioluminescence counts. Mice were returned to the home cage after imaging. Images were normalised to express average radiance (photons/second/cm^2/steradian (p/s/cm^2/sr)), and the scale was set according to the level of signal detected. Generally, the standard scale was set to 1.0 x10^5 – 1.0 x10^6 p/s/cm^2/sr, and was adjusted only if necessary, to display weaker or stronger signals. The scale was never set below 5.0 x10^3 p/s/cm^2/sr, in order to avoid visualising unspecific background noise. Signals were quantified by ROIs around the whole mouse, or a specific region of the mouse. Organs were imaged *ex vivo* after being dissected from the mouse soon after luciferin administration. Organs were placed on parafilm for *ex vivo* imaging. It was necessary to cut the kidneys open (coronally) in order to detect signals from within the kidney. All other organs (brain, heart, lungs, liver, and spleen) could be imaged whole.

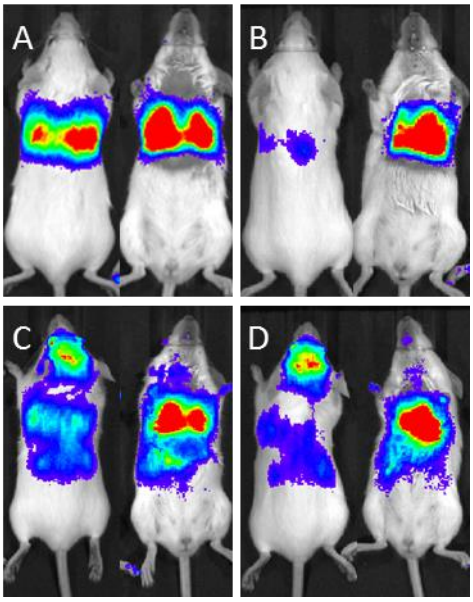

Figure 2.5: Unsuccessful IC injections. Mis-injection in to the right ventricle, leading to cells present in the lungs (**A**), and mis-injection in to the chest cavity (**B**). Partial mis-injection in to the right cardiac ventricle (**C**) and partial mis-injection in to the chest cavity (**D**).

Magnetic Resonance Imaging

Mice were anaesthetised using isoflurane and O_2. Mice were placed on a nose cone on the imaging bed appropriate for the anatomical region (abdominal or brain) being imaged. Ophthalmic ointment was applied to avoid corneal drying. A rectal probe was lubricated and inserted into the rectum, and a respiration pillow was secured on the mouse's back, for monitoring temperature and respiration respectively. A water-heated pad was secured in place over the animal to keep the body temperature constant. All MR data was acquired with a Bruker 9.4 T Avance III HD instrument (Bruker, UK). The mouse was inserted into an 86mm resonator and a 4-channel receive-only surface coil array was used for brain imaging, whereas a 4-channel receive-only cardiac array was used for abdominal imaging. All data acquisition and processing was carried out using Paravision 6.0.1 (Bruker). Imaging sequences are summarised in Table 2.1. FLASH T_2* sequences were designed to optimally detect signals from SPION-labelled cells. T_2* relaxation times were quantified from the T_2* map by drawing ROIs around the cortex of the kidney or the liver, in order to quantify the relative presence of SPIONs at various time points in the study. B0 field maps were obtained prior to T_2* mapping to optimize the field homogeneity. *Ex vivo* imaging was performed on organs fixed in 4% formaldehyde, and then immersed in Fomblin solution for imaging. All MR imaging and data analysis was performed with the help of Dr Arthur Taylor.

Fluorescence Microscopy for Tracking ZsGreen$^+$ Cells

7µm frozen tissue sections were removed from the freezer and allowed to thaw at room temperature for 10-15 minutes. DAPI diluted in distilled water to a working concentration of 100 µg/ml was applied to tissue sections and incubated at room temperature for 5 min. Slides were washed twice with PBS, and once with distilled water, mounted with antifade mounting media (Gelmount, Biomedia), and sealed with clear nail polish. DAPI-stained slides were stored at 4°C. Fluorescence images were acquired using a Leica DM2500 microscope with a Leica DFC350 FX camera (Leica, Germany).

The presence of ZsGreen$^+$ cells in the kidney was assessed by quantifying the percentage of glomeruli that contained ZsGreen$^+$ cells. All glomeruli in one kidney section per animal were evaluated, and scored as containing no cells, one cell, or multiple cells.

Table 2.1: Data acquisition details for MR imaging.

	In vivo				*Ex vivo*
	FLASH T_2* (Abdomen)	**FLASH T_2* (Brain)**	**B0 Map**	**T_2* Map**	**FLASH T_2* (Organs)**
Slices	20	20	1	20	70
Averages (NEX)	3	3	3	2	24
Repeat Time (TR)	262.6ms	262.6ms	10ms	900ms	1300
Echo Time (TE)	5.5ms	4.2ms	3.6ms	N/A	6.3
Flip Angle (FA)	20.0°	20.0°	15.0°	50.0°	20
Matrix Size (MTX)	386 x 386 pixels	256 x 256 pixels	64 x 64 x 64 pixels	256 x 256 pixels	386 x 386 pixels
Field of View (FOV	35 x 35mm	20 x 20mm	45 x 45 x 45mm	35 x 35mm	15 x 15mm
Slice Thickness (SI)	0.5/0.6mm	0.5/0.6mm	45mm	0.5/0.6mm	0.2/0.2mm
Echo Images	N/A	N/A	N/A	8	N/A
Echo Spacing	N/A	N/A	N/A	4.5ms, start at 4.5ms	N/A
Acquisition Time	5m 35s	4m 4s	2m 3s	5m 7s	3h 20m 43s

Isolectin Staining of Blood Vessels

Blood vessels in the brain were identified by isolectin IB4 staining on frozen tissue sections from the brains of perfusion-fixed mice. Immunostaining was performed within a humidified chamber. 7µm frozen tissue sections were removed from the freezer and allowed to thaw at room temperature for 10-15 minutes. The sections were washed three times with PBS, for 2-3 min each wash. Sections were permeabilised with 0.3% Triton-X 100 in PBS for 10 min at room temperature, and then washed three times in PBS. Each section on a slide was encircled with a hydrophobic pen, (Abcam) and then blocked with blocking solution (2% BSA, 2% normal goat serum (NGS) and 0.05% Triton X-100 in 0.1 M PBS) for 1h at room temperature. Isolectin IB4 (L2140, Sigma Aldrich, UK) was diluted 1:50 in $CaCl_2$-containing buffer and blocking solution, and sections were incubated with the isolectin for 72h at 4°C. Sections were washed thoroughly three times with PBS, for 5 min each wash, and then incubated with streptavidin (Alexa Fluorophore-Streptavidin, 016-580-084-JIR, Stratech) and DAPI, diluted 1:200 in $CaCl_2$-containing buffer and blocking solution, overnight at 4°C. Sections were washed three times with PBS, and once with distilled water, for 5 min each wash, mounted with antifade mounting media (Gelmount, Biomedia), and sealed with clear nail polish. Immunostained slides were stored at 4°C. Fluorescence images were acquired using a Leica

DM2500 microscope with a Leica DFC350 FX camera (Leica, Germany). IB4 staining was performed by MRes student, Lydia Beeken, ITM, UoL.

Prussian Blue Staining of Iron for Tracking SPIONs

SPIONs were detected in frozen tissue sections with the Prussian Blue Iron Detection Kit (Sigma, UK) according to manufacturer's instructions. Prussian blue-stained tissue sections were imaged under light microscopy. Prussian blue staining was performed by MRes student, Cai Astley, ITM, UoL.

Bone Marrow Extraction and FACS analysis

Mice were culled by cervical dislocation and their femurs and tibias were collected in PBS containing penicillin/streptomycin. In a sterile fume hood, muscle tissues were removed, and bone marrow was flushed out with PBS. Bone marrow was centrifuged (400g, 5 mins) and then resuspended in fresh PBS. Bone marrow suspensions were then analysed by FACS for ZsGreen expression. Bone marrow extraction and FACS analysis were performed by Dr Jack Sharkey, ITM, UoL.

Histological Analysis of Tumours

Tumours that developed as a result of cell administration were embedded in paraffin, and 5µm tissue sections were stained with Haematoxylin & Eosin (H&E). Slides were de-waxed and hydrated in two changes of xylene (5 min each) and graded alcohols (100% through to 50% ethanol, then distilled water; 2 min each). Slides were then immersed in haematoxylin for 5 min, rinsed in distilled water, and placed in acid-alcohol solution for 10 s before being immersed in eosin for 2 min. Slides were finally rinsed in distilled water, dehydrated in graded alcohols (50% through to 100% ethanol; 2 min each), cleared in two changes of xylene (5 min each) and mounted with a resinous medium (DPX Mountant). H&E-stained tissue sections were evaluated and characterised by a qualified veterinary pathologist (Dr Lorenzo Ressel, Institute of Veterinary Science, UoL).

2.4 Statistical Analyses

All statistical analyses were performed using Minitab 17 statistical software. A two-sample t-test was used to compare two unpaired groups, a paired t-test was used to compare two paired groups, and a one-way ANOVA (analysis of variance) was used to compare multiple groups. When an ANOVA resulted in a statistically significant result, a Tukey pairwise

comparison was performed in order to determine which groups were statistically significantly different. The Tukey pairwise comparison assigned each group at least one letter, and groups that did not share a letter were significantly different from one another. A p-value below 0.05 was considered statistically significant. $p < 0.05$ (*), $p < 0.01$ (**), $p < 0.001$ (***).

It must be noted that power calculations were not performed to determine optimal group sizes. This was because of practical considerations of performing complicated experiments, which limited the total number of animals possible per experiment.

CHAPTER 3

Characterising the adriamycin mouse model of chronic kidney disease, and minimally-invasive methods of assessing kidney function *in vivo*

This chapter was produced in entirety from a publication in Scientific Reports (2015). The text and figures have been formatted in line with the remainder of this thesis, but otherwise remain unedited from the published paper.

Measures of kidney function by minimally invasive techniques correlate with histological glomerular damage in SCID mice with adriamycin-induced nephropathy

Lauren Scarfe, Aleksandra Rak-Raszewska, Stefania Geraci, Darsy Darssan, Jack Sharkey, Jiaguo Huang, Neal C. Burton, David Mason, Parisa Ranjzad, Simon Kenny, Norbert Gretz, Raphaël Lévy, B. Kevin Park, Marta García-Fiñana, Adrian S. Woolf, Patricia Murray, Bettina Wilm

Scientific Reports (**5**) doi: 10.1038/srep13601 (2015)

3.1 Abstract

Maximising the use of preclinical murine models of progressive kidney disease as test beds for therapies ideally requires kidney function to be measured repeatedly in a safe, minimally invasive manner. To date, most studies of murine nephropathy depend on unreliable markers of renal physiological function, exemplified by measuring blood levels of creatinine and urea, and on various end points necessitating sacrifice of experimental animals to assess histological damage, thus counteracting the principles of Replacement, Refinement and Reduction. Here, we applied two novel minimally invasive techniques to measure kidney function in SCID mice with adriamycin-induced nephropathy. We employed i) a transcutaneous device that measures the half-life of intravenously administered FITC-sinistrin, a molecule cleared by glomerular filtration; and ii) multispectral optoacoustic tomography, a photoacoustic imaging device that directly visualises the clearance of the near infrared dye, IRDye 800CW carboxylate. Measurements with either technique showed a significant impairment of renal function in experimental animals *versus* controls, with significant correlations with the proportion of scarred glomeruli five weeks after induction of injury. These technologies provide clinically relevant functional data and should be widely adopted for testing the efficacies of novel therapies. Moreover, their use will also lead to a reduction in experimental animal numbers.

3.2 Introduction

Chronic kidney disease (CKD) represents a huge socioeconomic burden, with treatment options for severe disease being limited to dialysis and transplantation. By developing regenerative medicine therapies (RMTs) for CKD in preclinical models, novel and alternative clinical approaches may be established to halt progression to end stage renal disease (ESRD). In order to maximise the use of preclinical murine models of progressive kidney disease as experimentation platforms for novel therapies, including drugs and stem cells[151,185,312,313], kidney function, in concert with structural morphology, needs to be monitored repeatedly in a safe, minimally invasive manner. The glomerular filtration rate (GFR) is considered the gold standard measure of the main physiological function of the kidney, i.e. to efficiently clear small molecular waste products from the blood stream. However, its measurement generally requires repeated blood sampling, and for some methods, precisely timed urine collections. While these techniques are feasible in patients, it is much more cumbersome and challenging to apply them to small experimental animals. To date, therefore, most mouse studies have used surrogate markers of GFR, exemplified by measuring blood levels of creatinine and urea.

These are unreliable measures of GFR because levels only rise when over 50% of renal function is lost; moreover, factors such as food intake can affect blood levels independently of GFR. Furthermore, most studies of murine nephropathy have relied heavily on end point analysis for the assessment of histological damage, which necessitates killing experimental animals. While this provides useful data, the sole reliance on necropsy material is not compatible with optimal application of the principles of Replacement, Refinement and Reduction (the 3Rs).

Here, we have evaluated the ability of two minimally invasive *in vivo* technologies to monitor kidney function in an adriamycin (doxorubicin)-induced nephropathy mouse model. The anthracycline antibiotic adriamycin (ADR) primarily targets both glomerular endothelium and podocytes in rodents and is a model of focal segmental glomerulosclerosis (FSGS), which accounts for 2.3% of all cases of ESRD[314]. The incidence of primary FSGS has increased by up to 13 fold in the last 30 years[315]. Along with diabetic nephropathy, it is a common cause of severe proteinuria. Administration of a single dose of ADR in both BALB/c and BALB/c severe combined immunodeficient (SCID) mice leads to two phases of disease[163,169,172,185]. In the first, glomeruli are grossly histologically intact (i.e. they show no scarring) but their ability to act as a macromolecular barrier is severely compromised. This is manifest as 'proteinuria'. Its magnitude can be assessed by measuring the amount of albumin, which appears in the urine over unit time; the simpler measure, the urine albumin/creatinine ratio, can also be employed. In the second phase of disease, glomeruli become scarred or 'sclerotic' and this leads to the loss of total filtration surface. This occurs long after ADR has been cleared and it exemplifies the 'progression of CKD' often observed in clinical practice. This has two clinical outcomes: both the degree of proteinuria may fall and, at the same time, the GFR also falls. Given that an unchecked fall of GFR will ultimately lead to ESRD, minimally invasive measures which correlate with gross structural glomerular damage would be highly informative.

Importantly, we chose SCID mice in the current study with a longer-term view of using immunocompromised mice with drug-induced nephropathy as test beds for assessing the safety and efficacy of different types of human stem cells. The two minimally invasive technologies comprised firstly, a transcutaneous electronic device for measuring the clearance from the blood of (FITC)-sinistrin, a molecule of approximately 4000 Da cleared by glomerular filtration[234,237]. This device can be applied in conscious animals, which is a key advantage, given the well-described confounding effects of general anaesthesia on GFR[239,240]. The second technology was multispectral optoacoustic tomography (MSOT). This imaging technology was used to measure the passage of a near infra-red dye, IRDye 800CW

carboxylate (from now on referred to simply as IRDye), through the kidney parenchyma into the renal pelvis. Specifically, a recent report suggested that MSOT could effectively monitor renal clearance of IRDye in mice[248]. MSOT illuminates tissue with light pulses at multiple wavelengths and detects acoustic waves generated by the thermoelastic expansion which follows light absorption[316,317]. The technique is not harmful and offers very good temporal and spatial resolution in live animals; however, it requires the animals to be studied under general anaesthesia.

Results obtained with these techniques were compared with standard biochemical and histological indicators of kidney damage. This included 24-hour-albuminuria or urinary albumin-to-creatinine ratio, serum creatinine (SCr), blood urea nitrogen (BUN), and Picro-Sirius red (PSR) and Masson's Trichrome staining in order to detect structural histological damage. Subsequently, we applied an extensive range of statistical tests to determine whether the transcutaneous device and MSOT are appropriate tools for monitoring kidney function. Furthermore, we assessed whether both technologies could be used to predict histological damage during progression to CKD in the ADR model.

3.3 Materials and Methods

Animals

Female BALB/c severe combined immunodeficient (SCID) mice (Charles River, Margate, UK) were housed in individually ventilated cages at a 12 hour light/dark cycle, with *ad libitum* access to food and water. At age seven to eight weeks, ADR-induced nephropathy was induced in six mice by injecting once intravenously (iv) adriamycin (ADR, doxorubicin hydrochloride, Tocris, Bristol, UK) at 6.3mg/kg body weight (BW) in 0.9% saline (Braun, Melsungen, Germany), while five control mice received saline. The optimal dose had been previously determined in a dose-finding study, and is similar to previously reported adriamycin dose given to BALB/c SCID mice[172,185,318]. Mortality in the ADR-administered group during the five-week study period was zero. Experimental animal protocols were performed under a licence granted under the Animals (Scientific Procedures) Act 1986 and approved by the University of Liverpool Animal Ethics Committee. BALB/c SCID mice were used in order to determine parameters for future preclinical regenerative medicine studies in mice with ADR-induced nephropathy.

Albuminuria, serum creatinine and BUN

To collect urine, mice were housed individually in metabolic cages (Tecniplast, Buguggiate, Italy) once a week for 24 hours (h). Despite being gradually acclimated to the metabolic cages, 24h urine collection is stressful for mice, leading to weight loss of up to 1.5g during the time spent in the cages. Because the mice on average weigh less than 20g, it was necessary to omit urine collection at week five, since the long term anaesthesia for MSOT imaging is another stressful procedure for the mice. Total urine volume was measured and albumin levels were quantified using a Mouse Albumin ELISA Quantification Kit (Bethyl Laboratories, Montgomery, TX, USA) according to manufacturer's instructions. Urinary creatinine (UCr) was quantified using a plate based colourimetric assay. Blood was collected via cardiac puncture after sacrifice, and separated into serum. Serum creatinine (SCr) and blood urea nitrogen (BUN) were quantified according to manufacturer's instructions (Detect X Serum Creatinine Detection Kit, Arbor Assays, Ann Arbor, MI, USA; QuantiChrom Urea Assay Kit, BioAssay Systems, Hayward, CA, USA, respectively).

Histopathology

Kidneys were dissected at week 5, cut along the sagittal plane, and processed for histology using standard methods. Sections (4µm) were stained with Picro-Sirius Red (PSR, Sigma-Aldrich, Dorset, UK) or Masson's Trichrome following standard protocols. All glomeruli (on average 116 glomeruli) in one PSR-stained kidney section per animal were blindly scored for glomerular histological damage and the percentage of abnormal glomeruli calculated. Glomeruli were categorised as abnormal if the PSR staining extended beyond the confines of the mesangium into the glomerular tufts. Using one panorama kidney section per animal, fibrillar collagen was detected using polarised microscopy, while PSR-staining in the cortex was captured by bright field microscopy. Images were stitched together[319] and image analysis software (Fiji) was used for quantification.

Transcutaneous FITC-sinistrin decay

FITC-sinistrin half-life was measured weekly in all animals[234]. In short, the transcutaneous device was fixed to the depilated skin on the back of mice using a double-sided adhesive patch (Lohmann, Neuwied, Germany). Transcutaneous measurement started with background reading one to three min before 0.3mg/g BW FITC-Sinistrin (diluted in 0.9% saline; Braun, Melsungen, Germany) was administered iv. Animals were allowed to fully recover and move freely until transcutaneous measurement was stopped after 90 minutes

(min). Using a 1-compartment model, the half-life of FITC-Sinistrin was calculated from the transcutaneously measured kinetics[234] (Figure S3.3).

Measuring the clearance of IRDye 800CW carboxylate using MSOT

Five weeks after adriamycin or saline administration, anaesthetised (isoflurane) mice had hair removed from the abdominal region and were imaged in the inVision 256-TF MSOT imaging system (iThera Medical, Munich, Germany) using a multispectral protocol for 30 min (rate of 10 frames per second using wavelengths: 700, 730, 760, 775, 785, 800 and 850 nm, and averaging 20 consecutive frames to minimise influences of motion). Five min into the imaging mice received 200µl (20nmol) IRDye 800CW carboxylate (LI-COR, USA) in 0.9% saline through a tail vein cannula over a period of 10 seconds (s). Data was reconstructed and multispectral processing performed to resolve signals for the IRDye, including gradient scaling for each animal at a time prior to the injection of the IRDye. Regions of interest (ROIs) drawn around renal cortex and the renal papilla-pelvis region (in short: pelvis) of the right kidney of each mouse were used to determine the time between the mean peak pixel intensity (T_{MAX}) in the cortex and the pelvis (T_{MAX} delay). Exponential decay was fitted for mean cortex pixel intensities to determine the characteristic excretion half-life.

To depict the temporal dynamics of IRDye clearance in colour code, a Matlab routine was developed to process a stack of images and calculate a composite image on a pixel-by-pixel basis of T_{MAX}, defined as the time (or frame number in the stack) at which the highest intensity was recorded at that pixel. A pseudocolor was applied to display this time (or frame number) per pixel as different colours on the spectrum colour scale. Image stacks were typically composed of 15 images. With a temporal resolution from *in vivo* imaging of approximately 16 s this equated to approximately 4 min of imaging data after injection that were used for temporal analysis. A C_{MAX} image as a maximum intensity projection was computed of the same image stack. ImageJ was used to amplitude modulate the pseudocoloured T_{MAX} image using the C_{MAX} in order to dim areas with little contrast and therefore to reduce background noise in the T_{MAX} caused by an absence of substantial temporal change in a certain pixel.

Statistical analyses

Linear mixed-effects (LME) models were fitted to characterise changes of albuminuria and of FITC-sinistrin half-life over time. The advantage of using a linear mixed-effects model is that the correlation between measurements across time points within mice is taken into account in a term called the *random term*. Differences in albuminuria and FITC-sinistrin half-life

between the treatment and control group (e.g., differences in linear or quadratic changes over time) were subsequently tested using these models.

Multiple linear regression models were applied to test whether glomerular histological damage was associated with transcutaneous measurements of albuminuria (maximum observed values and week 4 values), FITC-sinistrin half-life (week 4 values), T_{MAX} delay and excretion half-life of IRDye (the latter measured at 5 weeks).

Independent t-tests were applied to compare measures of kidney function at 4 weeks and of post-mortem histology measurements at 5 weeks between the control and the treatment group. The assumptions of normality and homogeneity of variances were checked.

Plasma Protein Binding of IRDye

A dye-protein stock solution was prepared by incubating of 2ml IRDye (10µmol) with 8ml Sprague Dawley rat plasma Li Heparin (Innovative Research, Novi, MI, USA) in phosphate buffered saline (PBS) at 37°C, while 2ml PBS was incubated with 8ml rat plasma as control. Plasma protein-binding measurements were performed by equilibrium dialysis of PBS against dye-protein stock solution (or control stock solution) using a two-chamber dialysis set-up (Equilibrium Dialyzer, Havard Apparatus, Holliston, MA, USA)[320,321]. After 24h the absorption of IRDye in PBS and plasma were determined in three independent measurements by absorption spectroscopy in a microplate reader (Tecan Infinite M200) and the concentrations of IRDye was calculated on the basis of the corresponding molar absorption coefficients (Figure S3.4, Table S3.3).

Plasma protein binding (PPB) of IRDye in percent was determined by averaging three independent measurements and following the equation of Beer-Lambert law:

$$[A(plasma) - A(PBS)] / [A(plasma) + A(PBS)] * 100$$

where A is denoted as corresponding to UV absorption.

3.4 Results

3.4.1 The half-life of transcutaneously measured FITC-sinistrin becomes significantly increased over the course of ADR-induced nephropathy

Kidney injury was induced by intravenous (iv) ADR administration once in 6 SCID female mice while 5 control SCID females received saline injection. The weights of ADR-administered *versus* control mice reached their lowest point one week after nephrotoxin administration. Over the next four weeks, weights in the ADR group returned towards time-matched control values but did not attain them (Figure 3.1A, S3.1A). To determine damage to the glomerular macromolecular barrier, we measured total 24-hour urinary excretion and the albumin:creatinine ratio on a weekly basis (Figure 3.1B, C, S3.1B, C). Using either measure, albuminuria was significantly elevated in the ADR group at weeks 2 to 4, with attenuation at week 4 (Figure 3.1B, C, Table S3.1A, S3.3). Similar effects have been previously reported in ADR-induced SCID mice[172,185,318]. A linear mixed-effects (LME) model showed statistically significant linear and quadratic changes of albuminuria over time within the ADR group ($p<0.001$ for both the linear and second degree terms, Table 3.1).

To assess changes in glomerular filtration over time with the transcutaneous device, we undertook serial measurements of FITC-sinistrin half-life over 4 weeks. Representative examples of clearance curves from control and ADR animals are shown in Figure 3.2A-D. The FITC-sinistrin half-life in the ADR group was increased with statistical significance from week 2 onwards (Figure 3.2E, Table S3.1A, S3.3). Given that GFR is inversely correlated to the FITC-sinistrin half-life[237,322], these results suggest that GFR is slightly impaired 2 weeks after ADR administration and deteriorates further between weeks 3 and 4, reflecting the progressive nature of the nephropathy[171]. An LME model revealed statistically significant linear changes in the FITC-sinistrin half-life within the ADR group over time, with an average increment of 2.45 (= (0.02 + 0.33) x 7) minutes per week ($p<0.001$). These changes were statistically different when compared with controls, in which no significant changes in half-life were detected ($p=0.76$, Table 3.1). The levels of BUN and SCr as indicators of kidney function revealed no significant differences between the experimental control groups at week 5 (Figure S3.1D, E).

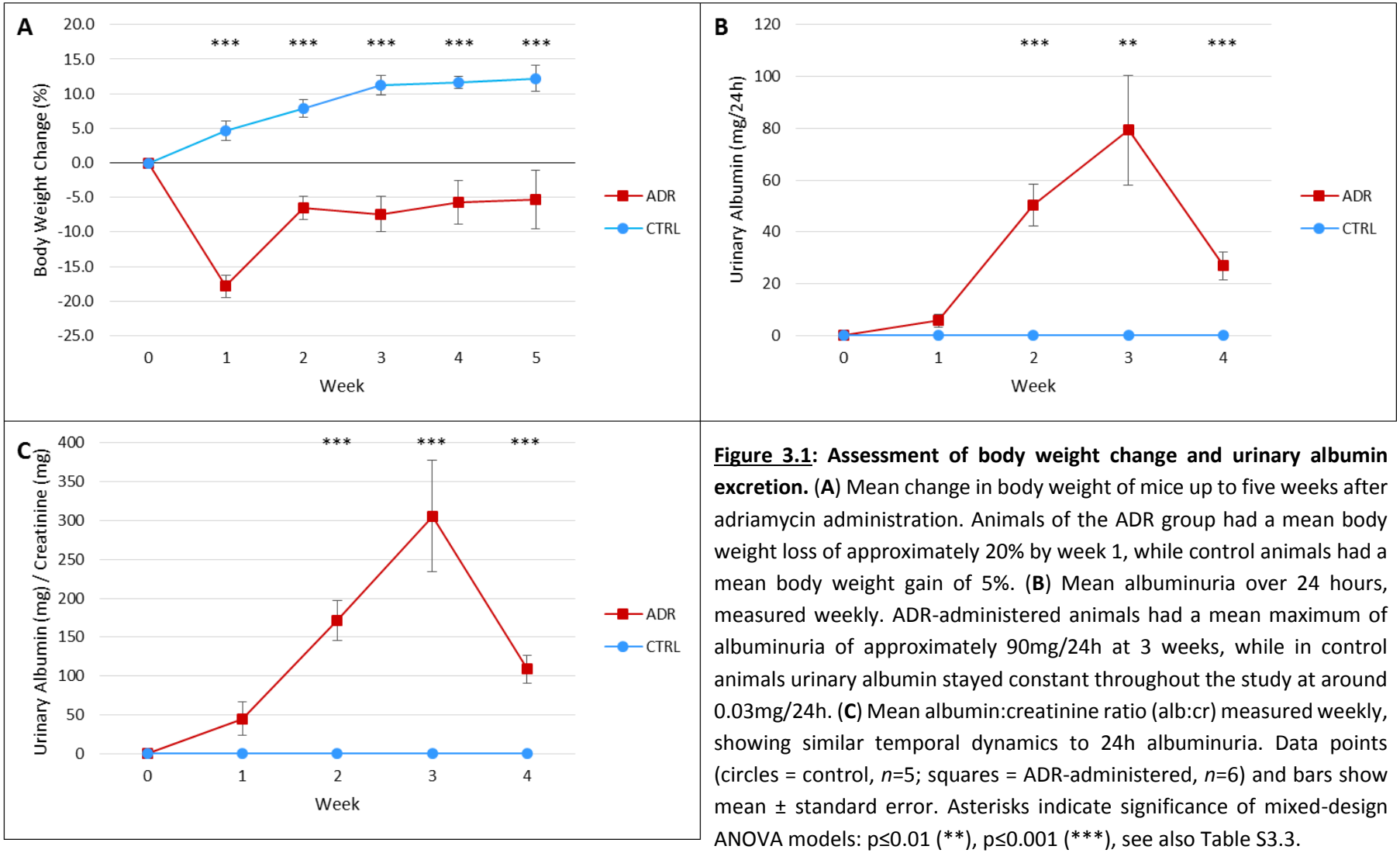

Figure 3.1: Assessment of body weight change and urinary albumin excretion. (**A**) Mean change in body weight of mice up to five weeks after adriamycin administration. Animals of the ADR group had a mean body weight loss of approximately 20% by week 1, while control animals had a mean body weight gain of 5%. (**B**) Mean albuminuria over 24 hours, measured weekly. ADR-administered animals had a mean maximum of albuminuria of approximately 90mg/24h at 3 weeks, while in control animals urinary albumin stayed constant throughout the study at around 0.03mg/24h. (**C**) Mean albumin:creatinine ratio (alb:cr) measured weekly, showing similar temporal dynamics to 24h albuminuria. Data points (circles = control, *n*=5; squares = ADR-administered, *n*=6) and bars show mean ± standard error. Asterisks indicate significance of mixed-design ANOVA models: p≤0.01 (**), p≤0.001 (***), see also Table S3.3.

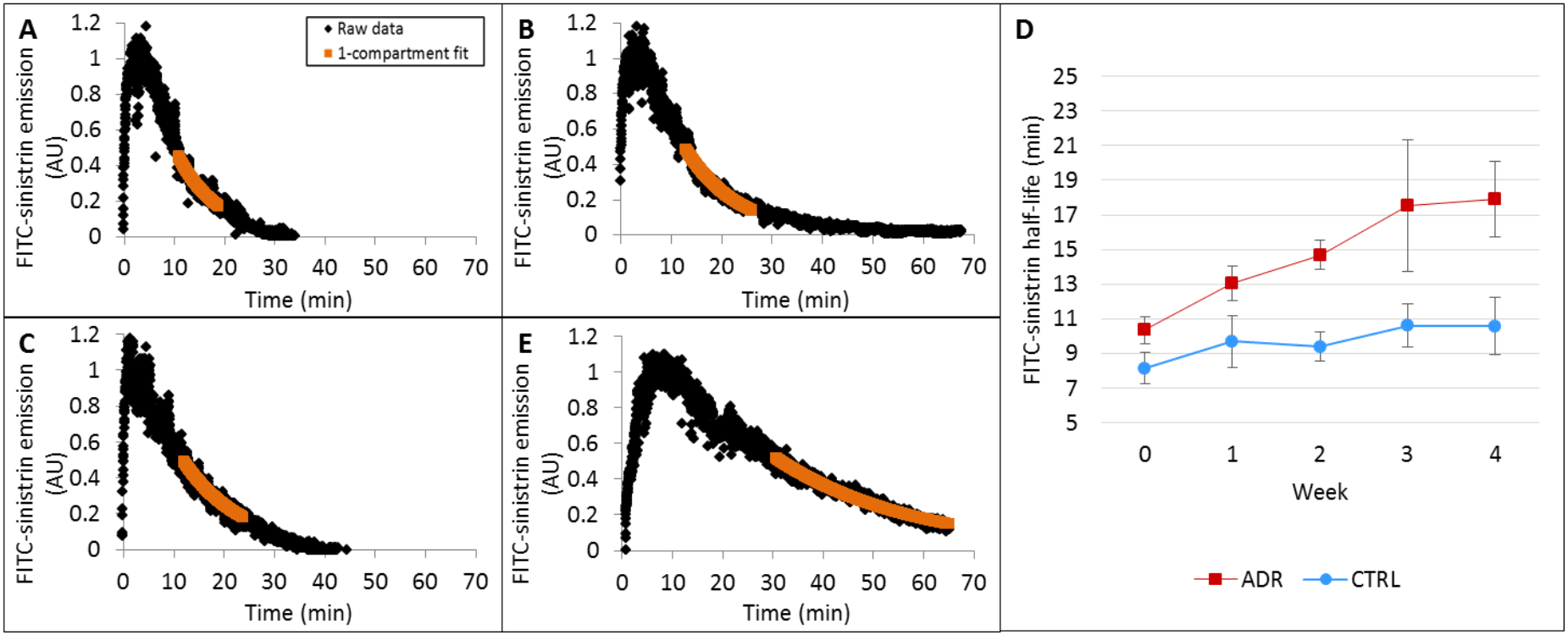

Figure 3.2: Transcutaneous assessment of FITC-sinistrin clearance over time. (**A-D**) Typical FITC-sinistrin kinetic curves (arbitrary units) in a control mouse at week zero (**A**), and four (**B**); and in an ADR-administered mouse prior to (**C**) and at four weeks post-adriamycin administration (**D**). (**E**) The mean half-life of FITC-sinistrin for the ADR-administered and control groups is shown weekly for four weeks. Data points (circles = control, *n*=5; squares = ADR-administered, *n*=6) and bars show mean ± standard error. Asterisks indicate significance of mixed design ANOVA models: p≤0.05 (*), p≤0.01 (**), see also Table S3.3.

Table 3.1: Statistical mixed-effects models that describe albuminuria and FITC-Sinistrin half-life over time. The model terms are listed with the corresponding coefficients estimates (Coef. estimate), standard error (SE) and p-value. The factor 'Group' is defined as 1 if the mouse belongs to the ADR group, and as 0 otherwise. The error terms of the model are also reported. *Follows a normal distribution with mean zero and standard deviation (SD).

Urinary Albumin			
Changes over time (LME)			
Factor (adriamycin)^	Coef.	SE	P-value
Group	-12.94	8.11	0.12
Group x Time	8.34	1.3	**<0.001**
Group x Time^2	-0.24	0.04	**<0.001**
Error terms	Mean	SD	
Random Error*	0	6.86	
Residual*	0	4.64	

FITC-sinistrin half-life			
Changes over time (LME)			
Factor (adriamycin)^	Coef.	SE	P-value
Intercept	9.96	0.91	<0.001
Time	0.02	0.07	0.76
Time x Group	0.33	0.07	**<0.001**
Error terms	Mean	SD	
Random Error*	0	0.71	
Residual*	0	3.74	

3.4.2 The passage of IRDye through the kidney measured using MSOT is delayed in ADR mice

To investigate the potential of MSOT for evaluating renal function in ADR mice, IRDye clearance was monitored in real-time at week 5, before killing for necropsy studies. Movies and snap-shot images taken prior to, and 15 s, 45 s, 1 min 30 s and 3 min after administration of IRDye showed that its passage through the kidney appeared to be delayed in ADR *versus* control mice (Figure 3.3A, supplementary movie 3.1, 3.2). More specifically, temporal colour maps of the clearance kinetics confirmed that in nephropathic mice, the dye took longer to transit from the kidney cortex to the papilla/pelvis region than in controls (Figure 3.3B). Visualisation of the T_{MAX} allows discrimination between the ADR and the control group, highlighted by the peak signal intensity in the cortex of the control animals appearing at ~30 s and visualised in yellow. By contrast, the yellow tone indicating 30 s peak signal intensity is absent in the ADR treated mice; instead, green colour tones visualise peak signal intensities that appear with a delay at around 1 min. Furthermore, the papilla/pelvis region of control animals show peak concentrations from 1.5 – 3 minutes (green, blue, violet, red), whereas the ADR treated mice show peak concentrations in this region only after 3 minutes (violet, red, Figure 3.3B). We determined the pharmacokinetics of IRDye clearance by calculating the T_{MAX} delay between the renal cortex and pelvis (Figure

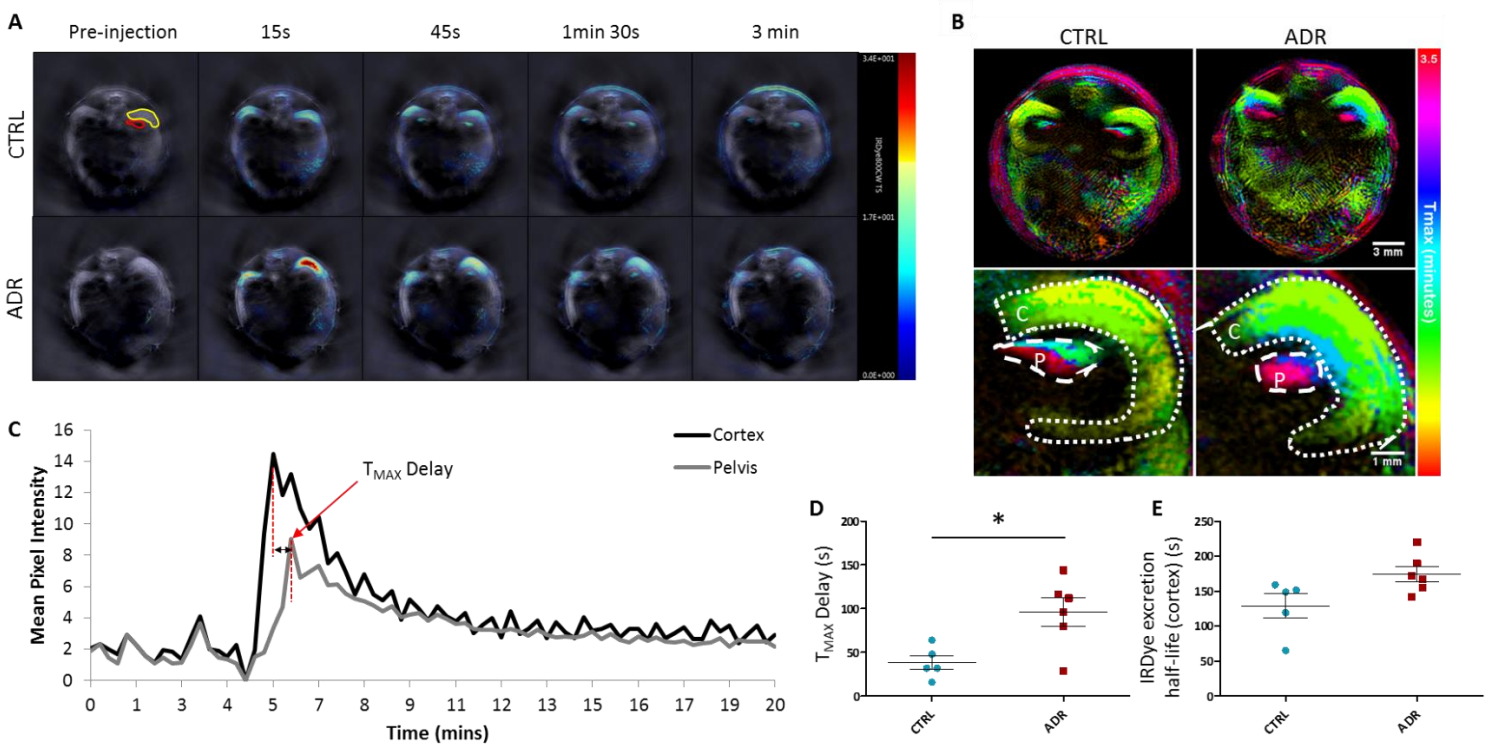

<u>Figure 3.3</u>: MSOT imaging of IRDye clearance kinetics. (**A**) MSOT images of a typical control (top) and ADR-administered (bottom) mouse before and after the administration of IRDye. Region of interests (ROIs) depicted in yellow (cortex) and red (papilla/pelvis region). Times indicated above apply to both control and ADR-treated animal. (**B**) Temporal colour maps of control and ADR-administered mice reveal a delay in IRDye clearance kinetics in the treated mice. (**C**) Characteristic plot of mean pixel intensity (MSOT arbitrary units) from ROIs drawn around the renal cortex (black) and papilla/pelvis region (grey). (**D-E**) Graphs showing distribution of T_{MAX} delay (**D**) and the excretion half-life in the cortex (**E**) in ADR-administered and control animals. Data points (**D-E**) represent individual animals (circles = control, *n*=5; squares = ADR-administered, *n*=6) and lines represent mean ± standard error. Asterisks indicate significance of two-sample t-tests: p≤0.05 (*), see also Table S3.2.

3.3C, D, Table S3.1B), and the clearance half-life in the cortex, using exponential decay fitting (Figure 3.3C, E, Table S3.1B). T_{MAX} delay was significantly increased in the ADR-administered group *versus* controls (p=0.015), and there was a non-significant increase in clearance half-life between these two groups (Figure 3.3D, E; Table S3.2). However, equilibrium dialysis revealed that over 40% of IRDye bound to plasma proteins (Table S3.4), suggesting that the exponential decay might be shorter than expected in ADR mice due to leakage of plasma proteins through the glomerular filtration barrier, thus leading to a potential underestimation of the true clearance half-life in the cortex.

3.4.3 Minimally invasively measured clearance kinetics of sinistrin and IRDye show a strong correlation with glomerular histological damage

To visualise and measure structural damage, we made use of Picro-Sirius Red (PSR) staining which binds specifically to fibrillar collagen type I and III under polarising microscopy. Analysing PSR staining on parasagittal kidney sections from mice necropsied at week 5, we determined that ADR kidneys contained a subset (12-29%, across the whole experimental group) of glomeruli with lesions (Figure 3.4B, C; Tables S3.1B, S3.2). In these glomeruli, there was a loss of capillary loops and extension of PSR staining into the glomerular tuft beyond the normal tree-like mesangial pattern. In control kidneys, such glomerular lesions were rarely detected (Figure 3.4A). Quantification of total PSR staining (i.e. not confined to glomeruli) under bright field microscopy, and of fibrillar collagen under polarising microscopy, failed to show significant differences in ADR *versus* control kidneys (Figure 3.4D, E, S3.2A, B; Tables S3.1B, S3.2). However, we noted the occurrence of proteinaceous casts together with flattened tubular epithelia in both PSR- and Masson's Trichrome-stained ADR kidneys viewed under bright field microscopy (Figure S3.2B, D), but not in control kidneys (Figure S3.2A, C). These observations show that in this model, at this particular time point, glomerular damage is the predominant lesion, while tubulo-interstitial changes are much less prominent.

Next, we evaluated whether the two novel minimally invasive dye clearance methods we have used here to detect kidney filtration function, are suitable for long-term regenerative medicine therapy studies through their statistical association with detected glomerular damage. Importantly, since we had observed a wide range in the proportions of scarred glomeruli (as assessed by the above criteria) in the ADR kidneys, we questioned whether specific glomerular damage in individual mice was associated with specific measures of kidney function. Therefore, we examined the relationship in individual animals between

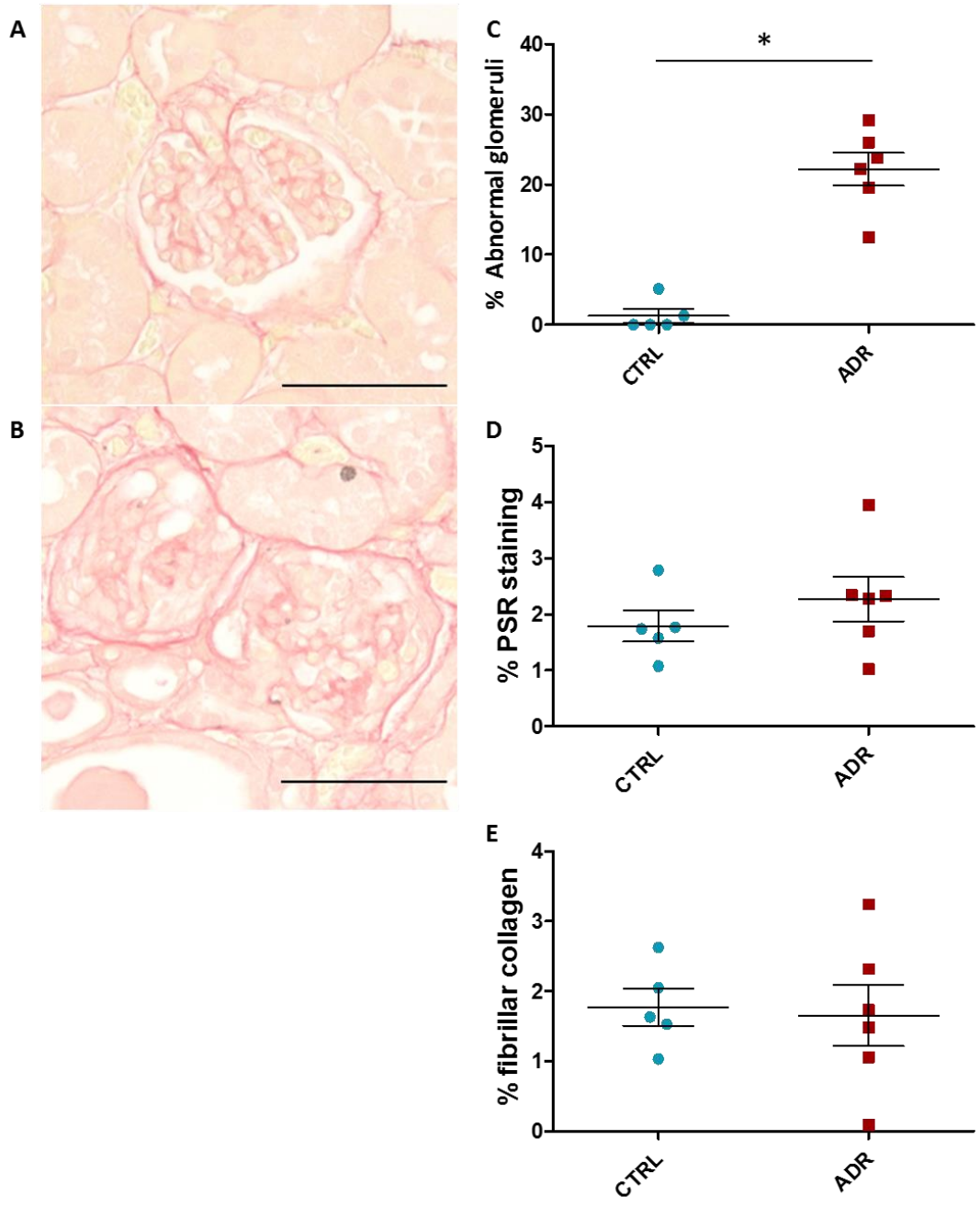

<u>Figure 3.4</u>: Histological evaluation and quantification of glomerulosclerosis and fibrosis. Typical examples of normal (**A**) and abnormal (**B**) glomeruli imaged under bright field microscopy in 4µm Picro-Sirius Red-stained paraffin sections at week five. On one kidney section per animal the percentage of abnormal glomeruli was determined (**C**). One whole kidney section per animal was photographed under bright field and polarised microscopy and the images were stitched together to produce one whole kidney image. On each whole-kidney image the percentage of PSR staining under bright field light (**D**) and the percentage of fibrillar collagen under polarised light (**E**) were quantified using image analysis software. Scale bars (**A-B**) represent 50 µm. Data points (**C-E**) represent individual animals (circles = control, *n*=5; squares = ADR-administered, *n*=6) and lines represent mean ± standard error. Asterisks indicate significance of two-sample t-tests: p≤0.01 (**), see also Table S2.

glomerular histological lesions and (i) albuminuria, (ii) FITC-sinistrin half-life and (iii) IRDye excretion kinetics in individual animals (Figure 3.5). In ADR mice, there was no significant association between glomerular histological damage (week 5) and the amount of albuminuria measured at the maximum (weeks 2-3) or at the final point of urine collection in week 4 (Table 3.2). Therefore, albuminuria is not a reliable measure of glomerular histological damage in this model. By contrast, assessment of the relationship between FITC-sinistrin half-life and the proportion of histologically damaged glomeruli revealed a significant positive correlation between FITC-sinistrin half-life values at week 4 and glomerular damage at week 5 (coefficient=0.94, p=0.001; see Table 3.2).

When we assessed the relationship at 5 weeks between glomerular histological damage and IRDye clearance half-life, we found a significant association in the ADR group (coefficient=0.12, p=0.02; Table 3.2). Furthermore, the T_{MAX} delay was significantly associated with glomerular histological damage in the ADR group (coefficient=0.16, p=0.002; Table 3.2). The coefficient suggests that an increment of 60 seconds in T_{MAX} delay is associated with an increment of glomerular histological damage of about 10%.

3.5 Discussion

Here, we report for the first time the use of transcutaneous measurement of FITC-sinistrin decay and MSOT detection of IRDye clearance as measures of glomerular filtration function in SCID mice with ADR-induced nephropathy. Our albuminuria measurements strongly suggest that ADR-induced nephropathy featured a loss of glomerular macromolecular barrier integrity in SCID mice from week 2, peaking at week 3, similarly to recently published results[172,185,318]. In ADR mice, the FITC-sinistrin half-life was significantly prolonged from week 2. The fact that the half-life continued to rise thereafter in the ADR group is a strong indicator of a progressive loss in the ability of the kidneys to excrete small molecules from the circulation, i.e. a progressive decline in GFR. Previous studies have demonstrated the accuracy and reliability of the transcutaneous measurement of FITC-sinistrin half-life as a measure of GFR in various strains of rats and mice[232,234,237,238,242,322,323]. Of note, although remaining elevated, the degree of albuminuria fell between weeks 3 and 4. This again might be explained by a loss in total filtration surface associated with glomerular damage as observed in week 5, consistent with the observed rise in FITC-sinistrin half-life during this period.

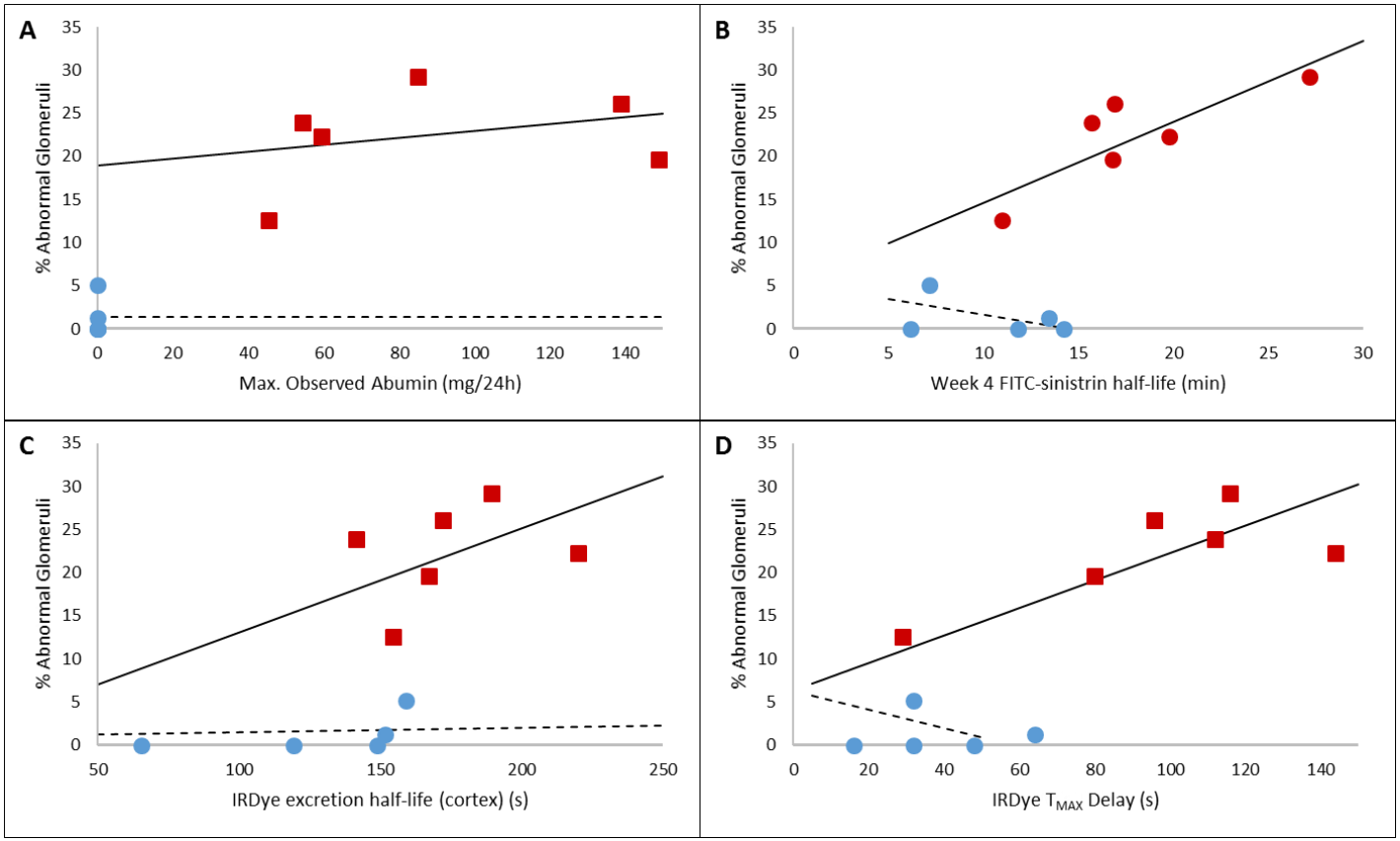

Figure 3.5: Correlation graphs between % abnormal glomeruli and minimally invasive methods of measuring kidney function. Correlation graphs showing the correlation of both control and ADR group data between the percentage of abnormal glomeruli and maximum observed albuminuria (**A**), FITC-Sinistrin half-life at week 4 (**B**), IRDye excretion half-life in the cortex at week 5 (**C**) and IRDye T_{MAX} delay (**D**) at week 5. Data points represent individual animals (circles = control, *n*=5; squares = ADR-administered, *n*=6). Trend lines for control (dashed line) and ADR-administered (solid line) animals are displayed.

Table 3.2: Table summarising the associations in the ADR group between abnormal glomeruli (5w) and the four biomarkers: albuminuria at the maximum observed and at four weeks, FITC-Sinistrin half-life, IRDye clearance half-life, IRDye T_{MAX} delay. The results included in this table were derived from the statistical models described in Supplementary Table S3.5 by using *contrast analysis*. Each coefficient estimate indicates the change in percentage of abnormal glomeruli per unit change of the corresponding biomarker.

Biomarker	Coefficient	SE	P-value
$Albuminuria_{MAX}$	0.04	0.05	0.45
$Albuminuria_{4w}$	0.2	0.15	0.21
FITC-sinistrin $half\text{-}life_{4w}$	0.94	0.18	**0.001**
IRDye excretion half-life	0.12	0.04	**0.02**
IRDye T_{MAX} delay	0.16	0.03	**0.002**

Using MSOT imaging, we showed here that IRDye is cleared in a dynamic fashion as it first appears in the kidney cortex and then transits to the renal pelvis, confirming a previous report[248]. The simplest interpretation of the T_{MAX} delay of IRDye clearance we measured in the ADR *versus* control group, is that the glomerular clearance of this small molecule is impaired. The observation that some IRDye binds to plasma proteins, and that the ADR model features proteinuria, may have led to an underestimation of the true 'T_{MAX} delay'. In addition, it is possible that the passage of IRDye along the lumen of kidney tubules may be compromised in the ADR model but this will require further study.

Our BUN and SCr measurements revealed that these are not useful indicators of ADR-induced nephropathy at a time point when sinistrin clearance deviated most from normal. Both BUN and SCr measurements have been questioned as biomarkers for the early detection of human and rodent kidney disease at the histological level since they frequently identify abnormal kidney function only in the later stages of the diseases[324,325]. Previously, an increase in SCr in ADR-induced nephropathy has only been observed in male rodents, while in female rodents, SCr levels remained unchanged when compared to control animals, even though pathohistology clearly indicated the full spectrum of renal damage[156,172,313,326-328].

Crucially, our observations that BUN and SCr fail to detect significant differences in kidney function at a time point when histological changes are clearly quantifiable, emphasises the need to develop novel molecular biomarkers that are better able to monitor renal health and

assess the efficacy of therapeutic interventions, including regenerative medicine therapies[324,329,330].

We conclude that transcutaneous measurements of FITC-sinistrin half-life provide a minimally invasive method to repeatedly assess GFR in conscious mice, thus allowing for longitudinal evaluation of kidney function. Furthermore, our analysis suggests that MSOT imaging has the potential to be employed for the repeated and minimally invasive measurement of kidney function in mice by assessing renal clearance of injected small near infrared dyes. The use of near infrared dyes with negligible plasma protein binding properties will further improve MSOT imaging performance for the measurement of renal clearance kinetics. Optoacoustic imaging can also be employed to track administered stem cells labelled with gold nanorods, expressing tyrosinase or near infrared fluorophores in whole animals[331-338]. Therefore, this imaging technology will be of high importance for preclinical studies in regenerative approaches to nephropathies as it will allow the detection of labelled cells in parallel with functional measurements of renal clearance kinetics.

In order to assess whether functional kidney data correlated with glomerular scarring, we performed histological analysis of sections by staining with PSR and Masson's Trichrome. While SCID animals with ADR-induced nephropathy showed a strong elevation in the number of abnormal glomeruli at 5 weeks, at this time point we only observed occasional pathohistological changes in the tubulo-interstitial zone of ADR mice. Cortical glomerular and tubulo-interstitial damage have been reported previously in mice with ADR-induced nephropathy[156,171,172,339,340].

Importantly, we aimed to statistically analyse whether any associations could be detected between glomerular histological damage and albuminuria, FITC-sinistrin half-life or IRDye clearance, respectively, in mice with ADR-induced nephropathy on the SCID background. Our evaluations provide evidence that FITC-sinistrin half-life and T_{MAX} of IRDye clearance were strongly correlated with glomerular scarring in SCID mice with ADR-induced nephropathy. We therefore conclude that FITC-sinistrin half-life and IRDye clearance (T_{MAX}) measurements may be good predictors of glomerular histological damage. In contrast, neither peak albuminuria nor albuminuria at 4 weeks after ADR-induced nephropathy were significantly correlated with glomerular scarring, suggesting that urinary albumin measurements fail to provide an accurate reflection of the histological glomerular damage in this model at this time point.

In a recent report, rats with ADR-induced nephropathy were analysed with magnetic resonance imaging to monitor changes in kidney function and histopathology during disease progression. This study is another example, similar to the one we report here, to demonstrate the feasibility of a longitudinal, minimally-invasive imaging technology as an approach to assessment of changes in the kidney over time[341].

In conclusion, our results indicate that the minimally invasive technologies for detecting FITC-sinistrin half-life and IRDye clearance kinetics could be widely adopted for *in vivo* monitoring of models of RMT in progressive kidney disease. Each technology potentially allows recurrent testing in individual animals, maximising the information obtained as nephropathy and/or regenerative effects progress. The observations that sinistrin clearance and IRDye kinetics significantly correlate with the proportions of damaged glomeruli in individual animals, indicates that these minimally invasive measurements could markedly reduce animal numbers in preclinical models of nephropathy.

3.6 Acknowledgements

We acknowledge funding from the Alder Hey Children's Kidney Fund (AR-R, BW, PM, SK), UKRMP Safety and Efficacy Hub (PM, PR, LS, JS, BW, DD, MG-F, ASW, BKP, RL), and the FP7 Marie Curie NephroTools ITN (PM, BW, NG, SG, JH). Part of this work was facilitated by the Manchester Biomedical Research Centre (PR and ASW).

3.7 Author Contributions Statement

LS, AR-R, PM and BW designed the experiments. LS, AR-R, JS performed the animal studies including measurements and analysis of weight change, albuminuria, SCr, BUN, and measurements of FITC-sinistrin and IRDye clearance. LS, PR, DM and ASW performed the histological analysis including scoring for glomerulosclerosis and image analysis for fibrosis. SG and NG analysed the FITC-sinistrin data; JH and NG measured the plasma protein binding capacity of IRDye. NCB, JS and RL performed the MSOT data and image analysis. DD, MG-F, LS, JS performed the statistical modelling and analysis. SK, ASW, NG, RL, BKP provided experimental advice. LS, JS, ASW, PM and BW wrote the manuscript and generated the figures, and all authors reviewed the manuscript.

3.8 Competing Financial Interests

NCB is an employee of iThera Medical, GmbH.

3.9 Supplementary Figures and Tables

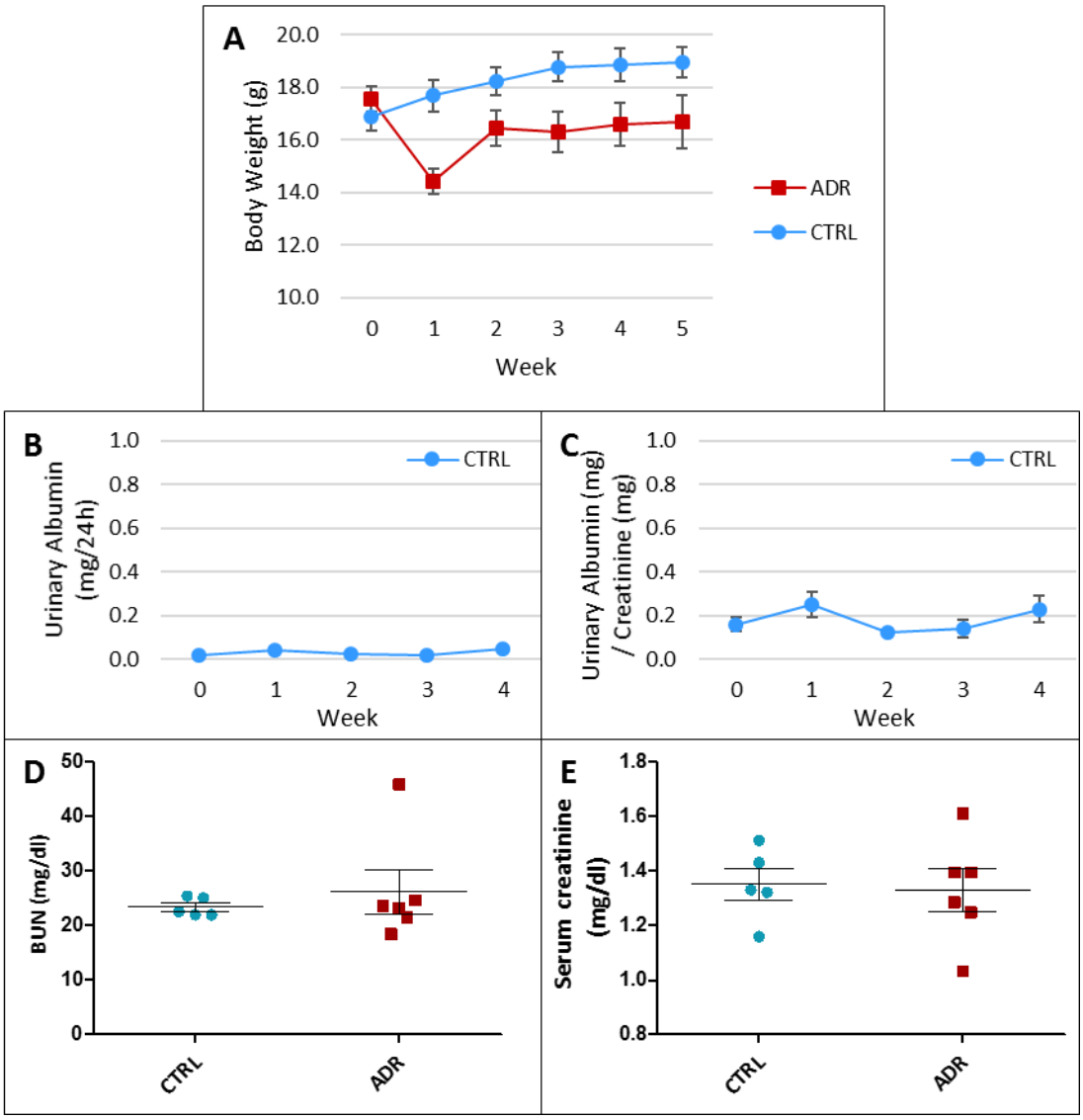

Supplementary Figure S3.1: **Additional body weight, urinary albumin, BUN and SCr data.** (**A**) Mean body weight measured weekly for 5 weeks. (**B-C**) Mean 24h urinary albumin levels (**B**) and urinary albumin:creatinine ratio (**C**) in control animals only, measured weekly up to week 4. (**D, E**) Blood urea nitrogen (BUN, **D**) and serum creatinine (**E**) in ADR-administered and control mice measured in serum collected via cardiac puncture immediately after sacrifice at week 5. Serum biomarkers in µmol/L for reference. BUN: ADR, mean = 2316.54, SE = 357.87; CTRL, mean = 2069.13, SE = 67.41. SCr: ADR, 117.44, SE = 6.94; CTRL, 119.47; SE = 5.25. Data points represent the group mean (**A-C**) or individual animals (**D, E**) (circles = control, *n*=5; squares = ADR-administered, *n*=6) and bars represent mean ± standard error.

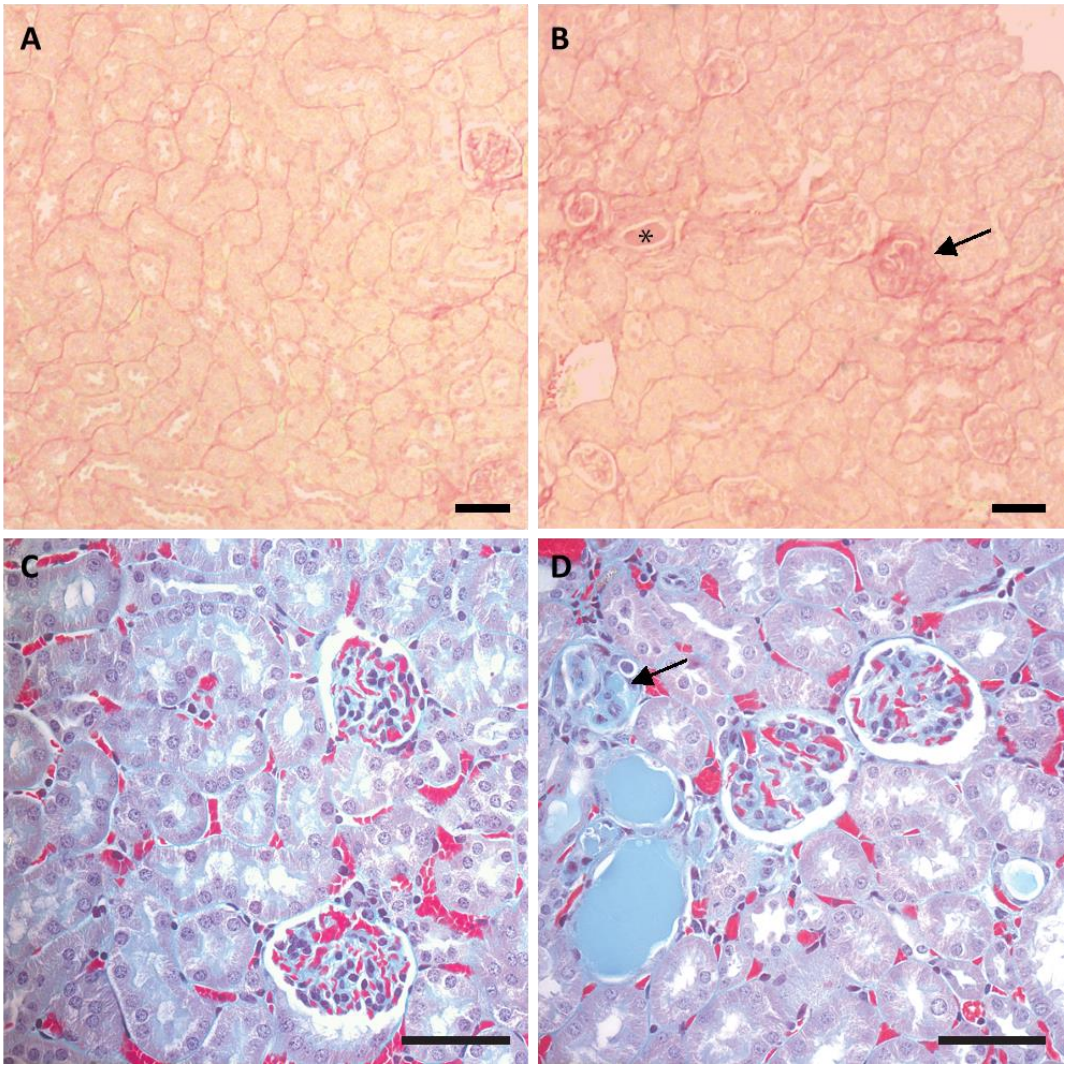

<u>Supplementary Figure S3.2</u>: Additional PSR and Masson's Trichrome images of renal injury. Typical examples of normal (A, C) and slightly scarred (B, D) regions of the renal cortex imaged under polarised microscopy in Picro-Sirus Red-stained (A, B) or under bright field microscopy in Masson's Trichrome-stained (C, D) paraffin sections at week 5. Scale bars represent 50µm. Tubular casts (*) and scarred glomerulus (arrow) can be observed within the cortex of Picro-Sirius Red-stained and Masson's Trichrome-stained kidneys.

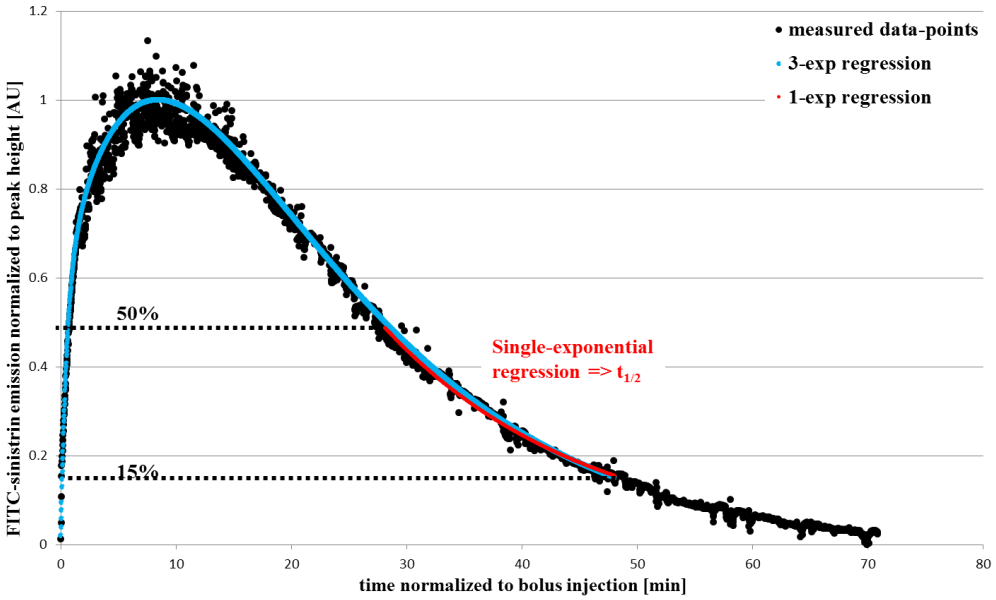

Supplementary Figure S3.3: **Sample graph depicting FITC-sinistrin emission data** points plotted against time after bolus injection to illustrate the way the 1-compartment fit is determined. The blue line shows the 3-exponential function, while the red line (1-exponential function) corresponds to the orange line in Figures 2A-D of the manuscript. Specifically, the 1-compartment fit was applied from 50% to 15% of the peak height (red curve) and t1/2 was calculated as described in Schreiber et al., 2012 (PMID: 22696603). The reference peak height was recognized as the peak of the 3-exponential function that was preliminary fitted to the whole measured curve.

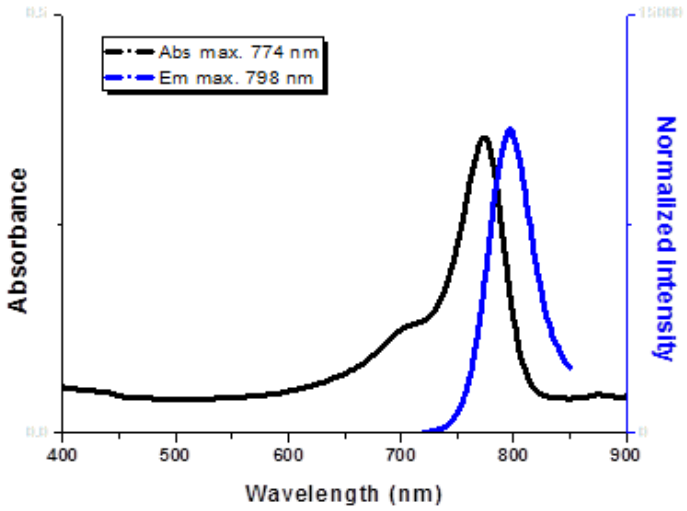

Supplementary Figure S3.4: **Absorption and emission spectrum scan of IRDye**. Normalised absorption (black) and emission (blue) spectrum scan of 10µmol IRDye in PBS. The absorption maximum is at 774 nm, while the emission maximum is at 798 nm.

Supplementary Table S3.1A: Table summarising the individual values of all longitudinal parameters measured in adriamycin (ADR)-administered and control (CTRL) mice from weeks zero to four. The mean and standard error (SE) for ADR-administered and control groups are shown. x = data unsuitable for analysis as the kinetics of the curves obtained at these time points were significantly affected by movement artefacts.

		Urinary Albumin (mg/24h)					**Urinary Albumin : Creatinine ratio (mg/mg)**					**FITC-Sinistrin Half-Life (minutes)**				
	Animal ID	Week 0	Week 1	Week 2	Week 3	Week 4	Week 0	Week 1	Week 2	Week 3	Week 4	Week 0	Week 1	Week 2	Week 3	Week 4
ADR	A1	0.02	16.10	59.49	34.11	23.23	0.20	123.61	176.84	153.16	176.00	8.14	X	15.05	14.25	19.80
	A2	0.01	4.30	45.53	32.30	9.06	0.14	35.34	176.21	226.65	46.02	10.60	10.10	14.90	10.76	11.00
	A3	0.04	11.08	85.16	66.98	32.19	0.16	97.98	271.34	192.71	114.56	12.19	14.11	14.10	17.47	27.19
	A4	0.01	0.74	37.21	139.00	16.19	0.13	3.40	180.82	372.47	90.78	10.64	14.67	17.67	13.18	16.91
	A5	0.04	0.87	28.34	54.40	44.71	0.19	3.91	82.12	260.72	132.80	12.43	X	11.34	X	15.75
	A6	0.01	1.16	46.57	149.05	35.89	0.14	6.78	140.94	629.59	92.70	8.10	13.32	15.11	32.11	16.82
	Mean	**0.02**	**5.71**	**50.38**	**79.31**	**26.88**	**0.16**	**45.17**	**171.38**	**305.88**	**108.81**	**10.35**	**13.05**	**14.69**	**17.55**	**17.91**
	SE	**0.01**	**2.63**	**8.14**	**21.18**	**5.39**	**0.01**	**21.57**	**25.18**	**71.57**	**17.94**	**0.77**	**0.83**	**0.83**	**3.46**	**2.19**
CTRL	C1	0.02	0.03	0.03	0.01	0.06	0.16	0.14	0.09	0.18	0.22	5.78	15.18	6.40	8.77	7.18
	C2	0.02	0.05	0.03	0.01	0.05	0.13	0.50	0.11	0.28	0.15	8.05	8.87	10.76	9.29	6.15
	C3	0.03	0.02	0.03	0.01	0.03	0.26	0.13	0.10	0.08	0.14	9.75	9.94	9.09	10.87	11.85
	C4	0.01	0.07	0.02	0.03	0.07	0.10	0.34	0.11	0.08	0.45	10.54	6.66	9.75	15.33	14.25
	C5	0.02	0.04	0.02	0.02	0.04	0.15	0.19	0.10	0.06	0.20	6.62	7.78	11.00	8.70	13.47
	Mean	**0.02**	**0.04**	**0.03**	**0.02**	**0.05**	**0.16**	**0.25**	**0.12**	**0.14**	**0.23**	**8.15**	**9.69**	**9.40**	**10.59**	**10.58**
	SE	**0.01**	**0.01**	**0.01**	**0.01**	**0.01**	**0.03**	**0.06**	**0.01**	**0.04**	**0.06**	**0.90**	**1.48**	**0.83**	**1.25**	**1.65**

Supplementary Table S3.1B: Table summarising the individual values of end-point measures in adriamycin (ADR)-administered and control (CTRL) mice 5 weeks after the administration of adriamycin. The mean and standard error (SE) for ADR-administered and control groups are shown.

		T_{MAX} Delay (s)	**Cortex Decay (s)**	**% Abnormal Glomeruli**	**% staining (bright field)**	**% staining (polarised light)**	**Serum Creatinine (mg/dl)**	**Blood Urea Nitrogen (mg/dl)**
	Animal ID	Week 5	Week 5	Week 5	Week 5	Week 5	Week 5	Week 5
ADR	A1	143.99	220.20	22.22	2.33	1.06	1.39	23.60
	A2	29.02	154.80	12.50	2.28	3.24	1.03	18.42
	A3	116.01	189.60	29.14	3.95	1.48	1.61	45.95
	A4	96.01	172.20	26.02	1.02	0.09	1.25	21.42
	A5	112.02	141.60	23.81	1.70	1.73	1.39	24.65
	A6	80.02	167.40	19.57	2.34	2.32	1.29	23.18
	Mean	**96.18**	**174.30**	**22.21**	**2.27**	**1.65**	**1.33**	**26.21**
	SE	**16.02**	**11.32**	**2.35**	**0.40**	**0.44**	**0.08**	**4.05**
CTRL	C1	31.99	159.00	5.13	1.58	1.53	1.32	22.56
	C2	32.00	148.80	0.00	1.74	1.63	1.43	21.99
	C3	47.99	65.40	0.00	2.79	2.62	1.16	25.07
	C4	15.98	119.40	0.00	1.77	2.05	1.51	25.43
	C5	64.01	151.80	1.30	1.08	1.03	1.33	21.99
	Mean	**38.40**	**128.88**	**1.29**	**1.79**	**1.77**	**1.35**	**23.41**
	SE	**8.16**	**17.25**	**0.99**	**0.28**	**0.27**	**0.06**	**0.76**

Supplementary Table S3.2: Table summarising the statistical analyses used to assess if there was a statistically significant difference between the adriamycin (ADR)-administered and control groups for parameters measured at week 5 only. Normality tests were applied to check the assumption that the data come from a normal distribution; when the normality hypothesis was rejected a non-parametric test was applied. No adjustment for multiple comparisons was made.

	Normally Distributed Data?	Statistical test	Test value	P-value	Degrees of Freedom
T_{MAX} Delay (s)	Yes	Two-sample t-test assuming unequal variance	T = 3.21	0.015	7
IRDye excretion half-life (cortex) (s)	Yes	Two-sample t-test assuming unequal variance	T = 2.2	0.064	7
% Abnormal Glomeruli	No	Wilcoxon rank sum test with continuity correction	W = 30	0.008	
% PSR staining	Yes	Two-sample t-test assuming unequal variance	T = 0.95	0.366	9
% Fibriallar collagen	Yes	Two-sample t-test assuming unequal variance	T = -0.25	0.809	9
Serum Creatinine (mg/dl)	Yes	Two-sample t-test assuming unequal variance	T = -0.23	0.821	8
Blood Urea Nitrogen (mg/dl)	No	Wilcoxon rank sum test with continuity correction	W = 14	0.927	

Supplementary Table S3.3: Table summarising the results of mixed-design ANOVA models carried out to assess the significance of comparisons between adriamycin-administered mice and time-matched controls at multiple time points.

	Week 0	Week 1	Week 2	Week 3	Week 4	Week 5
Weight Change		$p < 0.001$	$p < 0.001$	$p < 0.001$	$p < 0.001$	$p < 0.001$
24h Albumin	$p = 0.999$	$p = 0.194$	$p = 0.001$	$p = 0.004$	$p = 0.001$	
Alb:Cr	$p = 0.999$	$p = 0.223$	$p = 0.001$	$p = 0.001$	$p = 0.001$	
FITC-sinistrin half-life	$p = 0.510$	$p = 0.326$	$p= 0.029$	$p = 0.041$	$p = 0.005$	

Supplementary Table S3.4: IRDye protein plasma binding (PPB) determined by measuring the UV absorption (A) at 774nm of IRDye or phosphate buffered saline (PBS) incubated with rat plasma or PBS for 24 hours.

	Control group (no IRDye)			Sample group			Sample - Control
Plasma	0.1673	0.1663	0.1691	0.2046	0.202	0.2051	0.0364
Mean	0.1675			0.2039			
PLBS	0.0428	0.042	0.0416	0.0595	0.058	0.054	0.0151
Mean	0.0421			0.0572			
PPB	[A(plasma) - A(PBS)] / [A(plasma) + A(PBS)] * 100 =						**41%**

Supplementary Table S3.5: Mathematical representation (multiple regression models) of the association between abnormal glomeruli at week 5 and (i) maximum albuminuria, (ii) albuminuria at week 4, (iii) FITC-Sinistrin half-life at week 4, (iv) IRDye excretion half-life in the cortex at week 5, and (v) IRDye TMAX at week 5. The factor Group is defined as 1 if the mouse belonged to the adriamycin (ADR) group, and as 0 otherwise. Goodness-of-fit was assessed for each model using the R2 values: Model (i) R2 = 0.84, (ii) R2 = 0.86, (iii) R2 = 0.93, (iv) R2 = 0.84, (v) R2 = 0.88. *Follows a normal distribution with mean zero and standard deviation (SD).

(i) glomerular histological damage (5w) - maximum observed albuminuria			
Factor	Coef.	SE	P-value
Intercept	1.29	2.08	0.55
Group	17.65	4.97	0.008
$Albuminuria_{MAX}$ x Group	0.04	0.05	0.45
Error terms	Mean	SD	
Residual*	0.00	4.64	

(ii) glomerular histological damage (5w) - albuminuria (4w)			
Factor	Coef.	SE	P-value
Intercept	1.29	1.95	0.53
Group	15.57	4.76	0.01
$Albuminuria_{4w}$ x Group	0.2	0.15	0.21
Error terms	Mean	SD	
Residual*	0	4.35	

(iii) glomerular histological damage (5w) - FITC-sinistrin half-life (4w)			
Factor	Coef.	SE	P-value
Intercept	5.15	3.23	0.15
$FITC_{4w}$ half-life	-0.36	0.3	0.28
$FITC_{4w}$ half-life x Group	1.3	0.18	**0.001**
Error terms	Mean	SD	
Residual*	0.00	3.00	

(iv) glomerular histological damage (5w) - IRDye800CW excretion half-life (5w)			
Factor	Coef.	SE	P-value
Intercept	0.92	7.01	0.9
Extretion half-life	0.005	0.05	0.93
Excretion half-life x Group	0.116	0.02	**0.001**
Error terms	Mean	SD	
Residual*	0.00	4.74	

(v) glomerular histological damage (5w) - IRDye800CW T_{MAX} delay (5w)			
Factor	Coef.	SE	P-value
Intercept	6.27	3.29	0.09
T_{MAX} delay	-0.11	0.08	0.23
T_{MAX} delay x Group	0.27	0.06	**0.003**
Error terms	Mean	SD	
Residual*	0.00	4.03	

Supplementary Movie 3.1: Movie showing the clearance of IRDye (20nmol) through the kidney of an adriamycin (ADR)-administered mouse at week 5. IRDye was administered to the mouse through a tail vein cannula at 4.8 min and can be first seen in the renal cortex before it clears through the cortex and collects in the renal pelvis. Videos are displayed at 3 frames per second (1 frame is equal to approximately 15 seconds).
https://www.dropbox.com/s/ilg6u93jb24r4rm/A1.3%20IR%20Injection.avi?dl=0

Supplementary Movie 3.2: Movie showing the clearance of IRDye (20nmol) through the kidney of a control mouse at week 5. IRDye was administered to the mouse through a tail vein cannula at 4.4 minutes and can be first seen in the renal cortex before it clears through the cortex and collects in the renal pelvis. Videos are displayed at 3 frames per second (1 frame is equal to approximately 15 seconds).
https://www.dropbox.com/s/6ygm83f9m9sc1xi/C4.2%20Injection%20Scan.avi?dl=0

CHAPTER 4

Assessing the efficacy of human kidney-derived cells for ameliorating acute and chronic kidney disease

4.1 Introduction

Stem/progenitor cells isolated from the adult kidney have been proposed as a potential source of therapeutic cells for treating kidney disease[342,343]. Various methods of isolating stem/progenitor cells from the kidney have been explored, including by the identification of label-retaining cells, collecting side-population cells, through cell culture, and by the expression of specific cell surface markers[342]. In particular, the cell surface marker CD133 was first discovered on haematopoietic progenitor cells and, although its function remains unclear[344], cells expressing CD133 have been isolated from the adult kidney and proposed as a multipotent stem cell population[151]. A number of reports have described the efficacy of $CD133^+$ adult human kidney-derived cells for ameliorating kidney injury in various experimental models of kidney disease, such as adriamycin[185], rhabdomyolysis[147-149,345], and cisplatin[134] (Table 4.1). The necessity for the expression of CD133 for renal regeneration was emphasised in several of these studies, where it was reported that $CD133^+$ cells were able to ameliorate functional and structural damage, but $CD133^-$ cells had no effect, resulting in functional and structural injury levels that were comparable to control injured animals receiving saline only[147,148,185]. A report from our laboratory, however, has challenged this, indicating that while hKC therapy was beneficial for improving kidney function, the expression of CD133 had no effect on the therapeutic outcome[134].

In the majority of preclinical studies, the efficacy of stem/progenitor cells for ameliorating kidney injury is assessed primarily in models of AKI, such as rhabdomyolysis, cisplatin, and IRI. These models are ideally suited for testing the efficacy of RMTs for improving kidney function following an isolated insult which temporarily impairs kidney function, such as ischemia or drug exposure, and there is a great clinical need for such therapies for AKI[21,343,346]. However, these models do not represent the growing number of patients with CKD[31,347], for whom models of AKI do not accurately recapitulate the nature of their disease. Patients with CKD often do not present to clinicians in the early stages of disease, due to the large renal functional reserve capacity of the kidneys[226,348], meaning that symptoms of kidney impairment are not evident until the disease is more advanced. As such, CKD patients would not be able to benefit from the fast intervention, or even pre-emptive treatment, that RMTs for AKI may lead to. Experimental models of CKD are therefore vital to assess the feasibility of cell therapy for chronic disease, and to investigate the effect of the timing of RMT administration on therapeutic outcome. Notably, Ronconi *et al.* (2009) have assessed the therapeutic potential of hKCs in a mouse model of adriamycin nephropathy[185], a well-characterised model of chronic progressive glomerular injury[168,169,171,172]. Ronconi *et al.*

(2009) compared the efficacy of $CD133^+$ and $CD133^-$ hKCs, and found that when cells were administered on days one and four after the induction of injury, $CD133^+$, but not $CD133^-$ hKCs, were able to ameliorate albuminuria measured at day seven. While this study investigated the potential for therapeutic intervention in a chronic disease model, a drawback of the experimental design was that the cell therapy was administered very soon after induction of injury. The timing of cell administration in this study therefore did not reflect the clinical scenario, whereby patients would not present symptoms until they had well-established CKD; potentially months or years after the onset of kidney injury. We propose that in order to develop efficacious treatments for CKD, it is essential to assess the effect of timing of administration on the therapeutic outcome of a cell therapy. Chronic progressive kidney disease models, such as adriamycin nephropathy, are ideally suited to such investigations.

In many of the reports on the efficacy of $CD133^+$ hKCs, it was suggested that the cells homed to the injured kidney following IV administration, where they subsequently engrafted into the damaged tissue, and differentiated to form specialised renal cells, thereby exerting a therapeutic effect on the kidney[147,148,185]. However, these conclusions were largely based on histological tracking of cells labelled with PKH26, a lipophilic cell membrane dye. PKH26 has been reported to transfer from labelled cells to host tissues both *in vitro* and *in vivo*[263], and thus raises the possibility of false-positive cell tracking. Indeed, a recent study by Santeramo *et al.* (2017) demonstrated the unreliability of PKH26 as a cell tracking agent, by labelling green fluorescent protein (GFP)-expressing $CD133^+$ hKCs with PKH26, and tracking both labels by fluorescence microscopy. The authors showed that the PKH26 signals were often not associated with GFP^+ cells, suggesting that the PKH26 label had dissociated from the administered human cells. Moreover, they showed that following IV-administration of $GFP^+/PKH26^+$ hKCs to rats with cisplatin-induced AKI, PKH26 signals could occasionally be detected in the kidneys, while GFP^+ cells were only found in the lungs, and never in the kidneys[134].

While the tracking of GFP^+ cells is more reliable than PKH26-labelling, it still has a major disadvantage since it requires the sacrifice of many animals at multiple time points to detect the cells histologically, and to gain an understanding of the changes in biodistribution over time. As such, very large animal numbers are required for such experiments, which is against the principles of the 3Rs (Reduction, Refinement, Replacement)[262], and the response of individual animals cannot be assessed over time.

Table 4.1: Summary of published studies assessing the efficacy of hKCs in animal models of kidney injury. ADR, adriamycin; Alb:Cr, urinary albumin to creatinine ratio; α-SMA, α-smooth muscle actin; BUN, blood urea nitrogen; CP cisplatin; hKCs, human kidney-derived cells; HLA-I, human leukocyte antigen class I; IF, immunofluorescence; KIM-1, kidney injury molecule-1; MCP-1, monocyte chemotactic protein-1; qRT-PCR, quantitative reverse transcriptase polymerase chain reaction; RB, rhabdomyolysis; SCr, serum creatinine; TA, transcutaneous assessment (of FITC-sinistrin clearance); TGF-β, transforming growth factor-β; UCr, urinary creatinine; VEGF, vascular endothelial growth factor.

Reference	Injury Model & Animals	Cell Administration			Efficacy		Cell Tracking	
		Source of hKCs	Dose	Timing	Injury parameters	Results	Method	Results
Bussolati *et al.* (2005)	RB; SCID mice	Normal portion of cortex from surgically removed kidneys	1.0 x10^6 $CD133^+$ hKCs	day 3	Not measured	N/A	Histological detection of PHK26	Cells homed to injured but not healthy kidneys
Sagrinati *et al.* (2006)	RB; female SCID mice	Normal kidney fragments from nephrectomy patients with renal tumours	0.75 x10^6 $CD133^+$ or $CD133^-$ hKCs (two doses)	days 3 and 4	BUN & histology	$CD133^+$ treatment reduced BUN and improved histology compared with $CD133^-$ and saline-treated mice.	Histological detection of PKH26 and IF of HLA-I	HLA-I and PKH26-labelled $CD133^+$ cells detected in injured kidneys, but not $CD133^-$ cells.
Ronconi *et al.* (2009)	ADR; female SCID mice	Normal kidney fragments from nephrectomy patients with renal tumours	0.75 x10^6 $CD133^+$ or $CD133^-$ hKCs (two - five doses)	days 1, 4 (also days 9, 18, 25 for one expt. with $CD133^+$ cells)	Alb:Cr & histology	$CD133^+$ treatment reduced Alb:Cr and improved histology.	Histological detection of PKH26 and IF of HLA-I	HLA-I and PKH26-labelled $CD133^+$ cells detected in injured kidneys, and co-expressed podocyte-specific markers.
Angelotti *et al.* (2012)	RB; female SCID mice	Not stated	0.75 x10^6 $CD133^+$ or $CD133^-$ hKCs (two doses)	4h and 20h	BUN & histology	$CD133^+$ treatment reduced BUN and improved histology compared with $CD133^-$ and saline-treated mice.	Histological detection of PKH26. Y-chromosome detection	PKH26-labelled $CD133^+$ cells detected in injured kidneys, but not $CD133^-$ cells.

Reference	Injury Model & Animals	Cell Administration			Efficacy		Cell Tracking	
		Source of hKCs	Dose	Timing	Injury parameters	Results	Method	Results
Grange *et al.* (2014)	RB; SCID mice	Normal portion of inner medulla from surgically removed kidneys	0.5 x10^6 $CD133^+$ or $CD133^-$ hKCs	day 1	SCr, BUN & histology	$CD133^+$ treatment reduced SCr and BUN, and improved histology compared with saline-treated mice.	*In vivo* fluorescence imaging of DiD. IF or HLA-I	DiD-labelled hKCs detected in kidneys *in vivo,* engraftment confirmed histologically by HLA-I staining.
Aggarwal *et al.* (2016)	RB; SCID mice	Normal portion of inner medulla from surgically removed kidneys	0.5 x10^6 $CD133^+$ hKCs	day 1	BUN & histology.	$CD133^+$ treatment reduced BUN, and improved histology compared with saline-treated mice.	IF detection of human CD133. DNA/protein analysis of human markers	Human CD133 detected in renal tubules, and DNA analysis confirms cells present up to 30 days.
Santeramo *et al.* (2017)	CP; male athymic nude rats	Healthy infant kidney tissue	1.0 x10^6 $CD133^+$ or $CD133^-$ hKCs (two doses)	days 1 and 7	TA, SCr, BUN, Alb:Cr.	$CD133^+$ and $CD133^-$ treatments both improved TA, reduced SCr and BUN, but did not change Alb:Cr.	Histological detection of GFP and PKH26	GFP^+ cells were detected in the lungs only. PKH26 signals in the absence of GFP^+ cells in the kidney suggested false-positive staining.

Alternatively, BLI, an optical imaging modality, can be used to visualise the biodistribution of luciferase$^+$ cells *in vivo*. BLI is a fast and high-throughput imaging technology, and is highly sensitive for detecting luciferase-expressing cells *in vivo*, resulting from the low background signals produced by non-bioluminescent mammalian tissues[265,266]. Moreover, BLI is a minimally invasive method of tracking cells, and thus individual animals can be monitored longitudinally, precluding the need to sacrifice large numbers of animals. In addition, this strengthens the scientific data by avoiding the 'between-mice' variation associated with analysing different groups of mice at each time point, and thus reducing the overall variability within the study.

One of the main aims of this thesis was to assess the efficacy of cell therapies for ameliorating kidney injury in mouse models. This chapter is therefore focused on assessing the efficacy of hKCs in a mouse model of adriamycin nephropathy. The aims of these studies were:

1. To compare the efficacy of CD133$^+$ and CD133$^-$ hKCs in a mouse model of adriamycin nephropathy
2. To compare the beneficial effects of administering hKCs in the acute stage (days 1 and 4) or in the chronic stage (day 15) of adriamycin nephropathy
3. To determine the longitudinal biodistribution of IV-administered hKCs *in vivo* by BLI

4.2 Experimental Design

Following on from the results obtained in Chapter 3, some refinements were made to the experimental protocols of the adriamycin model for the current studies. Because urinary albumin and FITC-sinistrin half-life were not found to be significantly elevated until week two (Fig. 3.1B, 3.2D, respectively), measurements following adriamycin administration were not performed until week two in the current study. This strategy also improved the animals' welfare by reducing stress during the first week of the study, where animals typically lose a high percentage of their body weight (Fig. 3.1A). Moreover, SCr and BUN were not found to be significantly elevated in injured animals (Fig. S3.1D, E) and so were not measured in the current studies.

For the acute study (Fig. 4.1A), female BALB/c SCID mice age 5-6 weeks were administered 7.5 x10^5 ZsGreen$^+$/luciferase$^+$ hKCs (either CD133$^+$ or CD133$^-$) in 100µl PBS (IV) on days 1 and 4 after induction of adriamycin nephropathy. The ADR model was optimised in mice

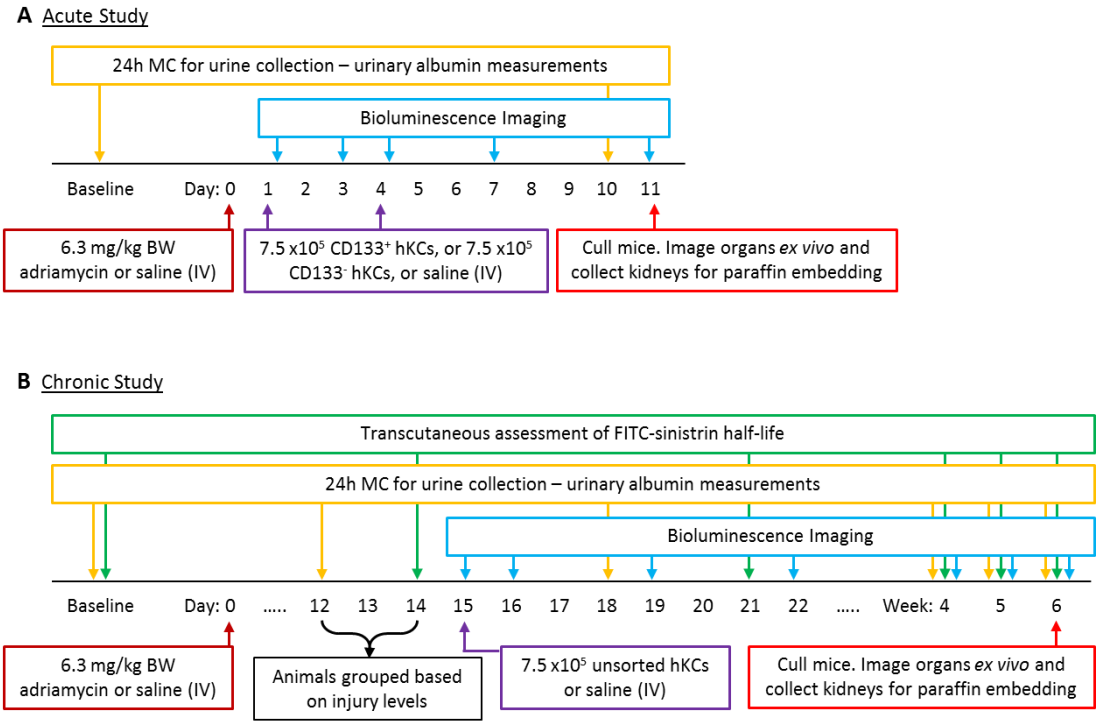

Figure 4.1: Experimental Design Schematics. Schematics showing the experimental design of the acute study (**A**) and the chronic study (**B**).

age 7-8 weeks, but younger mice were used in this study in order to recapitulate the study by Ronconi *et al.* (2009). Control mice received 100µl saline (IV). Treatment groups were as follows: ADR + CD133$^+$ hKCs (n = 6), ADR + CD133$^-$ hKCs (n = 6), ADR + saline (n = 6), healthy control (saline for all injections; n = 4). Urine was collected over 24h in metabolism cages at baseline, and on day 10. BLI was performed on days 1, 3, 4, 7, and 11. Mice were culled on day 11 with a rising concentration of CO_2, organs were imaged *ex vivo* for bioluminescence, and kidneys were collected and processed for paraffin embedding.

For the chronic study (Fig. 4.1B), adriamycin nephropathy was induced in 20 mice, and kidney function was assessed via urinary albumin at day 12 and FITC-sinistrin half-life at day 14. Mice were grouped based on the level of injury measured (or excluded from further study if deemed uninjured, $n = 4$), and subsequently assigned to receive hKCs or saline, such that the mean injury levels were similar for each group. 7.5 x10^5 ZsGreen$^+$/luciferase$^+$ hKCs (unsorted) were administered in 100µl PBS (IV) on day 15 after induction of adriamycin nephropathy. Control mice received 100µl saline (IV). Treatment groups were as follows: ADR + hKCs (n = 8), ADR + saline (n = 8). Urine was collected for 24h in metabolism cages at baseline, and on days 12, 18, 25, 32, and 42. FITC-sinistrin half-life was assessed via transcutaneous measurement at baseline, and on days 14, 21, 27, 35, and 42. BLI was performed immediately after cell/saline administration, and on days 1, 4, 7, 14, 21, and 28 following cell

administration. Mice were culled on day 42 with a rising concentration of CO_2, organs were imaged *ex vivo* for bioluminescence, and kidneys were collected and processed for paraffin embedding.

For both studies, details of urinary albumin measurements, kidney processing, sectioning, staining, and analysis were as described in the general methods.

4.3 Results

4.3.1 Acute Study

4.3.1.1 Morbidity and Mortality

Two mice in the ADR + $CD133^-$ hKC group did not survive this study. One mouse died soon after the first cell injection, and one mouse was culled on day 9 after losing 36% body weight. All mice that received ADR lost weight during the study, but mice that received hKCs lost less weight than the mice that received only saline (Fig. 4.2). There was no difference in weight loss between mice that received $CD133^+$ or $CD133^-$ hKCs. Healthy control mice maintained a relatively constant weight during the study and overall did not lose any weight. However, all mice lost weight between days 10 – 11, as a result of the highly stressful 24h urine collection in metabolism cages.

4.3.1.2 *In vivo* Cell Tracking

In order to evaluate the biodistribution of $luciferase^+$ hKCs, bioluminescence imaging was performed at multiple time points after administration of the cells. Mice from every treatment group were imaged at each time point, but signals were never detected from mice that received only saline (Fig. 4.3A). The signal intensity from mice that received $CD133^+$ and $CD133^-$ cells were comparable. Immediately following IV administration of cells on days 1 and 4, cells were found to be located mostly in the chest region of the animal, with a small amount of signal at the site of injection in the tail. Subsequent imaging two to three days later, on days 3 and 7, revealed that the majority of cells had died within a few days after administration. By day 11, only the cells at the site of injection could be detected, with no detectable signal remaining *in vivo* in the chest or elsewhere. *Ex vivo* imaging of organs on day 11 confirmed that the signal within the chest originated from the lungs (Fig 4.3B).

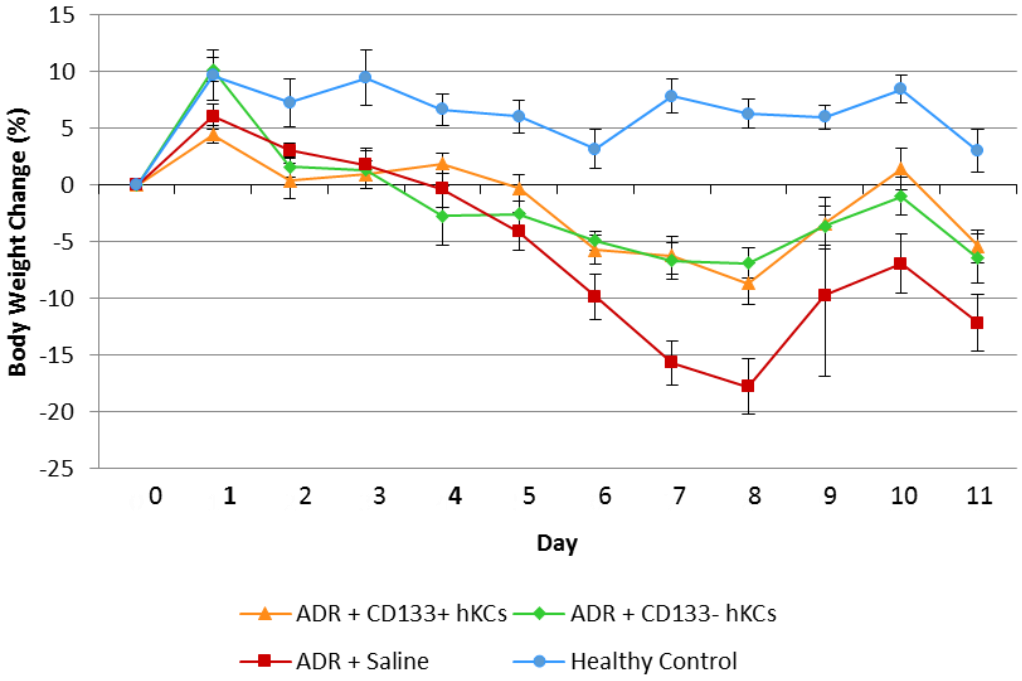

Figure 4.2: Mean body weight change of mice in the acute study. ADR mice that received either $CD133^+$ (orange triangle; *n* = 6) or $CD133^-$ (green diamond; *n* = 6) hKC therapy did not lose as much weight during the first week of the study as ADR mice that received only saline (red square; *n* = 6). Healthy control mice (blue circle; *n* = 4) maintained a steady body weight throughout the study and did not lose any weight overall. All animals lost some weight between days 10-11, as a result of 24h urine collection in MCs, which is highly stressful for mice. Days in bold indicate days of cell/saline administration, data points represent the group mean, and error bars represent standard error.

4.3.1.3 Kidney Function

Kidney function was assessed on day 10 by urinary albumin measurement. Urinary albumin increased for all mice that received ADR, but mice that received hKCs showed a marked reduction in urinary albumin levels ($CD133^+$, mean: 0.81 mg/24h, standard error (SE): 0.38; $CD133^-$, mean: 1.05 mg/24h, SE: 0.52) compared to mice that received only saline (mean: 3.90 mg/24h, SE: 2.29) (Fig. 4.4, Supplementary Table S4.1). This reduction was not statistically significant (one-way ANOVA, p = 0.090). Healthy control mice maintained baseline levels of urinary albumin at day 10 (baseline, mean: 0.04 mg/24h, SE: 0.01; day 10, mean: 0.03 mg/24h, SE: 0.01).

4.3.1.4 Histology

PSR-stained paraffin kidney sections were assessed by a qualified pathologist, but histological changes were not evident at this time point by light microscopy (data not shown).

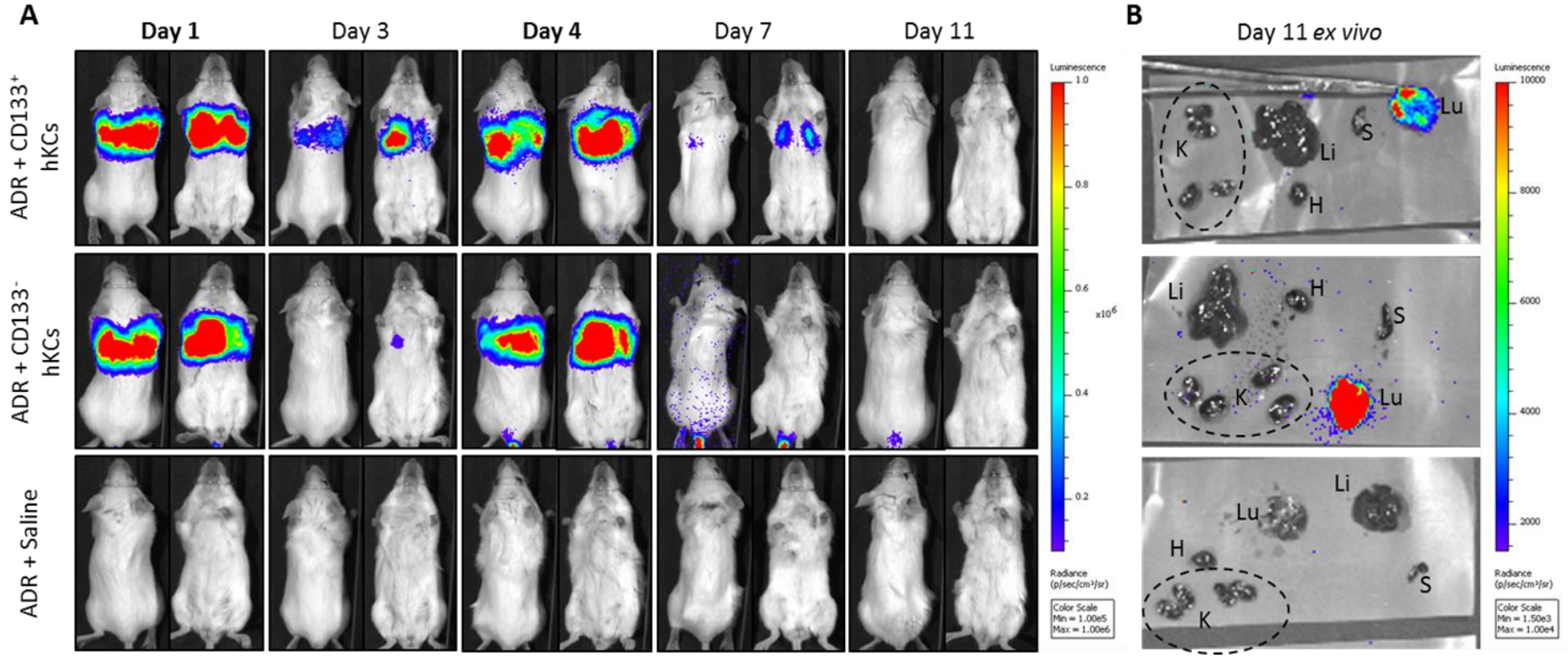

Figure 4.3: Bioluminescence imaging of ZsGreen^{+}/Luciferase^{+} hKC biodistribution *in vivo* and *ex vivo*. Representative *in vivo* (**A**) and *ex vivo* (**B**) bioluminescence images of ADR mice that received CD133^{+} hKCs (top), CD133^{-} hKCs (middle), or saline (bottom). (**A**) *in vivo* images: dorsal (left) and ventral (right) images of animals are shown for each time point. Time points in bold indicate dates where imaging occurred after cell/saline administration. (**B**) *ex vivo* images: kidneys (cut coronally; K, dashed circle), liver (Li), heart (H), spleen (S), lungs (Lu). *Ex vivo* imaging of organs confirmed that following IV administration cells were restricted to the lungs only, as suggested by the *in vivo* signal. Images show average radiance; *in vivo* scale (A) = 1.0 x10^{5} – 1.0 x10^{6} p/s/cm^{2}/sr; *ex vivo* scale (B) = 1.5 x10^{3} – 1.0 x10^{4} p/s/cm^{2}/sr.

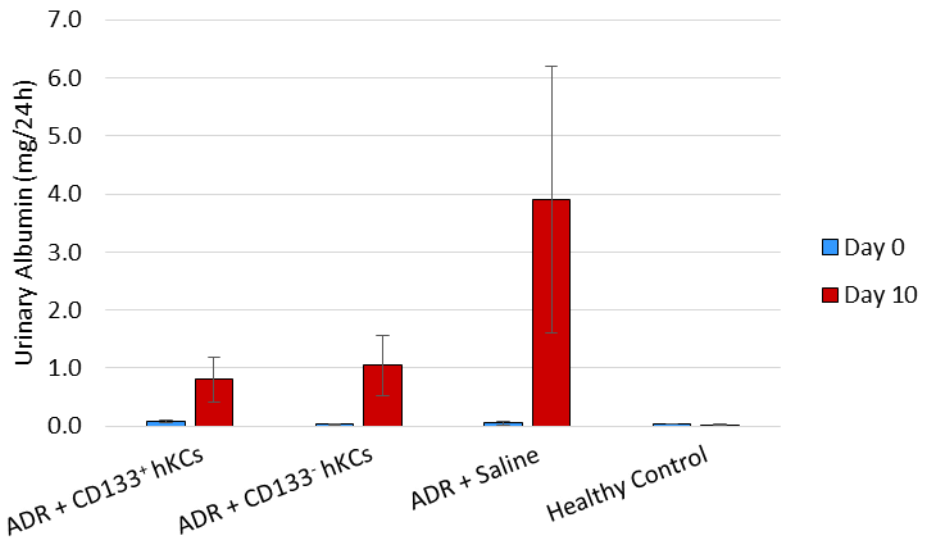

Figure 4.4: Mean urinary albumin of mice in the acute study. ADR mice that received either $CD133^+$ (*n* = 6) or $CD133^-$ (*n* = 6) hKC therapy had much lower urinary albumin levels at day 10 than ADR mice that received only saline (*n* = 6), although this reduction was not statistically significant (one-way ANOVA, p = 0.090). Healthy control mice (*n* = 4) maintained baseline levels of urinary albumin at day 10. Data represents the group mean, and error bars represent standard error.

4.3.2 Chronic Study

4.3.2.1 Morbidity and Mortality

All mice survived this study, and all mice lost weight within the first week, reaching a nadir between days 7-10, however there was no difference in weight loss between cell- and saline-treated mice (Fig. 4.5).

4.3.2.2 Initial Assessment of Kidney Injury and Grouping

Kidney injury levels were assessed at week two prior to assigning mice a treatment group. Urinary albumin revealed the most prominent change (Fig. 4.6A; paired t-test, $p < 0.001$) between baseline levels (mean: 0.28 mg/24h, median: 0.07 mg/24h, SE: 0.20) and day 12 (mean: 29.47 mg/24h, SE: 5.12). However, there was a high level of variation across the group, from 2.51 mg/24h to 74.97 mg/24h, which split it naturally into three categories: very low, low, and high levels of albumin (Fig. 4.6A, Table 4.2). Kidney injury levels assessed by transcutaneous measurements revealed a subtle but statistically significant (paired t-test, p = 0.026) increase in FITC-sinistrin half-life (Fig. 4.6B; baseline, mean: 7.95 min, SE: 0.22; day 14, mean: 8.84 min, SE: 0.37). Of note, the FITC-sinistrin half-life data did not show any natural grouping towards injury levels, so urinary albumin levels were used to assign mice in

to three injury level groups: 'very low-responders', with urinary albumin below 5 mg/24h (*n* = 4); 'low-responders', with urinary albumin between 5 and 21 mg/24h (*n* = 7); and 'high-responders', with urinary albumin above 38 mg/24h (*n* = 9) (Table 4.2). Very low-responders were deemed insufficiently injured and so were excluded from further study.

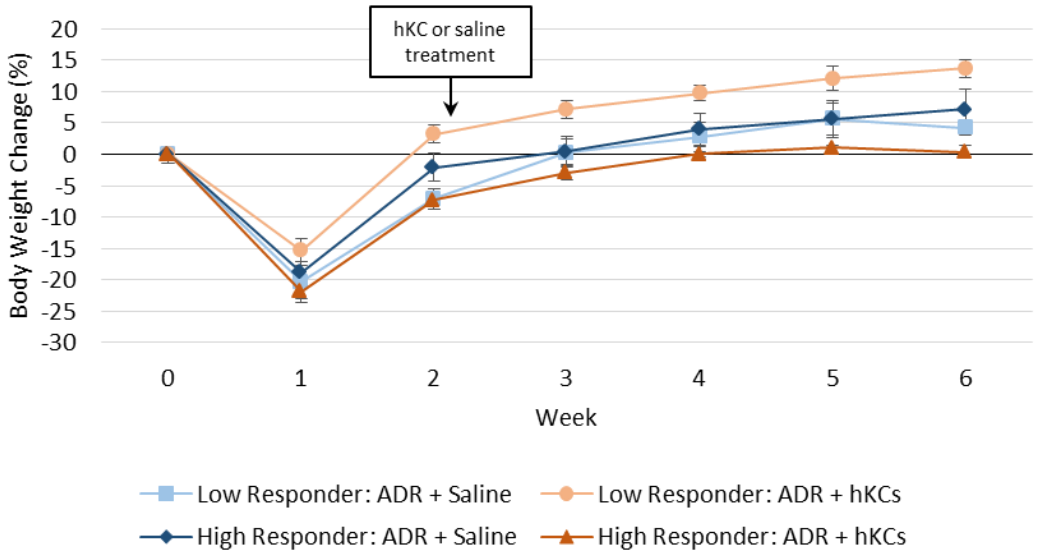

Figure 4.5: Mean body weight change of mice in the chronic study. All mice lost weight as expected in the first week, but returned towards the starting weight by week 2, and continued to gain weight for the remainder of the study. High-responding mice that received hKCs (dark orange triangle; *n* = 4) maintained a higher percentage of weight loss than high-responding mice that received saline (dark blue diamond; *n* = 5), whereas low-responding mice that received hKCs (light blue circle; *n* = 4) put on the most weight of all groups, (light orange square; *n* = 3). Data points represent the group mean, and error bars represent standard error.

Low- and high-responding mice were then divided within these groups as evenly as possible to achieve similar injury levels, before they received an administration of cell therapy or saline control (cell-treatment group, mean albumin: 36.41 mg/24h, mean change in FITC-sinistrin half-life from baseline to day 14: 1.14 min; saline-treatment group, mean albumin: 35.59 mg/24h, mean change in FITC-sinistrin half-life from baseline to day 14: 1.08 min; Table 4.3).

Of note, there were some discrepancies in the health of the animal as measured by the three different parameters: peak percentage body weight loss, change in FITC-sinistrin half-life between baseline and day 14, and urinary albumin at day 12. Generally, larger changes in FITC-sinistrin half-life (highlighted in orange, Table 4.2) which indicated more severe kidney damage, tended to be associated with higher urinary albumin levels. However, some mice exhibited conflicting data. For example, animal 3.2 had the third largest increase in FITC-

sinistrin half-life (1.99 min), but had relatively low urinary albumin levels (16.83 mg/24h). Conversely, animal 1.4 had a lower FITC-sinistrin half-life at day 14 than at baseline (change = -1.45 min), suggesting improved renal clearance, but had the second highest urinary albumin levels (67.97 mg/24h), suggesting substantial renal injury. Body weight loss, which is a good indicator of the general health status of the animal, tended to increase as urinary albumin increased, however mouse 4.1 in particular lost the most weight of all animals (-33.76%), but had low kidney injury levels as suggested by FITC-sinistrin half-life change (0.22 min) and urinary albumin (13.11 mg/24h).

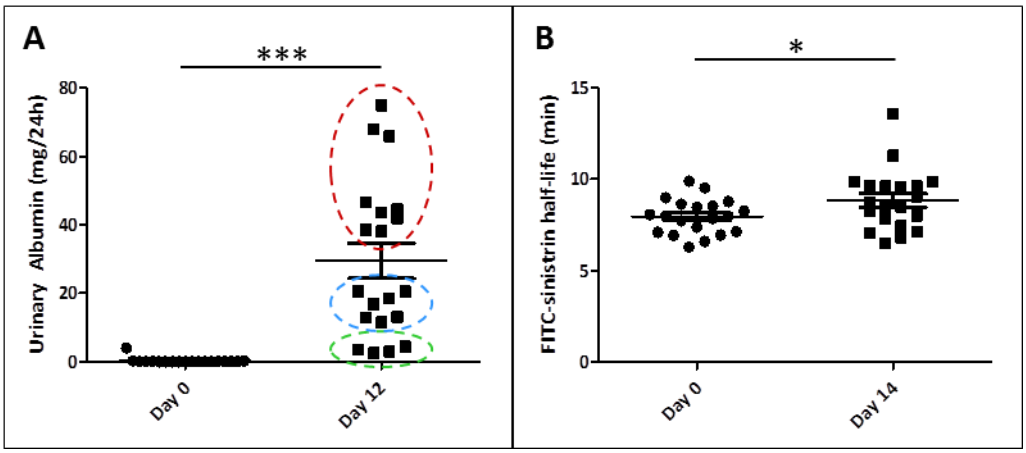

Figure 4.6: Pre-treatment assessment of kidney injury. Kidney injury levels were assessed at week two by urinary albumin (**A**) and FITC-sinistrin half-life (**B**). (**A**) Urinary albumin measurements were significantly elevated over baseline levels ($p < 0.001$) and appeared to naturally split into three injury levels: very low (encircled in green), low (blue) and high (red) injury. (**B**) Transcutaneous assessment of FITC-sinistrin half-life also revealed a statistically significant increase over baseline levels ($p = 0.026$), but the data did not naturally group into injury levels. Urinary albumin was used to categorise mice in to groups based on the degree of kidney injury. Data points represent individual animals, and bars represent mean (wide line) and standard error (short lines). Two-sample t-test, $p < 0.001$ (***), $p < 0.05$ (*).

4.3.2.3 Longitudinal Assessment of Kidney Function

Following cell or saline administration at week 2, kidney function was assessed weekly for four weeks by urinary albumin measurement and transcutaneous assessment of FITC-sinistrin half-life. Neither urinary albumin (Fig. 4.7A) nor FITC-sinistrin half-life (Fig. 4.7B) revealed any efficacy as a result of hKC-treatment, in the low- nor the high-responding groups.

Urinary Albumin

High-responding mice that received cells, and low-responding mice that received either hKCs or saline had increased urinary albumin levels between week two (before intervention) and week three (one week after intervention), whereas high-responding mice that received saline maintained urinary albumin levels between weeks two and three (Fig. 4.7A, Supplementary Table S4.2). From week four onwards, all groups showed a gradual decrease in urinary albumin levels, with comparable rates of decline towards baseline levels.

Table 4.2 : Pre-treatment evaluation of kidney function (sorted by increasing urinary albumin values). Animals were grouped in to injury level groups based on where the urinary albumin data naturally split in to three groups at day 12 or 14. Animals with a very low elevation in urinary albumin (below 5 mg/24h) were deemed to have insufficient renal injury and were excluded from further study. Animals with urinary albumin values below 21 mg/24h were considered to have 'low' injury, and animals with greater than 38 mg/24h had 'high' injury.

Animal ID	Peak Body Weight Lost (%)	Change in FITC-sinistrin half-life (baseline - day 14)	Urinary Albumin (day 12) (mg/24h)	Injury Level Grouping
1.3	-18.86	-2.49	2.51	Very low/no injury - excluded from further analyses
4.5	-3.31	-0.45	2.97	
3.4	-14.65	0.93	3.50	
4.4	-22.6	0.03	4.39	
4.3	-28.65	-0.05	11.52	Low injury: 'low-responders'
3.5	-18.52	0.86	12.85	
4.1	-33.76	0.22	13.11	
3.2	-20.11	1.99	16.83	
4.2	-13.71	-0.57	18.50	
2.1	-21.39	1.59	20.49	
3.3	-17.54	0.23	20.49	
1.1	-28.41	1.07	38.12	High injury: 'high-responders'
2.5	-30.53	4.94	38.51	
2.4	-22.86	1.93	41.98	
3.1	-23.9	3.56	43.64	
1.2	-25.27	1.40	44.56	
1.5	-14.63	1.62	46.57	
2.2	-30.05	1.76	65.90	
1.4	-20.61	-1.45	67.97	
2.3	-21.18	0.64	74.97	

Table 4.3: Assignment of animals to a cell therapy or control treatment group. Animals were randomly assigned a cell therapy or saline treatment, ensuring that the mean injury level data for each group was as even as possible.

Mice for hKC treatment			
Injury Response	Animal ID	Urinary Albumin (day 12) (mg/24h)	Change in FITC-sinistrin half-life (baseline - day 14) (min)
Low	4.3	11.52	-0.05
	3.2	16.83	1.99
	4.2	18.50	-0.57
	3.3	20.49	0.23
	Mean	**16.84**	**0.40**
High	2.5	38.51	4.94
	1.2	44.56	1.40
	2.2	65.90	1.76
	2.3	74.97	0.64
	Mean	**55.99**	**2.19**
Overall Mean		**36.41**	**1.14**

Mice for saline treatment			
Injury Response	Animal ID	Urinary Albumin (day 12) (mg/24h)	Change in FITC-sinistrin half-life (baseline - day 14) (min)
Low	3.5	12.85	0.86
	4.1	13.11	0.22
	2.1	20.49	1.59
	Mean	**15.48**	**0.89**
High	1.1	38.12	1.07
	2.4	41.98	1.93
	3.1	43.64	3.56
	1.5	46.57	1.62
	1.4	67.97	-1.45
	Mean	**47.66**	**1.35**
Overall Mean		**35.59**	**1.08**

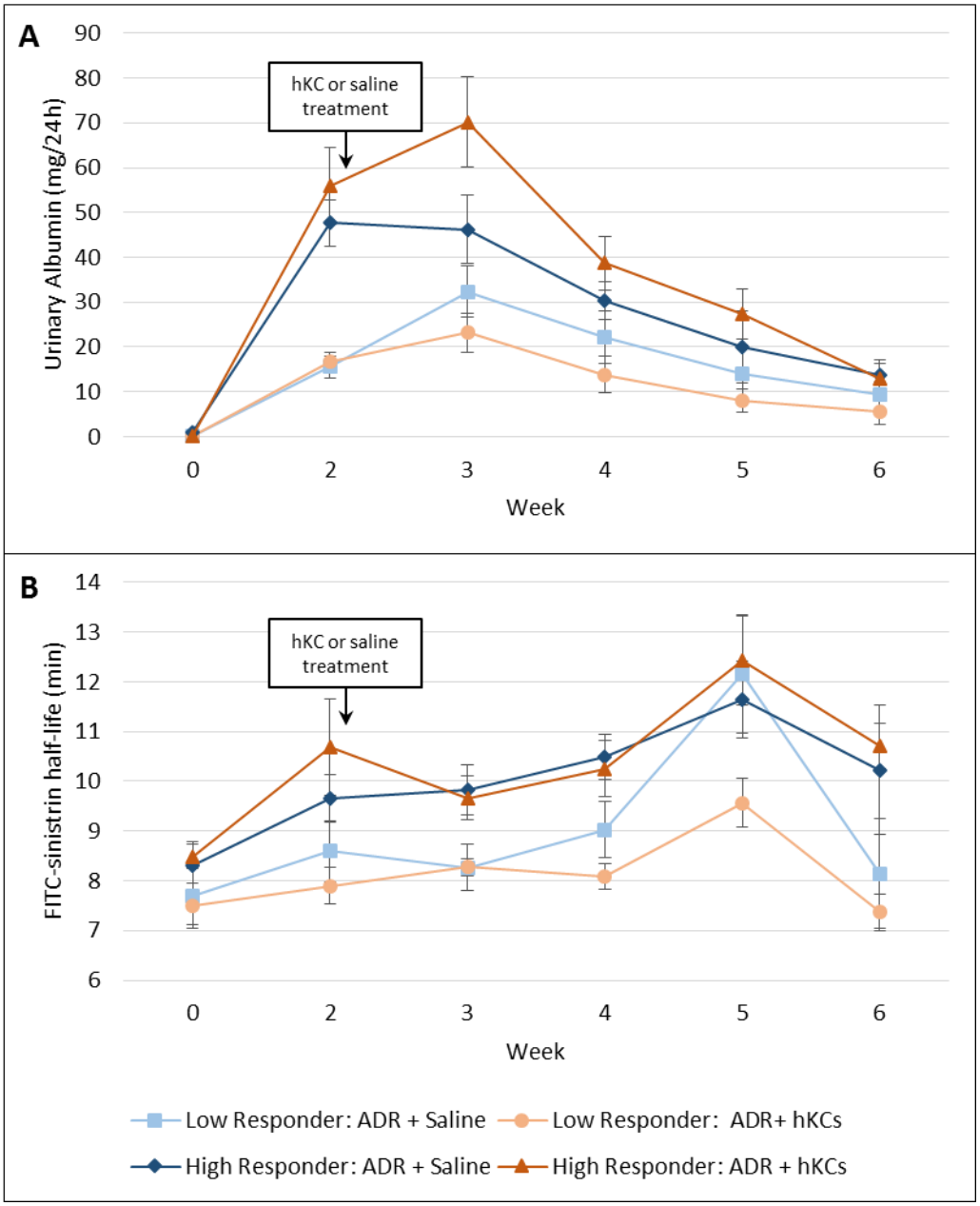

Figure 4.7: Longitudinal assessment of kidney function. Urinary albumin (**A**) and FITC-sinistrin half-life (**B**) were measured at baseline, and week two, immediately before experimental intervention, and then weekly thereafter until week six. There was no significant beneficial effect of hKC therapy (orange) compared with saline (blue) on either urinary albumin levels or FITC-sinistrin half-life in either the low-responding (light colours) or the high-responding (dark colours) groups. Data points represent the group mean, and error bars represent standard error.

In the high-responding group, mice that received hKC therapy had higher urinary albumin levels at week three than mice that received saline (cell-treated, mean: 70.17 mg/24h, SE: 10.09; saline-treated, mean: 46.24 mg/24h, SE: 7.71), however this difference was not statistically significant. A one-way ANOVA revealed that at least one group was significantly different from another group ($p < 0.001$), however a post-hoc Tukey pairwise comparison

test showed that none of these significant comparisons were of saline-treated vs cell-treated mice at the same time point, and were therefore not physiologically relevant (Supplementary Table S4.3A). A specific analysis of the week three time-point confirmed that the difference was not significant (two-sample t-test; $p = 0.292$). Conversely, in the low-responding group, mice that received hKC therapy had slightly lower urinary albumin levels at week three than mice that received saline (cell-treated, mean: 23.13 mg/24h, SE: 4.29; saline-treated, mean: 32.36 mg/24h, SE: 5.83). As above, many treatment/time point comparisons were significantly different (one-way ANOVA, $p < 0.001$), however none were physiologically relevant (Supplementary Table S4.3B). A specific analysis of the week three time-point confirmed that the difference was not significant (two-sample t-test; $p = 0.118$).

FITC-sinistrin Clearance

For all treatment groups, there was a trend of increased FITC-sinistrin half-life over time (Fig. 4.7B), indicating a progressive loss of kidney function. In the high-responding group, there was no difference in FITC-sinistrin half-life between mice that received hKC therapy and those that received saline at any time point (one-way ANOVA, $p = 0.021$; Tukey pairwise comparison, no physiologically relevant comparisons, Supplementary Table S4.3C). In the low-responding group, both treatment groups had very similar mean FITC-sinistrin half-lives at all time points except week 5, where mice that received hKC therapy had a lower FITC-sinistrin half-life (mean: 9.57 min, SE: 0.48) than mice that received saline (mean: 12.15 min, SE: 1.17), however this difference was not statistically significant (one-way ANOVA, $p < 0.001$; Tukey pairwise comparison, no physiologically relevant comparisons, Supplementary Table S4.3D; two-sample t-test at week five, $p = 0.185$).

4.3.2.6 *In vivo* Cell Tracking

Bioluminescence imaging was performed immediately after cell administration (0h), on days 1, 4, and 7, and then weekly thereafter in order to monitor the biodistribution of hKCs and detect any homing to the kidneys or abnormal behaviour such as tumour formation. Immediately after IV cell administration (0h) the signal was restricted to the lungs (Fig 4.8A). By day 1, the signal had decreased such that it could not be visualised using the same scale required at 0h ($1.0 \times 10^5 – 1.0 \times 10^6$ p/s/cm^2/sr, green frame). Reducing the scale to $5.0 \times 10^4 – 5.0 \times 10^5$ p/s/cm^2/sr (orange frame) allowed weaker signal to be detected, and revealed that some cells were still located in the lungs. By day 4, a very low scale of $5.0 \times 10^3 – 5.0 \times 10^4$ p/s/cm^2/sr (blue frame) was required to visualise very weak signals in the lungs. From day 7 and for the remainder of the four-week cell tracking period, signals could no longer be

detected anywhere in the body. *Ex vivo* imaging of organs at the end of the study confirmed that there were no bioluminescent hKCs remaining in any of the organs of any mice (Fig. 4.8B).

4.3.2.7 Histology

PSR-stained paraffin sections of kidney tissue were analysed by a blinded nephrologist for evidence of glomerulosclerosis. It was found that there were no significant differences in glomerulosclerosis scores between hKC-treated and control mice (high-responders: cell-treated, mean: 20.40% injured glomeruli, SE: 2.24; saline-treated, mean: 11.49%; SE: 3.56, two-sample t-test, p = 0.079; low-responders: cell-treated, mean: 7.20%, SE: 1.26; saline-treated, mean: 7.17%, SE: 2.62; two-sample t-test, p = 0.993; Figure 4.9, Table 4.4).

4.4 Discussion

The aim of the studies in this chapter was to assess the efficacy of hKCs in the adriamycin mouse model of CKD. The first experiment was designed to closely recapitulate the study by Ronconi *et al.* (2009), in order to confirm the efficacy of $CD133^+$ hKCs in the acute phase of the adriamycin model. In the second study, the potential for hKCs to ameliorate kidney injury when administered at a later stage of the disease was assessed.

These two experiments resulted in several important and novel findings:

(i) both $CD133^+$ and $CD133^-$ hKCs demonstrated a trend towards ameliorating kidney function when administered in the acute phase of adriamycin nephropathy, although this was not statistically significant.
(ii) IV-administered cells failed to reach the kidneys and survive.
(iii) hKCs did not ameliorate kidney injury when administered in the chronic phase of adriamycin nephropathy.

These results showed that when hKCs were administered in the acute stage (days 1 and 4) of adriamycin-induced chronic progressive glomerular disease, before the onset of albuminuria, cell-treated mice exhibited reduced urinary albumin levels at day 10 compared with saline-treated mice. While this change was not statistically significant, largely due to the high degree of variability in renal damage induced by adriamycin, it is important to point to the biological significance of the drastic reduction in urinary albumin excretion compared with saline-treated mice. Because histological evidence of damage by light microscopy was not evident at this early time point in the animals treated with adriamycin, any effects the cell therapies may have on structural repair could not be assessed.

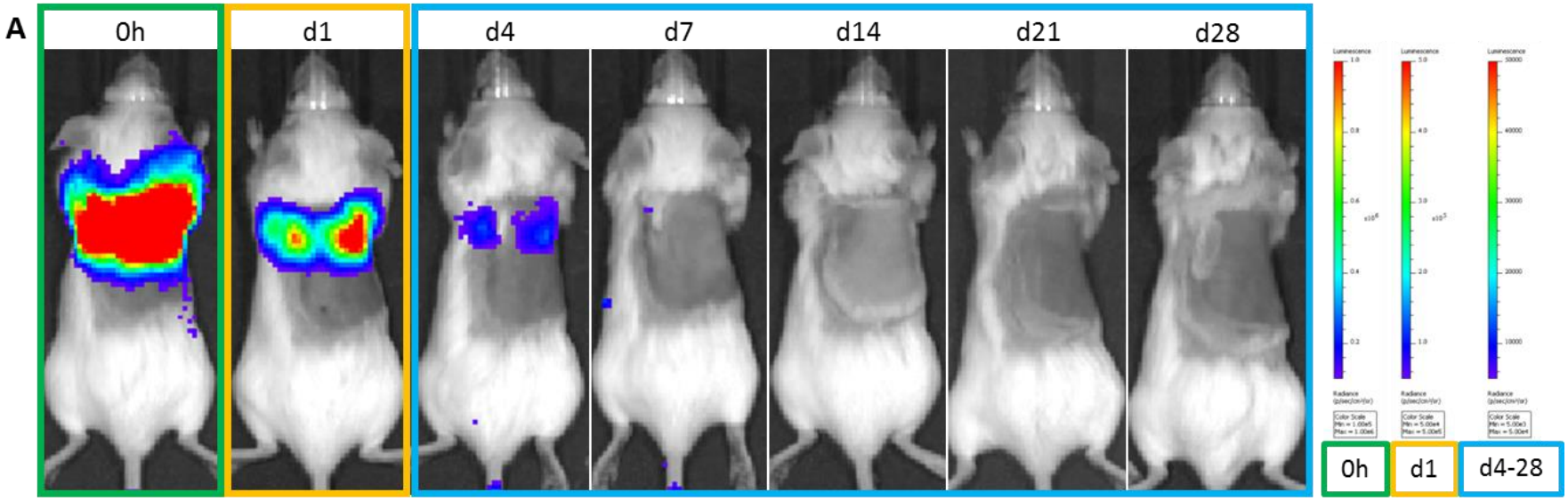

Figure 4.8: Bioluminescence imaging of ZsGreen$^+$/Luciferase$^+$ hKC biodistribution *in vivo* and *ex vivo*. Representative *in vivo* (dorsal) (**A**) and *ex vivo* (**B**) bioluminescence images of mice that received hKCs. (**A**) *in vivo* imaging suggested that cells were trapped in the lungs following IV administration, where they subsequently died. Bioluminescence signal on day 1 was much lower on at 0h, requiring a lower scale to display the signals. By day 4, a far lower scale was required to display very weak signals, and from day 7 – 28 no signal could be detected *in vivo.* (**B**) *ex vivo* images: clockwise from top right kidneys (cut coronally), spleen, liver, lungs, heart, brain. *Ex vivo* imaging of organs confirmed that there were no bioluminescent cells present in any organs four weeks after IV administration of hKCs. Images show average radiance; *in vivo* scale (day 0) = 1.0 x10^5 – 1.0 x10^6 p/s/cm^2/sr (green frame); *in vivo* scale (day 1) = 5.0 x10^4 – 5.0 x10^5 p/s/cm^2/sr (orange frame); *in vivo* scale (days 4 - 28) and *ex vivo* scale (B) = 5.0 x10^3 – 5.0 x10^4 p/s/cm^2/sr (blue frame).

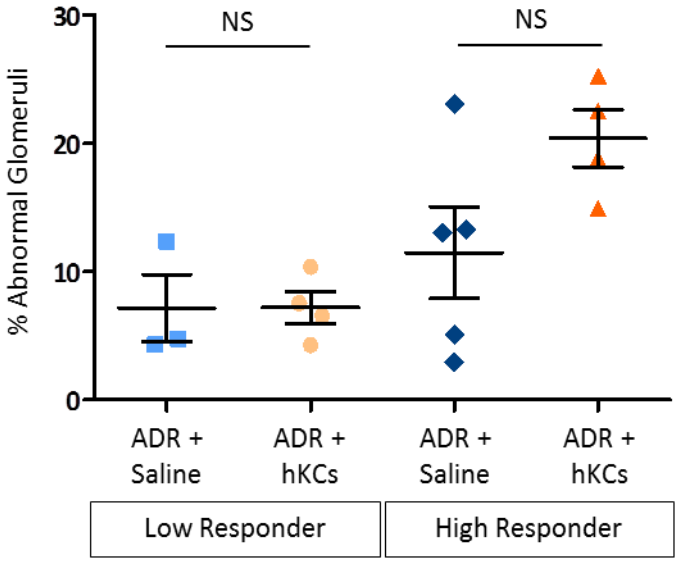

Figure 4.9: Histological evaluation of glomerulosclerosis. High-responding mice that received hKCs (dark orange triangles; mean: 20.4%) had a higher percentage of abnormal glomeruli than those that received saline (dark blue diamonds; mean: 11.49%), however this difference was not statistically significant (p = 0.079). There was no significant difference between low-responding mice that received hKCs (light orange circles; mean: 7.20%) and those that received saline (light blue squares; mean: 7.17%; p = 0.993). Data points represent individual animals, and bars represent mean (wide line) and standard error (short lines).

However, histological changes at early time points have previously been detected by electron microscopy (EM)[171], and further investigations could allude to early structural changes following cell therapy. Nonetheless, these results support previously published reports[134,147-149,151,185,345], which indicated that hKCs have the potential to ameliorate acute kidney injury. The majority of these studies tested the efficacy of hKCs in the rhabdomyolysis model of AKI, and used SCr and BUN as the primary methods of assessing efficacy (Table 4.1). As shown in Chapter 3, SCr and BUN are not significantly changed in adriamycin nephropathy, and so were not assessed here or by Ronconi *et al.* (2009). Alternatively, urinary albumin, also assessed by Ronconi *et al.* (2009), provided an early biomarker of kidney injury which detected differences in kidney function between cell- and saline-treated mice.

The efficacy of $CD133^+$ and $CD133^-$ hKCs administered on days one and four during the acute phase was assessed and it was found that there were no significant differences in amelioration of kidney injury based on the expression of the stem cell marker, CD133. This finding is surprising since it is in direct opposition to a number of other published studies, which report that CD133 is not only essential for ameliorating functional and structural injury, but is also necessary for cells to home to the injured kidneys[147,148,185]. However, this observation supports the findings of Santeramo *et al.* (2017), who reported that the

expression of CD133 had no effect on the therapeutic outcome of hKCs in a rat model of cisplatin-induced AKI[134].

It is important to note that the cells used in the current studies and in those described by Santeramo *et al*. (2017) were the same population of cells derived from one human kidney, and thus may exhibit unique characteristics that differ from the hKCs used in other studies, which were isolated from different kidneys. Additionally, the cells administered here and by Santeramo *et al.* (2017) were isolated from a healthy infant kidney deemed unsuitable for transplant, whereas the cells isolated for use in other studies were often described as being from the healthy portion of kidney tissue from patients with 'localised renal tumours', or patients undergoing nephrectomy for undisclosed reasons (Table 4.1). It is possible that the presence of renal carcinoma cells may have had an impact on the 'healthy' tissue surrounding the tumour, affecting the phenotype of the cells subsequently isolated from this tissue. These differences in cell origin may therefore explain the discrepancies observed in efficacy between the studies.

Adriamycin induces a chronic progressive renal damage in mice, resulting in a glomerular injury which closely resembles the human disease FSGS. This model is well-suited to studying the effect of timing of cell administration, as the progressive nature of the disease allows efficacy to be assessed when cells are administered at different stages of injury. A disadvantage to this model, however, is the large degree of variability associated with the level of injury induced in animals. It is known that adriamycin has a narrow therapeutic range, and small differences in the dose administered may cause large variances in response, ranging from no renal injury, to toxicity and subsequent death[169]. However, despite careful adriamycin dose preparation, it was found that some animals developed very high urinary albumin excretion, while others excreted relatively low levels of albumin. It was initially thought that this variability was due to technical difficulties in performing IV drug administration, as strong experience is required to avoid mis-injections. However, subsequent experiments with vastly improved IV administration technique did not reduce variability (data not shown). In addition, changing the source of adriamycin from a research-grade powder (Tocris) to a clinical-grade ready-to-use solution (Teva), did not impact the degree of variation observed in studies (data not shown).

Table 4.4: Histological evaluation of glomerulosclerosis. PSR-stained kidney sections were analysed by a clinical nephrologist and glomerulosclerosis was scored as the percentage of abnormal glomeruli in one kidney section per animal. The nephrologist's comments and glomerulosclerosis scores highlight the high degree of variability in this study, with mice in the same groups exhibiting vastly different histological injury scores.

Injury Response	Treatment	Animal ID	Number of Abnormal Glomeruli	Total Number of Glomeruli Analysed	Nephrologist's Comments	% Abnormal Glomeruli	Mean % Abnormal Glomeruli
Low	Saline	2.1	16	129	segmental damage	12.40	7.17
	Saline	3.5	6	126	?normal/a few casts	4.76	
	Saline	4.1	4	92	?normal/a few casts	4.35	
	hKCs	3.2	11	106	segmental damage	10.38	7.20
	hKCs	3.3	3	70	almost normal/a few casts	4.29	
	hKCs	4.2	8	106	mild segmental damage	7.55	
	hKCs	4.3	6	91	few casts in medulla	6.59	
High	Saline	1.1	4	135	normal	2.96	11.49
	Saline	1.4	17	128	major damage	13.28	
	Saline	1.5	21	91	lots of casts in medulla	23.08	
	Saline	2.4	6	118	minimal damage	5.08	
	Saline	3.1	15	115	segmental damage	13.04	
	hKCs	1.2	26	138	segmental damage	18.84	20.40
	hKCs	2.2	13	87	few casts in medulla	14.94	
	hKCs	2.3	16	71	quite damaged	22.54	
	hKCs	2.5	24	95	very damaged	25.26	

In the chronic cell therapy study where the efficacy of late administration of hKCs was analysed, the injury levels of mice were assessed prior to administration of the cell therapy by urinary albumin levels at day 12, and change in FITC-sinistrin half-life between baseline and day 14. The two injury parameters did not always correlate with one another, making it difficult to definitively class certain mice into injury levels, however urinary albumin measurements showed a natural grouping of mice, and as such was selected as the parameter by which mice would be categorised. Subsequently, mice were grouped into high- and low-responders, or excluded if they failed to develop kidney injury. Of the four mice that were excluded from the chronic study, the lack of renal damage could be explained for one mouse (mouse 4.5), due to a large mis-injection of approximately 50% of the dose of adriamycin. This mouse did not exhibit any significant weight loss, and urinary albumin excretion was very low, indicating that the kidneys suffered very minimal damage. However, the other three mice that failed to develop significant injury had received 100% of the adriamycin dose, and lost a similar percentage of body weight to all other mice, and so the minimal kidney damage indicated by urinary albumin levels is unexplained. As all known variables were controlled, it is possible that the variation in susceptibility to adriamycin is simply due to natural biological variability between individuals. Indeed, susceptibility to adriamycin has already been shown to have a genetic basis; the BALB/c strain is known to be highly susceptible to renal injury, while C57BL/6 mice are resistant[169].

Assessing the degree of functional damage prior to cell administration was highly beneficial as the true efficacy of a cell therapy is otherwise very difficult to assess when it is not known whether a cell-treated mouse would have developed mild, moderate, or severe injury without the therapy. This was only possible in the chronic study due to the late stage of cell administration.

As the results of the acute study indicated that expression of CD133 was not necessary for therapeutic efficacy, unsorted hKCs were used in the chronic study. In contrast to the acute study, administration of hKCs to mice in the chronic stage of the disease (day 15), after overt albuminuria was established, had no effect on urinary albumin excretion, FITC-sinistrin half-life, or structural histological damage compared with saline treatment. Regardless of whether mice had mild or severe injury (low- or high-responders to the initial injury), the half-life of FITC-sinistrin increased progressively over the six-week study period in both cell- and saline-treated groups, indicating a progressive loss of renal function in all animals, with no beneficial effect of hKC therapy. This data suggests that while hKCs may be a viable cell therapy for treating kidney disease in patients, it may be essential to administer the therapy

in one of the earlier stages of CKD, and late administration may have little to no therapeutic value. Indeed, administration of MSCs in a rat model of subtotal nephrectomy (5/6 nephrectomy) resulted in very little improvement in kidney damage compared with saline-treated rats. Over the course of a five-month study, the progression of proteinuria was attenuated in MSC-treated rats, but SCr, BUN, and histology failed to show any improvement over saline-treated rats[215]. A recent study by Caldas *et al.* (2016) assessed the therapeutic effect of MSCs in the subtotal nephrectomy model of chronic kidney disease[219]. By surgically removing different amounts of renal tissue (2/3 nephrectomy and 5/6 nephrectomy), the authors were able to model two different stages of CKD for assessing the importance of timing of therapeutic intervention. It was shown that MSC therapy significantly improved kidney function, as assessed by SCr, proteinuria, and creatinine clearance, equally in both models, however improvement was more pronounced in the 2/3 nephrectomy model, suggesting that intervention in the earlier stages of CKD is beneficial. Moreover, the number of doses of a cell therapy may be a key factor in obtaining a therapeutic effect in a chronic model. A single dose was used in the chronic study reported here, however Semedo *et al.* (2009) showed that while a single dose of MSCs was ineffective in a rat model of subtotal nephrectomy, dosing every two weeks for eight weeks resulted in improvement of kidney function[216].

The possibility for a cell therapy to exacerbate renal damage must also be considered. The hKC-treated mice in the high-responding group had almost twice as many abnormal glomeruli compared with saline-treated mice, indicating that the hKCs may have had a negative effect on the kidney. However, before therapeutic intervention, the mice assigned to hKC treatment already had slightly higher injury levels than the mice assigned to saline treatment, which may account for the higher percentage of glomerulosclerosis at week six. Nonetheless, further investigation is required to fully understand any negative effects of late administration of cell therapy on kidney function, and to determine the latest time point at which a cell therapy may still provide beneficial effects.

In the two studies described here, hKCs had been labelled with luciferase-expressing lentivirus, allowing for longitudinal *in vivo* cell tracking by BLI. The data from these studies showed that regardless of when hKCs were administered to mice (day one/four or day 15), the luciferase$^+$ cells became trapped in the lungs following IV administration, where they subsequently died and, in the chronic study, became undetectable within seven days. This supports the findings of multiple other studies, which showed that large cells such as hKCs and MSCs were unable to bypass the lungs and failed to home to the kidneys following IV

administration[111,134,267,349-351]. Indeed, *ex vivo* imaging of organs six days after the last hKC infusion in the acute study confirmed that both $CD133^+$ and $CD133^-$ cells were exclusively located in the lungs, and could not be detected in the kidneys or any other organs imaged. Furthermore, in the chronic study, *ex vivo* organ imaging four weeks after hKC administration failed to detect any $luciferase^+$ hKCs in any organs. Similarly to the efficacy results, the data presented here is more consistent with the data reported by Santeramo *et al*. (2017), than those reported by Ronconi *et al.* (2009), Sagrinati *et al.* (2006), and Angelotti *et al.* (2012), who relied primarily on histological detection of cell membrane dyes and human leukocyte antigen class I (HLA-I) detection. Key to this, is the use of reliable cell-tracking agents, such as reporter genes for detection by *in vivo* imaging, or *ex vivo* fluorescence microscopy, to avoid false-positive cell detection.

Despite the cells remaining in the lungs and dying soon after cell administration, a beneficial effect on kidney function was still observed when cells were administered in the acute phase of the disease. This phenomenon has been reported in multiple other studies[105,110,111,134,139,145,352,353], and supports the theory that the mechanism of action of the cell therapy is by endocrine/paracrine secretion of therapeutic factors, as opposed to physical integration and regeneration of damaged tissue. Geng *et al.* (2014) investigated the cytokine expression levels in the serum of mice with AKI, and showed that administration of MSCs led to decreased levels of the pro-inflammatory cytokines tumour necrosis factor alpha (TNF-α) and interleukin 6 (IL-6), and increased levels of the anti-inflammatory cytokine IL-10. Moreover, they showed that MSCs recruited macrophages to the site of injury, and could promote the polarisation of macrophages to the anti-inflammatory M2 phenotype, overall suggesting that MSCs may ameliorate kidney injury by modulating the immune response to reduce inflammation[145]. However, the cytokine expression levels following hKC administration have not yet been reported, and further investigation is required to determine whether a similar mechanism is also responsible for the amelioration by hKCs.

In conclusion, the data presented in this chapter provided evidence that cells derived from the human kidney may have therapeutic value for treating CKD, however the expression of the stem cell marker CD133 was not necessary for amelioration. Additionally, longitudinal *in vivo* cell tracking data confirmed that IV administration of cells resulted in lung entrapment, and cells did not home to the kidneys. The therapeutic effect, despite cells not homing to the kidneys, supports the theory that the mechanism of action of the cell therapy is by paracrine/endocrine secretion of therapeutic factors. Moreover, it may be necessary to administer a cell therapy in the earlier stages of CKD, and late administration may hold no

therapeutic value. Further investigation is required to determine the latest time point at which a cell therapy may still provide beneficial effects on kidney function.

4.5 Supplementary Tables

Supplementary Table S4.1: Acute study: individual urinary albumin values. This table highlights the high degree of variability in the urinary albumin values of mice in each treatment group.

Treatment	Animal ID	Urinary Albumin (mg/24h)	
		Day 0	**Day 10**
ADR + $CD133^{+}$ hKCs	A1.1	0.09	2.66
	A1.2	0.19	0.16
	A1.3	0.02	0.25
	A2.1	0.06	0.42
	A2.2	0.03	0.80
	A2.3	0.13	0.55
	Mean	**0.09**	**0.81**
	SE	**0.03**	**0.38**
ADR + $CD133^{-}$ hKCs	A5.1	0.05	ND
	A5.2	0.03	0.13
	A5.3	0.02	0.21
	A6.1	0.02	2.71
	A6.2	0.01	1.80
	A6.3	0.02	0.39
	Mean	**0.03**	**1.05**
	Mean	**0.00**	**0.52**
ADR + Saline	A3.1	0.02	0.73
	A3.2	0.03	1.33
	A3.3	0.21	0.80
	A7.1	0.03	12.78
	A7.2	0.01	3.86
	A7.3	0.02	ND
	Mean	**0.05**	**3.90**
	SE	**0.03**	**2.29**
Healthy Control	C4.1	0.06	0.02
	C4.2	0.03	0.05
	C8.1	0.02	0.02
	C8.2	0.04	0.01
	Mean	**0.04**	**0.03**
	SE	**0.01**	**0.01**

<u>Supplementary Table S4.2</u>: Chronic study: individual urinary albumin and FITC-sinistrin half-life values. This table highlights the high degree of variability in both kidney function parameters measured for mice in all treatment groups.

			Urinary Albumin (mg/24h)						FITC-sinistrin half-life (min)					
Response to ADR	Treatment	Animal ID	Week 0	Week 2	Week 3	Week 4	Week 5	Week 6	Week 0	Week 2	Week 3	Week 4	Week 5	Week 6
			Day 0	Day 12	Day 18	Day 25	Day 32	Day 40	Day 0	Day 14	Day 21	Day 28	Day 35	Day 42
Low	Saline	2.1	0.04	20.49	43.86	33.51	25.72	23.03	7.98	9.57	8.56	10.12	12.81	10.01
		3.5	0.06	12.85	28.29	13.34	3.63	2.37	6.60	7.45	8.88	8.76	9.88	6.09
		4.1	0.10	13.11	24.94	19.67	12.69	2.84	8.54	8.76	7.37	8.20	13.77	8.28
		Mean	**0.07**	**15.48**	**32.36**	**22.17**	**14.01**	**9.41**	**7.70**	**8.59**	**8.27**	**9.03**	**12.15**	**8.13**
		SE	**0.02**	**2.50**	**5.83**	**5.96**	**6.41**	**6.81**	**0.58**	**0.62**	**0.46**	**0.57**	**1.17**	**1.13**
	hKCs	3.2	0.02	16.83	19.12	24.58	7.84	7.37	6.28	8.27	7.79	7.97	ND	6.53
		3.3	0.02	20.49	17.38	8.21	4.64	3.70	8.27	8.50	8.32	ND	10.69	7.21
		4.2	0.04	18.50	35.90	15.56	15.17	5.19	7.38	6.82	8.47	7.65	9.04	7.61
		4.3	0.10	11.52	20.11	6.92	3.88	5.80	8.07	8.02	8.51	8.63	8.97	8.19
		Mean	**0.05**	**16.84**	**23.13**	**13.82**	**7.88**	**5.52**	**7.50**	**7.90**	**8.27**	**8.09**	**9.57**	**7.38**
		SE	**0.02**	**1.92**	**4.29**	**4.06**	**2.58**	**0.76**	**0.45**	**0.38**	**0.16**	**0.25**	**0.48**	**0.35**
High	Saline	1.1	0.21	38.12	45.21	22.38	6.01	7.18	8.78	9.85	11.35	10.57	9.84	9.32
		1.4	0.21	67.97	49.64	40.86	50.10	24.71	9.90	8.45	10.24	9.25	10.36	7.35
		1.5	4.00	46.57	31.32	35.45	22.18	18.21	7.98	9.60	10.18	11.25	11.53	15.09
		2.4	0.05	41.98	31.60	18.10	8.29	8.41	7.13	9.06	8.82	9.68	12.21	10.21
		3.1	0.13	43.64	73.44	34.56	13.41	10.50	7.73	11.29	8.57	11.71	14.27	9.15
		Mean	**0.92**	**47.66**	**46.24**	**30.27**	**20.00**	**13.80**	**8.30**	**9.65**	**9.83**	**10.49**	**11.64**	**10.22**
		SE	**0.77**	**5.26**	**7.71**	**4.29**	**8.02**	**3.33**	**0.48**	**0.48**	**0.51**	**0.46**	**0.78**	**1.30**
	hKCs	1.2	0.04	44.56	70.55	21.48	13.02	13.22	8.47	9.87	10.37	9.07	ND	ND
		2.2	0.07	65.90	61.07	42.99	27.89	13.38	7.86	9.62	8.55	9.90	12.95	11.70
		2.3	0.12	74.97	97.99	47.99	28.26	14.18	8.99	9.63	10.32	11.78	10.42	10.53
		2.5	0.02	38.51	51.06	42.05	40.22	10.97	8.64	13.58	9.42	10.24	13.93	9.92
		Mean	**0.06**	**55.99**	**70.17**	**38.63**	**27.35**	**12.94**	**8.49**	**10.68**	**9.67**	**10.25**	**12.44**	**10.72**
		SE	**0.02**	**8.63**	**10.09**	**5.86**	**5.57**	**0.69**	**0.24**	**0.97**	**0.43**	**0.57**	**0.91**	**0.45**

Supplementary Table S4.3: Tukey Pairwise Comparisons. Four separate post-hoc statistical analyses following statistically significant results from separate one-way ANOVAs comparing the urinary albumin (**A – B**), or the FITC-sinistrin half-life (**C – D**) data from high-responders (**A, C**), and low-responders (**B, D**). Groups that do not share a letter are significantly different from one another.

A

			Urinary Albumin (mg/24h)						
			n	Mean	Grouping				
High-responder	Day 0 (Baseline)	ADR + Saline	5	0.92					E
		ADR + hKCs	4	0.06					E
	Day 12	ADR + Saline	5	47.66	A	B			
		ADR + hKCs	4	55.99	A	B			
	Day 18	ADR + Saline	5	46.24	A	B	C		
		ADR + hKCs	4	70.17	A				
	Day 25	ADR + Saline	5	30.27		B	C	D	
		ADR + hKCs	4	38.63		B	C	D	
	Day 32	ADR + Saline	5	20.00			C	D	E
		ADR + hKCs	4	27.35		B	C	D	E
	Day 40	ADR + Saline	5	13.80				D	E
		ADR + hKCs	4	12.94				D	E

B

			Urinary Albumin (mg/24h)						
			n	Mean	Grouping				
Low-responder	Day 0 (Baseline)	ADR + Saline	5	0.07			C		
		ADR + hKCs	4	0.05			C		
	Day 12	ADR + Saline	5	15.48	A	B	C		
		ADR + hKCs	4	16.84	A	B	C		
	Day 18	ADR + Saline	5	32.36	A				
		ADR + hKCs	4	23.13	A	B			
	Day 25	ADR + Saline	5	22.17	A	B			
		ADR + hKCs	4	13.82	A	B	C		
	Day 32	ADR + Saline	5	14.01	A	B	C		
		ADR + hKCs	4	7.88		B	C		
	Day 40	ADR + Saline	5	9.41		B	C		
		ADR + hKCs	4	5.52		B	C		

C

			FITC-sinistrin half-life (min)						
			n	Mean	Grouping				
High-responder	Day 0 (Baseline)	ADR + Saline	5	8.30		B			
		ADR + hKCs	4	8.49	A	B			
	Day 14	ADR + Saline	5	9.65	A	B			
		ADR + hKCs	4	10.68	A	B			
	Day 21	ADR + Saline	5	9.83	A	B			
		ADR + hKCs	4	9.67	A	B			
	Day 28	ADR + Saline	5	10.49	A	B			
		ADR + hKCs	4	10.25	A	B			
	Day 35	ADR + Saline	5	11.64	A				
		ADR + hKCs	4	12.44	A				
	Day 42	ADR + Saline	5	10.22	A	B			
		ADR + hKCs	4	10.72	A	B			

D

			FITC-sinistrin half-life (min)						
			n	Mean	Grouping				
Low-responder	Day 0 (Baseline)	ADR + Saline	5	7.70		B			
		ADR + hKCs	4	7.50		B			
	Day 14	ADR + Saline	5	8.59		B			
		ADR + hKCs	4	7.90		B			
	Day 21	ADR + Saline	5	8.27		B			
		ADR + hKCs	4	8.27		B			
	Day 28	ADR + Saline	5	9.03		B			
		ADR + hKCs	4	8.09		B			
	Day 35	ADR + Saline	5	12.15	A				
		ADR + hKCs	4	9.57	A	B			
	Day 42	ADR + Saline	5	8.13		B			
		ADR + hKCs	4	7.38		B			

CHAPTER 5

Assessing the efficacy of human kidney-derived and mesenchymal cells in a mouse model of ischemia-reperfusion injury

5.1 Introduction

The previously held belief that AKI is a transient condition, and that those who survive AKI suffer no long-term consequences[42], has now been replaced with a more comprehensive understanding of the complexity of AKI, its relationship with CKD, and the long-term consequences of an episode of AKI[38,45-49]. It is now understood that AKI makes an individual more susceptible to subsequent AKI and/or CKD[38,46-48], and that the severity of initial AKI predicts the likelihood of progressing to CKD[46]. Consequently, there is a need to develop specific therapies that limit the initial severity of AKI and promote recovery, thus reducing the patient's risk of progressing to CKD.

Cell-based therapies may provide such a treatment option, and vast numbers of publications point to the efficacy of cell therapies in the IRI model of AKI (Table 1.3). Many different cell types have been shown to be efficacious in the IRI model, including MSCs derived from the bone marrow[108-112,352,354,355], adipose tissue[113-116,356], and the umbilical cord and its products[105,117,118], in addition to cells isolated from the kidney itself[120,121] and kidney cells generated from iPSCs[119,357]. Collectively, these cell therapies appear to have similar modes of action, acting to suppress inflammation and oxidative stress to reduce tubular cell damage and preserve renal function (Table 1.3). However, it is still unclear which cell type may provide the most effective therapy. The majority of studies have been carried out using MSCs, however it is unknown whether the source of the MSCs has any effect on ameliorative potential. Furthermore, it is not known whether cells derived from the kidney itself may provide an advantage over non-kidney cells, such as MSCs. Notably, human kidney derived cells have been shown to share some cell surface characteristics with MSCs, and had an ameliorative effect in cisplatin-induced AKI[134].

Renal IRI is a desirable experimental model of AKI. Ischemia is the predominant cause of AKI in the intensive care setting[95] and an inevitable consequence of kidney transplantation[99], making experimental IRI a clinically relevant model. Moreover, once optimised, the model is reproducible and amenable to modifications to alter the severity of injury and time course of disease, making it a versatile model. The IRI model is, however, highly sensitive to changes in experimental conditions, and as such it is vitally important to spend time optimising the ideal conditions of renal IRI prior to embarking upon experimental work.

There are multiple variations of the IRI model reported in the literature (Table 5.1). First of all, the kidneys can be accessed either via a ventral or a dorsal approach. A ventral approach by laparotomy provides easier access to the kidneys, but is associated with higher

Table 5.1: Table summarising the various approaches to the IRI model

Approach		**Advantages**	**Disadvantages**
Ventral		Easier access to the kidneys.	Longer recovery time, increased risk of systemic inflammation/infection, increased mortality
Dorsal		Less traumatic, allows faster recovery times, and improved survival.	More difficult to access kidneys.
Model		**Advantages**	**Disadvantages**
Bilateral		Approximates hypoperfusion in humans (both kidneys affected).	Variable results due to differences in effective clamp pressure and/or renal responses to ischemia. Renal injury is also less severe and there is higher mortality.
Unilateral	No nephrectomy	Allows for longer clamp times and subsequent development of interstitial fibrosis. Internal control kidney for histological evaluation.	Cannot measure renal function.
	Simultaneous contralateral nephrectomy	Substantially reduced variability compared with bilateral ischemia, and allows renal function to be assessed. Provides control renal tissue prior to ischemia.	Shorter clamp times than with no/delayed Nx leads to less severe injury
	Delayed contralateral nephrectomy	Allows for longer clamp times and subsequent development of interstitial fibrosis. Kidney function can be monitored from the day after Nx.	Requires two surgeries. Kidney function cannot be measured until after the Nx.

mortality, poorer recovery, and increased risk of infection[358,359]. A dorsal approach requires smaller incisions and is associated with faster recovery times[359], but the kidneys must be manipulated more in order to access the renal vasculature, increasing the risk of damaging the kidneys. Secondly, either one or both kidneys can be injured. The bilateral model involves clamping both kidneys[358,360] and more closely resembles certain human conditions in which systemic hypoperfusion is present, such as cardiac surgery[96]. Experimentally, however, the bilateral model is associated with higher variability, due to small differences in the conditions imposed on each kidney, such as effective clamp pressure from different clamps and the amount of tissue and fat also clamped with the renal vasculature[359]. Alternatively, the unilateral model involves clamping only one kidney, and this may be performed with[359,361] or without[362] a contralateral nephrectomy (Nx). Models of unilateral ischemia have been suggested to be associated with lower variability than the bilateral model[359]. In the unilateral ischemia without Nx model, the presence of a healthy contralateral kidney provides an internal control kidney, which may be of value in certain studies, and also allows for longer clamp times to induce severe renal ischemia without subsequent renal failure and death[359,362], and as such can be used to model the progression of AKI to CKD[362]. However, the presence of the healthy contralateral kidney compensates for the reduced function of the injured kidney, and precludes functional analyses of renal biomarkers in the urine or blood. The inclusion of a Nx to the unilateral model allows renal function in the damaged kidney to be measured unequivocally[359,361]. The Nx can either be performed simultaneously at the time of ischemia, or can be delayed and performed sometime after reperfusion, *e.g.* one week. A simultaneous Nx allows kidney function to be evaluated immediately after surgery, but requires shorter clamp times to avoid renal failure and death. A delayed Nx requires a second surgery, but allows for longer ischemia times due to the presence of an uninjured contralateral kidney, and therefore enhances the development of post-injury fibrosis, with the advantage of being able to evaluate kidney function following the Nx[359].

As expected, longer clamp times are associated with higher degrees of renal injury[362]. Temperature is also one of the most important factors determining renal injury, with increasing core body temperature during ischemia leading to increased renal injury[362,363]. Moreover, it is necessary to actively control body temperature during ischemia, as surgery performed without a heat mat leads to relative hypothermia and reduced renal injury[360,363], whereas surgery performed with a heat mat that does not feature feedback-loop temperature control may lead to effective hyperthermia and excessive renal injury[363]. The anaesthetic agent used during surgery has a profound effect on renal injury, with inhalation

anaesthetics such as isoflurane, sevoflurane, and halothane providing protection from renal IRI compared with injectable anaesthetics such as pentobarbital and ketamine[364]. Furthermore, the age, sex, and strain of the animal can affect renal injury. Older[365] and male[366] animals are more sensitive to renal IRI, and some strains, such as NIH Swiss mice, are highly resistant[367].

Kidney function is usually assessed by SCr and BUN measurements in published literature, but these methods are insensitive and not entirely specific to kidney injury[43,225,368]. The transcutaneous measurement of FITC-sinistrin clearance is a novel method of measuring kidney function in experimental animals[232,234,237] and its use has been demonstrated in various animal models of kidney injury, including unilateral nephrectomy[234,237], polycystic kidney disease[234,237], salt-sensitive hypertension[242], diabetic CKD[243], non-diabetic CKD[244], sepsis[245], cisplatin-induced AKI[134], and adriamycin-induced glomerular injury (Chapters 3 and 4). However, the use of the transcutaneous measurement of kidney function has not been described in a model of ischemic AKI, and its suitability and feasibility are unknown.

The aims of the experiments described in this chapter were:

1. To establish and optimise a model of renal IRI in our laboratory. Initial pilot studies were carried out to assess whether the unilateral model would provide a significant advantage over the bilateral model in terms of reducing variability. Subsequent experiments were carried out to optimise the clamp time and other experimental variables, and to characterise the injury induced.
2. To assess whether the transcutaneous measurement of FITC-sinistrin clearance would be an appropriate measure of kidney function in the IRI model
3. To assess the efficacy of different cell types in the IRI model, in order to determine the cell type with the greatest regenerative or repair capacity.

5.2 Experimental Design

Establishing and optimising the IRI model

Initially, we needed to decide which model (bilateral ischemia or unilateral ischemia with contralateral Nx) was preferable, and to determine an approximate clamp time that would induce moderate-severe renal injury with acceptable levels of mortality. Therefore, pilot experiments were carried out with each model, testing four clamp times of 25, 30, 35, and

40 min (or sham-operated) on one mouse per model/clamp time. Male BALB/c mice age 8 - 9 weeks were used for all pilot studies.

In the bilateral ischemia pilot study, kidney function was assessed by transcutaneous measurement of FITC-sinistrin clearance at baseline and days 1, 3, and 7. Urinary albumin and KIM-1 excretion were measured in urine collected at baseline and days 1, 2, 3, and 7. Mice were culled on day 7 and tubular injury was scored for each kidney on PAS-stained paraffin kidney sections.

In the unilateral ischemia with Nx pilot study, kidney function was assessed by transcutaneous measurement of FITC-sinistrin clearance at baseline (three repeated measurements) and days 1, 2, and 4. Mice were culled on day 4 and tubular injury was scored for each kidney on PAS-stained paraffin kidney sections.

Subsequent experiments were carried out to further optimise the clamp time using the unilateral ischemia with Nx approach, eventually leading to an optimal clamp time of 31 minutes in the final optimisation experiment (IRI, 31 min, *n = 5*; sham-operated, *n = 5*). Kidney function was assessed by transcutaneous measurement of FITC-sinistrin clearance at baseline and days 1, 2, and 4. Mice were culled on day 4, and blood was collected for SCr and BUN measurement. Tubular injury scoring was not performed due to time constraints, and instead immunofluorescence of tissue injury biomarkers, Ki67 for proliferation and KIM-1 for proximal tubule damage, was carried out on frozen kidney sections.

Assessing the Efficacy of Cell Therapy

27 male BALB/c mice age 8 – 10 weeks underwent unilateral ischemia (31 min clamping) with contralateral nephrectomy, and received either 7.5 $x10^5$ hKCs (*n = 6*), 7.5 $x10^5$ human umbilical cord-derived MSCs (hUC-MSCs; *n = 6*), 7.5 $x10^5$ human bone marrow-derived MSCs (hBM-MSCs; *n = 6*), or saline (*n = 9*) (all 100µl volume, IV) immediately after reperfusion. Mice were divided into three groups of nine mice, with six mice receiving one of the cell types and three mice receiving saline in each group. This experiment was carried out in a blinded fashion, and the treatment groups were not revealed until all analyses were complete. Kidney function was assessed by transcutaneous measurement of FITC-sinistrin clearance at baseline, and days 1, 2, and 4 after surgery. Mice were culled on day 4, blood was collected for SCr and BUN measurement. Tubular injury scoring was not performed due to time constraints, and instead immunofluorescence of tissue injury biomarkers, Ki67 for proliferation and KIM-1 for proximal tubule damage, was carried out on frozen kidney sections.

An additional 10 mice underwent unilateral ischemia (31 min clamping) with contralateral nephrectomy, and received either 7.5 x10^5 ZsGreen$^+$/luciferase$^+$ hKCs (*n = 5*) or saline (*n = 5*) (all 100µl volume, IV) immediately after reperfusion. Mice were imaged for bioluminescence after surgery (before recovering from anaesthesia) and at 24h. After imaging, mice were culled, organs imaged *ex vivo*, and blood was collected for SCr and BUN measurement.

5.3 Results

5.3.1 Optimising the IRI model

The bilateral IRI model is more clinically relevant and more commonly used in research, however the unilateral with Nx model is reported to be associated with lower levels of variability. As such, pilot studies were carried out: (1) to determine whether the bilateral or unilateral with Nx approach was more suitable, and (2) to determine the optimal clamping time under each approach for inducing a moderate-severe, but survivable injury.

5.3.1.1 Bilateral Ischemia Pilot Study

The sham-operated mouse, and mice with 25 or 35 min bilateral ischemia lost less than 10% body weight by day 2, and subsequently put weight on; reaching or exceeding the starting weight by the end of the study on day 7 (Fig 5.1A). Mice with 30 or 40 min bilateral ischemia, however, lost a maximum of 15.4% and 21.1% body weight during the study. While weight gain in these animals was evident from days 5-6, body weight loss was still at around 10% by day 7.

Renal function was assessed by transcutaneous measurement of FITC-sinistrin clearance at baseline and days 1, 3, and 7 following surgery (Fig. 5.1B). The sham-operated mouse and the mouse with 25 min bilateral ischemia displayed a decrease in FITC-sinistrin half-life over time, decreasing by over 5 min between baseline measurements and day 7 (Fig. 5.1B, Table 5.2). Conversely, all other injured mice showed a peak in FITC-sinistrin half-life at day 1 following surgery, with values returning towards baseline at day 3, and comparable to baseline levels by day 7. The FITC-sinistrin half-life tended to rise as clamp time increased, as the mouse with 40 min renal clamping displayed the highest FITC-sinistrin half-life at day 1, however the day 1 values for the mice with 30 and 35 min clamping were inverted based on what would have been expected, with $t_{1/2}$ = 30.60 min and 19.22 min respectively.

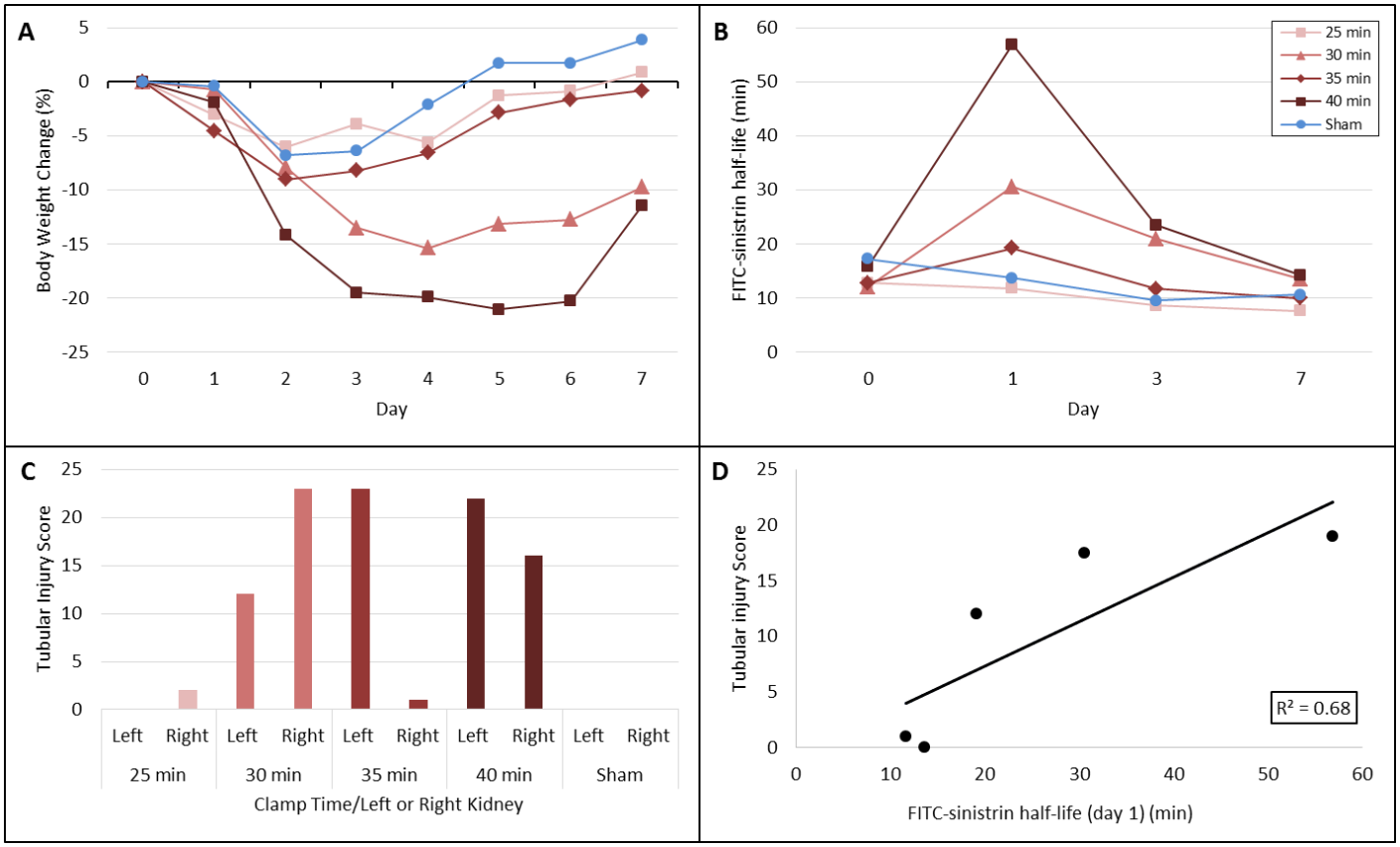

<u>Figure 5.1</u>: Pilot bilateral IRI model – renal injury analyses. (**A**) Body weight change of animals following bilateral ischemia, with clamp times ranging from 25 – 40 min, or sham-operated with no renal ischemia. (**B**) FITC-sinistrin half-life was vastly increased over baseline levels at day 1, and decreased over time from day 3 to 7. The half-life at day 1 tended to increase as clamp time increased, however a clamp time of 30 min yielded a higher half-life than a clamp time of 35 min. (**C**) Tubular injury was scored for each kidney individually, and showed that the injury induced by each clamp time varied to a large extent between the left and right kidneys. (**D**) A plot of the correlation between the tubular injury score and FITC-sinistrin half-life at day 1 showed that there was moderate correlation. All data points represent individual animals; one animal per clamp time.

Table 5.2: Pilot bilateral IRI model – renal injury analyses.

	FITC-sinistrin half-life (min)				Tubular Injury Score		
Clamp Time	Day 0	Day 1	Day 3	Day 7	Left Kidney	Right Kidney	Average
25 min	12.72	11.72	8.55	7.60	0	2	1
30 min	12.03	30.60	20.93	13.47	12	23	17.5
35 min	12.80	19.22	11.65	9.90	23	1	12
40 min	15.83	56.92	23.50	14.17	22	16	19
Sham	17.22	13.70	9.53	10.55	0	0	0

PAS-stained paraffin kidney sections were analysed blinded by a veterinary pathologist, and tubular injury was scored for each kidney individually (Fig. 5.1C), with a maximum possible score of 50. Kidneys from the sham-operated mouse and the mouse with 25 min bilateral ischemia displayed little/no evidence of tubular damage. At least one kidney from the 30, 35, and 40 min bilateral ischemia mice showed signs of strong kidney damage, but the damage induced in both kidneys was not consistent, with one kidney showing weaker signs of damage than the other (Fig. 5.1C, Table 5.2). In the most extreme example of the variability in injury levels, the mouse with 35 min ischemia had a tubular injury score of 23 for the left kidney, and just 1 for the right kidney (Table 5.2). The tubular injury score for both kidneys was then averaged, and indicated a similar trend as the FITC-sinistrin clearance data, with respect to the relationship between length of clamping and degree of injury induced. The average tubular injury scores displayed a moderate level of correlation with the transcutaneous assessment of kidney function at day 1 ($R^2 = 0.68$; Fig. 5.1D).

Additionally, urine was collected to measure urinary albumin and KIM-1 excretion. Urine collection was found to be difficult in these animals, with many mice not producing urine at certain time points (denoted on the graph by 'X'), and only one mouse producing urine at all time points (Table 5.3). When urinary albumin and KIM-1 levels were quantified, some samples yielded no detectable levels of either analyte (denoted on the graph by 'O'), suggesting that the liquid collected from hydrophobic sand was in fact water from the water bottle, and not urine (Fig. 5.2A, B). As a result, there were very few data points available for analysis of urine biochemistry. Generally, urinary albumin and KIM-1 levels peaked at day 1, decreased over time from day 2 to 7, and tended to be more increased with longer clamp times. However, urinary KIM-1 excretion was reduced in the mouse with 40 min bilateral ischemia compared with the mice with 30 and 35 min bilateral ischemia.

Table 5.3: Urine volumes produced throughout a typical experiment. The volume of urine collected from mice following 5h on hydrophobic sand was measured at various time points in the experiment. Instances where mice did not produce any collectable urine are highlighted by a grey box. Only one mouse (1.4) produced urine at every time point.

Animal ID	Day 0	Day 0 (Repeat)	Day 0.5	Day 1	Day 3
	Urine Volume (µl)				
1.1	160	90	0	110	60
1.2	<10	60	100	100	0
1.3	0	80	0	130	50
1.4	110	190	90	210	40
1.5	0	140	0	50	70
2.1	140	0	140	0	15
2.2	40	0	210	260	0
2.3	140	0	230	180	0
2.4	0	100	0	0	0
2.5	70	110	0	70	0

5.3.1.2 Unilateral Ischemia with Contralateral Nx Pilot Study

The sham-operated mouse, and mice with 25 or 30 min unilateral ischemia lost 10 - 12% body weight by day 2, and subsequently gained a small percentage of body weight over the next two days until the end of the study at day 4 (Fig 5.3A). Mice with 35 or 40 min unilateral ischemia, however, continued to lose weight throughout the study, to a maximum of 22% and 28% body weight loss, respectively, by day 4.

Renal function was assessed by transcutaneous measurement of FITC-sinistrin clearance at baseline and days 1, 2, and 4 following surgery (Fig. 5.3B). The sham-operated mouse displayed a slight increase in FITC-sinistrin half-life at day 1 following surgery compared with baseline (Table 5.4), which returned towards baseline levels at days 2 and 4. All IRI mice displayed a strong increase in FITC-sinistrin half-life at day 1, with longer clamping times resulting in longer half-lives. For all mice with a clamp time of 35 min or less, the peak of FITC-sinistrin half-life was at day 1, and measurements on subsequent days yielded decreasing values. However, the mouse with a clamp time of 40 min displayed a continued increase in FITC-sinistrin half-life at day 2, before decreasing at day 4.

The tubular injury scores of PAS-stained paraffin kidney sections increased as clamp time increased (Fig. 5.3C, Table 5.4), and this correlated strongly with transcutaneous assessment of FITC-sinistrin clearance (R^2 = 0.80; Fig. 5.3D).

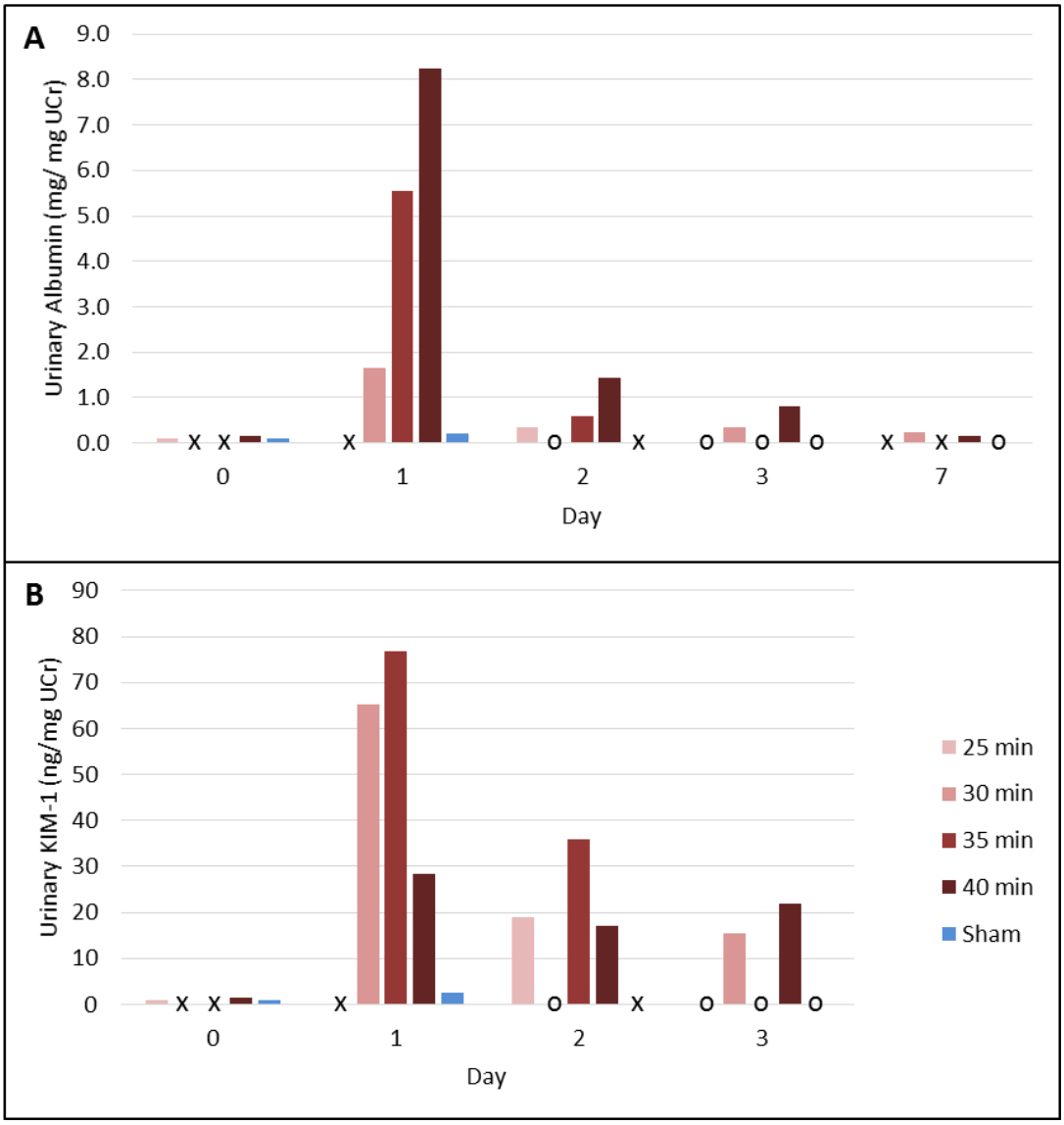

Figure 5.2: Urine biochemistry and problems collecting urine. Urinary excretion of albumin (**A**) and KIM-1 (**B**) was difficult to analyse due to difficulties in collecting urine from mice. X = no urine collected; O = liquid collected from sand, but yielded no detection of the analyte, and it is likely that water and not urine was collected. Both albumin and KIM-1 levels were highest at day 1, and decreased back towards baseline levels at subsequent time points. At day 1, both urinary albumin (**C**) and KIM-1 (**D**) excretion increased as the clamp time increased, however after 40 min ischemia, urinary KIM-1 excretion was reduced compared with 30 and 35 min ischemia. All data points represent one animal clamp time.

This pilot study was then repeated with an additional cohort of five animals, and while similar trends with respect to clamp times were observed in the second group, the injury levels obtained were lower compared with the first group (Fig. 5.4A, B). The temperature of the heat mat during surgery for the second group was later found to have been unintentionally lower than that for the first group, leading to a reduced level of renal injury induced in all mice.

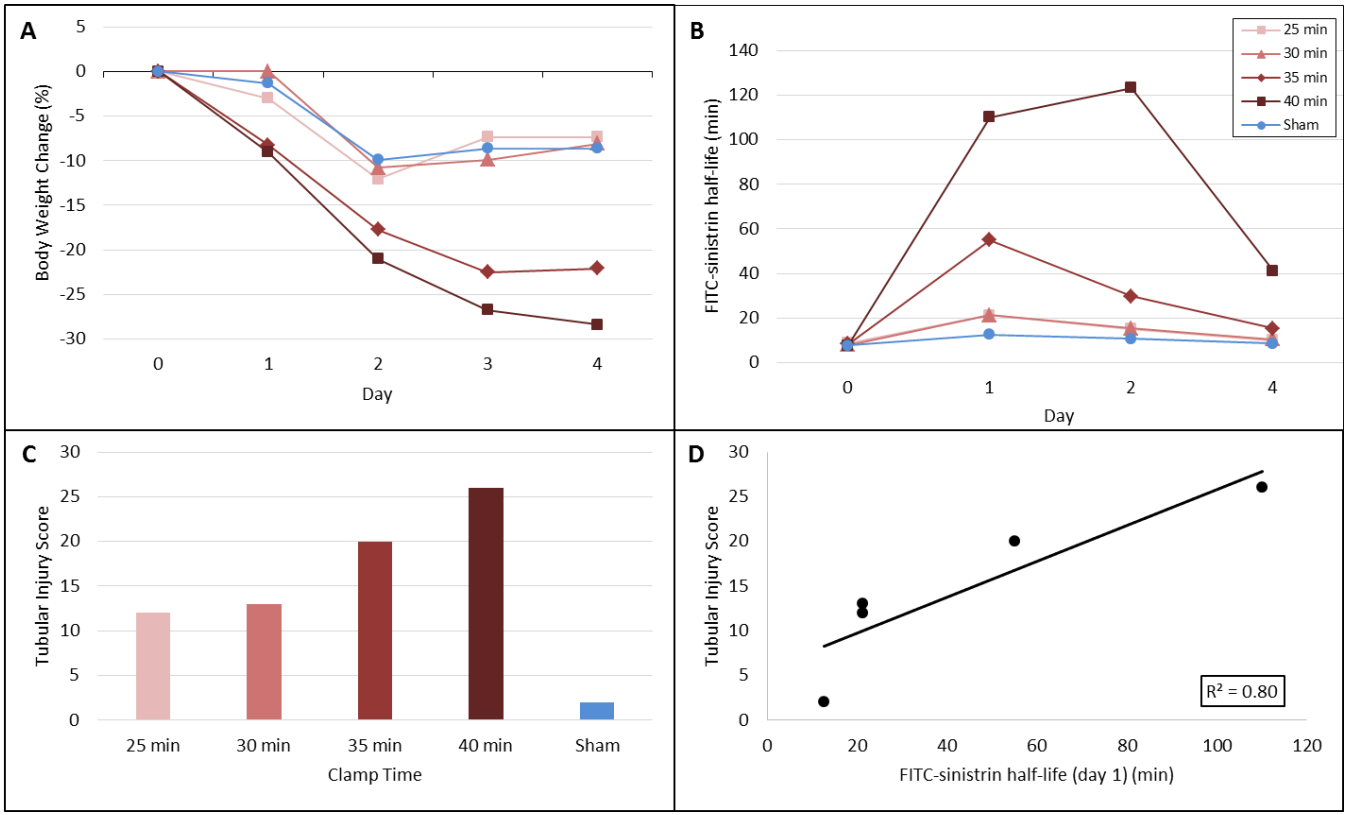

Figure 5.3: Pilot unilateral with nephrectomy IRI model – renal injury analyses. (**A**) Body weight change of animals following unilateral ischemia with nephrectomy, with clamp times ranging from 25 – 40 min, or sham-operated with no renal ischemia. Weight loss was more severe for the 35 and 40 min clamp times in the unilateral with nephrectomy model than in the bilateral model. (**B**) FITC-sinistrin half-life was vastly increased over baseline levels at day 1, and decreased over time at days 2 and 4. FITC-sinistrin half-life data shows that stronger injury levels were induced with the unilateral with nephrectomy model, than with the bilateral model. (**C**) Tubular injury was scored for each the injured kidney for each animal, and showed that as clamp time increased, tubular injury increased. (**D**) A plot of the correlation between the tubular injury score and FITC-sinistrin half-life at day 1 showed that there was strong correlation. All data points represent individual animals; one animal per clamp time.

Table 5.4: Pilot unilateral IRI model – renal injury analyses.

		FITC-sinistrin half-life (min)				Tubular Injury Score
	Clamp Time	Day 0	Day 1	Day 2	Day 4	Left Kidney
Group 1	25 min	8.76	21.31	15.18	10.16	12
	30 min	8.08	21.32	15.33	10.64	13
	35 min	8.51	55.00	29.78	15.31	20
	40 min	7.85	110.13	123.12	41.17	26
	Sham	7.73	12.65	10.85	8.70	2

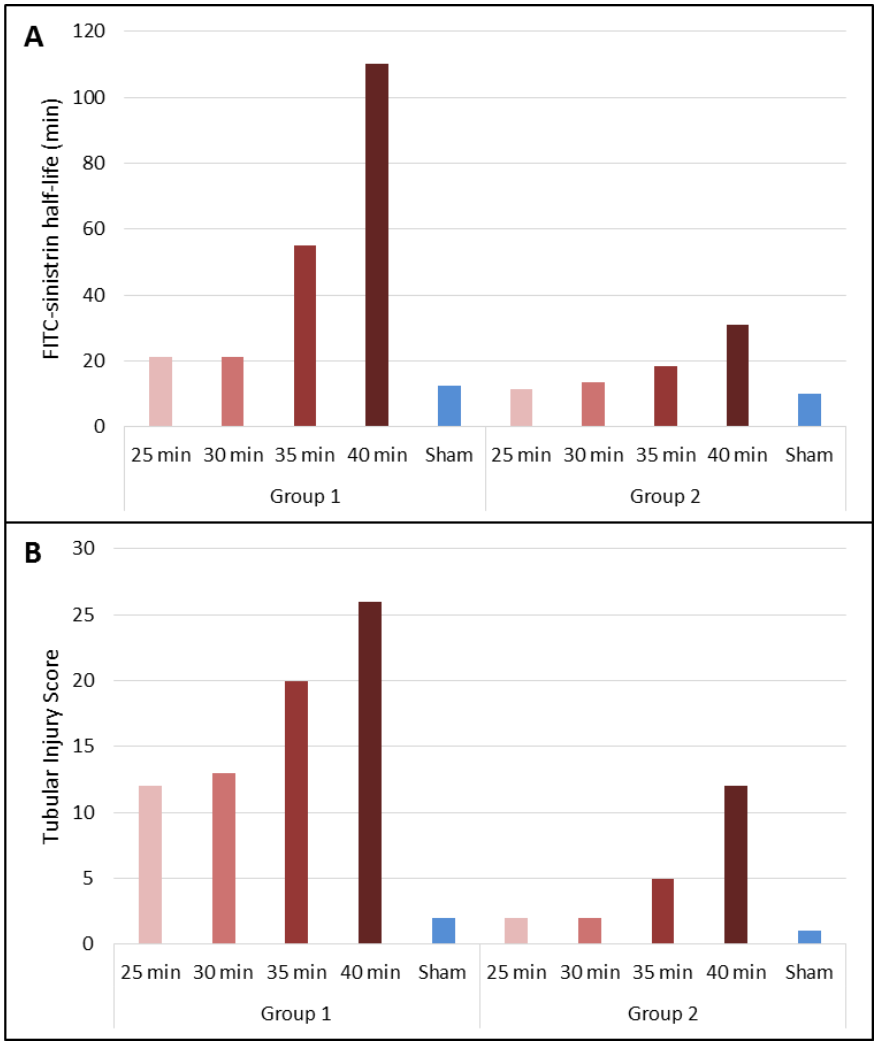

Figure 5.4: Highlighting the importance of careful temperature control. Surgery was performed on two groups of mice on two different days. In group 1 (same data as presented in Figure 5.2), the temperature of the heat mat was higher than for group 2. The cooler body temperature of mice in group two conferred a degree of protection from renal injury, as shown by FITC-sinistrin half-life (**A**) and histological assessment of tubular injury (**B**). The protective effect of temperature was more evident at the higher clamp times, where vast differences in injury levels can be observed.

As part of the analysis of the bilateral pilot study, it was noticed that the half-life of FITC-sinistrin in the sham and 25 min ischemia mice decreased over time between baseline and subsequent measurements. In order to assess the stability of FITC-sinistrin half-life in healthy male BALB/c mice, baseline FITC-sinistrin clearance was measured three times (once every two days). Repeated measurements showed that FITC-sinistrin half-life was significantly higher on the first measurement, compared to the second or third measurements (paired t-test, $p < 0.001$; Fig. 5.5A, B). The third measurement was significantly higher than the second (paired t-test, $p = 0.03$), however the difference in half-life was only around one minute, which is within normally observed fluctuations in clearance times and was not considered to be a problem.

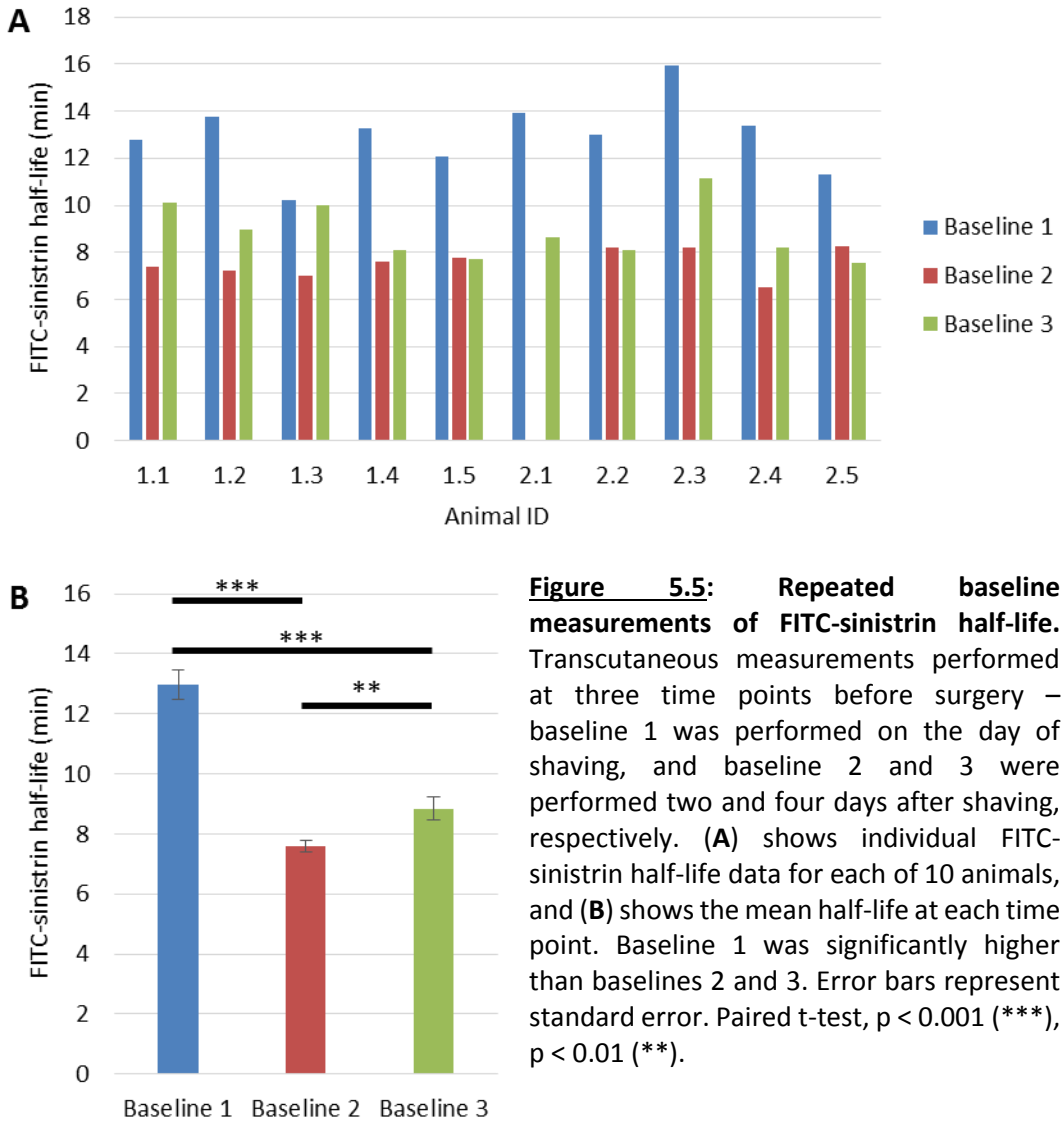

Figure 5.5: Repeated baseline measurements of FITC-sinistrin half-life. Transcutaneous measurements performed at three time points before surgery – baseline 1 was performed on the day of shaving, and baseline 2 and 3 were performed two and four days after shaving, respectively. (**A**) shows individual FITC-sinistrin half-life data for each of 10 animals, and (**B**) shows the mean half-life at each time point. Baseline 1 was significantly higher than baselines 2 and 3. Error bars represent standard error. Paired t-test, $p < 0.001$ (***), $p < 0.01$ (**).

Following the initial pilot studies, the tubular injury scores assessed histologically showed that there were large differences in the injury induced in each kidney in the bilateral model,

most likely due to differences in effective clamp pressure resulting from slight differences in individual clamps and differences in the amount of connective tissue and fat surrounding the renal artery and vein. As a result, the unilateral with Nx model was selected for future studies. Furthermore, it is possible that the shaving procedure caused the half-life for FITC-sinistrin to be increased when the measurement was carried out on the same day as shaving, and as such, mice were shaved two days in advance of the baseline measurement in subsequent experiments.

5.3.1.3 Finalising the Ischemia Time in the Unilateral Ischemia with Contralateral Nx Model

Additional experiments were carried out to further optimise the ischemia time in the unilateral ischemia with contralateral Nx model (data not shown). Initial data suggested 34 min ischemia would be optimal, however when the single heat mat used for all animals undergoing surgery at a time was replaced with individual infra-red mats that controlled individual body temperature more accurately, 34 min ischemia resulted in very severe injury (data not shown), and 31 min was instead determined as the optimal ischemia time. A final study was conducted to confirm that 31 min ischemia would induce renal injury that was severe enough for any efficacy by a cell therapy to be detected, with no mortality and acceptable variability between mice.

Following 31 min ischemia, all five mice survived the four-day study, and lost up to an average of 16.7% body weight (Fig. 5.6A). Body weight loss in IRI mice was significantly greater than that in sham mice at days three and four (Supplementary Table S5.1A). Renal function was assessed by transcutaneous measurement of FITC-sinistrin clearance at baseline and days 1, 2, and 4 following surgery. Sham mice displayed only a slight increase in FITC-sinistrin clearance one day following surgery, whereas IRI mice displayed a significant increase in FITC-sinistrin clearance, averaging a half-life of around 49 min at day one, compared with 13 min for sham mice, and 9 min at baseline (Fig 5.6B, Table 5.5). As expected, FITC-sinistrin half-life in IRI mice decreased at day two, and was elevated but not significantly different to baseline levels by day four (one-way ANOVA, $p < 0.001$, see Supplementary Table S5.1B for results of post-hoc Tukey pairwise comparison test).

Serum and tissue biomarkers were measured in IRI and sham mice. SCr and BUN were significantly elevated at day 4 in IRI mice compared with shams (SCr: Fig. 5.6C; two sample t-test, $p < 0.001$. BUN: Fig. 5.6D; two-sample t-test, $p = 0.013$). Tissue expression of KIM-1 and Ki67 were analysed to assess injury and repair, respectively. KIM-1 tissue expression was quantified as the mean percentage of KIM-1-positive staining in ten FOVs at 20x

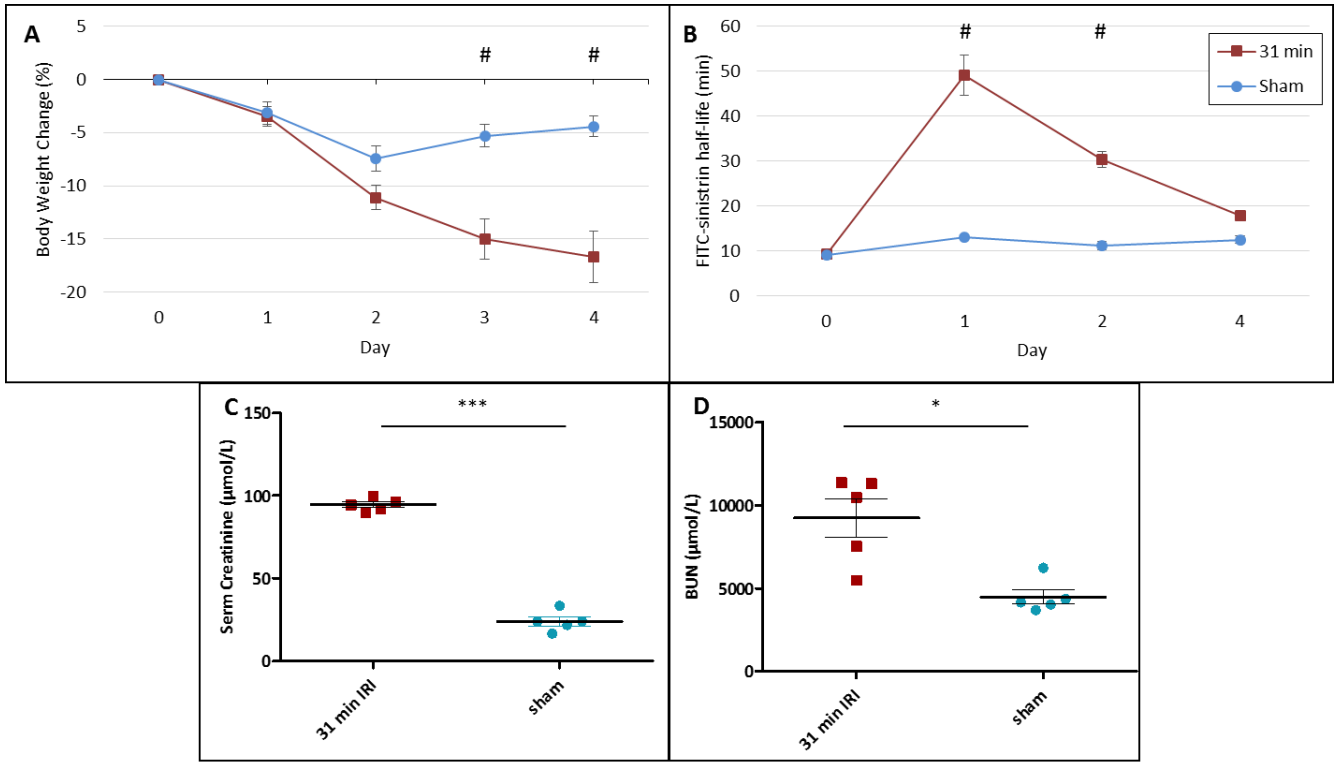

Figure 5.6: Characterisation of the renal injury induced by 31 min unilateral ischemia with contralateral nephrectomy. (**A**) Mean body weight change of mice with 31 min unilateral ischemia with contralateral Nx, and sham-operated mice. Sham mice lost a small percentage of body weight in the first few days after surgery, but began to put weight back on by days 3 and 4. Conversely, injured mice lost a large percentage of body weight during the experiment, and did not put weight back on before the end of the experiment at day 4. (**B**) FITC-sinistrin half-life increased significantly over baseline levels at day 1 in injured mice, and then decreased back towards baseline levels at days 2 and 4. Sham mice maintained a relatively constant FITC-sinistrin half-life throughout the study. SCr (**C**) and BUN (**D**) were significantly elevated in IRI mice compared to sham mice. Data points represent the group mean and error bars represent standard error (**A - B**). Data points represent individual animals, and bars represent mean (wide line) and standard error (short lines) (**C – F**). Significant difference between IRI and sham groups with Tukey test (#); paired t-test, $p < 0.001$ (***), $p < 0.05$ (*).

Table 5.5: 31 min IRI vs sham – renal injury analyses

		FITC-sinistrin half-life (min)				SCr (µmol/L)	BUN (µmol/L)	KIM-1 (% area)	Ki67 (counts)	
	Animal ID	Day 0	Day 1	Day 2	Day 4				Cortex	OSOM
31 min IRI	1.1	8.55	54.78	33.19	19.51	92.11	7535.56	14.96	17.10	77.8
	1.2	9.15	50.94	34.24	16.87	99.75	11362.63	19.70	16.40	101.6
	1.3	10.23	47.73	32.06	17.13	89.93	10473.24	15.05	17.80	135.7
	1.4	10.24	32.82	24.70	15.80	94.29	11308.73	16.40	11.60	83.2
	1.5	7.97	59.30	27.45	20.08	96.48	5487.27	11.65	17.00	65.6
	Mean	**9.23**	**49.11**	**30.33**	**17.88**	**94.51**	**9233.49**	**15.55**	**15.98**	**92.78**
	SD	**1.01**	**10.08**	**4.08**	**1.83**	**3.81**	**2612.18**	**2.90**	**2.50**	**27.27**
	SE	**0.45**	**4.51**	**1.82**	**0.82**	**1.70**	**1168.20**	**1.30**	**1.12**	**12.20**
Sham	2.1	8.93	10.95	8.16	9.24	24.03	3680.13	0.12	9.10	2.4
	2.2	9.53	14.27	10.52	12.83	24.03	4016.43	0.11	7.50	2.3
	2.3	8.38	14.20	10.46	11.80	16.72	4160.57	0.11	14.60	2.7
	2.4	8.44	13.30	14.49	14.92	21.94	6226.43	0.11	8.20	3.5
	2.5	10.17	12.23	12.06	13.58	33.44	4352.74	0.11	7.20	0.7
	Mean	**9.09**	**12.99**	**11.14**	**12.47**	**24.03**	**4487.26**	**0.11**	**9.32**	**2.32**
	SD	**0.76**	**1.41**	**2.34**	**2.14**	**6.05**	**1002.83**	**0.00**	**3.04**	**1.02**
	SE	**0.31**	**0.58**	**0.95**	**0.87**	**2.70**	**448.48**	**0.00**	**1.36**	**0.46**

magnification within the OSOM. KIM-1 staining was absent in sham mice (Fig. 5.7A), and significantly elevated in IRI mice (Fig. 5.7B, C; two-sample t-test, $p < 0.001$). Cell proliferation was assessed by counting Ki67-positive nuclei in ten FOVs at 40x magnification in each the cortex and the OSOM. There was a low level of cell proliferation in the cortex of both the sham and IRI mice (Fig 5.7D, E), which was significantly elevated in the IRI mice (Fig. 5.7H; two-sample t-test, $p = 0.007$). Cell proliferation in the OSOM was even lower than that in the cortex in sham mice (Fig. 5.7F; two-sample t-test, $p = 0.008$), but was vastly and significantly elevated in IRI mice (Fig. 5.7G, H; two-sample t-test, $p = 0.002$).

Histological tubular injury was not analysed for the final optimisation study using 31 min ischemia due to time constraints, but was determined for previous optimisation studies. The data from multiple optimisation studies conducted using various clamp times and temperature conditions was pooled, and tubular injury scores were correlated with FITC-sinistrin half-life on day one (*n = 39*), SCr on day four (*n = 30*), and BUN on day four (*n = 30*) (Fig. 5.8). Kidney function as assessed by transcutaneous measurement of FITC-sinistrin clearance correlated more strongly with histological assessment of kidney damage ($R^2 = 0.88$, Fig. 5.8A) than either SCr or BUN ($R^2 = 0.69$, 0.58, respectively, Fig. 5.8B,C), indicating FITC-sinistrin half-life was a more accurate predictor of histological kidney damage than

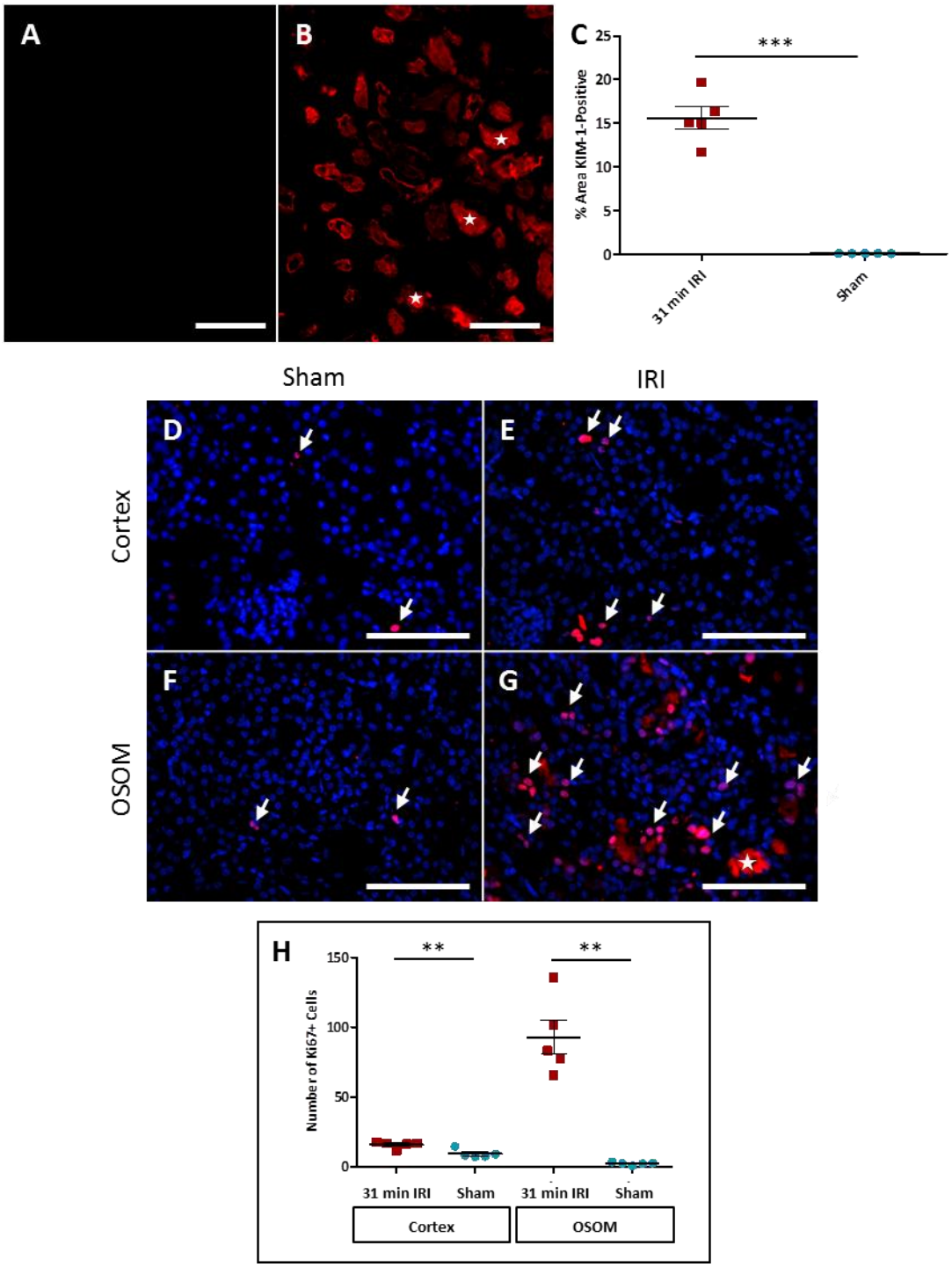

<u>Figure 5.7</u>: Expression of tissue biomarkers of injury and repair in IRI and sham mice. Representative images of KIM-1 expression in IRI mice (**A**) and sham mice (**B**). IRI mice displayed a significant upregulation of KIM-1 expression compared with sham mice (**C**). Representative images of Ki67 expression in the cortex of IRI mice (**D**) and sham mice (**E**), and the OSOM of IRI mice (**F**) and sham mice (**G**). Cell proliferation, assessed by the number of KI67+ nuclei (arrows), was modestly elevated in the cortex of IRI mice, and markedly increased in the OSOM, compared with sham mice. (**H**). Tubular casts were strongly autofluorescent (★). Data points represent the group mean and error bars represent standard error (**A - B**). Scale bars represent 100µm. Data points represent individual animals, and bars represent mean (wide line) and standard error (short lines) (**C – F**). Paired t-test, $p < 0.001$ (***), $p < 0.01$ (**).

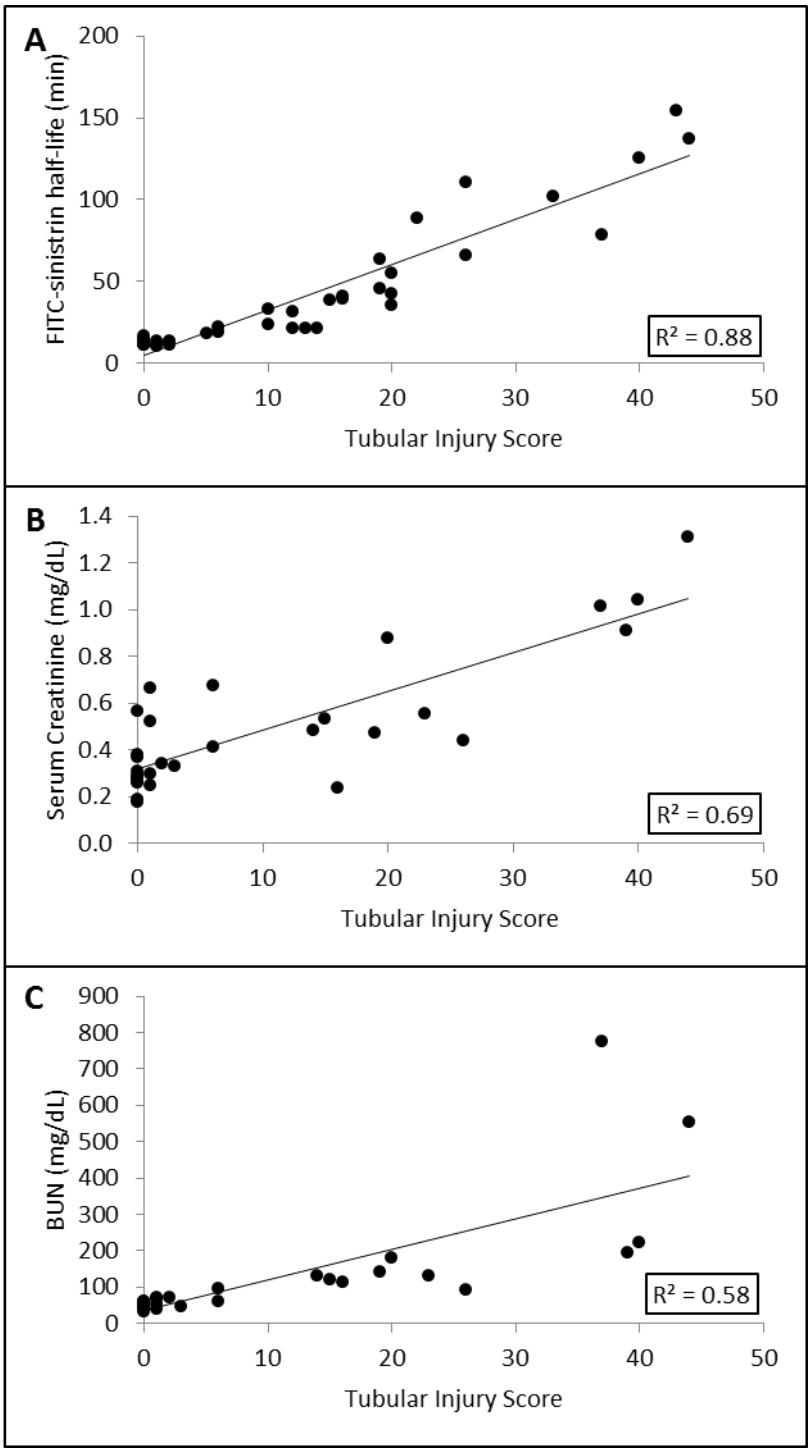

Figure 5.8: Correlation of three measures of kidney function (FITC-sinistrin clearance, SCr, BUN) with histological evaluation of tubular injury. Transcutaneous assessment of FITC-sinistrin clearance (**A**) showed strong positive correlation with histological evaluation of tubular injury ($R^2 = 0.88$), whereas SCr (**B**) and BUN (**C**) both showed positive but weaker correlation with tubular injury ($R^2 = 0.69$ and 0.58, respectively).

either serum biomarker. As such, the transcutaneous measurement was used as the primary measure of kidney function in all subsequent experiments.

5.3.2 Assessing the Efficacy of Human Cells in the IRI model

5.3.2.1 Four-day study

The efficacy of three different types of human-derived cells, hKCs, hUC-MSCs, and hBM-MSCs, was assessed in IRI mice, and compared with IRI mice that received saline. All 27 mice survived the four-day study, and lost a similar proportion of body weight throughout the experiment (Fig. 5.9A). There were no differences in body weight loss between any of the treatment groups (Supplementary Table S5.2A). Kidney function was assessed by transcutaneous measurement of FITC-sinistrin clearance at baseline, and days one, two, and four. All mice showed a significant increase in FITC-sinistrin half-life at day one compared with baseline, which decreased back towards baseline levels at days two and four (Fig. 5.9B). However, there were no significant differences between treatment groups at any time point (Supplementary Table S5.2B). The degree of improvement in FITC-sinistrin clearance was also assessed, to determine whether cell-treated mice recovered faster than saline-treated mice, but there were no significant differences in the percentage of improvement between days one and two (Fig. 5.9C). SCr and BUN measured at the end of the experiment on day four were comparable in all treatment groups (SCr: Fig. 5.9D; one-way ANOVA, $p = 0.501$. BUN: Fig. 5.9E; one-way ANOVA, $p = 0.936$). To assess whether cell therapy had an effect on tissue injury and repair biomarkers, KIM-1 and Ki67 tissue expression were analysed. The percentage of KIM-1-positive area and the number of Ki67-positive cells were comparable in all treatment groups (SCr: Fig. 5.10A; one-way ANOVA, $p = 0.772$. BUN: Fig.5.10B; one-way ANOVA, $p = 0.055$), indicating that cell therapy had no effect on tubular cell injury or repair.

5.3.2.2 One-day study

The results of the four-day study suggested that none of the three cell types tested had any efficacy in improving kidney function in IRI mice. It was unclear whether this may have been due to an inability of the transcutaneous measurement to detect amelioration, and the late time point (day four) for detecting differences in serum biomarkers. In the IRI model, SCr and BUN tend to peak at day one, so a one-day study was carried out to compare the efficacy of hKCs with saline. Moreover, ZsGreen$^+$/luciferase$^+$ hKCs were administered in this study, and their biodistribution *in vivo* was assessed with BLI.

As expected, hKCs were restricted to the lungs following IV administration (Fig. 5.11A) and there was no bioluminescence signal from mice that received saline (Fig. 5.11B). Unexpectedly, the intensity of bioluminescence signal did not decrease in the 24h following

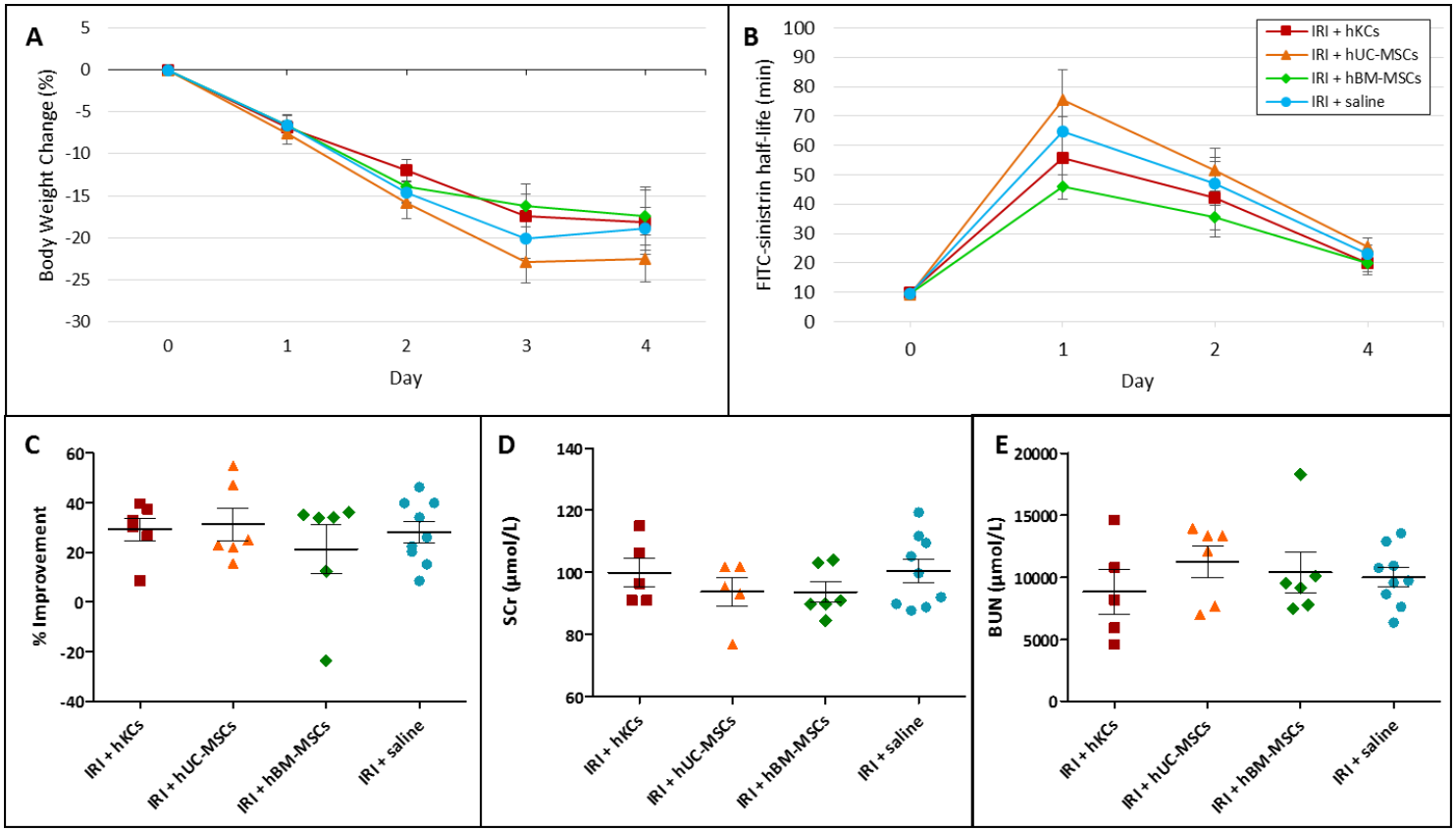

Figure 5.9: Efficacy of different types of human cells in the IRI model. (**A**) Mean body weight change of mice declined at approximately the same rate in all groups. (**B**) FITC-sinistrin half-life increased significantly over baseline levels at day 1 in all groups, and then decreased back towards baseline levels at days 2 and 4. There were no significant differences between treatment groups at any time point. The percentage of improvement in half-life between days 1 and 2 (**C**), and serum biomarkers at day 4 SCr (**D**) and BUN (**E**) were not significantly different between any treatment group. Data points represent the group mean and error bars represent standard error (**A - B**). Data points represent individual animals, and bars represent mean (wide line) and standard error (short lines) (**C – E**).

cell administration (Fig. 5.11A, C; paired t-test, p = 0.598). Furthermore, there were no significant differences in serum biomarkers at day 1 (SCr: Fig. 5.11D, two-sample t-test, p = 0.096; BUN: Fig. 5.11E, two-sample t-test, p = 0.564).

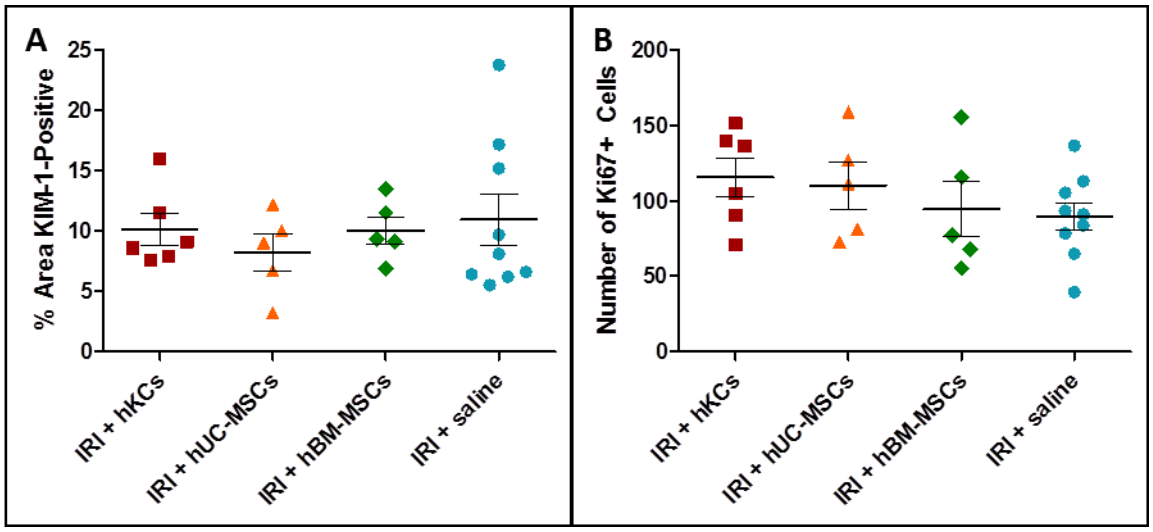

Figure 5.10: Expression of tissue biomarkers of injury and repair following cell therapy. There were no significant differences in tissue expression of KIM-1 (**A**) or Ki67 (**B**) between any of the treatment groups. Data points represent individual animals, and bars represent mean (wide line) and standard error (short lines).

5.4 Discussion

The overall aim of this chapter was to compare the efficacy of several cell types in a clinically-relevant model of AKI. Initial pilot studies were carried out to decide whether to set up a bilateral or unilateral model of IRI, and the duration of ischemia was then optimised in the unilateral with Nx model before the therapeutic efficacy of three different cell types was investigated. The key findings were as follows:

(i) Bilateral ischemia induced less severe injury than unilateral ischemia (with Nx) with comparable clamp times, however the injury induced in each kidney was highly variable.

(ii) unilateral ischemia with contralateral nephrectomy after 31 minutes clamp time induced renal injury that was severe but survivable, with acceptable weight loss.

(iii) The transcutaneous measurement of FITC-sinistrin clearance was a superior measure of kidney function in the IRI model, correlating with histological damage more strongly than either SCr or BUN.

(iv) None of the cell types assessed in this model had any effect on kidney function or injury.

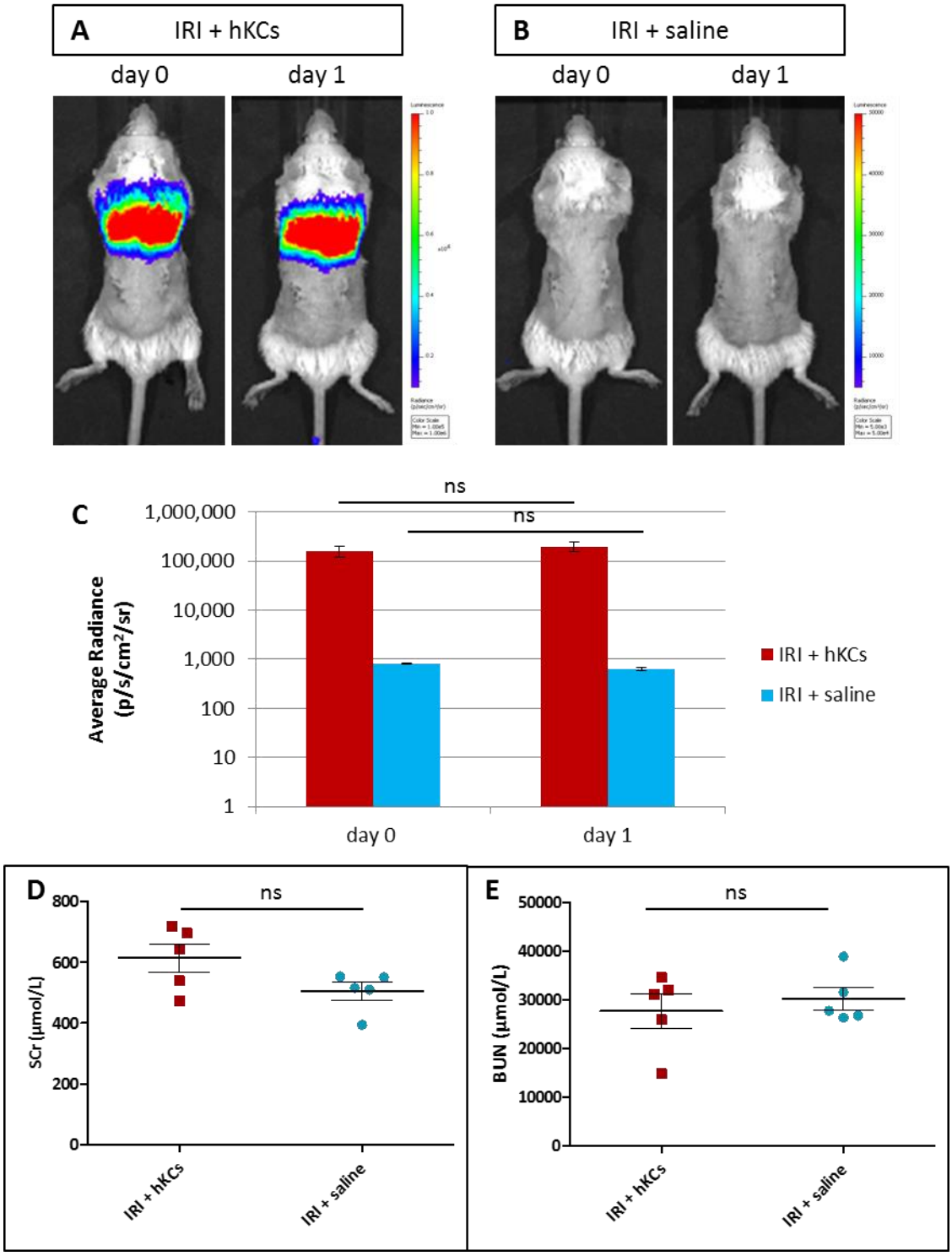

Figure 5.11: **Short-term cell tracking and efficacy of hKCs**. Representative bioluminescence images of a hKC-treated (**A**) and a saline-treated (**B**) mouse immediately after cell/saline administration (day 0) and at day 1. Unexpectedly, bioluminescence signals persisted at the same intensity 24h after administration (**C**). Bars represent the group mean, error bars represent standard error. There were no significant differences in SCr (**D**) or BUN (**E**) between hKC- and saline-treated mice at day 1 Data points represent individual animals, and bars represent mean (wide line) and standard error (short lines).

(v) hKCs remained in the lungs 24h following IV administration, which was an unexpected finding based on previous results, and may offer an insight into why the tested cell types had no ameliorative effect.

Establishing the IRI model by unilateral clamping with contralateral Nx

Several variables in the IRI model were decided upon before pilot studies began and were not modified throughout the experiments. These included the age, strain, and sex of the mice, surgical approach, and anaesthetic agent. Young adult male mice are commonly used in the IRI model and were chosen due to their increased susceptibility to renal injury over female mice. Whilst C57BL/6 mice are more commonly used in other studies, BALB/c mice were chosen here due to our familiarity with this strain, our preference for white mice for imaging experiments, and no need to genetically manipulate the mice. A dorsal surgical approach was chosen for its reported superiority in improving recovery and survival and reducing the risk of dehydration and infection, compared with the ventral approach. Isoflurane, an inhalation anaesthetic, is reported to exert a protective effect on the kidney, but was deemed preferable to injection anaesthetics (which are not renoprotective) due to faster recovery times and the ability to tune the depth of anaesthesia with isoflurane. The reason that many other groups choose injectable anaesthetics for the IRI model is likely due to the ability to perform surgery on multiple animals at once, which is difficult with inhalation anaesthetics due to the need for extra equipment (nosecones *etc.*). To overcome this problem, we commissioned the design of a multi-way nosecone system, which allowed surgery to be performed on four animals at once.

Although not described in this thesis, many optimisation studies were carried out between the initial pilot studies and the final study characterising the injury induced with 31 min ischemia. These numerous studies taught many lessons about the IRI model, and its sensitivities to varying experimental conditions.

First, it was not feasible to collect urine for biomarker analysis. Because of license restrictions it was not possible to use metabolic cages for 24h urine collection at multiple time points within a four-day post-surgery time frame. An alternative method of placing mice on hydrophobic sand was therefore tested, although this was associated with several problems, including the need to withhold food, accidentally collecting water that had dripped from the water bottle instead of urine, and mice not producing urine at all time points. Afternoon collections tended to yield a higher volume of urine than morning collections, however this meant that urine collection had to occur after morning transcutaneous measurements, and

mice that were more severely injured had not yet fully cleared FITC-sinistrin from their system, meaning that the urine collected was contaminated with FITC-sinistrin. This was a major problem for the quantification of urine creatinine, which was necessary for the normalisation of albumin and KIM-1 measurements, as the urine creatinine assay relied on a colorimetric measurement.

Second, transcutaneous measurements were very well-tolerated by all mice after surgery. The incisions tended to be low enough that the transcutaneous device could be placed proximal to the sutures, and small sections of cotton swab could be used to protect the sutures from being pulled open by the adhesive plaster. The transcutaneous measurement of FITC-sinistrin clearance revealed greater changes in kidney function in the IRI model compared with the ADR model. The clearance curve showed a more drastic delay in clearance in IRI mice at day one (Supplementary Fig. S5.1) compared with week four in the ADR model (Fig. 3.2), where only a very subtle change in clearance could be observed in the clearance curve. Importantly, renal function as measured by transcutaneous measurement correlated much more strongly with histological assessment of renal damage than either SCr or BUN, indicating that this method is not only reliable, but that it is also superior to traditional measures of kidney function. Moreover, the transcutaneous measurement could identify mice that were likely in renal failure, by a lack of clearance of FITC-sinistrin during the 90-minute measurement period (Supplementary Fig. S5.1C). Invariably, mice that showed an absence of FITC-sinistrin clearance at day one either died or did not improve at day two and had to be sacrificed early due to severe ill health and suspected renal failure. An interesting finding whilst carrying out baseline measurements in this model was that it was essential to shave mice prior to the first measurement. The half-life of FITC-sinistrin was significantly higher if the measurement was carried out on the day of shaving than if it was carried out two days later. This finding was exclusive to the male BALB/c mice used in the IRI model; it did not apply to the female SCID mice used in the ADR model.

Third, the optimisation studies highlighted just how sensitive the IRI model is to subtle changes in temperature. As shown in Fig. 5.4, and in numerous published studies[360,362,363], a slight decrease in temperature during surgery protects the kidney from injury. Initial experiments with the IRI model were carried out using a single large heat mat for all mice undergoing surgery, however the heat was not well-distributed across the mat, and surgeries carried out using this heat mat lead to variable responses in kidney injury. Subsequently, the single heat mat was switched for individual infrared feedback-loop heat mats, which accurately controlled each mouse's body temperature to within 0.5°C of the desired

temperature, leading to more consistent renal injury. An additional observation not described in this chapter was the effect of the kidney's location during ischemia. The kidney was initially placed under the skin during the period of ischemia, but in the initial studies the kidney did not always reperfuse very well following the release of the clamp, and it was thought that the manipulation of the clamped kidney to place it under the skin may have been causing damage to the vasculature. As such, an alternative method of keeping the kidney out of the body but covered in saline-soaked swabs to prevent drying was tried. This of course led to the kidney being too cool during ischemia, and led to low levels of renal injury. Further optimisations regarding temperature control included waiting until the mouse's body temperature was up to 37°C before starting surgery, and standardising the time spent recovering in the heat box after surgery to 30 minutes.

Ultimately, an ischemia time of 31 minutes was optimised for the experimental conditions imposed in our laboratory, and was influenced by:

(i) the strain, age, and sex of mice,
(ii) the choice of isoflurane to anaesthetise the mice,
(iii) the hydration status of mice during morning surgery, which is likely to be greater than if surgery was carried out in the afternoon, and is also influenced by the choice of dorsal surgical approach, and the volume of fluids given before surgery, and finally,
(iv) the temperature, including core body temperature during surgery, temperature of the heat box during the initial period of recovery, and ambient temperature at which mice are maintained post-surgery.

Assessing efficacy of human cells in the IRI model

Following optimisation of the IRI model, the efficacy of three cell types, hKCs, hUC-MSCs, and hBM-MSCs, was assessed. These cell types were chosen in order to determine whether there were any differences in the efficacy of (i) kidney derived cells compared with MSCs, and (ii) MSCs depending on the source of the tissue that MSCs were isolated from. Unexpectedly, none of the cell types showed any efficacy in the IRI model. Efficacy was predominantly assessed by transcutaneous measurement of FITC-sinistrin clearance as a measure of kidney function. This method was chosen as the primary outcome due to its superiority over SCr and BUN as a measure of kidney function, and its value in detecting ameliorative effects of hKCs in a rat model of cisplatin-induced AKI[134]. However, there were no significant differences in FITC-sinistrin half-life at any time point between any of the treatment groups in this study.

Moreover, there were no significant differences between the treatment groups in body weight loss, as a measure of general health, or in the serum and tissue biomarkers analysed at the end of the study on day four. Tissue KIM-1 expression demonstrated that there were no differences in tubular injury, and tissue Ki67 expression showed that there was no difference in tubular cell proliferation, and therefore renal recovery, between any of the cell-treated groups and the saline-treated group.

To explain the lack of efficacy observed, the initial hypothesis included the following arguments: (i) the transcutaneous measurement was unable to detect kidney repair in the IRI model as it had not been reported before in this AKI model; (ii) the day four time point was too late to detect any differences in SCr and BUN.

The levels of these serum biomarkers tend to peak at day one to two and then decrease at later time points[110,118,352,356,357], and as such any differences between treatment groups may have been evident at an earlier time point, but undetectable by day four. However, in an additional experiment analysing day one biomarkers, the values of SCr and BUN were still not significantly different between treatment groups.

An additional feature of the one-day study was the inclusion of bioluminescence imaging to track the *in vivo* biodistribution of ZsGreen^{+}/luciferase^{+} hKCs. As expected, the bioluminescence signal was restricted to the lungs on the day of IV administration of hKCs, indicating that the cells were trapped in the lungs. However, 24h later the bioluminescence signal remained present in the lungs, but was not detectable in the kidney or any other organ. This was an unexpected result since it was assumed that the bioluminescence signal would decrease within 24h of cell administration, in line with previous results from this thesis (Fig. 4.3A, 4.8A, 6.6A) and our general experience of imaging the biodistribution of various cell types. Surprisingly, the intensity of the bioluminescence signal persisted at approximately similar levels or even increased slightly, suggesting that the cells did not undergo cell death as usually occurs following *in vivo* administration, and possibly even proliferated. An explanation for the increase in bioluminescence signal in these mice could be a slight loss of body mass between day zero and day one, resulting in the appearance of a stronger bioluminescence signal; however, further studies to assess any proliferation of the cells would be required to determine this.

Studies have shown that intravenously administered cells become trapped in the lungs due to their large size physically entrapping them in small pulmonary capillaries[349,350], and also due to the expression of adhesion molecules such as vascular cell adhesion molecule-1

(VCAM-1)[349], integrins[369,370], and possibly also fibronectin[370]. It is also known that the cells do not persist in the lungs for very long after administration, with a half-life of about 24h[371]. This is supported by other studies in this thesis, which have shown that weak bioluminescence signals persist for several days following IV administration (Fig. 4.3A, 4.8A, 6.6A), suggesting that small numbers of cells do survive in the lungs for up to one week (Fig. 4.8A), however the vast majority of cells die very quickly following cell administration. Furthermore, Santeramo and colleagues have shown evidence of hKCs undergoing cell death in the lungs from as early as one hour following IV administration in a rat model of cisplatin-induced AKI[134]. However, it is not known what mechanisms initiate cell death, nor why the cells survived in the lungs of IRI mice for 24h after administration in the study described in this chapter.

It is widely known that ischemic AKI is not a disease restricted to the kidney, and in fact causes widespread effects on distant organs[372-375]. Patients with AKI may suffer consequences to the lungs, heart, liver, and brain, and it is thought that the accumulation of deleterious effects on multiple organs may actually be responsible for the very high morbidity and mortality levels in patients with AKI[372,373]. In particular, renal IRI is known to cause injury to the lung[376], and this may provide insights into the reason why the hKCs did not die following IV administration to mice with renal IRI, and further insights into the mechanism of action of cell therapy *in vivo*.

Clinically, respiratory failure is a common complication in AKI patients[377,378], and conversely, AKI is frequently diagnosed in patients requiring mechanical ventilation or following a lung transplantation[379-381]. Experimentally, AKI-associated acute lung injury (ALI) can be induced following renal IRI, however it is unclear whether ALI is a consequence of renal failure itself, or specifically the damage induced by ischemia. One research group has demonstrated that renal failure without ischemia, modelled by bilateral nephrectomy, resulted in negligible lung injury[224,382,383], whereas another group has reported similar severities of ALI following both 30 minutes bilateral IRI and bilateral nephrectomy[384]. This difference could be due to the different parameters of ALI measured by each group. A recent review on AKI-associated ALI suggested that the release of cytokines, inflammatory mediators, and products of cell death following ischemia may act to directly damage the lung endothelium to cause non-cardiogenic ALI (pulmonary oedema as a result of direct damage to lung endothelium), whereas the systemic accumulation of uremic products and subsequent fluid accumulation resulting from kidney failure may lead to cardiogenic ALI (pulmonary oedema as a result of fluid overload)[376].

Experimental data has demonstrated that renal IRI in rodents causes apoptosis of pulmonary endothelial, but not epithelial, cells, leading to microvascular dysfunction and subsequent increased pulmonary vascular permeability and pulmonary oedema[224,383,385]. Immune cells such as T cells[386], neutrophils[387], and macrophages[388], in addition to various serum cytokines[384,387,389,390], also play a role in the complicated pathogenesis of AKI-associated ALI.

To the best of our knowledge, lung injury following renal IRI has not previously been reported to promote the survival of intravenously administered cells. However, BLI has been used in two publications to monitor the biodistribution of MSCs in mice with ALI, induced either by smoke inhalation injury[279] or intranasal endotoxin administration[280]. Both studies showed greater bioluminescence signals in mice with ALI compared with healthy controls. However, the mechanism behind the survival of the cells is still unclear. One hypothesis could be that healthy pulmonary endothelial cells induce the death of cells that come into contact with their apical surface. This may occur via contact with a death receptor such as the Fas ligand (FasL), which is constitutively expressed on the pulmonary endothelium and initiates apoptosis in cells expressing Fas[391,392]. Gordon et al., (2007) have shown that activation of the Fas-FasL apoptosis pathway was involved in the lung clearance of pulmonary metastases, and that dysregulation of this pathway permitted osteosarcoma cells to persist and grow in the lungs[392]. The Fas-FasL apoptosis pathway may explain why intravenously administered cells undergo cell death soon after *in vivo* administration and do not persist in high numbers in the lungs, but it is not definitively known whether the hKCs administered in the studies described in this chapter express Fas. Fas is a cell surface protein belonging to the TNF receptor family, and is ubiquitously expressed in the body, with high abundance in the kidney, as well as the thymus, liver, and heart[393]. As such, it may be likely that hKCs express Fas, and that the Fas-FasL apoptosis pathway is activated when these cells are delivered to the lungs following IV administration, leading to rapid cell death. However, when the pulmonary endothelium is damaged, it may not be possible for the endothelial cells to carry out such a function of inducing the death of exogenously administered cells. Furthermore, the breakdown of the endothelial barrier leads to extravasation of fluid and, presumably, exogenously administered cells, into the interstitium, where the death of these cells may be less likely to be initiated.

It has been suggested that the process of cell death stimulates anti-inflammatory cytokines to inhibit inflammation and reduce injury[134,394-396], the so-called 'dying stem cell hypothesis'[394], and that death of the pulmonary-entrapped cells may therefore play a key role in the ameliorative effects observed in the injured kidney, and other organs. Santeramo

et al., (2017) demonstrated the role of macrophages in clearing apoptotic debris from dead hKCs in the lungs, and showed that the infiltrating macrophages secreted the anti-inflammatory cytokine, IL-10[134]. This hypothesis is supported by the fact that microvesicles derived from MSCs have been shown to improve organ function in a wide range of disease models[397], including the kidney[398]. However, in contrast, the administration of apoptotic thymocytes to mice with ischemic IRI significantly worsened kidney function[399], suggesting that the factors released by different cell types may have different effects on kidney injury. The results of this chapter, showing no efficacy of cell therapy on kidney injury alongside a lack of cell death in the lungs, may potentially support this hypothesis, as it suggests that cell death may be necessary for efficacy. However, it is unknown if the lack of efficacy of cell therapy in this chapter was due to the absence of cell death, or instead due to some other cause. The cell death hypothesis has not yet been widely investigated, and as such further work is required to elucidate the role of cell death in the ameliorative effect of cell therapies.

These results open up a multitude of questions for further experimental investigation regarding the mechanisms behind the survival of hKCs in the IRI model, but not in healthy animals or the ADR model, and subsequently, the mechanisms behind cell efficacy in kidney injury. Important questions that should be addressed include:

1. Is the survival of hKCs a direct consequence of lung injury induced by renal IRI?
2. Is the survival of hKCs the reason for their lack of efficacy in improving kidney function and injury?
    a. If so, why do the cells need to die in order to have a beneficial effect?
    b. Will administering the cells before the onset or after the peak of lung injury lead to increased cell death and therefore improved efficacy?
    c. If the severity of renal injury, and therefore the severity of ALI, is reduced, will the cells have a greater ameliorative effect?
3. Do hUC-MSCs and hBM-MSCs also survive in the lungs, and is that the reason why they also had no beneficial effect on kidney function or injury?
4. If the cells need to die in order to have a beneficial effect on the kidney, and if they cannot die in the lungs of mice with ischemic AKI due to ALI, then why are there so many other papers that report beneficial effects of various cell types in models of IRI? What is different about the model described in this chapter that leads to such vastly opposing results?

In summary, the results presented in this chapter identified the unilateral ischemia with nephrectomy model as a preferable model of renal IRI over the bilateral model, due to reduced variability, and an ischemia time of 31 minutes was optimised for the particular experimental conditions imposed in our laboratory. The results showed that the transcutaneous measurement of FITC-sinistrin was an appropriate and reliable method of measuring kidney function in the IRI model, with superior correlation with histological tubular injury compared with SCr and BUN. Importantly, the results demonstrated that hKCs administered to mice following reperfusion persisted in the lungs for at least 24h following administration, and this may be associated with the lack of amelioration of kidney injury. Further investigation is required to dissect out the mechanisms behind cell survival, and to determine what modifications to the therapy protocol would be required in order to achieve an ameliorative effect.

5.5 Supplementary Figures and Tables

Supplementary Tables S5.1: Tukey pairwise comparisons – characterisation of 31 min ischemia

A

		Body Weight Change (%)							
		n	Mean	Grouping					
Day 0 (Baseline)	31 min IRI	5	0.00	A					
	Sham	5	0.00	A					
Day 1	31 min IRI	5	-3.51	A	B				
	Sham	5	-3.16	A	B				
Day 2	31 min IRI	5	-11.13			C	D		
	Sham	5	-7.45		B	C			
Day 3	31 min IRI	5	-15.00				D		
	Sham	5	-5.30	A	B	C			
Day 4	31 min IRI	5	-16.70				D		
	Sham	5	-4.41	A	B				

B

		FITC-sinistrin half-life (min)							
		n	Mean	Grouping					
Day 0 (Baseline)	31 min IRI	5	9.23				D		
	Sham	5	9.09				D		
Day 1	31 min IRI	5	49.11	A					
	Sham	5	12.99			C	D		
Day 2	31 min IRI	5	30.33		B				
	Sham	5	11.14			C	D		
Day 4	31 min IRI	5	17.88			C			
	Sham	5	12.47			C	D		

Supplementary Tables S5.2: Tukey pairwise comparisons – efficacy of hKCs

A

		Body Weight Change (%)								
		n	Mean	Grouping						
Day 0	IRI + hKCs	6	0.00	A						
	IRI + hUC-MSCs	6	0.00	A						
	IRI + hBM-MSCs	6	0.00	A						
	IRI + saline	9	0.00	A						
Day 1	IRI + hKCs	6	-6.81	A	B	C				
	IRI + hUC-MSCs	6	-7.64	A	B	C	D			
	IRI + hBM-MSCs	6	-6.58	A	B					
	IRI + saline	9	-6.63	A	B					
Day 2	IRI + hKCs	6	-12.01		B	C	D	E		
	IRI + hUC-MSCs	6	-15.88		B	C	D	E	F	
	IRI + hBM-MSCs	6	-13.86		B	C	D	E	F	
	IRI + saline	9	-14.59		B	C	D	E	F	
Day 3	IRI + hKCs	6	-17.41			C	D	E	F	
	IRI + hUC-MSCs	6	-22.84						F	
	IRI + hBM-MSCs	6	-16.18		B	C	D	E	F	
	IRI + saline	9	-20.09					E	F	
Day 4	IRI + hKCs	6	-18.13			C	D	E	F	
	IRI + hUC-MSCs	6	-22.49				D	E	F	
	IRI + hBM-MSCs	6	-17.44			C	D	E	F	
	IRI + saline	9	-18.92					E	F	

B

		FITC-sinistrin half-life (min)							
		n	Mean	Grouping					
Day 0	IRI + hKCs	6	9.86				D		
	IRI + hUC-MSCs	6	9.35				D		
	IRI + hBM-MSCs	6	9.54				D		
	IRI + saline	9	9.54				D		
Day 1	IRI + hKCs	6	55.76	A	B	C			
	IRI + hUC-MSCs	6	75.69	A					
	IRI + hBM-MSCs	6	45.88	A	B	C			
	IRI + saline	9	64.75	A	B				
Day 2	IRI + hKCs	6	42.34	A	B	C	D		
	IRI + hUC-MSCs	6	51.64	A	B	C			
	IRI + hBM-MSCs	6	35.71		B	C	D		
	IRI + saline	9	47.00	A	B	C			
Day 4	IRI + hKCs	6	20.08			C	D		
	IRI + hUC-MSCs	6	25.38			C	D		
	IRI + hBM-MSCs	6	19.83			C	D		
	IRI + saline	9	23.17			C	D		

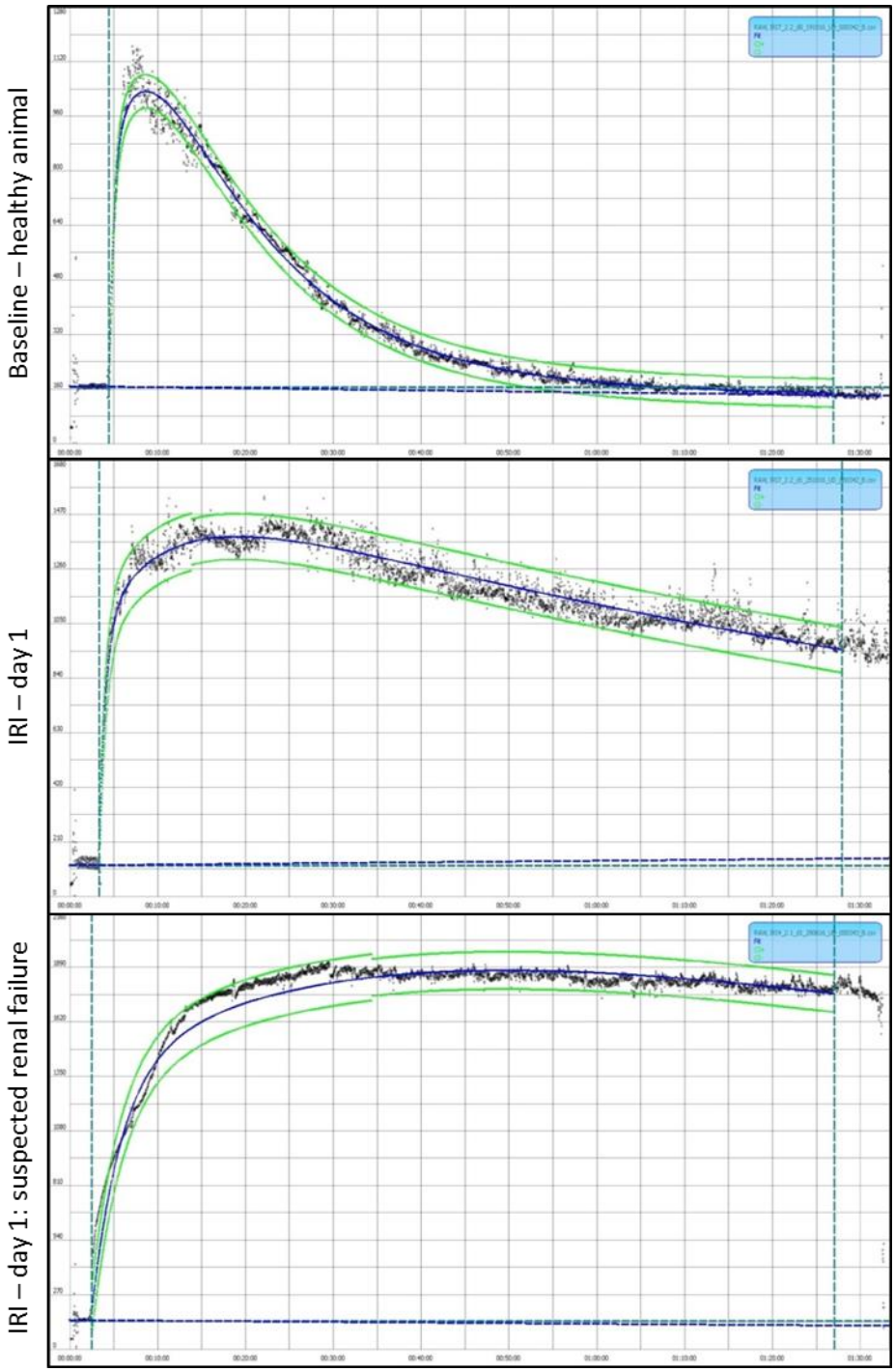

<u>Supplementary Figure S5.1</u>: Example FITC-sinistrin clearance curves. (**A**) Baseline measurement, showing that the fluorescence levels returned to baseline within the measurement period, indicating that FITC-sinistrin was completely cleared from the system quickly ($t_{1/2}$ = 8.41 min). (**B**) Clearance curve of the same mouse in (A), one day after IRI surgery. The clearance was much slower in the injured mouse, and fluorescence levels did not return to baseline within the measurement period ($t_{1/2}$ = 94.04 min). (**C**) Clearance curve from a severely injured mouse one day after IRI surgery. There was no clearance of FITC-sinistrin during the measurement period, indicating complete renal failure. As there was no clearance, it was not possible to calculate an accurate half-life. Black data points represent raw data, blue lines represent the 3-compartment fit, and green lines represent 95% confidence intervals.

CHAPTER 6

Preclinical imaging approaches for assessing the short- and long-term biodistribution of stem cells following intracardiac or intravenous administration to mice

6.1 Introduction

Regenerative medicine therapies have great potential to treat, and possibly cure, many different diseases and as such have gained considerable attention in recent years by scientists, medical professionals, and also the general public. Despite extensive research into the efficacy of various stem cell therapies for a wide range of health conditions, including but not limited to diabetes mellitus[400], neurodegenerative disorders[401], spinal cord injury[402], human immunodeficiency virus (HIV)[403] and diseases of the kidney[342,343,404], liver[405], heart[406], and eye[407], there are currently only three fully-approved stem cell therapies available to patients: 1) blood stem cells for the treatment of blood disorders/cancers, 2) s stem cells to produce grafts for burn victims, and 3) limbal stem cells for corneal replacement[88].

A major hurdle in the clinical translation of RMTs is a lack of robust safety data. While the efficacy of cell therapies is frequently investigated preclinically, the long-term safety of these therapies is often neglected. The primary concerns for the safe use of cell-based medicinal products in humans include[90-92]:

1. **Biodistribution** – it is important to know where the cells go once they are administered to the patient, for example if they remain in the intended organ in the case of local administration, or if they are able to migrate to the target organ following systemic administration. It is also vital to know if cells migrate to non-target organs.
2. **Tumourigenicity** – PSC-based therapies in particular have a risk of tumour formation if the cell product is contaminated with undifferentiated cells, or if the cells de-differentiate back to a pluripotent state.
3. **Immunogenicity** – allogeneic stem cells may evoke an immune response in the recipient, leading to graft rejection, or alternatively, transplanted cells may mount an immune response against the host, leading to graft-versus-host disease. Moreover, autologous stem cells may have the capacity to elicit an immune response following epigenetic changes during culture.

It is vitally important to carry out extensive safety studies prior to clinical translation of a therapy, as severe complications in clinical trials not only endanger lives, but also negatively impact public confidence in stem cell therapies and hinder the overall progress in the development of regenerative medicine therapies. Recently, the fatal outcomes of tracheal transplants, which were performed in humans without adequate preclinical assessment of safety or efficacy, were well-publicised in the media[408-410].

Traditionally, safety concerns would be investigated by sacrificing large numbers of animals at various time points, in order to analyse tissues *ex vivo*. This approach does not permit the responses of individual animals to be monitored over time, and may not allow for off-target effects to be detected in unexpected locations in the body. Alternatively, *in vivo* imaging is becoming more widely used in preclinical research. Administered cells can be tracked *in vivo* in a minimally invasive manner, allowing various parameters involving the biodistribution, tumourigenicity, and immunogenicity of cells to be monitored longitudinally in individual animals.

In order to track cells *in vivo*, they must first be labelled in a manner appropriate for the intended imaging modality and required length of tracking time. Generally, cell labels can be split into two categories: (1) Genetic reporters, which require the genetic modification of cells to introduce reporter genes encoding proteins which generate signals either constitutively or following interaction with a substrate[260,266,411]; (2) Cell probes, which are small particles such as paramagnetic agents, nanoparticles, radionuclides, or fluorophores, which are taken up by the cells[260,411,412]. Each cell label has unique characteristics which will be ideally suited to only one or possibly two imaging modalities. While cell probes often provide a high signal-to-noise ratio, they suffer from the disadvantage that it is the probe, and not the cell which is being imaged, thus raising the possibility for false-positive detection if the labelled cell dies and the released probes are taken up by host cells[412-414]. Moreover, the probes will be divided between daughter cells during cell division, leading to signal dilution in proliferating cells[411,412,414]. On the other hand, genetic reporters are only expressed while the cell is alive and the reporter gene is passed on to daughter cells, making them useful for long-term tracking and tumour monitoring[411,415-417].

The two cell labels employed for cell tracking in this chapter are the bioluminescence reporter gene, firefly luciferase, and SPIONs, which are cell probes used in MRI. There are several different luciferases used in bioluminescence imaging, including firefly luciferase (*Photinus pyralis*, FLuc), Renilla luciferase (*Renilla reniformis*, RLuc), and Gaussia luciferase (*Gaussia princeps*, GLuc)[265,266]. Genes encoding the transcription of luciferase enzymes are introduced into the genome of the cell of interest, which can then be administered to the animal and tracked *in vivo* with bioluminescence imaging. The luciferase enzyme catalyses the oxidation of an exogenously administered substrate, resulting in light production. In the case of FLuc, the substrate is luciferin, and the oxidation process also requires ATP, magnesium ions, and oxygen[265,266]. Thus, only living cells are able to produce light, making FLuc an ideal tracking agent for monitoring the survival of administered cells. Renilla and

Gaussia luciferases use the substrate coelenterazine, which does not require ATP, and thus permits imaging of extracellular biological processes[265,266]. FLuc is the most commonly used luciferase for BLI, largely due to its brightness, and the ease with which luciferin is handled. Luciferin can be administered intraperitoneally or subcutaneously, and has 'slow glow' kinetics, reaching peak light emission 10 - 15 minutes after administration and persisting in the body for some time, eventually being cleared around two hours after administration[266]. Coelenterazine, however, has very fast 'flash' kinetics and is rapidly cleared from the animal, and must be administered intravenously. This is technically more challenging, and limits imaging to just one animal at a time. Moreover, coelenterazine is prone to air oxidation, leading to non-specific background signals around the site of injection. Finally, each luciferase emits light at a characteristic wavelength: RLuc and GLuc emit blue/green light at around 480nm, which is readily absorbed by endogenous chromophores such as haemoglobin, fat, and melanin, thus reducing the amount of light that can reach the detector, whereas FLuc emits red-shifted light at 562nm, which is less absorbed by endogenous chromophores, thus resulting in stronger signal detection of FLuc[265,266].

SPIONs are clinically-available contrast agents that were originally developed to enhance the contrast of organs for MRI, but have since been applied to cell tracking purposes[412]. Paramagnetic and superparamagnetic materials only become magnetised when placed in an external magnetic field, where they then disturb the local magnetic field homogeneity[412]. Paramagnetic agents, such as gadolinium, contain a metal lanthanide complex which alters the T_1 (longitudinal) relaxation time of surrounding water protons, producing a bright, positive signal, whereas superparamagnetic agents contain an iron oxide core less than 20nm in diameter, and alter the T_2 (transverse) relaxation time, producing dark negative contrast (loss of signal)[292,412]. Protocols for synthesising SPIONs are now well-established, and as they are also highly sensitive, biocompatible, and exhibit higher paramagnetism than T_1 agents, SPIONs are now commonly used in preclinical cell tracking[292]. Cell labelling with SPIONs is very easy, simply requiring incubation in the cell culture media for 24 hours before administration to the animals[293].

The combination of firefly luciferase and SPIONs for cell tracking allows more information to be gained from a single animal. Luciferase cell tracking by BLI permits fast, whole body imaging and allows the assessment of cell survival, however the spatial resolution is poor, and inter- and intra-organ biodistribution cannot be assessed *in vivo*. SPION cell tracking by MRI provides images at higher spatial resolution with unlimited penetration depth, providing anatomical information on the inter- and intra-organ biodistribution of SPION-labelled cells,

however MRI takes longer to perform for each animal, and is not suited for long-term tracking. Therefore, by employing a multi-modal imaging approach using two complementary imaging strategies, more data can be obtained than is possible with a single modality: high resolution, organ-specific biodistribution of cells with MRI, and longitudinal whole body assessment of cell survival with BLI.

Various aspects of the safety of stem cells may differ not only with the stem cell type, but also with the route by which the cells are administered. The most common route of systemic administration of stem cell therapies in experimental animals is intravenous[404]. However, as discussed in Chapter 4, this injection route delivers cells via the venous circulation directly to the lungs where they become trapped as consequence of the pulmonary first-pass effect[111,134,267,349-351,371]. Despite the lack of renal engraftment of administered cells following IV administration, preclinical efficacy studies largely report therapeutic effects of cell therapies for ameliorating kidney injury[89,105,110,111,139,145,352,353], suggesting a paracrine or endocrine role in efficacy. However, it is possible that delivery of cells to the kidneys may result in improved efficacy superior to that achieved by paracrine mechanisms alone. In such circumstances, it would be necessary to deliver cells to the kidney, and while direct administration to the renal artery is a commonly used method in rats and other large mammals[111,127,418], this is not feasible in mice due to the small diameter of the renal artery. Alternatively, administration into the carotid artery is sometimes reported in mice[267], however this method is invasive as it requires surgery. However, intracardiac (IC) administration provides a viable, less-invasive method of delivering cells to the kidneys in experimental mouse models. By administering cells directly to the left ventricle of the heart, cells will travel through the arterial circulation, passing through all organs of the body, including the kidneys, before entering the venous circulation and reaching the lungs. The IC administration route therefore permits cells to be delivered to the kidneys in mice, without the use of invasive surgical techniques. However, the IC administration route also delivers cells to all other organs of the body, and as such may pose a higher safety risk compared with IV administration which restricts cells to just one organ, the lungs. It is necessary to carry out comprehensive preclinical safety assessments using the most clinically-relevant administration route. While intracardiac administration is not intended to be used in patients, it may model the clinical scenario more closely if cells are administered arterially in patients.

This chapter utilises *in vivo* imaging strategies in order to address the following aims:

1. Optimise an ultrasound-guided method of intracardiac cell administration in order to facilitate cell delivery to the kidneys
2. Fully characterise cell delivery to the kidneys following intracardiac administration and compare with intravenous administration
3. Compare the effect of administration route on the long-term safety of cell administration

6.2 Experimental Design

Optimising Intracardiac Cell Administration

Three different methods of performing intracardiac cell administration (of 5.0 $x10^5$ $ZsGreen^+$/$luciferase^+$ mKSCs in 100µl) were trialled in BALB/c mice: via the diaphragm, via the intercostal space, and ultrasound-guided. Success was assessed by BLI of the $luciferase^+$ cells to determine if cells were correctly administered to the left ventricle and by evaluating the well-being of animals following IC injection.

Comparing the immediate biodistribution of cells following IV and IC administration routes

The biodistribution of $ZsGreen^+$/$luciferase^+$ mouse- and human-derived cells (mMSC, mKSC, hMSC, hKC) were each compared following IV and IC administration to BALB/c mice by BLI. Mice were culled on the day of cell administration and organs imaged *ex vivo*.

Evaluating cell delivery to the kidney

Increasing doses of 1.0 $x10^5$ – 1.0 $x10^6$ $ZsGreen^+$/$luciferase^+$ mKSCs were administered to BALB/c mice (1.0 $x10^5$, *n = 2*; 2.0 $x10^5$, *n = 3*; 4.0 $x10^5$, *n = 3*; 5.0 $x10^5$, *n = 6*; 6.0 $x10^5$, *n = 5*; and 1.0 $x10^6$, *n = 3*). Biodistribution of cells was assessed *in vivo* by BLI, and *ex vivo* by BLI of organs and analysis of ZsGreen reporter gene expression by fluorescence microscopy of frozen kidney sections. *Ex vivo* analyses were performed on mice sacrificed on the day of cell administration.

MR imaging of cell biodistribution to the kidneys and brain

1.0 $x10^6$ $ZsGreen^+$/$luciferase^+$/$SPION^+$ mMSCs were administered to BALB/c SCID mice (IC, *n = 2*; IV, *n = 2*). BLI and MR imaging of the abdomen (kidneys) and brain were performed at baseline and immediately after cell administration. Mice were culled after imaging and organs were imaged *ex vivo* in both modalities.

1.0 x10^6 ZsGreen$^+$/luciferase$^+$/SPION$^+$ mMSCs were administered to BALB/c SCID mice (IC, *n = 5*). BLI and MR imaging of the abdomen were performed at baseline (MRI only), and 0h, 24h, 48h after cell administration. At least one mouse was culled at each time point for *ex vivo* imaging and histological evaluation of tissues.

Long-Term Bioluminescence Imaging

1.0 x10^6 ZsGreen$^+$/luciferase$^+$ mMSCs were administered to BALB/c SCID mice (IV, *n = 3*; or IC, *n = 5*), and to immunocompetent BALB/c, FVB, and MF1 mice (IC, *n = 4*). The biodistribution of the cells was monitored regularly by BLI up to day 30. At day 30, mice were sacrificed, and organs and any identifiable tumours were imaged *ex vivo*.

To facilitate the comparison of bioluminescence images displaying different signal intensity scales throughout the longitudinal study, different coloured frames have been used to indicate the different scale ranges required to display bioluminescence signals of different intensities (Table 6.1).

Table 6.1: Table of different bioluminescence scales used.

Scale (p/s/cm^2/sr)	Use	Frame colour
1.0 x10^4 – 1.0 x10^5	Lower scale, used to display weaker signals	Blue
1.0 x10^5 – 1.0 x10^6	Standard scale required for signals on the day of administration	Green
1.0 x10^7 – 1.0 x10^8	Higher scale, used to display stronger signals	Orange
1.0 x10^8 – 1.0 x10^9	Very high scale, used to display very strong signals	Red

6.3 Results

6.3.1 Optimising Intracardiac Cell Administration

In order to facilitate cell delivery to the kidneys, three methods of intracardiac cell administration were trialled. The first method attempted to 'blindly' administer cells into the left ventricle, via the diaphragm in a similar manner to the widely used cardiac puncture for terminal blood collection. This method was found to be highly inaccurate, as it was impossible to determine whether the needle was in the heart before cells were administered. The second method, described by Campbell *et al.* (2012), delivered cells to the heart by measuring the approximate location of the left ventricle, and administering cells via the intercostal space[419]. This method was somewhat more successful, as the pulsatile entrance of blood in to the syringe indicated when the needle had penetrated the heart, but was still

a ‘blind’ method, and was associated with a high degree of failure, both in terms of mis-injections and mouse mortality.

The third method was an ultrasound-guided method[420,421], where the left ventricle of the heart was directly visualised by ultrasound (Fig. 2.4), and correct placement of the needle could be confirmed prior to administration of the cells (Fig. 2.4G). This method was found to be superior, and led to the completion of over 150 IC injections with a success rate of over 90%, where ‘success’ was defined as the presence of a typical distribution of bioluminescence signal over the body of the mouse, with no signs of mis-injection into the right ventricle or chest cavity (Fig. 2.5), and the absence of side-effects to the well-being of the mouse. A detailed description of the fully optimised ultrasound-guided method is provided in Chapter 2 (General Methods).

It was possible for adverse effects to occur following IC administration of cells. The least severe side effect was a loss of balance which resulted in mice leaning to one side (usually the left) and walking in circles for some time, however this was recoverable and generally wore off after 30 minutes to one hour. More severe side effects included:

(i) Hind limb paralysis, where the mouse lost complete function of the hind legs, and function generally did not return. This therefore negatively affected the welfare of the mouse, but was not lethal.

(ii) ‘Spinning’, where the mouse would twist and spin very violently. Mice never recovered from this behaviour and so had to be sacrificed immediately if ‘spinning’ was observed.

(iii) Death.

Generally, adverse effects were either observed immediately after the mice woke from anaesthesia, or developed over the first hour. While it was difficult to know the exact cause of adverse effects and death, the most likely causes were embolism resulting from clumped cells lodged in vessels, or damage to the heart during the injection, resulting in fatal blood loss. Careful cell preparation to avoid cell clumping, and a steady hand during the injection to avoid damaging the heart, appeared to improve the outcome. It was found that increasing the volume administered to 200µl, and thus decreasing the density of the cell solution, did not have any effect on the outcome with regards to adverse effects, and as such further cell injections were performed with the smaller volume of 100µl.

6.3.2 Comparing the Biodistribution of Mouse and Human Cells Following IV and IC Administration Routes

To compare the biodistribution of cells following different administration routes, both mouse and human mesenchymal/stromal and kidney-derived cells (ranging in diameter from 15 – 25 µm) were administered to healthy mice either IC, by using ultrasound-guidance to inject into the left ventricle of the heart, or IV, by injecting via the tail vein. All cells had previously been transduced to genetically express the ZsGreen/luciferase reporter gene construct, allowing cell tracking *in vivo* by bioluminescence imaging of luciferase, and *ex vivo* by fluorescence microscopy of ZsGreen. Invariably, IV administration of cells resulted in bioluminescence signals restricted to the lungs (Fig. 6.1A), regardless of cell type or size. In contrast, IC administration resulted in a whole-body distribution of bioluminescence signals, with stronger signals in the head and kidney regions of the animals. This pattern of signal distribution was consistent between all cell types investigated (Fig. 6.1A). *Ex vivo* imaging of organs within one hour of cell administration confirmed that bioluminescence signals were only detected in the lungs of IV-administered mice, but could be detected in the lungs, kidneys, heart, liver, spleen, and brain of IC-administered mice (Fig. 6.1B). Quantification of organ-specific bioluminescence signals *ex vivo* confirmed that following IV administration, on average 98.51% of the signal (SE: 0.58, *n = 3*) was found in the lungs, while following IC administration, the bioluminescent signal was found in the lungs at a lower percentage (mean: 62.24%, SE: 6.33), and also in the kidneys (mean: 11.73%, SE: 2.52), heart (mean: 1.66% SE: 0.45), liver (mean: 8.53%, SE: 1.44), spleen (mean: 7.17, SE: 1.01), and brain (mean: 5.96%, SE: 0.91; *n = 3;* Fig. 6.1C). Histological examination of frozen sections of the same organs under fluorescence microscopy confirmed the presence of $ZsGreen^+$ cells in all assessed organs after IC administration, but only in the lungs after IV (Fig. 6.2).

6.3.3 Quantification of Labelled Cells in the Kidneys using Bioluminescence and Histology

Next, a detailed analysis of the cell biodistribution within the kidneys was performed histologically. $ZsGreen^+$ mKSCs were only found in the glomeruli; none were located in tubules or the interstitium (Fig. 6.2, 6.3A). To determine whether the cell dose affected the number of cells found in the kidney, the percentage of glomeruli that contained $ZsGreen^+$ cells was calculated in both coronal and axial sections of kidneys following IC administration of increasing doses of mKSCs: 1.0 $x10^5$, *n = 2*; 2.0 $x10^5$, *n = 3*; 4.0 $x10^5$, *n = 3*; 5.0 $x10^5$, *n = 6*; and 6.0 $x10^5$, *n = 5* (Fig. 6.3B).

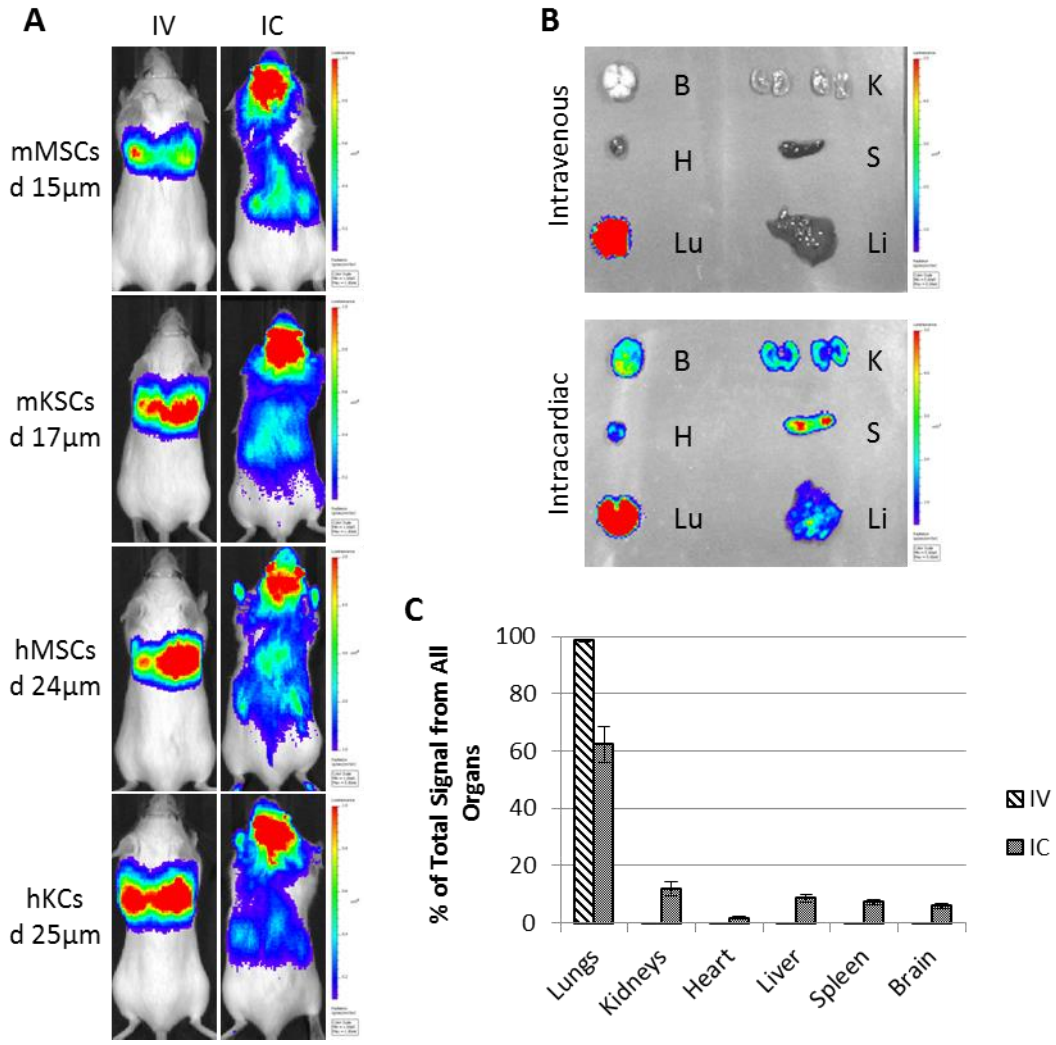

Figure 6.1: Biodistribution of cells following intravenous or intracardiac administration of various cell types. (**A**) Bioluminescence imaging showed that regardless of the cell type or size, cells were always confined within the lungs after intravenous (IV) administration, but distributed throughout the body after intracardiac (IC) administration. From top: 1M mMSCs, average diameter (d) 15 µm, BLI scale 1.0 x10^5 – 1.0 x10^6 p/s/cm^2/sr; 1M mKSCs, d = 17 µm, BLI scale 1.5 x10^5 – 1.5 x10^6 p/s/cm^2/sr; 1M hMSCs, d = 24 µm, BLI scale 1.0 x10^6 – 5.0 x10^6 p/s/cm^2/sr; 300K hKCs, d = 25 µm, BLI scale 1.0 x10^5 – 1.0 x10^6 p/s/cm^2/sr. (**B**) *Ex vivo* bioluminescence imaging of organs within 1h after administration of mKSCs in (**A**) confirmed the *in vivo* cell biodistribution. Clockwise from top right: kidneys (K), spleen (S), liver (Li), lungs (Lu), heart (H), brain (B). BLI scale: IV, 5.0 x10^5 – 5.0 x10^6 p/s/cm^2/sr; IC, 5.0 x10^4 – 5.0 x10^5 p/s/cm^2/sr. (**C**) Quantification of the bioluminescence signal of organs *ex vivo.* Bars represent the mean signal expressed per organ as a percentage of the total flux from all organs (*n* = 3 each group) and error bars represent standard error.

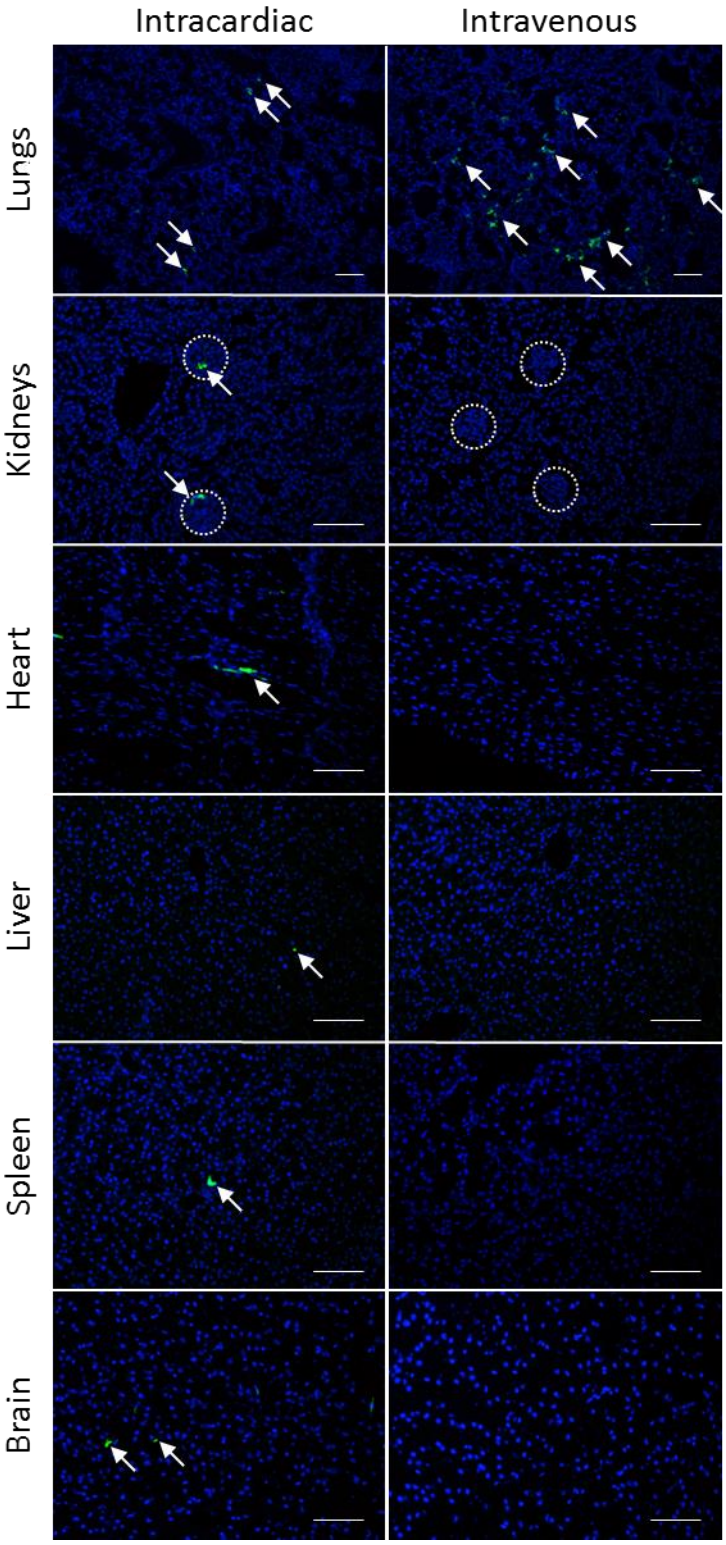

Figure 6.2: Tissue biodistribution of mKSCs following intravenous or intracardiac administration. Fluorescence microscopy confirmed the presence of ZsGreen^{+} mKSCs in organs. After IC administration, cells could be detected in the lungs (arrows), the glomeruli in kidneys, heart, liver, spleen, and brain (arrows). After IV administration, cells were only present in the lungs (arrows), and were absent from all other organs. Glomeruli within kidneys are delineated with a dashed line. Scale bars = 100µm.

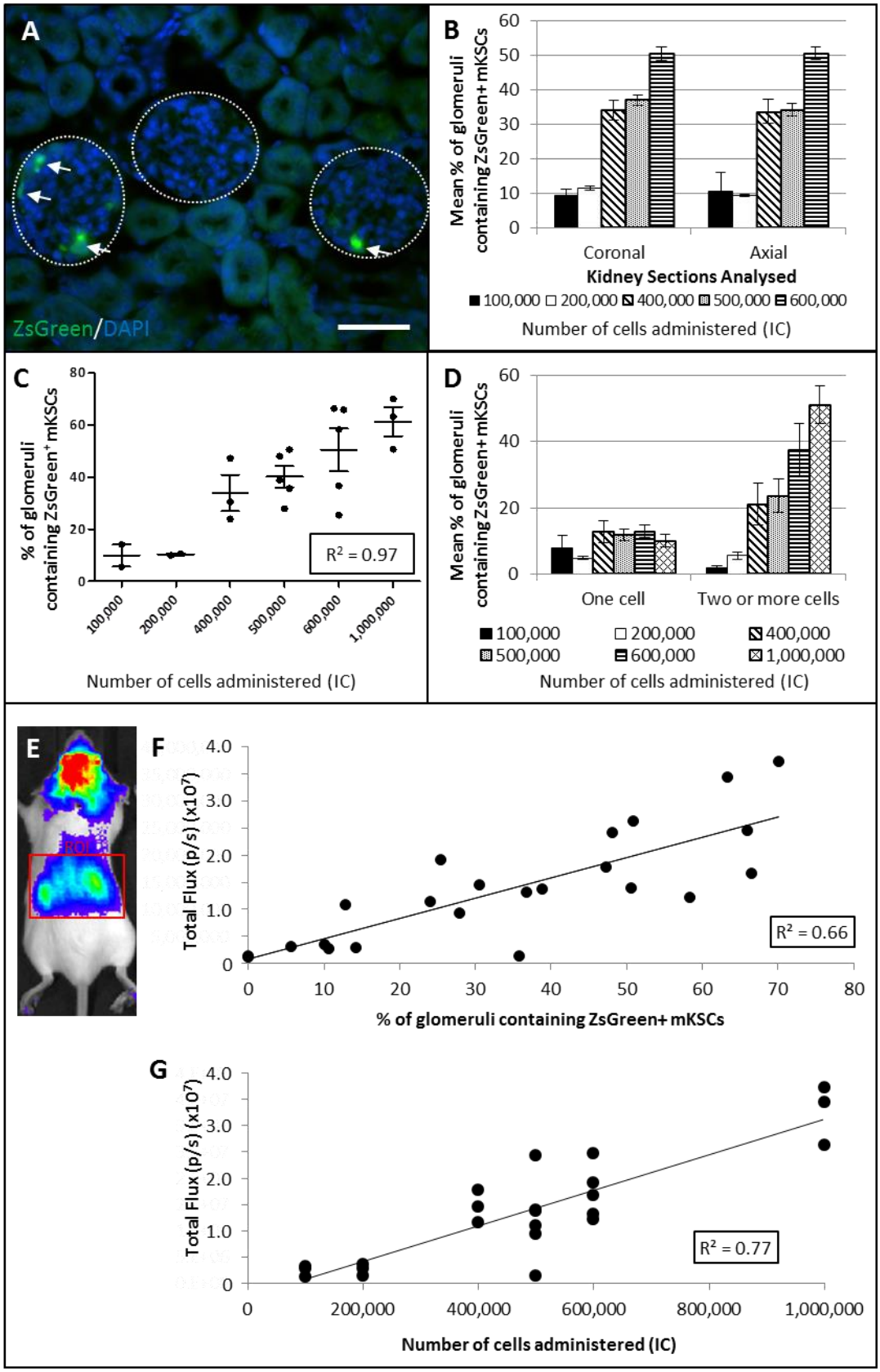
A
ZsGreen/DAPI
B
Mean % of glomeruli containing ZsGreen+ mKSCs
60
50
40
30
20
10
0
Coronal
Axial
Kidney Sections Analysed
100,000 200,000 400,000 500,000 600,000
Number of cells administered (IC)
C
% of glomeruli containing ZsGreen+ mKSCs
80
60
40
20
0
R² = 0.97
100,000
200,000
400,000
500,000
600,000
1,000,000
Number of cells administered (IC)
D
Mean % of glomeruli containing ZsGreen+ mKSCs
60
40
20
0
One cell
Two or more cells
100,000
200,000
400,000
500,000
600,000
1,000,000
Number of cells administered (IC)
E
ROI
F
Total Flux (p/s) (x10⁷)
4.0
3.0
2.0
1.0
0
R² = 0.66
0
10
20
30
40
50
60
70
80
% of glomeruli containing ZsGreen+ mKSCs
G
Total Flux (p/s) (x10⁷)
4.0
3.0
2.0
1.0
0
R² = 0.77
0
200,000
400,000
600,000
800,000
1,000,000
Number of cells administered (IC)

← Figure 6.3: Quantification of ZsGreen$^+$ mKSCs in kidneys and correlation with BLI. (**A**) ZsGreen$^+$ mKSCs localised exclusively to the glomeruli (dashed circles) of the kidneys after IC administration. Scale bar represents 50μm. (**B-C**) Quantification of ZsGreen$^+$ mKSCs within the kidneys showed similar distribution of glomeruli containing cells in both the coronal or axial sections (**B**), and thus indicated a homogenous spread of cells throughout the kidney. (**C**) There was a strong correlation (R^2 = 0.97) between the number of administered cells and the % of glomeruli containing ZsGreen$^+$ mKSCs. (**D**) When 200,000 or fewer cells were administered, most cell-containing glomeruli had only one cell, however when 400,000 or more cells were administered, most cell-containing glomeruli contained multiple cells. (**E**) Region of interest (ROI) drawn around the kidneys of an animal injected IC with ZsGreen$^+$ mKSCs. The total flux (photons/second) for the ROI was quantified for each animal and correlated with the percentage of glomeruli containing cells (**F**) and the number of cells administered to the animal (**G**).

The analysis of an average of 119 glomeruli in coronal sections, and 70 glomeruli in axial sections, showed that the percentage of glomeruli containing ZsGreen$^+$ mKSCs increased as the cell dose increased, and that there was no difference in the percentage of glomeruli containing ZsGreen$^+$ mKSCs in either orientation, suggesting a homogenous spread of administered cells throughout the kidney (paired t-test, axial vs coronal: 1.0 x10^5, p = 0.704; 2.0 x10^5, p = 0.484; 4.0 x10^5, p = 0.974; 5.0 x10^5, p = 0.615; 6.0 x10^5, p = 0.954). Importantly, the analysis demonstrated a strong correlation (R^2 = 0.97) between the number of cells administered and the percentage of glomeruli containing ZsGreen$^+$ mKSCs following IC administration (Fig. 6.3C). In addition, quantification showed that after IC administration of 1.0 x10^6 mKSCs, on average 61% of glomeruli contained ZsGreen$^+$ mKSCs (SE: 5.64, *n = 3*), in comparison to 0% after IV administration (SE: 0.00, *n = 3*) (data not shown).

Further, the relationship between the number of cells administered IC to the animal, and the number of cells identified within the glomeruli, was assessed by categorising cell-containing glomeruli as having one cell, or two or more cells. This revealed that when 2.0 x10^5 or fewer cells were administered, the percentage of glomeruli containing one cell was equal to or less than the percentage containing multiple cells. However, when doses of 4.0 x10^5 or more cells were administered, the majority of cell-containing glomeruli had multiple cells, and the percentage of glomeruli that contained two or more cells increased as cell dose increased, while the percentage of glomeruli that contained just one cell remained at around 10% for all cell doses (Fig. 6.3D).

Finally, to determine whether there was a relationship between the *in vivo* bioluminescence imaging of luciferase$^+$ mKSCs, and the percentage of glomeruli that contained ZsGreen$^+$ cells, an ROI was drawn around the region of the kidneys (Fig. 6.3E), and the bioluminescence signal was correlated with (1) the percentage of glomeruli that contained ZsGreen$^+$ cells for

each mouse (Fig 6.3F), and (2) with the number of cells administered IC to the mouse (Fig. 6.3G). These analyses revealed a moderate positive correlation (R^2 = 0.66 and 0.77 respectively) for both relationships.

6.3.4 MR Imaging to Track Cell Biodistribution Within the Kidneys and Brain at Higher Spatial Resolution

BLI of luciferase$^+$ cells indicated a whole-body biodistribution of cells following IC administration, however the poor spatial resolution of BLI meant that animals had to be sacrificed and organs dissected and imaged *ex vivo* in order for organ-specific signals to be evaluated. MRI has a much higher spatial resolution than BLI, in addition to unlimited penetration depth, enabling organ-specific imaging. To assess the intra-organ biodistribution, ZsGreen$^+$/luciferase$^+$/SPION$^+$ mMSCs were administered IV or IC, and imaged *in vivo* with BLI and MRI. Additionally, MRI scans of the brain were performed to assess whether BLI signals in the head resulted from cells within the brain, or simply the meninges or blood vessels surrounding the brain.

BLI revealed typical cell biodistribution following IV and IC administration respectively, with cells restricted to the lungs following IV administration, and dispersed throughout the whole body following IC administration (Fig. 6.4A). FLASH T_2* MR imaging revealed hypointensive signals in the cortex of the kidneys, and homogenously throughout the brains of mice that received an IC administration of SPION-labelled cells (Fig. 6.4B). These hypointensive signals were not present in baseline images of the kidneys and brain, indicating that they resulted from the SPION-labelled cells. In contrast, hypointensive signals were not detected in the kidneys or brain of IV-injected mice, and post-administration images were comparable to baseline images (Fig. 6.4B), confirming that IV-administration does not deliver cells to the kidneys or the brain.

Ex vivo MR imaging of organs could be performed at higher resolution than that *in vivo*, and confirmed the presence of hypointensive signals in the renal cortex and throughout the brain of IC-injected mice, but not IV-injected mice (Fig. 6.4C). Isolectin staining of the blood vessels in frozen brain sections showed that ZsGreen$^+$ mMSCs were restricted to the lumen of blood vessels, and were never detected in the parenchyma of the brain (Fig. 6.4D), suggesting that the cells were physically trapped in capillaries, and did not cross the blood brain barrier.

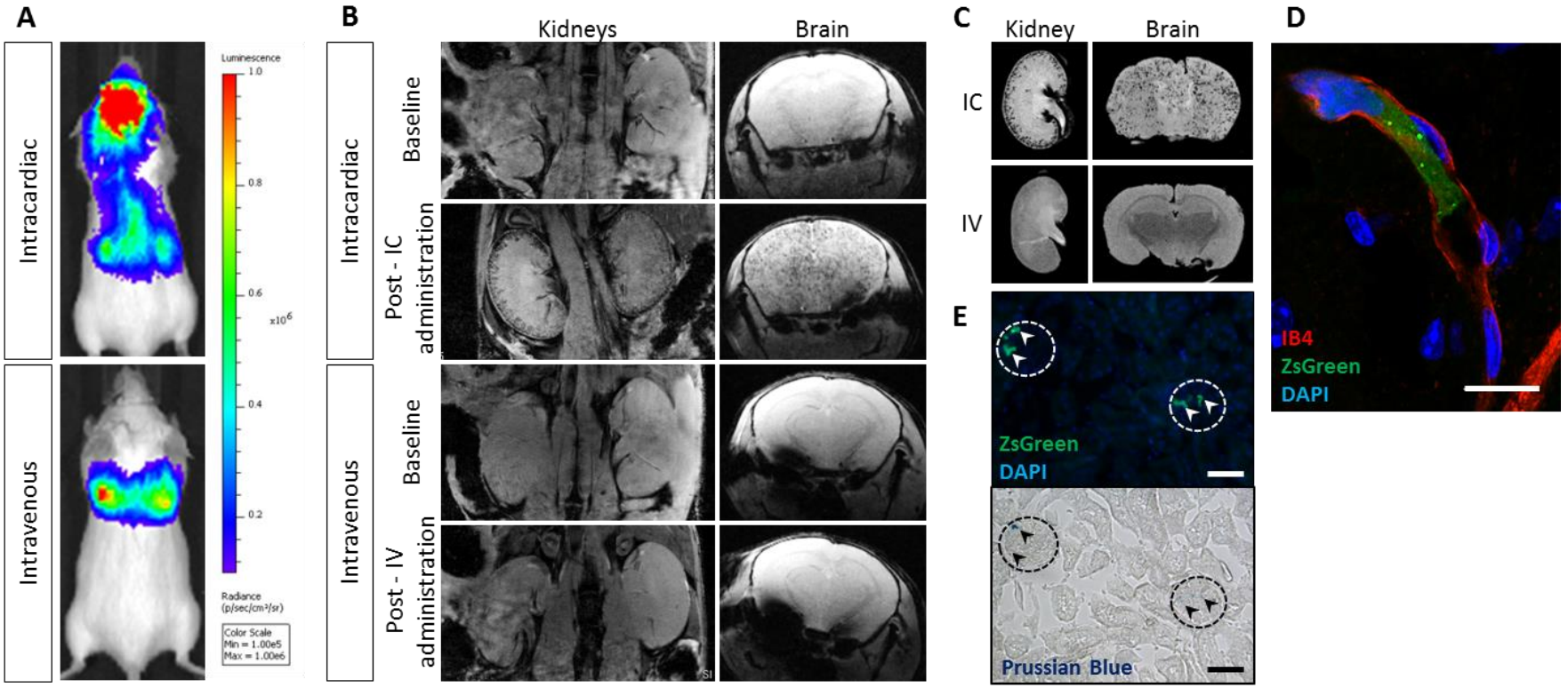

Figure 6.4: *in vivo* and *ex vivo* tracking of ZsGreen⁺/Luciferase⁺/SPION⁺ mMSCs in the kidneys and brain following IC or IV administration. (**A**) Representative *in vivo* bioluminescence images of mice following IC (top) or IV (bottom) administration of $1x10^6$ mMSCs. BLI scale $1.0 x10^5 – 1.0 x10^6$ p/s/cm^2/sr. (**B**) *in vivo* FLASH T_2* MR imaging of the kidneys and brain at baseline, and following IC or IV administration of mMSCs, showing hypointensive signals in the cortex of the kidney and throughout the brain following IC, but not IV administration of SPION⁺ mMSCs. (**C**) FLASH T_2* MR imaging of the dissected kidney and brain could be performed at higher resolution. (**D**) isolectin staining of blood vessels in the brain, showing a ZsGreen⁺ cell within the lumen of a blood vessel in the brain. Scale bar represents 50µm. (**E**) Histological tracking of cells by fluorescence imaging of ZsGreen reporter gene (top) and Prussian Blue-staining of SPIONs (bottom). Dashed circles delineate glomeruli, and the scale bar represents 50µm.

Histological tracking of the ZsGreen reporter gene by fluorescence microscopy, and the SPIONs by Prussian Blue staining of iron, showed that labelled cells were located in the glomeruli within kidneys. Co-localisation of ZsGreen and Prussian Blue signals confirmed that the SPIONs were located within the ZsGreen$^+$ mMSCs, and that *in vivo* hypointensive signals were unlikely to result from false-positive detection of free SPIONs at this time point (Fig. 6.4E).

6.3.5 Longitudinal MRI/BLI Tracking of Labelled Cells

Nanoparticle-based cell tracking relies on the detection of the cell label, not the cell itself, and false positive cell tracking can occur if the cell label is released from the cell. Bi-modal imaging using BLI to detect live cells at low spatial resolution, and MRI to detect SPION-labelled cells at high spatial resolution, can give more confidence in nanoparticle-based cell tracking results. To assess the relationship between the luciferase and the SPION signals in the kidney over time, mice were imaged with BLI and MRI at 0h, 24h, and 48h following IC administration of ZsGreen$^+$/luciferase$^+$/SPION$^+$ mMSCs.

MRI of the kidneys of IC-injected mice revealed extensive hypointensive signals in the cortex at 0h, fewer hypointensive signals at 24h, and by 48h the kidneys were comparable to baseline images, indicating that SPION-labelled cells were being cleared from the kidneys. BLI of mice at the same time points showed a decrease in overall bioluminescence signal over time, indicating that cells were dying. Fluorescence microscopy of ZsGreen$^+$ cells in frozen kidney tissue supported *in vivo* MRI and BLI, as the number of ZsGreen$^+$ mMSCs in the glomeruli decreased over time (Fig. 6.5A).

Changes in the overall presence of hypointensive signals in MR images were quantified by calculating the T_2* relaxation time in the cortex of the kidney, thus giving an indication of the relative quantity of SPION-labelled cells present at each time point. Hypointensive signals are associated with shorter T_2* relaxation times, so the shorter the relaxation time, the greater the number of SPIONs present. The T_2* relaxation time in the cortex of the kidney was statistically significantly lower on the day of cell administration (Fig. 6.5B; 0h, mean = 7.98 ms, SE = 0.29) than at baseline (mean = 14.56 ms, SE = 0.32; One-way ANOVA, $p < 0.001$, see Supplementary Table S6.1A for Tukey pairwise comparisons). The T_2* relaxation time then increased towards baseline levels at 24h (mean = 12.57 ms, SE = 0.50) and 48h (mean 13.19 ms, SE = 0.23), and by 48h the difference compared with baseline levels was no longer statistically significant (Supplementary Table S6.1A).

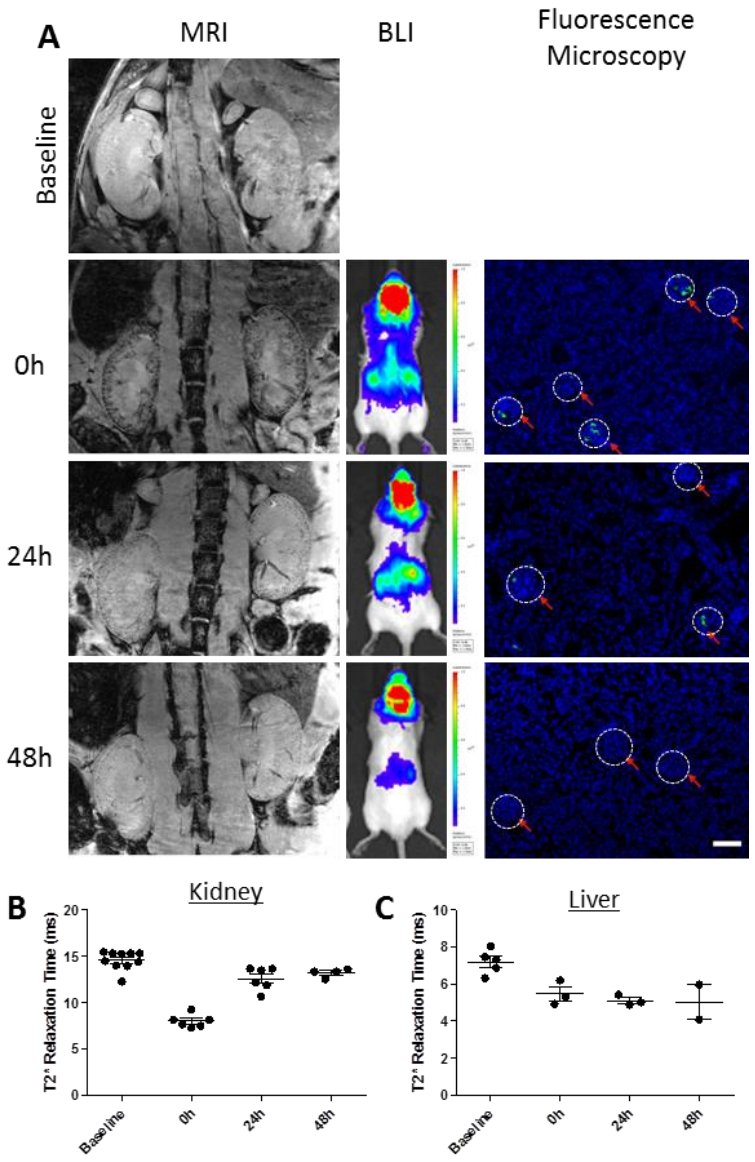

Figure 6.5: Multi-modal imaging of ZsGreen$^+$/luciferase$^+$/SPION$^+$ mMSCs in the kidneys for 48h following IC administration. (**A**) Tracking mMSCs in the kidneys of mice via MRI (left), BLI (middle), and fluorescence microscopy (right). MR imaging of the kidneys showed hypointensive signals in the cortex of the kidney immediately following IC administration of ZsGreen$^+$/luciferase$^+$/SPION$^+$ mMSCs (0h). The amount of hypointensive signal decreased at 24h, and the kidneys were comparable to baseline by 48h, suggesting that the SPION-labelled cells were cleared from the kidneys within this time. This clearance corresponded with BLI data, where the bioluminescence signals in the region of the kidneys decreased over time. The *in vivo* imaging data was confirmed with fluorescence microscopy of fewer ZsGreen$^+$ mKSCs in glomeruli over time. BLI scale: 1.0 x10^5 – 1.0 x10^6 p/s/cm^2/sr. Microscopy scale bar represents 50µm. (**B-C**) Quantification of T_2* relaxation time in the kidney (**B**) and liver (**C**). T_2* relaxation time decreased in the cortex of the kidney at 0h, due to the presence of SPION$^+$ mMSCs. The T_2* relaxation time then increased towards baseline levels at 24h and 48h, as SPION-labelled cells were cleared from the kidney. In the liver, there was a gradual decrease in T_2* relaxation time over time, indicating the SPION-labelled cells may have accumulated in the liver.

Incidentally, due to the size of the region imaged, the liver was also included when imaging the abdomen for cell tracking in the kidneys. Although there were no obvious differences in the visual appearance of the liver following IC-administration of SPION-labelled cells (data not shown), quantification of the T_2* relaxation time revealed a subtle but significant decrease in relaxation time between baseline through to 48h following cell administration (Fig. 6.5C; baseline, mean = 7.19 ms, SE = 0.29; 0h, mean = 5.48 ms, SE = 0.38; 24h, mean = 5.10 ms, SE = 0.16; 48h, mean = 5.02 ms, SE = 0.94; One-way ANOVA, p = 0.006, see Supplementary Table S6.1B for Tukey pairwise comparisons) and suggested that SPION-labelled cells may be cleared from the kidneys into the liver.

6.3.7 Comparison of Administration Route on the Long-Term Biodistribution of mMSCs

The long-term distribution of mMSCs following IV or IC administration was then assessed by BLI; (1) to determine whether entrapped cells were able to leave the lungs following IV administration, and (2) to determine whether cells persisted in any organs following IC administration. 1.0 x10^6 mMSCs, were administered IV or IC to immunocompromised mice (BALB/c SCID), and mice were monitored via BLI for 30 days.

Unsurprisingly, cells became trapped in the lungs following IV-administration of mMSCs. Within 6h of administration the bioluminescence signal decreased, suggesting that the cells had started to die, and by 24h and for the remainder of the 30-day study, signals in two out of three mice could no longer be detected with the original signal scale used at 0h (1.0 x10^5 – 1.0 x10^6 p/s/cm^2/sr, green frame; Fig. 6.6A). In one mouse, weak signals in the lungs were detectable from day 14 when the signal scale was lowered (1.0 x10^4 – 1.0 x10^5 p/s/cm^2/sr, blue frame; Fig. 6.6B), and these signals continued to increase at a slow rate for the remainder of the study, becoming detectable using the original scale by day 30 (1.0 x10^5 – 1.0 x10^6 p/s/cm^2/sr, green frame; Fig. 6.6C). In all three IV-administered mice, small foci of bioluminescence signal could be detected in the lungs *ex vivo*, but tumours were not visible by eye and could not be detected histologically, suggesting very small numbers of mMSCs were present. Changes in the bioluminescence signal over time were quantified by drawing an ROI around the body of each mouse, and this confirmed the observations from the images: that signals decreased rapidly within 6h, and remained very close to background levels for much of the study; increasing only towards the end of the 30-day experiment, with one mouse expressing much stronger signals than the other two (Fig 6.6E).

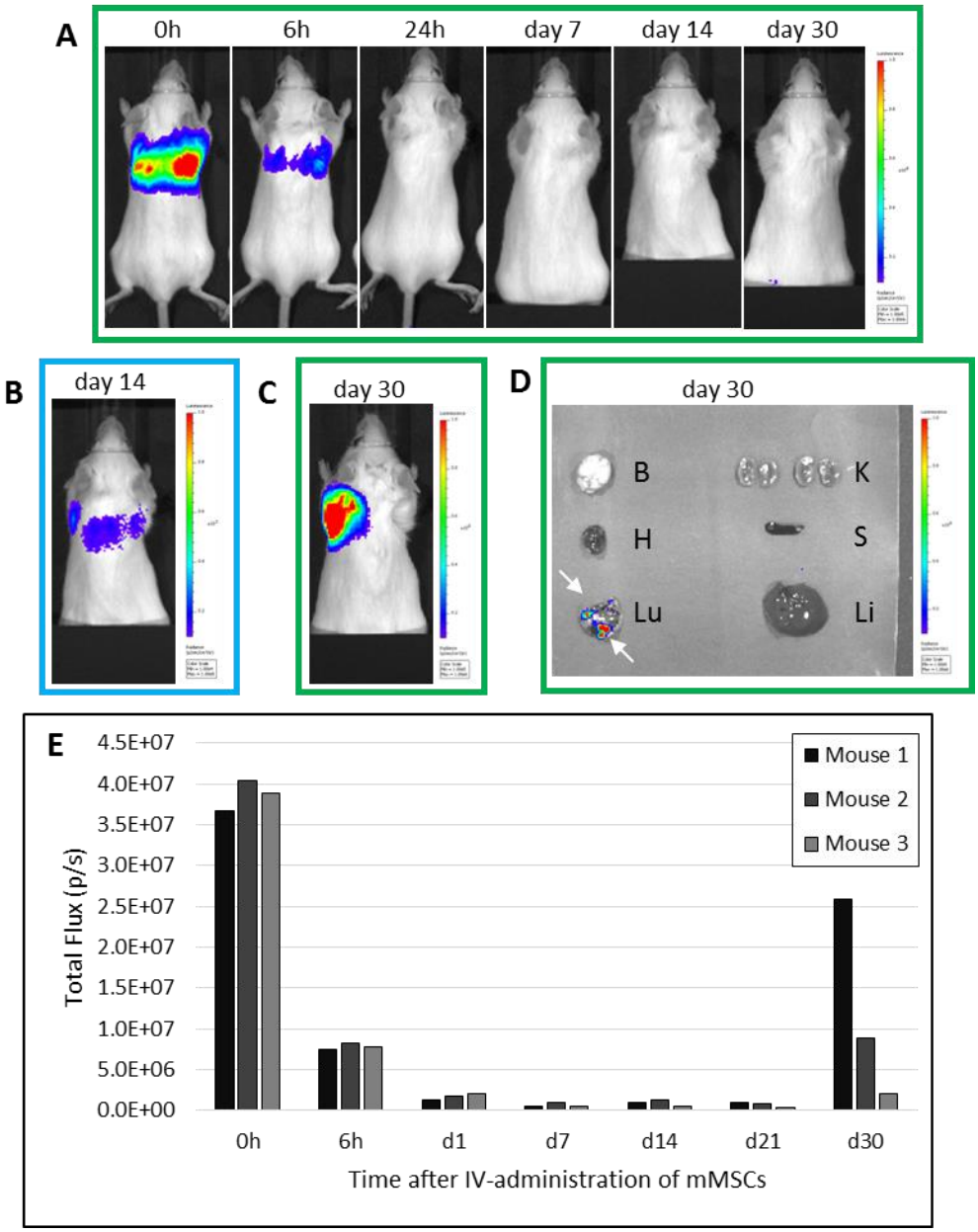

Figure 6.6: Longitudinal cell tracking following IV-administration of mMSCs. (**A**) Representative bioluminescence images of a mouse administered with mMSC (IV) (BLI scale 1.0 x10^5 – 1.0 x10^6 p/s/cm^2/sr, green frame) showed that cells were initially located in the lungs, but most of the signal was lost by 6h, indicating the majority of the cells had died, and in two out of three mice, the *in vivo* signal did not return by day 30. (**B**) Weaker signals could be displayed with a lower scale (BLI scale 1.0 x10^4 – 1.0 x10^5 p/s/cm^2/sr, blue frame), showing that cells began to proliferate in the lungs from d14, and continued to grow at a slow rate until the end of the experiment (day 30), but the signals could only be visualised using the original scale (green frame) in one mouse (**C**). (**D**) *Ex vivo* organ imaging showed small foci of bioluminescence in the lungs, but no solid tumours were observable by eye, and could not be detected by microscopy. (**E**) Quantification of the bioluminescence signal from a region of interest drawn around the whole body of the mouse. The signals decreased in all mice between 0 - 6h, and were close to background levels by day 1. The signals had started to increase in all mice by day 30, but did not reach the starting signal level at 0h in any mouse. Each bar represents an individual mouse (*n = 3*).

A typical whole-body biodistribution of cells was observed following IC-administration of mMSCs and, similar to the IV-administration, the signals decreased within 6h of administration, and were almost completely absent by 24h using the original signal scale (1.0 $x10^5$ – 1.0 $x10^6$ p/s/cm^2/sr, green frame; Fig 6.7A). Lowering the signal scale to 1.0 $x10^4$ – 1.0 $x10^5$ p/s/cm^2/sr (blue frame) showed that signals began to increase in the bodies of all IC-injected mice from day 7, forming small foci of bioluminescence around the hindquarters (Fig. 6.7B). Signals then rapidly grew over the remainder of the study, with a mean fold-change from day 0 of 680-fold (Table 6.2), becoming detectable using the original scale by day 14 (Fig. 6.7A), and by the end of the experiment requiring a signal scale that was two orders of magnitude greater (1.0 $x10^7$ – 1.0 $x10^8$ p/s/cm^2/sr, orange frame) than the original scale (Fig. 6.7C). The development of bioluminescence signals was highly comparable in all IC-injected mice with respect to timing, location, and rate of increase. *Ex vivo* imaging of organs revealed small foci of bioluminescence in some organs, however this was less consistent between mice, with some mice having signals in the kidneys, heart, liver, or lungs, but no mouse had signals in all four organs (Fig. 6.7D). Bioluminescence signals were never observed in the spleen or brain. Note that the intensity of bioluminescence foci in the organs of IC-injected mice was weaker than those of the IV-injected mice, requiring a lower scale to display the signals. Quantification of the bioluminescence signals again confirmed the observations from the images, and showed that all mice were comparable in the timing of the onset of the increase in bioluminescence signal (Fig. 6.7E). Quantification is only shown up to day 14 in Fig. 6.7E, as the signal increase thereafter was so great that the signals from earlier time points would no longer be visible on the graph. Comparison of the

Figure 6.7 ➔ : Longitudinal cell tracking following IC-administration of mMSCs. (**A**) Representative bioluminescence images of a mouse administered with mMSC (IC) (BLI scale 1.0 $x10^5$ – 1.0 $x10^6$ p/s/cm^2/sr, green frame) showed a typical whole-body distribution of cells at 0h, but cells started to die within 6h and were almost completely absent by 24h. Bioluminescence signals then started to increase, forming foci in the hindquarters of the mice, and weak bioluminescence signals were detectable from day 7 (**B**; BLI scale 1.0 $x10^4$ – 1.0 $x10^5$ p/s/cm^2/sr, blue frame). Bioluminescence signals continued to increase throughout the experiment, requiring a very large scale (1.0 $x10^6$ – 1.0 $x10^7$ p/s/cm^2/sr, orange frame) to display strong signals by the end of the experiment (**C**). *Ex vivo* imaging of organs revealed weak foci of bioluminescence signal in some organs, but no solid tumours were observable by eye, and could not be detected by microscopy. (**E**) Quantification of the bioluminescence signal from a region of interest drawn around the whole body of the mouse. The signals decreased in all mice initially, but were clearly increasing by day 14. Each bar represents an individual mouse (*n = 5*). (**F**) Comparison of the mean bioluminescence signals of IV- and IC-administered mice shows that signals proliferated much more rapidly following IC-administration. Data points represent the mean, error bars represent standard error.

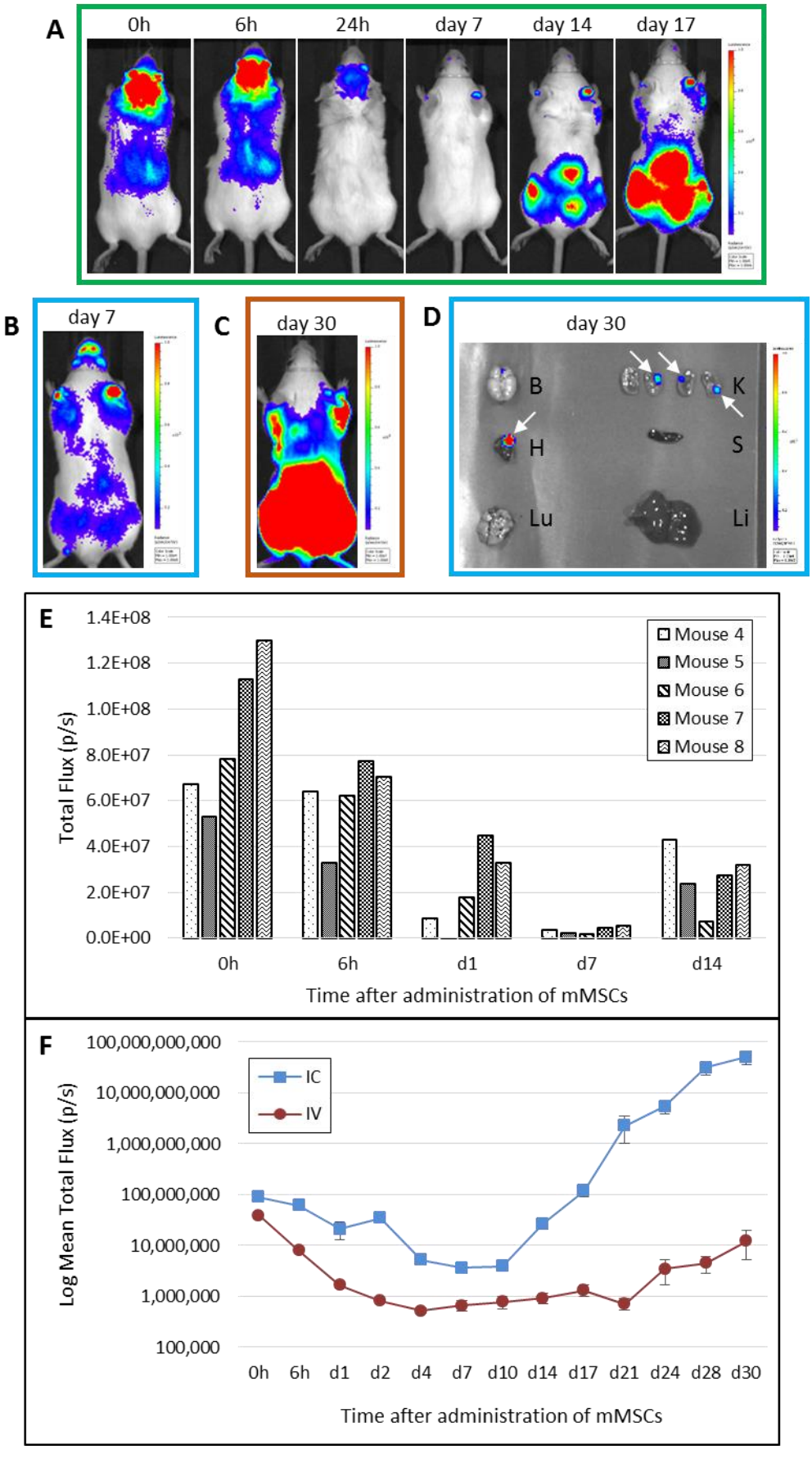
A
0h
6h
24h
day 7
day 14
day 17
B
day 7
C
day 30
D
day 30
B
K
H
S
Lu
Li
E
1.4E+08
1.2E+08
1.0E+08
8.0E+07
6.0E+07
4.0E+07
2.0E+07
0.0E+00
Total Flux (p/s)
Mouse 4
Mouse 5
Mouse 6
Mouse 7
Mouse 8
0h
6h
d1
d7
d14
Time after administration of mMSCs
F
100,000,000,000
10,000,000,000
1,000,000,000
100,000,000
10,000,000
1,000,000
100,000
Log Mean Total Flux (p/s)
IC
IV
0h
6h
d1
d2
d4
d7
d10
d14
d17
d21
d24
d28
d30
Time after administration of mMSCs

highlighted the rapid proliferation of cells following IC-administration, surpassing the original level of bioluminescence at 0h by several orders of magnitude towards the end of the study. By contrast, signals following IV-administration increased slowly and remained below the original level of bioluminescence for the duration of the study (Fig. 6.7F, Table 6.2).

Table 6.2: Bioluminescence signal quantification. Table displays the total flux (p/s) measured from individual animals on the day of cell administration (day 0), at day 30, and the fold-change between day 0 and day 30.

		Bioluminescence Signal (p/s)			
Animal	**Route of Cell Administration**	**Day 0**	**Day 30**	**Fold change**	**Mean fold change**
Mouse 1	IV	3.68E+07	2.60E+07	-0.29	-0.68
Mouse 2	IV	4.05E+07	8.80E+06	-0.78	
Mouse 3	IV	3.90E+07	2.01E+06	-0.95	
Mouse 4	IC	6.74E+07	9.83E+10	1457.08	680.41
Mouse 5	IC	5.31E+07	5.76E+10	1084.36	
Mouse 6	IC	7.84E+07	1.29E+10	163.71	
Mouse 7	IC	1.13E+08	2.99E+10	262.87	
Mouse 8	IC	1.30E+08	5.65E+10	434.03	

6.3.7.1 Analysis of MSC-derived tumours

Ex vivo imaging of organs of IC-injected mice showed weak bioluminescence signals in some organs, but this did not account for the very strong signals imaged *in vivo*. Inspection of the carcasses of IC-injected mice revealed numerous solid tumours in the skeletal muscle, predominantly located around the femurs, hips, and lower spine (Fig. 6.8A), but also occasionally around the tibia, upper spine, ribs, and forelegs (data not shown). BLI of the dissected tumours confirmed that they were strongly bioluminescent (note the very large signal scale of $1.0 \times 10^8 – 1.0 \times 10^9$ p/s/cm^2/sr, red frame), confirming that they were derived from ZsGreen$^+$/luciferase$^+$ mMSCs, and not host tissue. Analysis of the border between tumour tissue and normal tissue by light microscopy (H&E-stained; Fig. 6.8C) and fluorescence microscopy (fluorescence of ZsGreen reporter gene, Fig. 6.8D) highlighted the difference in composition between the normal host tissue (*) and tumour tissue (**), and further confirmed that the tumour tissue was derived from ZsGreen$^+$/luciferase$^+$ mMSCs.

Tumour samples were analysed by a qualified veterinary pathologist and were classified as osteosarcoma based on the presence of proliferating cancer cells (Fig. 6.8E) and both

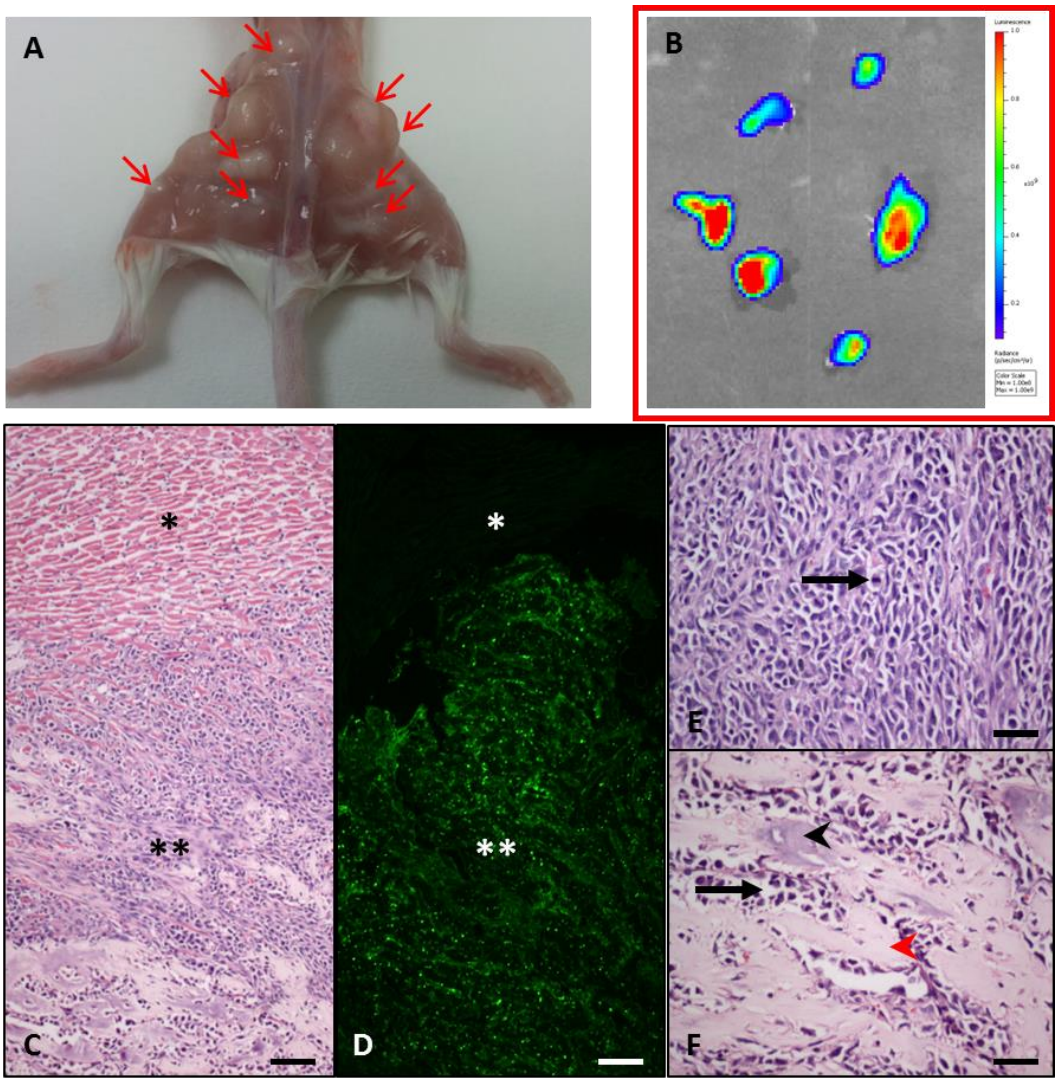

Figure 6.8. Analysis of mMSC tumours formed 30 days after IC administration. (**A**) Photograph of the hindquarters of a mouse with multiple tumours, after removal of the skin. Red arrows indicate the location of the tumour foci, demonstrating their presence in the skeletal muscle close to the femurs, hips, and spine. (**B**) Bioluminescence imaging of tumours dissected from an IC-injected mouse. Tumours were strongly bioluminescent, confirming that they originated from the administered mMSCs and not host tissue (BLI scale BLI scale 1.0 x10^8 – 1.0 x10^9 p/s/cm^2/sr). (**C - F**) Histological examination of tumour tissue. H&E staining (**C**) and fluorescence imaging for the ZsGreen reporter protein (**D**) of similar regions of a tumour show the difference in cell composition between the tumour (**) and normal tissue (*). (**E – F**) Higher magnification of H&E-stained tumour tissue showing cancer cells (arrow) (in (**E**) showing a mitotic figure), un-mineralised osteoid (black arrowhead), and partially mineralised osteoid (red arrowhead). Scale bars represent 100µm (C, D) and 50µm (E, F)

mineralised and unmineralised osteoid formation (Fig. 6.8F). Further, the bone marrow of IC-injected mice was extracted and analysed by FACS for the presence of ZsGreen$^+$ cells.

FACS analysis detected less than 1% fluorescent cells in the bone marrow of IC-injected mice, which was comparable to that of a control mouse which did not receive any cells (Fig. 6.9).

This confirmed that the IC-injected mMSCs did not migrate to the bone marrow, and that the strong signals imaged *in vivo* resulted predominantly from osteosarcoma formation in the skeletal muscle, with only very weak foci of bioluminescence in some organs. Inspection of the carcasses of IV-injected mice did not reveal any solid tumours observable by eye (data not shown), suggesting that the bioluminescence signals imaged *in vivo* resulted exclusively from the small foci of signals observed in the lungs *ex vivo*.

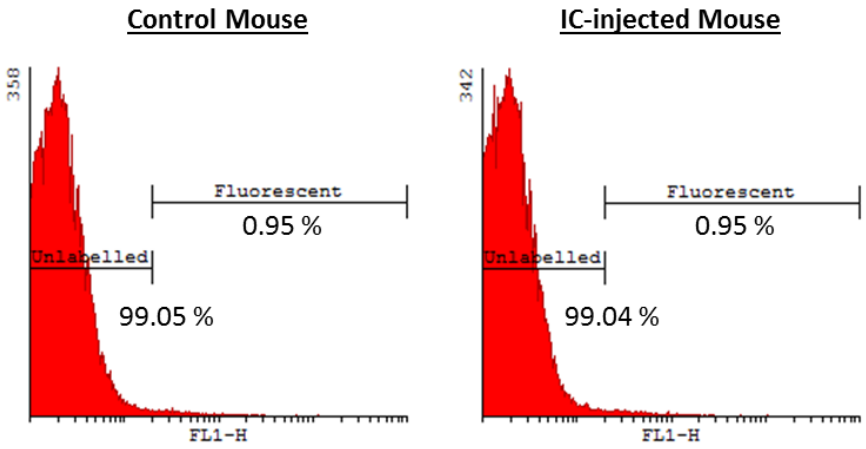

Figure 6.9: Fluorescence Activated Cell Sorting (FACS) analysis of bone marrow. FACS analysis of the bone marrow from the femurs and tibias of a uninjected control mouse (**A**) and a representative IC-injected mouse (**B**) showed that there were no ZsGreen^{+} mMSCs present in the bone marrow.

6.3.7.2 Comparison of tumour-forming potential based on genetic background and immune status of mice

In order to determine whether the persistence and growth of mMSCs in the mice after IC injection was due to the fact that immunocompromised BALB/c SCID mice had been used, or because the mMSCs were derived from a BALB/c mouse, mMSCs were next administered IC into immunocompetent BALB/c, FVB (inbred strain), and MF1 (outbred strain) mice. The initial biodistribution of cells was similar to that in the BALB/c SCID mice, with a whole-body distribution of cells at 0h, and a decrease in bioluminescence signal at 24h. In the BALB/c mice, tumour growth was highly comparable to that in BALB/c SCID mice, with respect to the timing, location, rate of growth, and intensity of signals developed (Fig. 6.10A, B, E). While tumours formed at around the same time point in the FVB and MF1 mice as in the BALB/c and BALB/c SCID mice, these grew more slowly, and the distribution of tumours was not consistent between mice (Fig. 6.10C, D, E).

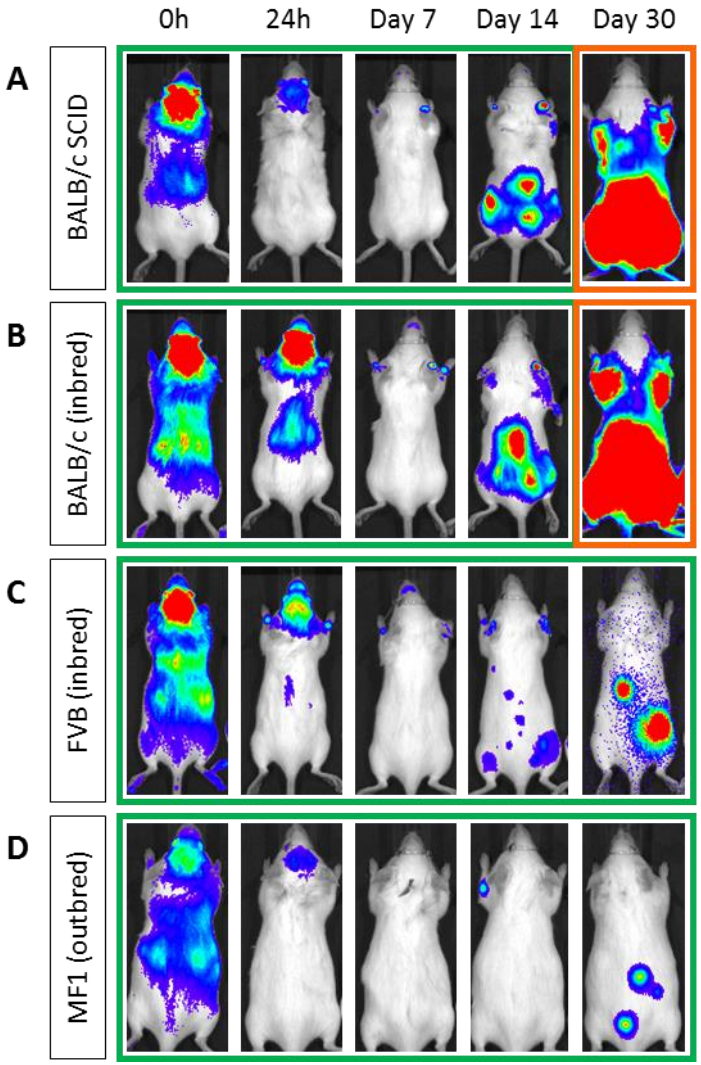

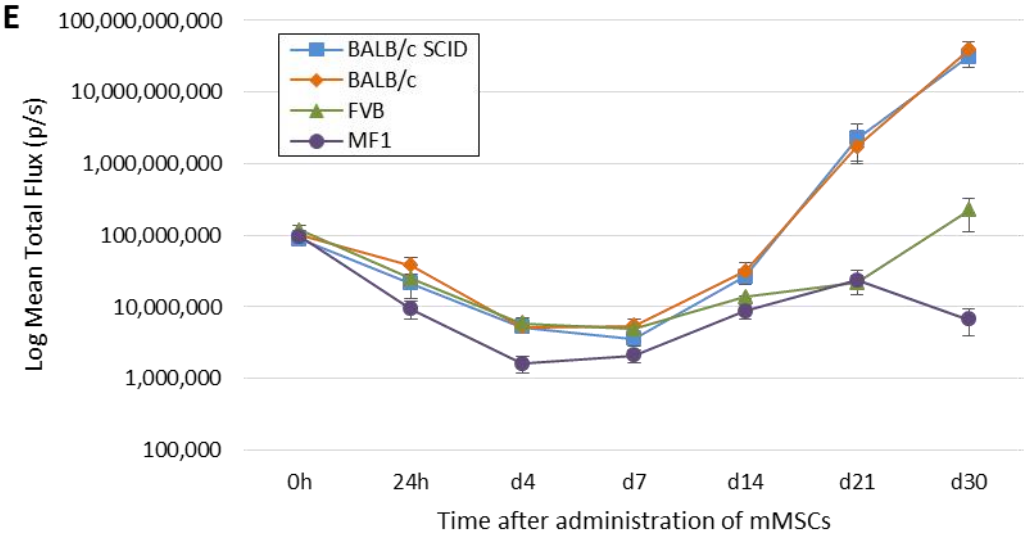

Figure 6.10: Comparison of tumour-formation potential in different mouse strains. Representative bioluminescence images of longitudinal tumour monitoring in four strains of mouse following IC administration of mMSCs; immunocompromised BALB/c SCID mice (**A**), and immunocompetent BALB/c (**B**), FVB (**C**), and MF1 (**D**) mice. BALB/c mice showed very similar tumour formation potential to BALB/c SCID mice, with respect to timing, size and location of tumour development (**A-B**), requiring a BLI scale two orders of magnitude greater ($1.0 \times 10^7 – 1.0 \times 10^8$ p/s/cm^2/sr, orange frame) than that at 0h ($1.0 \times 10^5 – 1.0 \times 10^6$ p/s/cm^2/sr, green frame) in order to display the strong signals. FVB and MF1 mice displayed weaker foci of bioluminescence signals at d30, and not all animals displayed the same biodistribution of foci (**C-D**). (**E**) Whole-body quantification of bioluminescence signals over time showed that the intensity and timing of increase of bioluminescence signals was highly comparable in BALB/c and BALB/c SCID mice, whereas the signals in FVB and MF1 mice increased at a slower rate. Data points represent the group means, error bars represent standard error.

6.4 Discussion

The experiments presented in this chapter were designed to answer a series of aims regarding the short- and long-term biodistribution of cells following intravenous or intracardiac routes of administration. The key findings were:

(i) Intracardiac administration in mice successfully delivered cells to all major organs of the body, with a high degree of correlation between the number of cells administered and cell delivery to the kidneys.
(ii) Multi-modal imaging using BLI and MRI allowed for the combination of whole-body and intra-organ imaging of cell biodistribution, and together showed that: (1) tracking SPION-labelled cells with MRI was reliable in the short-term, and (2) SPION-labelled cells were cleared from the kidneys within 48h of administration.
(iii) mMSCs had a far greater potential to form tumours *in vivo* following IC administration compared with IV, and this propensity to form tumours was affected by the mouse strain.

As shown with BLI in Chapter 4, intravenous administration of cells does not result in cell delivery to the kidneys. As such, a key objective of these studies was to establish a method of reliably delivering cells to the kidneys. While the intracardiac injection route is commonly used in the cancer research field to monitor the metastasis potential of cancer cell lines[419,422,423], it is rarely reported in regenerative medicine research.

Because the method is seldom described in detail, making it difficult to learn, the feasibility of several IC injection methods were compared: (1) via the diaphragm, similar to cardiac puncture for terminal blood collection, (2) via the intercostal space[419], and (3) ultrasound-guided[420,421]. Of the three methods trialled here, the ultrasound-guided method was superior in terms of success of injection and animal health. Ultrasound guidance allowed the direct visualisation of the needle within the mouse heart (Fig. 2.4G), which provided the researcher with confidence in the correct placement of the needle before administering the cell solution, thus reducing the chance of mis-injections into the right ventricle, cardiac muscle, or chest cavity. This was an advantage over an alternatively described method of performing IC injections[419], where the position of needle insertion was measured using anatomical features, but the needle was inserted into the heart blindly. Moreover, it was far less invasive than the method described by Arguello and colleagues, where the chest was surgically opened to visualise the heart for IC injection[424].

Following optimisation of the IC method of cell administration, the initial biodistribution of a range of cell types was assessed by BLI and histological detection of cells, and was compared with IV administration. IC administration of MSCs and kidney cells of both mouse and human origin consistently resulted in a whole-body distribution of cells, delivering cells to the kidneys, lungs, heart, liver, spleen, and brain, and while the intensity of the signal sometimes varied depending on the transduction efficiency of the different cell types, the pattern of distribution was always the same. Moreover, MRI of SPION-labelled MSCs showed hypointensive signals in the cortex of the kidneys of IC-injected mice, which was consistent with the exclusively glomerular location of MSCs as determined by fluorescence microscopy. Conversely, IV administration delivered cells to the lungs only, and long-term imaging showed that the majority of lung-entrapped cells died within 24h and did not migrate to any other organs within the 30-day study. These results were consistent with previously published reports, which showed that IV-administration of cells lead to their accumulation in the capillaries in lungs due to the pulmonary first-pass effect[111,134,267,349-351,371]. However, as discussed in Chapter 4, many preclinical studies assessing the efficacy of cell therapies in rodent models of kidney disease report migration of IV-administered cells to injured kidneys, and direct engraftment of administered cells into damaged tissues[115,130,131,147,148,185]. These conclusions were largely based on the tracking of cells by histological detection of cell membrane dyes such as PKH26 or DiI, which have been shown to be unreliable[263]. Moreover, multi-modal imaging of ZsGreen$^+$/luciferase$^+$/SPION$^+$ cells by BLI and MRI in this chapter provided further evidence that cells did not reach the kidneys following IV administration.

Despite many studies reporting beneficial effects on kidney structure and function following IV administration, it is possible that delivering cells to the kidneys may result in improved efficacy over delivering cells to the lungs with IV administration. While there are many studies assessing the efficacy of a cell therapy following arterial (either via the renal artery or carotid artery) administration of cells[267,296,353,355,425-427], only a few reports provide a direct comparison between intravenous and arterial routes of administration on the efficacy of a cell therapy in rodent models of kidney injury, and the results are conflicting. While some studies reported no difference between intravenous and arterial administration[111,127,418], others reported a beneficial effect of intra-arterial administration over intravenous[426,428,429]. However, a meta-analysis of 21 studies analysing MSC therapy for experimental kidney disease found that overall, arterial administration resulted in a greater reduction in serum creatinine than intravenous administration[430].

It is important to note that all three of the studies that showed no difference in efficacy between the administration routes were carried out in rat models of AKI (either IRI[111,418] or cisplatin[127]). A large body of work[105,110,116,134,139,207,352,353,426,427,431-433], predominantly carried out in rodent models of AKI, suggests that the mechanism of action of a cell therapy is by paracrine/endocrine influences which reduce inflammation in acute injury. This is still poorly understood and much more work is required to further elucidate the mechanism of action of a cell therapy. However, it might be possible that the location of the cells within the body (*i.e.* renal vs lung-entrapped) may have no influence on the paracrine/endocrine signalling of the cells, and amelioration of AKI might be possible regardless of the route of administration. However, the amelioration of CKD represents a different challenge to AKI. While therapies for AKI are generally administered at the onset of injury and therefore act to prevent injury from occurring, in CKD the renal tissue is already damaged, and the replacement of damaged cells may be necessary for amelioration in CKD. As such it might be unlikely that immune-modulation alone would result in amelioration of CKD, and direct engraftment and replacement of damaged renal cells may be a more viable therapeutic strategy for CKD.

The intracardiac administration route can be used in mice to assess the regenerative capacity of stem cells with renal potential for integration and differentiation. Cells that have the potential to become functional renal cells, such as pluripotent stem cells (PSC), may be able to integrate into damaged renal tissue and generate new functional renal cells, and thus potentially restore normal structure and function to the damaged kidney.

PSCs have the capacity to form any cell in the body, and are therefore an attractive cell type for regenerative medicine. The generation of renal cells from PSCs *in vitro* has gained a lot of interest in recent years, and there are now various established protocols for the directed differentiation of PSCs to renal cells[434]. Despite the advances in PSC technology for renal regenerative medicine, relatively few preclinical studies assessing the efficacy of these cells *in vivo* have been conducted, although the results so far have been promising. Renal progenitor cells derived from reprogrammed human bone marrow stromal cells[435] or reprogrammed human fibroblasts[135] have shown efficacy in mouse models AKI, while undifferentiated iPSCs had no effect in restoring kidney function[135,357]. iPSC-derived renal progenitor cells have been demonstrated to integrate into embryonic kidney rudiments *in vitro* and form tubular structures[435], alluding to their potential capacity to engraft within damaged kidneys and form new renal tissue. The delivery of iPSC-derived renal progenitor cells to the kidneys *in vivo* via an arterial administration route may therefore result in

improved efficacy over intravenous administration. Indeed, results from a research group in Taiwan have reported that in the same model of AKI (8-week old Sprague-Dawley rats; IRI induced by 45-minute unilateral renal ischemia with contralateral nephrectomy), adipose-derived MSCs had equal efficacy when administered intravenously or arterially[418], however arterially-administered iPSCs had improved efficacy over IV-administered iPSCs[428]. It is possible that the improved efficacy of arterially-administered iPSC resulted from engraftment and differentiation of pluripotent cells, however more robust cell tracking experiments are required in order to confirm the direct engraftment of renal progenitor cells. In many of these studies using iPSCs and their differentiated progeny, the authors reported engraftment of iPSC-renal progenitor cells in injured kidneys, however, as previously discussed, they primarily relied on cell membrane dyes and human nuclear staining to track the iPSC-derived cells in these studies, and any staining appeared to be sparse. Further investigation is therefore required to reliably track iPSC-derived cells *in vivo* and to further elucidate the mechanism of action of iPSC therapy. Moreover, as these studies were performed in cisplatin and IRI models of AKI, it will be important to determine whether a similar advantage of arterial administration could be observed in a model of chronic kidney disease.

A major factor impeding the clinical translation of cell-based therapies for kidney disease is the lack of long-term safety data. Particularly for PSCs, whose defining characteristics include the ability to proliferate indefinitely, a serious concern is the risk for tumour formation. In the context of PSCs, the key factors involving tumour risk are:

1. Contamination of the differentiated cell product (therapy) with undifferentiated PSCs, which may proliferate *in vivo,* forming teratomas
2. The introduction of retroviruses for cell transduction, in the case of iPSCs; particularly the introduction of Klf4 and c-Myc, which are known oncogenes
3. Epigenetic changes during reprogramming or culture *in vitro*[65,436]

There are various measures that can be taken to reduce the risk of tumour formation[90,92], however it is vital to carry out robust, long-term preclinical safety studies prior to clinical translation. While many investigators studying the efficacy of cell therapies do acknowledge the safety concerns surrounding tumour formation, relatively few studies follow the animals for an extended period of time. This chapter highlighted the importance of prolonged monitoring of mice. Following the administration of luciferase$^+$ mMSCs, the bioluminescence signal initially decreased below background levels, and had the experiment been terminated

at that time point, the formation of tumours at a later time point would not have been detected. Similarly, Kunter *et al.* published a report in 2006 describing the beneficial effects of MSCs on glomerular healing in a rat model of glomerulonephritis[437]. However, it was not until the following year when the authors tested the efficacy of the MSCs in a chronic version of the same model that adverse effects were discovered[426]. 60 days following arterial administration of MSCs, the authors discovered that the MSCs had maldifferentiated to form adipocytes in the glomeruli; a complication that was not detected in the initial 10-day study. A relatively short period of only 30 days was used in the studies in this chapter. D1 mouse MSCs, a highly tumourigenic cell type[438], were chosen specifically to investigate the effect that route of administration and genetic background of the host would have on tumour formation. As such, longer analysis was not possible due to the tumour burden on animals. However, when assessing the safety of cell therapies intended for the clinic, longer studies of six to twelve months are likely to be required[92].

One of the aims of this chapter was to determine whether route of administration had any effect on tumour formation. It was shown that IV administration led to the formation of very small, slow-growing tumours restricted to the lungs, while intracardiac administration promoted the rapid development and proliferation of multiple large tumours in mouse skeletal muscle. Additionally, there were some very small foci of bioluminescence in some organs following IC administration, but not after IV. These results were obtained from highly tumourigenic mMSCs, and as such are not intended to suggest that clinical MSC therapies pose such a high tumour risk. Rather, they highlight the importance that the route of administration may have on various aspects of RMT safety, such as tumour formation. It is therefore vital to carry out robust safety studies in a model that resembles the clinical scenario as closely as possible. This involves administering a clinically-appropriate dose, via a clinically-relevant administration route, and in an animal model that resembles the clinical disease as closely as possible[92].

A key feature of this chapter is the use of preclinical imaging to facilitate the monitoring of cells *in vivo*. Traditionally, preclinical research has largely involved the histological examination of tissues for a variety of purposes, including the analysis of tissue damage, degree of amelioration by a cell therapy, and the biodistribution of exogenously administered cells. Not only does this approach require the sacrifice of a large number of animals at many time points, and precludes the monitoring of individuals over time, it makes it difficult to detect abnormalities in unexpected locations. For example, following the intravenous

administration of iPSC-derived renal progenitor cells for treatment of cisplatin-induced AKI, Imberti *et al.* inspected only the organ of interest - the kidneys - and reported no maldifferentiation eight weeks following cell treatment[135]. While this is good news for the kidney, it does not consider the possibility of off-target effects on other organs of the body.

Imaging technologies are highly advantageous in preclinical research. However, each modality is associated with various advantages and disadvantages, and as such no single imaging technology alone is ideal. The combination of two or more imaging modalities can however strengthen the scientific data obtained in an experiment, with each modality complementing the other. As shown in this chapter, BLI is an excellent tool for whole-body imaging and is ideal for monitoring the biodistribution of cells over time. However, the spatial resolution is poor and it is not possible to definitively identify the organ in which the signals are located without sacrificing the animal and imaging the organs *ex vivo*. By incorporating MRI into the imaging regime, the inter- and intra-organ biodistribution of cells can also be ascertained, thus providing more information from each animal. Multi-modal imaging approaches are not limited to monitoring cell biodistribution, and are gaining increased interest in regenerative medicine research for a wide range of applications[281,414,439]. Notably, Ngen *et al*. developed a clinically-translatable, dual-modality cell imaging system, whereby live and dead cells could be distinguished *in vivo* using MRI, and the results were validated with BLI[439], and Galisova *et al.* investigated the effect that MSCs had on the neovascularisation of subcutaneously implanted scaffolds, using MRI to monitor the scaffolds and image tissue perfusion and vessel permeability, and BLI to monitor the survival of MSCs[281].

In summary, the data presented in this chapter highlighted the importance of the route of administration and long-term safety assessment of RMTs. Arterial administration resulted in cell delivery to the kidneys, and thus may provide a therapeutic advantage over intravenous administration for chronic disease. Intracardiac cell administration provided a reliable method of delivering cells to the kidneys in mouse models, where renal artery administration is not feasible, and thus the IC method will be valuable for assessing the benefits of cell delivery to the kidneys in mouse models of CKD. Importantly, this chapter emphasised the need for long-term safety studies prior to clinical translation of RMTs, and preclinical imaging is a valuable asset for this purpose; reducing the number of animals required for long-term studies, increasing the data obtained from each animal by longitudinal imaging, and providing more reliable cell tracking than some more traditional methods.

6.5 Supplementary Table

Supplementary Table S6.1: Tukey Pairwise Comparisons. Two separate post-hoc statistical analyses following statistically significant results from separate one-way ANOVAs comparing the T_2* relaxation time in the kidneys (**A**) and in the liver (**B**) Groups that do not share a letter are significantly different from one another.

A		*n*	Mean	Grouping		
Kidneys	Baseline	10	14.56	A		
	0h	6	7.98			C
	24h	6	12.57		B	
	48h	4	13.19	A	B	

		T_2* Relaxation Time				
B		*n*	Mean	Grouping		
Liver	Baseline	5	7.19	A		
	0h	3	5.48		B	
	24h	3	5.10		B	
	48h	2	5.02		B	

CHAPTER 7

Final Discussion and Summary

The experiments described in this thesis were designed to explore various aspects of the safety and efficacy of cell-based regenerative medicine therapies in models of kidney disease. Two models were utilised here, adriamycin nephropathy as a model of chronic glomerular kidney disease, and ischemia-reperfusion injury as a model of acute kidney injury, predominantly featuring tubular injury. The experiments focussed primarily on using novel imaging-based methods of assessing kidney function and tracking cells *in vivo*, rather than more traditional biochemical and histological techniques. There were several key findings and themes throughout this thesis:

1. **Novel methods of assessing kidney function in mice were superior to traditional biochemical assays.**

Two novel methods of monitoring renal function were explored in this thesis: transcutaneous measurement of FITC-sinistrin clearance, and photoacoustic imaging of IRDye clearance kinetics. The experiments in Chapter 3 demonstrated that both novel methods correlated very strongly with histological scoring of glomerular damage, whereas urinary albumin did not correlate as strongly with histological scoring, and both serum creatinine and BUN measured at week 5 did not show any statistically significant changes between injured and control mice. Even though both the transcutaneous device and the MSOT provided a reliable assessment of kidney function, the transcutaneous device was chosen as the method to be used in further studies as it had several practical advantages over the MSOT:

a. Multiple animals could undergo the transcutaneous measurement at a time, making this method very high-throughput and time-effective. Conversely, only one animal could be imaged in the MSOT at a time, and there was significant preparation and temperature-equilibration time required, thus limiting the number of animals that could be imaged in a day.
b. Data processing and interpretation from the transcutaneous device was very fast and simple, requiring only a few minutes to calculate the half-life, whereas data from the MSOT took several hours to process, reconstruct, and analyse, and analysis and interpretation could be more complicated.
c. Required anaesthesia time was vastly lower for the transcutaneous measurement (less than 10 minutes) compared with MSOT imaging (approximately two hours). This was advantageous to avoid anaesthesia-related effects on renal function[239,240], and

was also better for the welfare of animals. This was particularly important in the IRI model, where multiple measurements in a short space of time was required.

d. In the IRI model, the incision site/sutures interfered with the imaging data. MSOT imaging was carried out in IRI mice (data not shown), however it was found that the incision site/sutures, which were unavoidably directly above the kidney and therefore in the imaging plane, produced a photoacoustic signal which interfered with the signals in the kidney. Undyed suture material was used to try to avoid this, however the suture became dyed with blood, and the incision site would have contained small amounts of dried blood, which would have contributed to interference with the photoacoustic signal. This made it difficult to delineate the kidney and determine where to set the imaging plane, and also where to draw ROIs for signal quantification. Conversely, the sutures were not an obstacle for the transcutaneous device, as the location of the device could be altered to accommodate the sutures, without affecting the data.

The transcutaneous device was therefore chosen as the primary method of measuring kidney function in IRI mice and was used to inform the choice of ischemia time in the initial optimisation studies whilst setting up the IRI model (Chapter 5). An additional advantage of the transcutaneous measurement in the IRI model was that data on the renal function of animals was available immediately after measurement, and thus animals in suspected renal failure could be identified in a timely manner, which was a particularly valuable tool whilst setting up a new model. Furthermore, the transcutaneous device proved to be sensitive and reliable in detecting kidney injury in IRI mice, correlating very strongly with histological assessment of tubular damage.

Previous data have shown that the transcutaneous device is useful for monitoring kidney function in healthy animals, in addition to a range of kidney injury models, including unilateral nephrectomy[234,237], polycystic kidney disease[234,237], salt-sensitive hypertension[242], diabetic CKD[243], non-diabetic CKD[244], sepsis[245], and cisplatin-induced AKI[134]. The data presented in this thesis add to this list, demonstrating that the transcutaneous device is also useful in the adriamycin (Chapter 3) and IRI (Chapter 5) models. The transcutaneous device has been shown in Chapter 3 and by Cowley and colleagues to be more sensitive to changes in kidney function than serum biomarkers, with significant changes in FITC-sinistrin clearance but not in SCr or BUN[242]. Additionally, the transcutaneous measurement is minimally invasive and less stressful to the animals than repeated blood and urine sampling. Therefore, the transcutaneous device is highly recommended as a method of measuring kidney function in

preclinical models of kidney injury, especially in cases where longitudinal assessment of kidney function is required.

Furthermore, the transcutaneous device is clinically translatable. MediBeacon (Missouri, USA) have developed a clinical version of the device[440] to be used as point-of-care method of measuring GFR in real time in hospitalised patients. Clinical studies began in 2013, assessing the use of the device in healthy patients[247]. The next clinical study will enrol patients with impaired renal function, and the ultimate goal is to provide a new gold-standard for measuring renal function, and enable early detection of impaired renal function and thus rapid intervention[440].

Although the MSOT was not preferred as a method of measuring kidney function, it has some advantages over the transcutaneous device that must be acknowledged. The transcutaneous device only has one function, whereas the MSOT is capable of imaging multiple different physiological parameters, such as tissue perfusion and oxygenation status[441], and kidney and liver function[248], and can also be used to track appropriately-labelled cells *in vivo*. Thus, MSOT has multiplexing capabilities, and it is possible to monitor kidney function and track labelled cells in the same imaging session. Cells can be labelled with probes that maximally absorb in the near infrared, such as gold nanoparticles[442-444] or carbon nanotubes[445], or by transducing cells with reporter genes such as infrared fluorescent protein (iRFP)[335] or tyrosinase[332], thus allowing detection of administered cells *in vivo* by photoacoustic imaging. Recently, Nam and colleagues demonstrated the value of photoacoustic imaging in regenerative medicine[444]. The authors aimed to assess the therapeutic efficacy of adipose-derived stem cells to improve a burn injury. They used photoacoustic imaging to track gold nanorod-labelled cells *in vivo*, and to assess the severity of injury and the degree of tissue regeneration following cell therapy in a cutaneous burn model. Furthermore, an interesting study by Ricles and colleagues labelled cells with both gold nanorods and gold nanospheres in order to differentiate between live and dead cells *in vivo*, and also image the immune response to cell administration[443]. The peak absorption of gold nanospheres is changed when they are endocytosed by macrophages, allowing the differential identification of signals coming from live cells labelled with gold nanorods, and those coming from endocytosed cells labelled with the now-visible gold nanospheres. Using this sophisticated method, Ricles *et al.* could monitor the viability of administered cells *in vivo* and the rate of tissue macrophage infiltration over time.

In addition to cell tracking, photoacoustic imaging also has applications in preclinical regenerative medicine research through its ability to image tumours. Due to the high vascularisation of most tumours, endogenous haemoglobin contrast allows tumour imaging[251]. However, by using a contrast agent which passively accumulates in tumours, such as a fluorescent dye, indocyanine green, conjugated to human serum albumin[446], the sensitivity and depth of tumour visualisation can be increased by up to 380%. More specific tumour targeting can be achieved by conjugating photoacoustic probes, such as gold nanoparticles, to antibodies specific to particular cancer cell antigens[447].

Photoacoustic imaging was previously limited to preclinical use, but it is now being developed for clinical applications, with a handheld MSOT scanner recently developed by iThera Medical[448]. The penetration depth limits clinical photoacoustic imaging to relatively superficial tissues, but recent work has demonstrated the potential of photoacoustic imaging for non-invasive assessment of Crohn's disease activity[259], in addition to imaging human vasculature[258] and cancer[257].

2. Human kidney-derived cells showed a trend towards improved kidney injury when administered early (day one), but not when administered late (day 15) to mice with adriamycin nephropathy.

The efficacy of cells derived from the human kidney has previously been shown in the rhabdomyolysis[147-149,345] and cisplatin[134] models of AKI, and the adriamycin model of CKD[185]. All studies report beneficial effects of hKCs in the various models, either with faster recovery of serum biomarkers of kidney injury[148,345] or an earlier and/or lower peak in kidney injury[134,147,149,185]. In all of these reports, the hKCs were administered very early in the course of injury. The results of the acute study in Chapter 4 agreed with this, with attenuated weight loss and lower urinary albumin levels at day 10 in ADR mice administered hKCs on day one, compared with saline treated ADR mice. However, when treatment was delayed to a later stage in the progression of the disease (day 15), the hKCs no longer had a beneficial effect on urinary albumin excretion, and furthermore, had no effect on FITC-sinistrin clearance or histological scoring of glomerular injury.

These results are somewhat similar to those described by Magnasco and colleagues who reported that when MSCs were administered to rats that the same time as ADR, the rats were protected from severe glomerulosclerosis, however when MSC treatment was delayed to 60 days after ADR, glomerulosclerosis was comparable to saline-treated rats[184]. Regardless of

administration time, the authors reported no differences in serum creatinine or proteinuria between MSC- and saline-treated rats. Furthermore, Caldas and colleagues reported that MSC therapy was less effective in the later stage of CKD, modelled by 5/6 Nx, compared with an earlier stage of CKD, modelled by 2/3 Nx[219].

The vast majority of published studies administered cells very early following the induction of injury, however this will not be possible for most human patients. The data presented in Chapter 4 and the results described by Magnasco and colleagues and by the team around Caldas highlight the importance of investigating the timing of therapeutic intervention, and indicate that cell-based therapies may offer no or limited amelioration to patients in the later stages of CKD. Very few preclinical studies have assessed the effect of late timing of administration, and importantly, relatively few studies used CKD models, rather than AKI models. Recent reviews have suggested that cell-based therapies hold great promise for treating CKD[404,449], however further investigation is therefore required using models of CKD to assess the latest time point at which cell therapy may offer a beneficial effect to patients with CKD.

3. Human kidney-derived cells had no beneficial effect on kidney function in the IRI model, and this may have been due to IRI-induced lung injury preventing cell death.

There are a great number of published studies demonstrating ameliorating effects of many different types of cells in the IRI model. As such, it was a surprise when this was not the case in the experiments described in Chapter 5: none of the three cell types assessed, hKCs, hUC-MSCs, or hBM-MSCs had a significant effect on FITC-sinistrin clearance throughout the course of the experiment, or on SCr, BUN, tubular injury (KIM-1 tissue expression), or tubular cell proliferation (Ki67 tissue expression) at days one (only hKCs assessed) or four (all cell types assessed). The results from bioluminescence imaging of luciferase$^+$ hKCs 24h following cell administration were also unexpected. In previous studies using BLI to track cells over time, the signal was always markedly decreased 24h following cell administration, due to death of the luciferase$^+$ cells *in vivo*. By contrast, the intensity of the bioluminescence signal was maintained over 24h in the experiments described in Chapter 5, and this was the first time that we had observed this in our laboratory.

A possible explanation for the survival of the IV-administered hKCs could be IRI-induced acute lung injury[376], and that the survival of the cells prevented the amelioration of AKI. There are two studies showing increased bioluminescence signals of MSCs in mice with ALI[279,280],

however there are no reports describing this phenomenon following renal IRI. As such, the mechanisms behind pulmonary cell survival and the relationship with renal amelioration are unknown.

Further, it is unclear why other studies on cell efficacy in the IRI model have not reported this phenomenon. It is possible that the renal injury induced in our laboratory is more severe than in others, and that this leads to more severe ALI. FITC-sinistrin clearance was shown to be a more reliable measure of kidney function than serum biomarkers, and as such, this was the primary parameter used to assess injury levels when setting up the IRI model. However, this meant that published FITC-sinistrin data in the IRI model were not available to compare to ours. Subsequent comparison of serum biomarker levels between our model and other published studies show higher SCr and BUN in our model, indicating more severe renal injury (Fig. 7.1, Table 7.1). It is difficult to directly compare different studies due to variations in the models, however Figure 7.1 gives an idea of the approximate injury levels induced in other models, and how the model described in this thesis compares. Jang *et al.,* (2014) and Xing *et al.,* (2014) used a bilateral model with 27 and 28 minutes ischemia respectively, and reported mean SCr levels at day one of approximately 2.4 and 1.1 mg/dL respectively[105,110], compared with the much higher level of 5.71 mg/dL in the study in Chapter 5. Toyohara *et al.,* (2015) used a model of IRI that is more similar to the one described here, with unilateral ischemia and a contralateral nephrectomy, but a much longer ischemia time of 40 minutes[357]. Despite the longer ischemia time, Toyohara *et al.,* reported much lower SCr levels of approximately 0.06 mg/dL at day four, compared with 1.14 mg/dL in Chapter 5. Ranghino *et al.,* (2017) also used a unilateral ischemia with contralateral nephrectomy model, with a long ischemia time of 35 minutes[120]. They only reported SCr levels at day two, and therefore cannot be compared with the day one and four measurements reported in this thesis, however the levels they described at day two are roughly comparable to those reported by other studies at the same time point. The difference in BUN levels between those reported in Chapter 5 and in other studies follow a similar trend, with higher levels in the IRI model in this thesis (Fig. 7.1B, Table 7.1).

Therefore, it is possible that the more severe renal injury induced in the model described in Chapter 5 resulted in more severe ALI than would be seen in other IRI models. I propose that this increased lung injury could account for the lack of cell death following IV administration of hKCs. Consequently, if cell death is required for the ameliorating effects of cell therapy on kidney injury, then this may explain why we did not detect any beneficial effects following administration of any of the three different types of cells investigated.

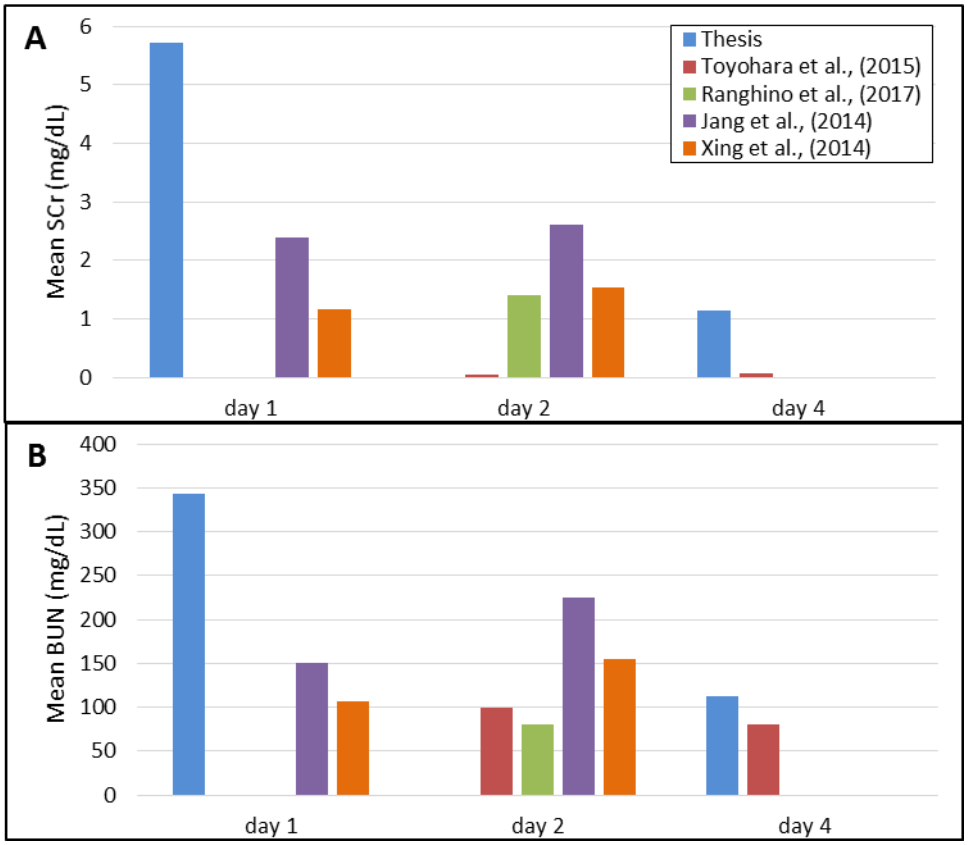

Figure 7.1: Comparison of the mean (actual or estimated from graph) SCr (**A**) and BUN (**B**) values in IRI mice between the model used in this thesis, and four other published models.

Table 7.1: Comparison of the mean (actual or estimated from graph) SCr and BUN values in IRI mice between the model used in this thesis, and four other published models.

		SCr (mg/dL)			BUN (mg/dL)		
	Model	day 1	day 2	day 4	day 1	day 2	day 4
Thesis	male BALB/c mice unilateral w/Nx, 31 min	5.71	ND	1.14	342.6	ND	113.1
Toyohara *et al.*, (2015)	male NOD/SCID mice unilateral w/Nx, 40 min	ND	0.05	0.06	ND	100	80
Ranghino *et al.*, (2017)	male SCID mice unilateral w/Nx, 35 min	ND	1.40	ND	ND	80	ND
Jang *et al.*, (2014)	male C57BL/6 mice bilateral, 27 min	2.40	2.60	ND	150	225	ND
Xing *et al.*, (2014)	male BALB/c mice bilateral, 28 min	1.16	1.54	ND	106.9	154.4	ND

These results have opened up a very interesting aspect of regenerative medicine research, and a great deal of further investigation is required to understand the role of ALI and cell death in the ameliorative capacity of a cell therapy for renal injury.

4. Preclinical imaging methods are valuable tools for monitoring cell biodistribution *in vivo*, and this can inform the mechanism of action, in addition to the safety, of a cell therapy.

Conventional methods of tracking exogenously-administered cells generally involve histological detection of cells labelled with fluorescent cell membrane dyes. As discussed throughout this thesis, this method is not ideal due to the likelihood of false positive cell identification, the inability to track cell biodistribution in individual animals over time, and the large number of animals that must be sacrificed for these types of experiment. Importantly, the high chance of false positive cell detection may not only lead to erroneous data, but may result in incorrect conclusions being drawn from the data. Alternatively, preclinical imaging offers a far more reliable method of tracking cells *in vivo*, allows longitudinal monitoring of individual animal, and thus reduces the number of animals required.

There are several published studies that have used cell membrane dyes to track cells histologically and, upon detecting the dye in the kidney, have concluded that the therapeutic cells engrafted into the kidney[147,148,185]. Further, the cell membrane dye sometimes co-localised with markers of specialised renal cells, such as the proximal tubule marker lotus tetragonolobus agglutinin (LTA)[147,148], distal tubule marker dolichos biflorus agglutinin (DBA)[147], and podocyte markers podocin, synaptopodin, Wt1, and nephrin[185], and as such the authors further concluded that the administered cells differentiated *in vivo*, following their engraftment, and that this was how the cells exerted their beneficial effect on kidney injury. Importantly, Santeramo and colleagues have recently shown that this method of cell tracking results in false positive signals in the kidney[134]. Other studies have used slightly different methods to track cells histologically, for example by detection of male cells in female recipients[130,215,352,433], or by immunostaining of human cell markers[134,149]. These methods are somewhat more reliable than cell membrane dyes, but still require the sacrifice of animals for histological analysis of tissues *ex vivo* and do not allow the differentiation between live and dead cells. Many of these studies have also reported the presence of administered cells in the kidney, however the number of cells detected must be taken into context when drawing conclusions about the role of cell presence in the kidney in terms of amelioration.

It must be noted that under certain conditions a very small number of cells may be able to bypass the lungs. Hypoxic conditions have been shown to recruit intrapulmonary arteriovenous anastomoses, which are large (at least 70µm in the rat) vessels that connect the pulmonary arterial and venous circulations, thus bypassing the capillary beds[450,451]. AKI is known to cause acute lung injury[376], and the subsequent hypoxia may therefore lead to the recruitment of intrapulmonary arteriovenous anastomoses. Bates and colleagues showed that when one million 25µm microspheres were intravenously administered to rats under normoxic conditions, no microspheres were detected in the kidneys, but under hypoxic conditions, on average around 1,000 microspheres were detected in a single kidney[450]. Furthermore, this number was highly variable, ranging from 11 to 5,004 microspheres in a single kidney across five rats. This data may explain why cells are occasionally detected in the kidneys of some animals, but the very small number of cells that are able to reach the kidneys are highly unlikely to significantly contribute to the ameliorative effect[89,134].

The results of cell tracking studies in this thesis, and by other authors have demonstrated that intravenously administered cells predominantly remain trapped in the lungs[134,349,350,371], and therefore renal homing, engraftment, and differentiation do not contribute to the ameliorative effect of the cells. Furthermore, recent data from our laboratory indicates that it may be essential for the cells to die in order to instigate the inflammatory response that leads to renal amelioration[134]. In this context, the results in Chapter 5 are important, as they suggest that the lack of cell death 24h following cell administration may be responsible for the lack of amelioration of kidney injury. This is in contrast to the results in Chapter 4, where the hKCs promptly died in the lungs of mice following IV administration, and led to a beneficial effect on kidney function. Thus, preclinical imaging is a useful tool for gaining insights into the mechanism of action of a cell therapy.

Furthermore, the minimally invasive nature of preclinical imaging allows the long-term safety of cell therapies to be monitored in individual animals. Importantly, the data in Chapter 6 highlights the need for long-term monitoring, as the bioluminescence signals initially decreased to near-background levels, and had imaging ceased at that timepoint, the high tumourigenicity of the mMSCs would not have been identified. Bioluminescence imaging was very useful for high throughput, whole body imaging of animals, and is highly recommended as a valuable tool for further preclinical safety assessment of RMTs in the future.

However, a disadvantage of BLI is the poor spatial resolution, meaning that the exact anatomical location of the signals is unknown. As such, a multimodal imaging approach is

useful to gain additional information on the biodistribution of cells *in vivo*. As shown in Chapter 5, by labelling cells in two ways, with a luciferase gene and with SPIONs, the cells could be tracked *in vivo* by both BLI and MRI. Thus, the benefits and limitations of each modality complemented the other, allowing sensitive whole-body imaging of live cells by BLI, and organ-specific, high resolution imaging of cells by MRI. It must be noted that cell labelling methods that involve probes such as SPIONs suffer from signal dilution when cells divide, and risk false positive cell detection if the probes are released from labelled cells, for example when they die or are phagocytosed, thus limiting the long-term monitoring of cells by this method. However, this particular multi-modal combination is highly useful for short-term analysis of cell biodistribution.

5. Ultrasound-guided administration is a safe and feasible method of arterial cell administration in mice, which successfully delivers cells to the kidney, however the potential for tumour formation differs following intravenous and arterial administration.

The vast majority of preclinical studies assessing the efficacy of cell therapies in animal models administer the cells intravenously. However, a meta-analysis of 21 studies found that arterial administration of MSCs resulted in improved efficacy over intravenous administration[430]. Despite this, individual studies directly comparing the effect of administration route on efficacy have yielded conflicting results[111,127,418,428,429,437], and as such, further investigation is required to determine the optimal route of administration. Therefore, it is important to establish safe and reliable methods of arterial administration in mice. In Chapter 6, an ultrasound-guided intracardiac method of arterial cell administration was described. Once optimised, this method was found to be safe and highly reproducible, with limited side-effects and mis-injections. Further, this method successfully delivered cells to the kidneys, with a dose-dependent response in the number of cells found in the kidneys. Other methods of arterial administration for renal cell delivery include renal artery and carotid artery injections[296,353,355,425-427], however both methods require surgery, and in particular, the renal artery injection is difficult in mice due to the small size of the vessel, and requires highly invasive surgery, with a large abdominal incision and manipulation of the intestines in order to access the renal artery. By contrast, intracardiac cell administration is a fast procedure that requires only brief anaesthesia, and the use of ultrasound imaging to guide the injection makes it highly reproducible and reliable. This method is commonly used in preclinical cancer research as a model of metastasis[419,422,423], but is rarely reported in

regenerative medicine. This injection route is therefore recommended as a method of arterial cell administration in mice, and will be valuable in further assessments of the effect of route of administration on cell efficacy.

In addition to affecting the efficacy of a cell therapy, the results of Chapter 6 demonstrated that the route of administration may also affect the safety of a cell therapy, with arterial administration of mMSCs leading to rapid and aggressive tumour formation, compared to limited and slow-growing tumour formation following intravenous administration. Furthermore, the strain of the animals used affected the tumour formation. BALB/c mice were highly susceptible to tumour formation, whereas FVB and MF1 mice were less susceptible. The increased sensitivity of BALB/c mice was most likely due to the fact that the mMSCs were derived from a BALB/c mouse, and the inbred nature of this strain meant that the mMSCs were unlikely to have been recognised by the immune system, allowing unrestricted tumour growth. Nonetheless, these results highlighted the need for extensive and robust safety assessment of stem cell therapies in animals prior to clinical translation.

Taken together, many studies have shown that a range of cell types have a beneficial effect on kidney function, and that this beneficial effect is most likely mediated by paracrine effects which modulate the immune system to promote an anti-inflammatory microenvironment. However, there are some key questions that still need to be addressed.

(i) If the cells have a paracrine action, can the same effect be achieved by administering only the appropriate cytokines/chemokines (*i.e.* conditioned medium), instead of the cells?
(ii) If cells themselves are indeed necessary to achieve a beneficial effect, which is the best cell type to achieve maximum effect?
(iii) Which is the best administration route?
(iv) When is the best time to administer a cell therapy?
(v) What is the ideal dose of cells?

Several studies have assessed each of these questions individually, however the results between studies are conflicting, and there is not yet a general consensus on the efficacy of conditioned medium, nor on the most appropriate cells and administration regime. Furthermore, it may be necessary to answer these questions for AKI and CKD separately, as

different types of kidney injury may have different requirements. Further work is therefore required to answer these questions.

There are additional features of preclinical studies that must be considered and addressed in order to advance progress towards clinical translation. Almost all preclinical studies, including the studies described in this thesis, are conducted in animals that are inbred, young, of a single sex (generally male), and otherwise healthy. Whilst these conditions work in favour of the researcher, as controlling these factors leads to lower degree of variation in the response of the animals, and therefore a higher chance of obtaining statistically significant data, this is clearly not representative of human patients. As such, the promising results observed in preclinical studies may not be replicated when clinical trials begin. It is therefore imperative to assess the efficacy of a promising cell therapy in diverse models that use outbred animals, older animals, both genders, and animals with co-morbidities, such as underlying CKD, diabetes, or hypertension[222]. Moreover, the current publication bias towards only reporting positive results on surviving animals, and ignoring negative data, animal mortality, and side-effects[221], ultimately impedes the overall progress towards clinical translation. As such, more emphasis should be placed on conducting carefully-designed studies that report on all outcomes, regardless of whether they are seen as positive or negative. This will provide the research community with a more comprehensive understanding of both positive and negative results, and will help to drive preclinical research to clinical translation.

Overall, the experiments described throughout this thesis have demonstrated the use and value of novel methods of assessing kidney function and tracking cells *in vivo* with the ultimate aim of assessing the safety and efficacy of cell-based therapies. All methods described are minimally invasive, allowing individual animals to be monitored over time and reducing the number of animal required for experiments. Furthermore, all novel methods used are more reliable than conventional methods, thus delivering stronger and more accurate data, and provide important insights into the mechanism of action of cell therapy that are not confounded by false-positive results. Consequently, these novel methods of measuring renal function and tracking cells are recommended for widespread use in preclinical assessment of regenerative medicine therapies for kidney disease. By using more accurate and reliable methods, in addition to more diverse and robust experimental models, greater progress will be made in developing therapies for future clinical use.

LIST OF REFERENCES

1 Hallgrímsson, B., Benediktsson, H. & Vize, P. D. in *The Kidney : From Normal Development to Congenital Disease* (eds Peter D. Vize, Adrian S. Woolf, & Johnathan B.L. Bard) 149-164 (2003).

2 McBride, J. M. in *The Kidney: A Comprehensive Guide to Pathologic Diagnosis and Management* (eds Donna E. Hansel, Christopher J. Kane, Gladell P. Paner, & Sam S. Chang) 1-18 (Springer New York, 2016).

3 Dworkin, L. D., Sun, A. M. & Brenner, B. M. in *Brenner and Rector's The Kidney* Vol. One (eds Barry M. Brenner & Samuel A. Levine) Ch. 7, 277-318 (W.B Saunders Company, 2000).

4 Bertram, J. F., Douglas-Denton, R. N., Diouf, B., Hughson, M. D. & Hoy, W. E. Human nephron number: implications for health and disease. *Pediatric nephrology (Berlin, Germany)* **26**, 1529-1533, doi:10.1007/s00467-011-1843-8 (2011).

5 Dantzler, W. H. in *Comparative Physiology of the Vertebrate Kidney* 7-36 (Springer New York, 2016).

6 Menon, M. C., Chuang, P. Y. & He, C. J. The glomerular filtration barrier: components and crosstalk. *International journal of nephrology* **2012**, 749010, doi:10.1155/2012/749010 (2012).

7 Tojo, A. & Kinugasa, S. Mechanisms of Glomerular Albumin Filtration and Tubular Reabsorption. *International journal of nephrology* **2012**, 9, doi:10.1155/2012/481520 (2012).

8 Moe, O. W., Berry, C. A. & Floyd C. Rector, J. in *Brenner & Rector's The Kidney* Vol. One (eds Barry M. Brenner & Samuel A. Levine) Ch. 9, 375-415 (W. B. Saunders Company, 2000).

9 Brewster, U. C. & Perazella, M. A. The renin-angiotensin-aldosterone system and the kidney: effects on kidney disease. *The American journal of medicine* **116**, 263-272, doi:10.1016/j.amjmed.2003.09.034 (2004).

10 Bellomo, R., Kellum, J. A. & Ronco, C. Acute kidney injury. *Lancet (London, England)* **380**, 756-766, doi:10.1016/s0140-6736(11)61454-2 (2012).

11 Susantitaphong, P. *et al.* World incidence of AKI: a meta-analysis. *Clinical journal of the American Society of Nephrology : CJASN* **8**, 1482-1493, doi:10.2215/cjn.00710113 (2013).

12 Rewa, O. & Bagshaw, S. M. Acute kidney injury-epidemiology, outcomes and economics. *Nature reviews. Nephrology* **10**, 193-207, doi:10.1038/nrneph.2013.282 (2014).

13 Bonventre, J. V. & Yang, L. Cellular pathophysiology of ischemic acute kidney injury. *The Journal of clinical investigation* **121**, 4210-4221, doi:10.1172/jci45161 (2011).

14 Fuhrman, D. Y. & Kellum, J. A. Epidemiology and pathophysiology of cardiac surgery-associated acute kidney injury. *Current opinion in anaesthesiology* **30**, 60-65, doi:10.1097/ACO.0000000000000412 (2017).

15 Goldstein, S. L. Nephrotoxicities. *F1000Research* **6**, 55, doi:10.12688/f1000research.10192.1 (2017).

16 Azzalini, L., Spagnoli, V. & Ly, H. Q. Contrast-Induced Nephropathy: From Pathophysiology to Preventive Strategies. *The Canadian journal of cardiology* **32**, 247-255, doi:10.1016/j.cjca.2015.05.013 (2016).

17 Awdishu, L. & Mehta, R. L. The 6R's of drug induced nephrotoxicity. *BMC Nephrology* **18**, doi:10.1186/s12882-017-0536-3 (2017).

18 Liangos, O. Drugs and AKI. *Minerva Urologica e Nefrologica* **64**, 51-62 (2012).

19 Shum, H. P., Yan, W. W. & Chan, T. M. Recent knowledge on the pathophysiology of septic acute kidney injury: A narrative review. *Journal of critical care* **31**, 82-89, doi:10.1016/j.jcrc.2015.09.017 (2016).

20 Morrell, E. D., Kellum, J. A., Pastor-Soler, N. M. & Hallows, K. R. Septic acute kidney injury: molecular mechanisms and the importance of stratification and targeting therapy. *Critical Care* **18**, 501, doi:10.1186/s13054-014-0501-5 (2014).

21 Cerda, J. *et al.* Promoting Kidney Function Recovery in Patients with AKI Requiring RRT. *Clinical journal of the American Society of Nephrology : CJASN* **10**, 1859-1867, doi:10.2215/cjn.01170215 (2015).

22 Chertow, G. M., Burdick, E., Honour, M., Bonventre, J. V. & Bates, D. W. Acute kidney injury, mortality, length of stay, and costs in hospitalized patients. *Journal of the American Society of Nephrology : JASN* **16**, 3365-3370, doi:10.1681/asn.2004090740 (2005).

23 Hoste, E. A. *et al.* The epidemiology of cardiac surgery-associated acute kidney injury. *The International journal of artificial organs* **31**, 158-165 (2008).

24 Bellomo, R. *et al.* Acute renal failure – definition, outcome measures, animal models, fluid therapy and information technology needs: the Second International Consensus Conference of the Acute Dialysis Quality Initiative (ADQI) Group. *Critical Care* **8**, R204-R212, doi:10.1186/cc2872 (2004).

25 Mehta, R. L. *et al.* Acute Kidney Injury Network: report of an initiative to improve outcomes in acute kidney injury. *Critical care (London, England)* **11**, R31, doi:10.1186/cc5713 (2007).

26 Kidney Disease: Improving Global Outcomes (KDIGO) Acute Kidney Injury Work Group. KDIGO Clinical Practice Guidline for Acute Kidney Injury. *Kidney International Supplements* **2**, 1-138 (2012).

27 Basile, D. P., Anderson, M. D. & Sutton, T. A. Pathophysiology of Acute Kidney Injury. *Comprehensive Physiology* **2**, 1303-1353, doi:10.1002/cphy.c110041 (2012).

28 Berger, K. & Moeller, M. J. Mechanisms of epithelial repair and regeneration after acute kidney injury. *Seminars in nephrology* **34**, 394-403, doi:10.1016/j.semnephrol.2014.06.006 (2014).

29 Humphreys, B. D. *et al.* Repair of injured proximal tubule does not involve specialized progenitors. *Proceedings of the National Academy of Sciences of the United States of America* **108**, 9226-9231, doi:10.1073/pnas.1100629108 (2011).

30 Ferenbach, D. A. & Bonventre, J. V. Mechanisms of maladaptive repair after AKI leading to accelerated kidney ageing and CKD. *Nature reviews. Nephrology* **11**, 264-276, doi:10.1038/nrneph.2015.3 (2015).

31 Kidney Disease: Improving Global Outcomes (KDIGO) Chronic Kidney Disease Work Group. KDIGO Clinical Practice Guideline for the Evaluation and Management of Chronic Kidney Disease. *Kidney International Supplements* **3** (2013).

32 Hill, N. R. *et al.* Global Prevalence of Chronic Kidney Disease – A Systematic Review and Meta-Analysis. *PloS one* **11**, e0158765, doi:10.1371/journal.pone.0158765 (2016).

33 Suckling, R. & Gallagher, H. Chronic kidney disease, diabetes mellitus, and cardiovascular disease: risks and commonalities. *Journal of Renal Care* **38**, 4-11, doi:10.1111/j.1755-6686.2012.00274.x (2012).

34 Hall, M. E. *et al.* Obesity, hypertension, and chronic kidney disease. *International journal of nephrology and renovascular disease* **7**, 75-88, doi:10.2147/ijnrd.s39739 (2014).

35 Kokubo, Y. & Iwashima, Y. Higher blood pressure as a risk factor for diseases other than stroke and ischemic heart disease. *Hypertension (Dallas, Tex. : 1979)* **66**, 254-259, doi:10.1161/hypertensionaha.115.03480 (2015).

36 Snyder, S., Turner, G. A. & Turner, A. Obesity-related kidney disease. *Primary care* **41**, 875-893, doi:10.1016/j.pop.2014.08.008 (2014).

37 Taal, M. W. Chronic kidney disease in older people - diagnosis, aetiology and consequences. *Curr Opin Nephrol Hypertens* **24**, 475-479, doi:10.1097/mnh.0000000000000164 (2015).

38 Ferenbach, D. A. & Bonventre, J. V. Acute kidney injury and chronic kidney disease: From the laboratory to the clinic. *Nephrologie & therapeutique* **12 Suppl 1**, S41-48, doi:10.1016/j.nephro.2016.02.005 (2016).

39 Kazancioğlu, R. Risk factors for chronic kidney disease: an update. *Kidney International Supplements* **3**, 368-371, doi:10.1038/kisup.2013.79 (2013).

40 Vivante, A. & Hildebrandt, F. Exploring the genetic basis of early-onset chronic kidney disease. *Nature reviews. Nephrology* **12**, 133-146, doi:10.1038/nrneph.2015.205 (2016).

41 Neild, G. H. Primary renal disease in young adults with renal failure. *Nephrology, dialysis, transplantation : official publication of the European Dialysis and Transplant Association - European Renal Association* **25**, 1025-1032, doi:10.1093/ndt/gfp653 (2010).

42 Kjellstrand, C. M., Ebben, J. & Davin, T. Time of death, recovery of renal function, development of chronic renal failure and need for chronic hemodialysis in patients with acute tubular necrosis. *Transactions - American Society for Artificial Internal Organs* **27**, 45-50 (1981).

43 Edelstein, C. L. in *Biomarkers of Kidney Disease (Second edition)* 241-315 (Academic Press, 2017).

44 Eisner, C. *et al.* Major contribution of tubular secretion to creatinine clearance in mice. *Kidney international* **77**, 519-526, doi:10.1038/ki.2009.501 (2010).

45 Chawla, L. S., Eggers, P. W., Star, R. A. & Kimmel, P. L. Acute kidney injury and chronic kidney disease as interconnected syndromes. *The New England journal of medicine* **371**, 58-66, doi:10.1056/NEJMra1214243 (2014).

46 Chawla, L. S., Amdur, R. L., Amodeo, S., Kimmel, P. L. & Palant, C. E. The severity of acute kidney injury predicts progression to chronic kidney disease. *Kidney international* **79**, 1361-1369, doi:10.1038/ki.2011.42 (2011).

47 Jones, J. *et al.* Association of complete recovery from acute kidney injury with incident CKD stage 3 and all-cause mortality. *American journal of kidney diseases : the official journal of the National Kidney Foundation* **60**, 402-408, doi:10.1053/j.ajkd.2012.03.014 (2012).

48 Coca, S. G., Singanamala, S. & Parikh, C. R. Chronic kidney disease after acute kidney injury: a systematic review and meta-analysis. *Kidney international* **81**, 442-448, doi:10.1038/ki.2011.379 (2012).

49 Chawla, L. S. & Kimmel, P. L. Acute kidney injury and chronic kidney disease: an integrated clinical syndrome. *Kidney international* **82**, 516-524, doi:10.1038/ki.2012.208 (2012).

50 Yang, Y. *et al.* Renoprotective approaches and strategies in acute kidney injury. *Pharmacology & therapeutics* **163**, 58-73, doi:10.1016/j.pharmthera.2016.03.015 (2016).

51 Fleming, G. M. Renal replacement therapy review: Past, present and future. *Organogenesis* **7**, 2-12, doi:10.4161/org.7.1.13997 (2011).

52 NHS Choices. *Dialysis - How it's performed*, <http://www.nhs.uk/Conditions/Dialysis/Pages/How-haemodialysis-is-performed.aspx> (2015).

53 NHS Choices. *Dialysis - Risks and side effects* <http://www.nhs.uk/Conditions/Dialysis/Pages/Side-effects.aspx> (2015).

54 NHS Blood and Transplant. Organ Donation and Transplantation Activity Report. (2008/09 - 2015/16).

55 U.S. Department of Health & Human Services. *Organ Procurement and Transplant Network: National Data*, <https://optn.transplant.hrsa.gov/data/view-data-reports/national-data/#> (2017).

56 Metzger, R. A. *et al.* Expanded criteria donors for kidney transplantation. *Am J Transplant* **3 Suppl 4**, 114-125 (2003).

57 Aubert, O. *et al.* Long term outcomes of transplantation using kidneys from expanded criteria donors: prospective, population based cohort study. *BMJ (Clinical research ed.)* **351**, h3557, doi:10.1136/bmj.h3557 (2015).

58 van Ittersum, F. J. *et al.* Increased risk of graft failure and mortality in Dutch recipients receiving an expanded criteria donor kidney transplant. *Transplant international : official journal of the European Society for Organ Transplantation* **30**, 14-28, doi:10.1111/tri.12863 (2017).

59 Ma, M. K. *et al.* Mortality among Younger and Older Recipients of Kidney Transplants from Expanded Criteria Donors Compared with Standard Criteria Donors. *Clinical journal of the American Society of Nephrology : CJASN* **11**, 128-136, doi:10.2215/cjn.03760415 (2016).

60 Pellegrini, G. *et al.* From discovery to approval of an advanced therapy medicinal product-containing stem cells, in the EU. *Regen Med* **11**, 407-420, doi:10.2217/rme-2015-0051 (2016).

61 Reya, T., Morrison, S. J., Clarke, M. F. & Weissman, I. L. Stem cells, cancer, and cancer stem cells. *Nature* **414**, 105-111 (2001).

62 Stechman, M. J. *et al.* Establishing normal plasma and 24-hour urinary biochemistry ranges in C3H, BALB/c and C57BL/6J mice following acclimatization in metabolic cages. *Laboratory animals* **44**, 218-225, doi:10.1258/la.2010.009128 (2010).

63 Thomson, J. A. *et al.* Embryonic stem cell lines derived from human blastocysts. *Science (New York, N.Y.)* **282**, 1145-1147 (1998).

64 Hochedlinger, K. Embryonic stem cells: testing the germ-cell theory. *Current biology : CB* **21**, R850-852, doi:10.1016/j.cub.2011.09.024 (2011).

65 Andrews, P. W. *et al.* Embryonic stem (ES) cells and embryonal carcinoma (EC) cells: opposite sides of the same coin. *Biochemical Society transactions* **33**, 1526-1530, doi:10.1042/bst20051526 (2005).

66 Takahashi, K. *et al.* Induction of pluripotent stem cells from adult human fibroblasts by defined factors. *Cell* **131**, 861-872, doi:10.1016/j.cell.2007.11.019 (2007).

67 Takahashi, K. & Yamanaka, S. Induction of pluripotent stem cells from mouse embryonic and adult fibroblast cultures by defined factors. *Cell* **126**, 663-676, doi:10.1016/j.cell.2006.07.024 (2006).

68 Spangrude, G. J., Heimfeld, S. & Weissman, I. L. Purification and characterization of mouse hematopoietic stem cells. *Science (New York, N.Y.)* **241**, 58-62 (1988).

69 Baum, C. M., Weissman, I. L., Tsukamoto, A. S., Buckle, A. M. & Peault, B. Isolation of a candidate human hematopoietic stem-cell population. *Proceedings of the National Academy of Sciences of the United States of America* **89**, 2804-2808 (1992).

70 Osawa, M., Hanada, K.-i., Hamada, H. & Nakauchi, H. Long-Term Lymphohematopoietic Reconstitution by a Single CD34-Low/Negative Hematopoietic Stem Cell. *Science (New York, N.Y.)* **273**, 242-245, doi:10.1126/science.273.5272.242 (1996).

71 Tyndall, A. *et al.* Autologous haematopoietic stem cell transplants for autoimmune disease--feasibility and transplant-related mortality. Autoimmune Disease and Lymphoma Working Parties of the European Group for Blood and Marrow Transplantation, the European League Against Rheumatism and the International

Stem Cell Project for Autoimmune Disease. *Bone marrow transplantation* **24**, 729-734, doi:10.1038/sj.bmt.1701987 (1999).

72 Smith, A. R. & Wagner, J. E. Alternative Hematopoietic Stem Cell Sources for Transplantation: Place of Umbilical Cord Blood. *British journal of haematology* **147**, 246-261, doi:10.1111/j.1365-2141.2009.07828.x (2009).

73 Bianco, P., Riminucci, M., Gronthos, S. & Robey, P. G. Bone marrow stromal stem cells: nature, biology, and potential applications. *Stem Cells* **19**, 180-192, doi:10.1634/stemcells.19-3-180 (2001).

74 Uccelli, A., Moretta, L. & Pistoia, V. Mesenchymal stem cells in health and disease. *Nature reviews. Immunology* **8**, 726-736, doi:10.1038/nri2395 (2008).

75 Horwitz, E. M. *et al.* Clarification of the nomenclature for MSC: The International Society for Cellular Therapy position statement. *Cytotherapy* **7**, 393-395, doi:10.1080/14653240500319234 (2005).

76 Dominici, M. *et al.* Minimal criteria for defining multipotent mesenchymal stromal cells. The International Society for Cellular Therapy position statement. *Cytotherapy* **8**, 315-317, doi:10.1080/14653240600855905 (2006).

77 Friedenstein, A. J., Chailakhyan, R. K., Latsinik, N. V., Panasyuk, A. F. & Keiliss-Borok, I. V. Stromal cells responsible for transferring the microenvironment of the hemopoietic tissues. Cloning in vitro and retransplantation in vivo. *Transplantation* **17**, 331-340 (1974).

78 Erices, A., Conget, P. & Minguell, J. J. Mesenchymal progenitor cells in human umbilical cord blood. *Br J Haematol* **109**, 235-242 (2000).

79 Wang, H. S. *et al.* Mesenchymal stem cells in the Wharton's jelly of the human umbilical cord. *Stem Cells* **22**, 1330-1337, doi:10.1634/stemcells.2004-0013 (2004).

80 Zuk, P. A. *et al.* Human adipose tissue is a source of multipotent stem cells. *Molecular biology of the cell* **13**, 4279-4295, doi:10.1091/mbc.E02-02-0105 (2002).

81 In 't Anker, P. S. *et al.* Isolation of mesenchymal stem cells of fetal or maternal origin from human placenta. *Stem Cells* **22**, 1338-1345, doi:10.1634/stemcells.2004-0058 (2004).

82 da Silva Meirelles, L., Chagastelles, P. C. & Nardi, N. B. Mesenchymal stem cells reside in virtually all post-natal organs and tissues. *Journal of cell science* **119**, 2204-2213, doi:10.1242/jcs.02932 (2006).

83 Keating, A. Mesenchymal stromal cells: new directions. *Cell stem cell* **10**, 709-716, doi:10.1016/j.stem.2012.05.015 (2012).

84 Le Blanc, K., Tammik, C., Rosendahl, K., Zetterberg, E. & Ringden, O. HLA expression and immunologic properties of differentiated and undifferentiated mesenchymal stem cells. *Experimental hematology* **31**, 890-896 (2003).

85 Dotoli, G. M. *et al.* Mesenchymal stromal cell infusion to treat steroid-refractory acute GvHD III/IV after hematopoietic stem cell transplantation. *Bone marrow transplantation*, doi:10.1038/bmt.2017.35 (2017).

86 Cetin, M. *et al.* Additional infusions of mesenchymal stem cells improve response rate in multidrug-resistant GvHD patients. *Bone marrow transplantation*, doi:10.1038/bmt.2017.1 (2017).

87 Le Blanc, K. *et al.* Treatment of severe acute graft-versus-host disease with third party haploidentical mesenchymal stem cells. *Lancet (London, England)* **363**, 1439-1441, doi:10.1016/s0140-6736(04)16104-7 (2004).

88 Euro Stem Cell. *What diseases and conditions can be treated with stem cells?*, <http://www.eurostemcell.org/what-diseases-and-conditions-can-be-treated-stem-cells> (2017).

89 Sharkey, J. *et al.* Imaging technologies for monitoring the safety, efficacy and mechanisms of action of cell-based regenerative medicine therapies in models of

kidney disease. *European Journal of Pharmacology* **790**, 74-82, doi:10.1016/j.ejphar.2016.06.056 (2016).

90 Heslop, J. A. *et al.* Concise review: workshop review: understanding and assessing the risks of stem cell-based therapies. *Stem Cells Transl Med* **4**, 389-400, doi:10.5966/sctm.2014-0110 (2015).

91 Goldring, C. E. *et al.* Assessing the safety of stem cell therapeutics. *Cell stem cell* **8**, 618-628, doi:10.1016/j.stem.2011.05.012 (2011).

92 Sharpe, M. E., Morton, D. & Rossi, A. Nonclinical safety strategies for stem cell therapies. *Toxicology and applied pharmacology* **262**, 223-231, doi:10.1016/j.taap.2012.05.007 (2012).

93 Hewitson, T. D., Ono, T. & Becker, G. J. Small animal models of kidney disease: a review. *Methods in molecular biology (Clifton, N.J.)* **466**, 41-57, doi:10.1007/978-1-59745-352-3_4 (2009).

94 Yang, H.-C., Zuo, Y. & Fogo, A. B. Models of chronic kidney disease. *Drug discovery today. Disease models* **7**, 13-19, doi:10.1016/j.ddmod.2010.08.002 (2010).

95 Mehta, R. L. *et al.* Spectrum of acute renal failure in the intensive care unit: the PICARD experience. *Kidney international* **66**, 1613-1621, doi:10.1111/j.1523-1755.2004.00927.x (2004).

96 O'Neal, J. B., Shaw, A. D. & Billings, F. T. Acute kidney injury following cardiac surgery: current understanding and future directions. *Critical Care* **20**, 187, doi:10.1186/s13054-016-1352-z (2016).

97 Shin, S. R., Kim, W. H., Kim, D. J., Shin, I.-W. & Sohn, J.-T. Prediction and Prevention of Acute Kidney Injury after Cardiac Surgery. *BioMed Research International* **2016**, 10, doi:10.1155/2016/2985148 (2016).

98 Majumdar, A. Sepsis-induced acute kidney injury. *Indian journal of critical care medicine : peer-reviewed, official publication of Indian Society of Critical Care Medicine* **14**, 14-21, doi:10.4103/0972-5229.63031 (2010).

99 Ditonno, P. *et al.* Effects of ischemia-reperfusion injury in kidney transplantation: risk factors and early and long-term outcomes in a single center. *Transplant Proc* **45**, 2641-2644, doi:10.1016/j.transproceed.2013.07.025 (2013).

100 Saat, T. C., van den Akker, E. K., Ijzermans, J. N. M., Dor, F. J. M. F. & de Bruin, R. W. F. Improving the outcome of kidney transplantation by ameliorating renal ischemia reperfusion injury: lost in translation? *Journal of translational medicine* **14**, 20, doi:10.1186/s12967-016-0767-2 (2016).

101 Brezis, M. & Rosen, S. Hypoxia of the renal medulla--its implications for disease. *The New England journal of medicine* **332**, 647-655, doi:10.1056/nejm199503093321006 (1995).

102 Kalogeris, T., Baines, C. P., Krenz, M. & Korthuis, R. J. Cell Biology of Ischemia/Reperfusion Injury. *International review of cell and molecular biology* **298**, 229-317, doi:10.1016/B978-0-12-394309-5.00006-7 (2012).

103 Aksu, U., Demirci, C. & Ince, C. The pathogenesis of acute kidney injury and the toxic triangle of oxygen, reactive oxygen species and nitric oxide. *Contributions to nephrology* **174**, 119-128, doi:10.1159/000329249 (2011).

104 Bonventre, J. V. & Zuk, A. Ischemic acute renal failure: an inflammatory disease? *Kidney international* **66**, 480-485, doi:10.1111/j.1523-1755.2004.761_2.x (2004).

105 Jang, H. R. *et al.* Effect of preemptive treatment with human umbilical cord blood-derived mesenchymal stem cells on the development of renal ischemia-reperfusion injury in mice. *American journal of physiology. Renal physiology* **307**, F1149-1161, doi:10.1152/ajprenal.00555.2013 (2014).

106 Murray, P. J. & Wynn, T. A. Protective and pathogenic functions of macrophage subsets. *Nature reviews. Immunology* **11**, 723-737, doi:10.1038/nri3073 (2011).

107 Lee, S. *et al.* Distinct macrophage phenotypes contribute to kidney injury and repair. *Journal of the American Society of Nephrology : JASN* **22**, 317-326, doi:10.1681/asn.2009060615 (2011).

108 Ornellas, F. M. *et al.* Bone Marrow-Derived Mononuclear Cell Therapy Accelerates Renal Ischemia-Reperfusion Injury Recovery by Modulating Inflammatory, Antioxidant and Apoptotic Related Molecules. *Cellular physiology and biochemistry : international journal of experimental cellular physiology, biochemistry, and pharmacology* **41**, 1736-1752, doi:10.1159/000471866 (2017).

109 Wise, A. F. *et al.* Human mesenchymal stem cells alter macrophage phenotype and promote regeneration via homing to the kidney following ischemia-reperfusion injury. *American journal of physiology. Renal physiology* **306**, F1222-1235, doi:10.1152/ajprenal.00675.2013 (2014).

110 Xing, L. *et al.* Mesenchymal stem cells, not conditioned medium, contribute to kidney repair after ischemia-reperfusion injury. *Stem Cell Res Ther* **5**, 101, doi:10.1186/scrt489 (2014).

111 Zhuo, W. *et al.* Efficiency of endovenous versus arterial administration of mesenchymal stem cells for ischemia-reperfusion-induced renal dysfunction in rats. *Transplant Proc* **45**, 503-510, doi:10.1016/j.transproceed.2012.07.162 (2013).

112 Semedo, P. *et al.* Early modulation of inflammation by mesenchymal stem cell after acute kidney injury. *International immunopharmacology* **9**, 677-682, doi:10.1016/j.intimp.2008.12.008 (2009).

113 Zhou, L. *et al.* Comparison of human adipose stromal vascular fraction and adipose-derived mesenchymal stem cells for the attenuation of acute renal ischemia/reperfusion injury. *Sci Rep* **7**, 44058, doi:10.1038/srep44058 (2017).

114 Lin, K. C. *et al.* Combination of adipose-derived mesenchymal stem cells (ADMSC) and ADMSC-derived exosomes for protecting kidney from acute ischemia-reperfusion injury. *International journal of cardiology* **216**, 173-185, doi:10.1016/j.ijcard.2016.04.061 (2016).

115 Chen, Y. T. *et al.* Adipose-derived mesenchymal stem cell protects kidneys against ischemia-reperfusion injury through suppressing oxidative stress and inflammatory reaction. *Journal of translational medicine* **9**, 51, doi:10.1186/1479-5876-9-51 (2011).

116 Donizetti-Oliveira, C. *et al.* Adipose tissue-derived stem cell treatment prevents renal disease progression. *Cell transplantation* **21**, 1727-1741, doi:10.3727/096368911x623925 (2012).

117 Liang, C. J. *et al.* Endothelial Progenitor Cells Derived From Wharton's Jelly of Human Umbilical Cord Attenuate Ischemic Acute Kidney Injury by Increasing Vascularization and Decreasing Apoptosis, Inflammation, and Fibrosis. *Cell transplantation* **24**, 1363-1377, doi:10.3727/096368914x681720 (2015).

118 Li, W. *et al.* Macrophages are involved in the protective role of human umbilical cord-derived stromal cells in renal ischemia-reperfusion injury. *Stem cell research* **10**, 405-416, doi:10.1016/j.scr.2013.01.005 (2013).

119 Li, Q. *et al.* Transplantation of induced pluripotent stem cell-derived renal stem cells improved acute kidney injury. *Cell & bioscience* **5**, 45, doi:10.1186/s13578-015-0040-z (2015).

120 Ranghino, A. *et al.* The effects of glomerular and tubular renal progenitors and derived extracellular vesicles on recovery from acute kidney injury. *Stem Cell Res Ther* **8**, 24, doi:10.1186/s13287-017-0478-5 (2017).

121 Gupta, A. K., Jadhav, S. H., Tripathy, N. K. & Nityanand, S. Fetal Kidney Cells Can Ameliorate Ischemic Acute Renal Failure in Rats through Their Anti-Inflammatory, Anti-Apoptotic and Anti-Oxidative Effects. *PloS one* **10**, e0131057, doi:10.1371/journal.pone.0131057 (2015).

122 Sun, P. *et al.* Human endometrial regenerative cells attenuate renal ischemia reperfusion injury in mice. *Journal of translational medicine* **14**, 28, doi:10.1186/s12967-016-0782-3 (2016).
123 Schetz, M., Dasta, J., Goldstein, S. & Golper, T. Drug-induced acute kidney injury. *Current opinion in critical care* **11**, 555-565 (2005).
124 Uchino, S. *et al.* Acute renal failure in critically ill patients: a multinational, multicenter study. *Jama* **294**, 813-818, doi:10.1001/jama.294.7.813 (2005).
125 Miller, R. P., Tadagavadi, R. K., Ramesh, G. & Reeves, W. B. Mechanisms of Cisplatin Nephrotoxicity. *Toxins* **2**, 2490-2518, doi:10.3390/toxins2112490 (2010).
126 Perazella, M. A. & Moeckel, G. W. Nephrotoxicity from chemotherapeutic agents: clinical manifestations, pathobiology, and prevention/therapy. *Seminars in nephrology* **30**, 570-581, doi:10.1016/j.semnephrol.2010.09.005 (2010).
127 Moustafa, F. E. *et al.* Study of the Effect of Route of Administration of Mesenchymal Stem Cells on Cisplatin-Induced Acute Kidney Injury in Sprague Dawley Rats. *International journal of stem cells* **9**, 79-89, doi:10.15283/ijsc.2016.9.1.79 (2016).
128 Ramesh, G. & Ranganathan, P. Mouse models and methods for studying human disease, acute kidney injury (AKI). *Methods in molecular biology (Clifton, N.J.)* **1194**, 421-436, doi:10.1007/978-1-4939-1215-5_24 (2014).
129 Sharp, C. N. *et al.* Repeated administration of low-dose cisplatin in mice induces fibrosis. *American journal of physiology. Renal physiology* **310**, F560-568, doi:10.1152/ajprenal.00512.2015 (2016).
130 Morigi, M. *et al.* Mesenchymal stem cells are renotropic, helping to repair the kidney and improve function in acute renal failure. *Journal of the American Society of Nephrology : JASN* **15**, 1794-1804 (2004).
131 Morigi, M. *et al.* Human bone marrow mesenchymal stem cells accelerate recovery of acute renal injury and prolong survival in mice. *Stem Cells* **26**, 2075-2082, doi:10.1634/stemcells.2007-0795 (2008).
132 Ashour, R. H. *et al.* Comparative study of allogenic and xenogeneic mesenchymal stem cells on cisplatin-induced acute kidney injury in Sprague-Dawley rats. *Stem Cell Research & Therapy* **7**, 126, doi:10.1186/s13287-016-0386-0 (2016).
133 Yao, W. *et al.* Human adipose-derived mesenchymal stem cells repair cisplatin-induced acute kidney injury through antiapoptotic pathways. *Experimental and therapeutic medicine* **10**, 468-476, doi:10.3892/etm.2015.2505 (2015).
134 Santeramo, I. *et al.* Human kidney-derived cells ameliorate acute kidney injury without engrafting into renal tissue. *Stem Cells Translational Medicine (In Press)* (2017).
135 Imberti, B. *et al.* Renal progenitors derived from human iPSCs engraft and restore function in a mouse model of acute kidney injury. *Sci Rep* **5**, 8826, doi:10.1038/srep08826 (2015).
136 Bagshaw, S. M., George, C. & Bellomo, R. Early acute kidney injury and sepsis: a multicentre evaluation. *Critical care (London, England)* **12**, R47, doi:10.1186/cc6863 (2008).
137 Mehta, R. L. *et al.* Sepsis as a cause and consequence of acute kidney injury: Program to Improve Care in Acute Renal Disease. *Intensive care medicine* **37**, 241-248, doi:10.1007/s00134-010-2089-9 (2011).
138 Doi, K., Leelahavanichkul, A., Yuen, P. S. & Star, R. A. Animal models of sepsis and sepsis-induced kidney injury. *The Journal of clinical investigation* **119**, 2868-2878, doi:10.1172/jci39421 (2009).
139 Luo, J. *et al.* Mesenchymal-like progenitors derived from human embryonic stem cells promote recovery from acute kidney injury via paracrine actions. *Cytotherapy* **15**, 649-662, doi:10.1016/j.jcyt.2013.01.009 (2013).

140 Bosch, X., Poch, E. & Grau, J. M. Rhabdomyolysis and acute kidney injury. *The New England journal of medicine* **361**, 62-72, doi:10.1056/NEJMra0801327 (2009).
141 Elsayed, E. F. & Reilly, R. F. Rhabdomyolysis: a review, with emphasis on the pediatric population. *Pediatric nephrology (Berlin, Germany)* **25**, 7-18, doi:10.1007/s00467-009-1223-9 (2010).
142 Sauret, J. M., Marinides, G. & Wang, G. K. Rhabdomyolysis. *American family physician* **65**, 907-912 (2002).
143 Rabe, M. & Schaefer, F. Non-Transgenic Mouse Models of Kidney Disease. *Nephron* **133**, 53-61, doi:10.1159/000445171 (2016).
144 Geng, X. *et al.* Biological Membrane-Packed Mesenchymal Stem Cells Treat Acute Kidney Disease by Ameliorating Mitochondrial-Related Apoptosis. *Scientific Reports* **7**, 41136, doi:10.1038/srep41136

https://www.nature.com/articles/srep41136#supplementary-information (2017).
145 Geng, Y. *et al.* Mesenchymal stem cells ameliorate rhabdomyolysis-induced acute kidney injury via the activation of M2 macrophages. *Stem Cell Res Ther* **5**, 80, doi:10.1186/scrt469 (2014).
146 Hauser, P. V. *et al.* Stem cells derived from human amniotic fluid contribute to acute kidney injury recovery. *The American journal of pathology* **177**, 2011-2021, doi:10.2353/ajpath.2010.091245 (2010).
147 Angelotti, M. L. *et al.* Characterization of renal progenitors committed toward tubular lineage and their regenerative potential in renal tubular injury. *Stem Cells* **30**, 1714-1725, doi:10.1002/stem.1130 (2012).
148 Sagrinati, C. *et al.* Isolation and characterization of multipotent progenitor cells from the Bowman's capsule of adult human kidneys. *Journal of the American Society of Nephrology : JASN* **17**, 2443-2456, doi:10.1681/asn.2006010089 (2006).
149 Aggarwal, S., Grange, C., Iampietro, C., Camussi, G. & Bussolati, B. Human CD133(+) Renal Progenitor Cells Induce Erythropoietin Production and Limit Fibrosis After Acute Tubular Injury. *Scientific Reports* **6**, 37270, doi:10.1038/srep37270 (2016).
150 Herrera Sanchez, M. B. *et al.* Human liver stem cells and derived extracellular vesicles improve recovery in a murine model of acute kidney injury. *Stem Cell Res Ther* **5**, 124, doi:10.1186/scrt514 (2014).
151 Bussolati, B. *et al.* Isolation of renal progenitor cells from adult human kidney. *The American journal of pathology* **166**, 545-555, doi:10.1016/s0002-9440(10)62276-6 (2005).
152 Carvalho, C. *et al.* Doxorubicin: the good, the bad and the ugly effect. *Current medicinal chemistry* **16**, 3267-3285 (2009).
153 Medicines and Healthcare Products Regulatory Agency (MHRA). Public Assessment Report: Doxorubicin 2mg/ml Concentrate for Soloution for Infusion (doxorubicin hydrochloride).
154 Chatterjee, K., Zhang, J., Honbo, N. & Karliner, J. S. Doxorubicin Cardiomyopathy. *Cardiology* **115**, 155-162, doi:10.1159/000265166 (2010).
155 Zima, T. *et al.* ICRF-187 (dexrazoxan) protects from adriamycin-induced nephrotic syndrome in rats. *Nephrology, dialysis, transplantation : official publication of the European Dialysis and Transplant Association - European Renal Association* **13**, 1975-1979 (1998).
156 Deman, A. *et al.* Altered antioxidant defence in a mouse adriamycin model of glomerulosclerosis. *Nephrology, dialysis, transplantation : official publication of the European Dialysis and Transplant Association - European Renal Association* **16**, 147-150 (2001).

157 Gwinner, W. & Grone, H. J. Role of reactive oxygen species in glomerulonephritis. *Nephrology, dialysis, transplantation : official publication of the European Dialysis and Transplant Association - European Renal Association* **15**, 1127-1132 (2000).
158 Wang, H. *et al.* p47phox contributes to albuminuria and kidney fibrosis in mice. *Kidney international* **87**, 948-962, doi:10.1038/ki.2014.386 (2015).
159 Bertelli, R., Ginevri, F., Gusmano, R. & Ghiggeri, G. M. Cytotoxic effect of adriamycin and agarose-coupled adriamycin on glomerular epithelial cells: role of free radicals. *In vitro cellular & developmental biology : journal of the Tissue Culture Association* **27a**, 799-804 (1991).
160 Balbi, A. L., Franco, R. J. S., Barretti, P., Gavras, I. & Gavras, H. Renal artery clipping attenuates the progression of adriamycin nephropathy. *American Journal of Hypertension* **11**, 1124-1128, doi:https://doi.org/10.1016/S0895-7061(98)00119-8 (1998).
161 Zoja, C., Abbate, M. & Remuzzi, G. Progression of chronic kidney disease: insights from animal models. *Curr Opin Nephrol Hypertens* **15**, 250-257, doi:10.1097/01.mnh.0000222691.53970.83 (2006).
162 Yamashita, M., Yoshida, T., Suzuki, S., Homma, K. & Hayashi, M. Podocyte-specific NF-kappaB inhibition ameliorates proteinuria in adriamycin-induced nephropathy in mice. *Clin Exp Nephrol* **21**, 16-26, doi:10.1007/s10157-016-1268-6 (2017).
163 Jeansson, M., Björck, K., Tenstad, O. & Haraldsson, B. Adriamycin Alters Glomerular Endothelium to Induce Proteinuria. *Journal of the American Society of Nephrology : JASN* **20**, 114-122, doi:10.1681/ASN.2007111205 (2009).
164 Remuzzi, G., Ruggenenti, P. & Benigni, A. Understanding the nature of renal disease progression. *Kidney international* **51**, 2-15 (1997).
165 Zoja, C. *et al.* Protein overload stimulates RANTES production by proximal tubular cells depending on NF-kappa B activation. *Kidney international* **53**, 1608-1615, doi:10.1046/j.1523-1755.1998.00905.x (1998).
166 Abbate, M. *et al.* In progressive nephropathies, overload of tubular cells with filtered proteins translates glomerular permeability dysfunction into cellular signals of interstitial inflammation. *Journal of the American Society of Nephrology : JASN* **9**, 1213-1224 (1998).
167 Okuda, S. *et al.* Adriamycin-induced nephropathy as a model of chronic progressive glomerular disease. *Kidney international* **29**, 502-510 (1986).
168 Chen, A. *et al.* Experimental focal segmental glomerulosclerosis in mice. *Nephron* **78**, 440-452 (1998).
169 Lee, V. W. & Harris, D. C. Adriamycin nephropathy: a model of focal segmental glomerulosclerosis. *Nephrology (Carlton, Vic.)* **16**, 30-38, doi:10.1111/j.1440-1797.2010.01383.x (2011).
170 Zheng, Z. *et al.* A Mendelian locus on chromosome 16 determines susceptibility to doxorubicin nephropathy in the mouse. *Proceedings of the National Academy of Sciences of the United States of America* **102**, 2502-2507, doi:10.1073/pnas.0409786102 (2005).
171 Wang, Y., Wang, Y. P., Tay, Y. C. & Harris, D. C. Progressive adriamycin nephropathy in mice: sequence of histologic and immunohistochemical events. *Kidney international* **58**, 1797-1804, doi:10.1046/j.1523-1755.2000.00342.x (2000).
172 Lee, V. W. *et al.* Adriamycin nephropathy in severe combined immunodeficient (SCID) mice. *Nephrology, dialysis, transplantation : official publication of the European Dialysis and Transplant Association - European Renal Association* **21**, 3293-3298, doi:10.1093/ndt/gfl413 (2006).
173 Wang, Y. *et al.* Depletion of CD4+ T cells aggravates glomerular and interstitial injury in murine adriamycin nephropathy. *Kidney International Supplements* **59**, 975-984, doi:10.1046/j.1523-1755.2001.059003975.x (2001).

174 Wang, Y., Wang, Y. P., Tay, Y.-C. & Harris, D. C. H. Role of CD8+ cells in the progression of murine adriamycin nephropathy. *Kidney international* **59**, 941-949, doi:10.1046/j.1523-1755.2001.059003941.x (2001).

175 Bosma, G. C., Custer, R. P. & Bosma, M. J. A severe combined immunodeficiency mutation in the mouse. *Nature* **301**, 527-530 (1983).

176 Zheng, G. *et al.* NK cells do not mediate renal injury in murine adriamycin nephropathy. *Kidney international* **69**, 1159-1165, doi:10.1038/sj.ki.5000244 (2006).

177 Wang, Y. *et al.* Partial depletion of macrophages by ED7 reduces renal injury in Adriamycin nephropathy. *Nephrology (Carlton, Vic.)* **10**, 470-477, doi:10.1111/j.1440-1797.2005.00438.x (2005).

178 Wang, Y. *et al.* By Homing to the Kidney, Activated Macrophages Potently Exacerbate Renal Injury. *The American journal of pathology* **172**, 1491-1499, doi:10.2353/ajpath.2008.070825 (2008).

179 Rangan, G. K., Wang, Y., Tay, Y. C. & Harris, D. C. Inhibition of nuclear factor-kappaB activation reduces cortical tubulointerstitial injury in proteinuric rats. *Kidney international* **56**, 118-134, doi:10.1046/j.1523-1755.1999.00529.x (1999).

180 Guo, J. *et al.* Protective effects of mesenchymal stromal cells on adriamycin-induced minimal change nephrotic syndrome in rats and possible mechanisms. *Cytotherapy* **16**, 471-484, doi:10.1016/j.jcyt.2013.08.002 (2014).

181 Anan, H. H., Zidan, R. A., Shaheen, M. A. & Abd- El Fattah, E. A. Therapeutic efficacy of bone marrow derived mesenchymal stromal cells versus losartan on adriamycin-induced renal cortical injury in adult albino rats. *Cytotherapy* **18**, 970-984, doi:10.1016/j.jcyt.2016.05.004 (2016).

182 Zoja, C. *et al.* Mesenchymal stem cell therapy promotes renal repair by limiting glomerular podocyte and progenitor cell dysfunction in adriamycin-induced nephropathy. *American journal of physiology. Renal physiology* **303**, F1370-1381, doi:10.1152/ajprenal.00057.2012 (2012).

183 Sarhan, M. *et al.* Impact of bone-marrow-derived mesenchymal stem cells on adriamycin-induced chronic nephropathy. *Canadian journal of physiology and pharmacology* **92**, 733-743, doi:10.1139/cjpp-2013-0503 (2014).

184 Magnasco, A. *et al.* Mesenchymal stem cells protective effect in adriamycin model of nephropathy. *Cell transplantation* **17**, 1157-1167 (2008).

185 Ronconi, E. *et al.* Regeneration of glomerular podocytes by human renal progenitors. *Journal of the American Society of Nephrology : JASN* **20**, 322-332, doi:10.1681/asn.2008070709 (2009).

186 Chevalier, R. L. Congenital urinary tract obstruction: the long view. *Advances in chronic kidney disease* **22**, 312-319, doi:10.1053/j.ackd.2015.01.012 (2015).

187 Warady, B. A. & Chadha, V. Chronic kidney disease in children: the global perspective. *Pediatric nephrology (Berlin, Germany)* **22**, 1999-2009, doi:10.1007/s00467-006-0410-1 (2007).

188 Eddy, A. A., Lopez-Guisa, J. M., Okamura, D. M. & Yamaguchi, I. Investigating mechanisms of chronic kidney disease in mouse models. *Pediatric nephrology (Berlin, Germany)* **27**, 1233-1247, doi:10.1007/s00467-011-1938-2 (2012).

189 Chevalier, R. L., Forbes, M. S. & Thornhill, B. A. Ureteral obstruction as a model of renal interstitial fibrosis and obstructive nephropathy. *Kidney international* **75**, 1145-1152, doi:10.1038/ki.2009.86 (2009).

190 Chevalier, R. L., Kim, A., Thornhill, B. A. & Wolstenholme, J. T. Recovery following relief of unilateral ureteral obstruction in the neonatal rat. *Kidney international* **55**, 793-807, doi:10.1046/j.1523-1755.1999.055003793.x (1999).

191 Hesketh, E. E. *et al.* A Murine Model of Irreversible and Reversible Unilateral Ureteric Obstruction. *Journal of visualized experiments : JoVE*, 52559, doi:10.3791/52559 (2014).

192 da Silva, A. F., Silva, K., Reis, L. A., Teixeira, V. P. C. & Schor, N. Bone marrow-derived mesenchymal stem cells and their conditioned medium attenuate fibrosis in an irreversible model of unilateral ureteral obstruction. *Cell transplantation* **24**, 2657-2666, doi:10.3727/096368915X687534 (2015).

193 Wang, B. *et al.* Mesenchymal Stem Cells Deliver Exogenous MicroRNA-let7c via Exosomes to Attenuate Renal Fibrosis. *Molecular therapy : the journal of the American Society of Gene Therapy* **24**, 1290-1301, doi:10.1038/mt.2016.90 (2016).

194 Song, Y. *et al.* Adipose-derived stem cells ameliorate renal interstitial fibrosis through inhibition of EMT and inflammatory response via TGF-β1 signaling pathway. *International immunopharmacology* **44**, 115-122, doi:10.1016/j.intimp.2017.01.008 (2017).

195 Caskey, F. *et al.* UK Renal Registry: 18th Annual Report of the Renal Association. *Nephron* **132** (2016).

196 Shaw, J. E., Sicree, R. A. & Zimmet, P. Z. Global estimates of the prevalence of diabetes for 2010 and 2030. *Diabetes research and clinical practice* **87**, 4-14, doi:10.1016/j.diabres.2009.10.007 (2010).

197 Leslie, R. D., Williams, R. & Pozzilli, P. Clinical review: Type 1 diabetes and latent autoimmune diabetes in adults: one end of the rainbow. *The Journal of clinical endocrinology and metabolism* **91**, 1654-1659, doi:10.1210/jc.2005-1623 (2006).

198 Olokoba, A. B., Obateru, O. A. & Olokoba, L. B. Type 2 Diabetes Mellitus: A Review of Current Trends. *Oman Medical Journal* **27**, 269-273, doi:10.5001/omj.2012.68 (2012).

199 Papadopoulou-Marketou, N., Chrousos, G. P. & Kanaka-Gantenbein, C. Diabetic nephropathy in type 1 diabetes: a review of early natural history, pathogenesis, and diagnosis. *Diabetes/Metabolism Research and Reviews* **33**, e2841-n/a, doi:10.1002/dmrr.2841 (2017).

200 Gross, J. L. *et al.* Diabetic nephropathy: diagnosis, prevention, and treatment. *Diabetes care* **28**, 164-176 (2005).

201 Breyer, M. D. *et al.* Mouse models of diabetic nephropathy. *Journal of the American Society of Nephrology : JASN* **16**, 27-45, doi:10.1681/asn.2004080648 (2005).

202 Mallipattu, S. K. *et al.* Diabetic nephropathy in a nonobese mouse model of type 2 diabetes mellitus. *American journal of physiology. Renal physiology* **306**, F1008-1017, doi:10.1152/ajprenal.00597.2013 (2014).

203 Pugliese, G. Updating the natural history of diabetic nephropathy. *Acta diabetologica* **51**, 905-915, doi:10.1007/s00592-014-0650-7 (2014).

204 Betz, B. & Conway, B. R. An Update on the Use of Animal Models in Diabetic Nephropathy Research. *Curr Diab Rep* **16**, 18, doi:10.1007/s11892-015-0706-2 (2016).

205 Paulini, J., Higuti, E., Bastos, R. M., Gomes, S. A. & Rangel, E. B. Mesenchymal Stem Cells as Therapeutic Candidates for Halting the Progression of Diabetic Nephropathy. *Stem Cells Int* **2016**, 9521629, doi:10.1155/2016/9521629 (2016).

206 Ezquer, F. E. *et al.* Systemic administration of multipotent mesenchymal stromal cells reverts hyperglycemia and prevents nephropathy in type 1 diabetic mice. *Biol Blood Marrow Transplant* **14**, 631-640, doi:10.1016/j.bbmt.2008.01.006 (2008).

207 Nagaishi, K. *et al.* Mesenchymal stem cell therapy ameliorates diabetic nephropathy via the paracrine effect of renal trophic factors including exosomes. *Scientific Reports* **6**, doi:10.1038/srep34842 (2016).

208 Schnaper, H. W. Remnant nephron physiology and the progression of chronic kidney disease. *Pediatric nephrology (Berlin, Germany)* **29**, 193-202, doi:10.1007/s00467-013-2494-8 (2014).

209 Luyckx, V. A., Shukha, K. & Brenner, B. M. Low nephron number and its clinical consequences. *Rambam Maimonides medical journal* **2**, e0061, doi:10.5041/rmmj.10061 (2011).

210 Huang, W. C. *et al.* Chronic kidney disease after nephrectomy in patients with renal cortical tumours: a retrospective cohort study. *The lancet oncology* **7**, 735-740, doi:10.1016/S1470-2045(06)70803-8 (2006).

211 Schachtner, T. & Reinke, P. Estimated nephron number of the remaining donor kidney: impact on living kidney donor outcomes. *Nephrology, dialysis, transplantation : official publication of the European Dialysis and Transplant Association - European Renal Association* **31**, 1523-1530, doi:10.1093/ndt/gfv458 (2016).

212 Zhang, Y. & Kompa, A. R. A practical guide to subtotal nephrectomy in the rat with subsequent methodology for assessing renal and cardiac function. *Nephrology (Carlton, Vic.)* **19**, 552-561, doi:10.1111/nep.12279 (2014).

213 Kren, S. & Hostetter, T. H. The course of the remnant kidney model in mice. *Kidney international* **56**, 333-337, doi:10.1046/j.1523-1755.1999.00527.x (1999).

214 Leelahavanichkul, A. *et al.* Rapid CKD progression in a new mouse kidney remnant model: strain-dependent resistance is overcome by angiotensin II. *Kidney international* **78**, 1136-1153, doi:10.1038/ki.2010.287 (2010).

215 Choi, S. *et al.* The role of mesenchymal stem cells in the functional improvement of chronic renal failure. *Stem cells and development* **18**, 521-529, doi:10.1089/scd.2008.0097 (2009).

216 Semedo, P. *et al.* Mesenchymal stem cells attenuate renal fibrosis through immune modulation and remodeling properties in a rat remnant kidney model. *Stem Cells* **27**, 3063-3073, doi:10.1002/stem.214 (2009).

217 Lee, S. R. *et al.* Repeated administration of bone marrow-derived mesenchymal stem cells improved the protective effects on a remnant kidney model. *Ren Fail* **32**, 840-848, doi:10.3109/0886022x.2010.494803 (2010).

218 Villanueva, S. *et al.* Mesenchymal stem cell injection ameliorates chronic renal failure in a rat model. *Clinical science (London, England : 1979)* **121**, 489-499, doi:10.1042/cs20110108 (2011).

219 Caldas, H. C. *et al.* Comparative effects of mesenchymal stem cell therapy in distinct stages of chronic renal failure. *Clinical and Experimental Nephrology* **19**, 783-789, doi:10.1007/s10157-015-1079-1 (2015).

220 Becker, G. J. & Hewitson, T. D. Animal models of chronic kidney disease: useful but not perfect. *Nephrology, dialysis, transplantation : official publication of the European Dialysis and Transplant Association - European Renal Association* **28**, 2432-2438, doi:10.1093/ndt/gft071 (2013).

221 de Caestecker, M. *et al.* Bridging Translation by Improving Preclinical Study Design in AKI. *Journal of the American Society of Nephrology : JASN* **26**, 2905-2916, doi:10.1681/asn.2015070832 (2015).

222 Skrypnyk, N. I., Siskind, L. J., Faubel, S. & de Caestecker, M. P. Bridging translation for acute kidney injury with better preclinical modeling of human disease. *American Journal of Physiology - Renal Physiology* **310**, F972-F984, doi:10.1152/ajprenal.00552.2015 (2016).

223 Chawla, A., Chawla, R. & Jaggi, S. Microvasular and macrovascular complications in diabetes mellitus: Distinct or continuum? *Indian Journal of Endocrinology and Metabolism* **20**, 546-551, doi:10.4103/2230-8210.183480 (2016).

224 Hassoun, H. T. *et al.* Ischemic acute kidney injury induces a distant organ functional and genomic response distinguishable from bilateral nephrectomy. *American journal of physiology. Renal physiology* **293**, F30-40, doi:10.1152/ajprenal.00023.2007 (2007).
225 Waikar, S. S., Betensky, R. A., Emerson, S. C. & Bonventre, J. V. Imperfect gold standards for kidney injury biomarker evaluation. *Journal of the American Society of Nephrology : JASN* **23**, 13-21, doi:10.1681/asn.2010111124 (2012).
226 Sharma, A., Mucino, M. J. & Ronco, C. Renal functional reserve and renal recovery after acute kidney injury. *Nephron. Clinical practice* **127**, 94-100, doi:10.1159/000363721 (2014).
227 Thomas, D. M., Coles, G. A. & Williams, J. D. What does the renal reserve mean? *Kidney international* **45**, 411-416 (1994).
228 Bonventre, J. V. Kidney injury molecule-1 (KIM-1): a urinary biomarker and much more. *Nephrology, dialysis, transplantation : official publication of the European Dialysis and Transplant Association - European Renal Association* **24**, 3265-3268, doi:10.1093/ndt/gfp010 (2009).
229 Hoppe, C. C., Moritz, K. M., Fitzgerald, S. M., Bertram, J. F. & Evans, R. G. Transient hypertension and sustained tachycardia in mice housed individually in metabolism cages. *Physiological research* **58**, 69-75 (2009).
230 Tsai, P. P. *et al.* Effects of different blood collection methods on indicators of welfare in mice. *Lab animal* **44**, 301-310, doi:10.1038/laban.738 (2015).
231 Madetoja, J., Madetoja, M., MÃ¤kinen, J., Riuttala, E. & Jokinen, J. Blood Sampling from the Tail Vein, in Comparison with Two Other Techniques, Causes Less Stress to Mice. *Scandinavian Journal of Laboratory Animal Science* **36**, 215-221 (2009).
232 Ellery, S. J., Cai, X., Walker, D. D., Dickinson, H. & Kett, M. M. Transcutaneous measurement of glomerular filtration rate in small rodents: through the skin for the win? *Nephrology (Carlton, Vic.)* **20**, 117-123, doi:10.1111/nep.12363 (2015).
233 Herrera Pérez, Z., Weinfurter, S. & Gretz, N. Transcutaneous Assessment of Renal Function in Conscious Rodents. *Journal of visualized experiments : JoVE*, 53767, doi:10.3791/53767 (2016).
234 Schreiber, A. *et al.* Transcutaneous measurement of renal function in conscious mice. *American journal of physiology. Renal physiology* **303**, F783-788, doi:10.1152/ajprenal.00279.2012 (2012).
235 Pill, J. *et al.* Pharmacological profile and toxicity of fluorescein-labelled sinistrin, a novel marker for GFR measurements. *Naunyn-Schmiedeberg's archives of pharmacology* **373**, 204-211, doi:10.1007/s00210-006-0067-0 (2006).
236 Pill, J. *et al.* Fluorescein-labeled sinistrin as marker of glomerular filtration rate. *European journal of medicinal chemistry* **40**, 1056-1061, doi:10.1016/j.ejmech.2005.03.020 (2005).
237 Schock-Kusch, D. *et al.* Transcutaneous assessment of renal function in conscious rats with a device for measuring FITC-sinistrin disappearance curves. *Kidney international* **79**, 1254-1258, doi:10.1038/ki.2011.31 (2011).
238 Schock-Kusch, D. *et al.* Reliability of transcutaneous measurement of renal function in various strains of conscious mice. *PloS one* **8**, e71519, doi:10.1371/journal.pone.0071519 (2013).
239 Fusellier, M. *et al.* Influence of three anesthetic protocols on glomerular filtration rate in dogs. *American journal of veterinary research* **68**, 807-811, doi:10.2460/ajvr.68.8.807 (2007).
240 Mazze, R. I., Cousins, M. J. & Barr, G. A. Renal effects and metabolism of isoflurane in man. *Anesthesiology* **40**, 536-542 (1974).

241 Rieg, T. A High-throughput method for measurement of glomerular filtration rate in conscious mice. *Journal of visualized experiments : JoVE*, e50330, doi:10.3791/50330 (2013).
242 Cowley, A. W., Jr. *et al.* Progression of glomerular filtration rate reduction determined in conscious Dahl salt-sensitive hypertensive rats. *Hypertension (Dallas, Tex. : 1979)* **62**, 85-90, doi:10.1161/hypertensionaha.113.01194 (2013).
243 Su, Z. *et al.* Longitudinal Changes in Measured Glomerular Filtration Rate, Renal Fibrosis and Biomarkers in a Rat Model of Type 2 Diabetic Nephropathy. *Am J Nephrol* **44**, 339-353, doi:10.1159/000449324 (2016).
244 Ma, Q., Steiger, S. & Anders, H. J. Sodium glucose transporter-2 inhibition has no renoprotective effects on non-diabetic chronic kidney disease. *Physiological reports* **5**, e13228, doi:10.14814/phy2.13228 (2017).
245 Sims, C. R. *et al.* Rolipram Improves Outcome in a Rat Model of Infant Sepsis-Induced Cardiorenal Syndrome. *Frontiers in pharmacology* **8**, 237, doi:10.3389/fphar.2017.00237 (2017).
246 Dorshow, R. B. in *Renal Business Today* (2013).
247 Dorshow, R. B., Debreczeny, M. P., Fink, J. C. & Dowling, T. C. in *American Society of Nephrology Kidney Week*.
248 Taruttis, A., Morscher, S., Burton, N. C., Razansky, D. & Ntziachristos, V. Fast Multispectral Optoacoustic Tomography (MSOT) for Dynamic Imaging of Pharmacokinetics and Biodistribution in Multiple Organs. *PloS one* **7**, e30491, doi:10.1371/journal.pone.0030491 (2012).
249 Marshall, M. V., Draney, D., Sevick-Muraca, E. M. & Olive, D. M. Single-dose intravenous toxicity study of IRDye 800CW in Sprague-Dawley rats. *Molecular imaging and biology : MIB : the official publication of the Academy of Molecular Imaging* **12**, 583-594, doi:10.1007/s11307-010-0317-x (2010).
250 Bell, A. G. On the production and reproduction of sound by light. *Am J Sci* **20**, 305-324, doi:10.2475/ajs.s3-20.118.305 (1880).
251 Xu, M. & Wang, L. V. Photoacoustic imaging in biomedicine. *Review of Scientific Instruments* **77**, 041101, doi:10.1063/1.2195024 (2006).
252 Yao, J. & Wang, L. V. Photoacoustic tomography: fundamentals, advances and prospects. *Contrast media & molecular imaging* **6**, 332-345, doi:10.1002/cmmi.443 (2011).
253 Ma, R., Taruttis, A., Ntziachristos, V. & Razansky, D. Multispectral optoacoustic tomography (MSOT) scanner for whole-body small animal imaging. *Optics express* **17**, 21414-21426, doi:10.1364/oe.17.021414 (2009).
254 Buehler, A., Deán-Ben, X. L., Claussen, J., Ntziachristos, V. & Razansky, D. Three-dimensional optoacoustic tomography at video rate. *Optics express* **20**, 22712-22719, doi:10.1364/OE.20.022712 (2012).
255 Dima, A., Burton, N. C. & Ntziachristos, V. Multispectral optoacoustic tomography at 64, 128, and 256 channels. *Journal of biomedical optics* **19**, 36021, doi:10.1117/1.jbo.19.3.036021 (2014).
256 Ermolayev, V., Dean-Ben, X. L., Mandal, S., Ntziachristos, V. & Razansky, D. Simultaneous visualization of tumour oxygenation, neovascularization and contrast agent perfusion by real-time three-dimensional optoacoustic tomography. *European radiology* **26**, 1843-1851, doi:10.1007/s00330-015-3980-0 (2016).
257 McNally, L. R. *et al.* Current and Emerging Clinical Applications of Multispectral Optoacoustic Tomography (MSOT) in Oncology. *Clin Cancer Res* **22**, 3432-3439, doi:10.1158/1078-0432.ccr-16-0573 (2016).
258 Taruttis, A. *et al.* Optoacoustic Imaging of Human Vasculature: Feasibility by Using a Handheld Probe. *Radiology* **281**, 256-263, doi:10.1148/radiol.2016152160 (2016).

259 Waldner, M. J. *et al.* Multispectral Optoacoustic Tomography in Crohn's Disease: Noninvasive Imaging of Disease Activity. *Gastroenterology* **151**, 238-240, doi:10.1053/j.gastro.2016.05.047 (2016).

260 James, M. L. & Gambhir, S. S. A molecular imaging primer: modalities, imaging agents, and applications. *Physiological reviews* **92**, 897-965, doi:10.1152/physrev.00049.2010 (2012).

261 Bentzon, J. F. *et al.* Tissue distribution and engraftment of human mesenchymal stem cells immortalized by human telomerase reverse transcriptase gene. *Biochemical and biophysical research communications* **330**, 633-640, doi:10.1016/j.bbrc.2005.03.072 (2005).

262 National Centre for the Replacement Refinement and Reduction of Animals in Research. *The NC3Rs*, <https://www.nc3rs.org.uk/> (2017).

263 Li, P. *et al.* PKH26 can transfer to host cells in vitro and vivo. *Stem cells and development* **22**, 340-344, doi:10.1089/scd.2012.0357 (2013).

264 Kim, J. E., Kalimuthu, S. & Ahn, B.-C. In Vivo Cell Tracking with Bioluminescence Imaging. *Nuclear Medicine and Molecular Imaging* **49**, 3-10, doi:10.1007/s13139-014-0309-x (2015).

265 Paley, M. A. & Prescher, J. A. Bioluminescence: a versatile technique for imaging cellular and molecular features. *MedChemComm* **5**, 255-267, doi:10.1039/C3MD00288H (2014).

266 Lyons, S. K., Patrick, P. S. & Brindle, K. M. Imaging mouse cancer models in vivo using reporter transgenes. *Cold Spring Harbor protocols* **2013**, 685-699, doi:10.1101/pdb.top069864 (2013).

267 Togel, F., Yang, Y., Zhang, P., Hu, Z. & Westenfelder, C. Bioluminescence imaging to monitor the in vivo distribution of administered mesenchymal stem cells in acute kidney injury. *American journal of physiology. Renal physiology* **295**, F315-321, doi:10.1152/ajprenal.00098.2008 (2008).

268 Katsuoka, Y. *et al.* Intra-arterial catheter system to repeatedly deliver mesenchymal stem cells in a rat renal failure model. *Clin Exp Nephrol* **20**, 169-177, doi:10.1007/s10157-015-1161-8 (2016).

269 Gao, J. *et al.* The use of chitosan based hydrogel for enhancing the therapeutic benefits of adipose-derived MSCs for acute kidney injury. *Biomaterials* **33**, 3673-3681, doi:10.1016/j.biomaterials.2012.01.061 (2012).

270 Zhang, Z. *et al.* Autophagy mediates the beneficial effect of hypoxic preconditioning on bone marrow mesenchymal stem cells for the therapy of myocardial infarction. *Stem Cell Res Ther* **8**, 89, doi:10.1186/s13287-017-0543-0 (2017).

271 Chen, H. *et al.* Mesenchymal Stem Cells Combined with Hepatocyte Growth Factor Therapy for Attenuating Ischaemic Myocardial Fibrosis: Assessment using Multimodal Molecular Imaging. *Sci Rep* **6**, 33700, doi:10.1038/srep33700 (2016).

272 Riegler, J. *et al.* Human Engineered Heart Muscles Engraft and Survive Long Term in a Rodent Myocardial Infarction Model. *Circulation research* **117**, 720-730, doi:10.1161/circresaha.115.306985 (2015).

273 Cao, J. *et al.* Dual-modular molecular imaging to trace transplanted bone mesenchymal stromal cells in an acute myocardial infarction model. *Cytotherapy* **17**, 1365-1373, doi:10.1016/j.jcyt.2015.05.003 (2015).

274 Li, Z. *et al.* Optimization of mesenchymal stem cells (MSCs) delivery dose and route in mice with acute liver injury by bioluminescence imaging. *Molecular imaging and biology : MIB : the official publication of the Academy of Molecular Imaging* **17**, 185-194, doi:10.1007/s11307-014-0792-6 (2015).

275 Liu, J. J. *et al.* In Vivo Bioluminescence Imaging of Transplanted Mesenchymal Stromal Cells and Their Rejection Mediated by Intrahepatic NK Cells. *Molecular*

imaging and biology : MIB : the official publication of the Academy of Molecular Imaging **19**, 31-40, doi:10.1007/s11307-016-0962-9 (2017).

276 Ho, S. S. *et al.* Bone Morphogenetic Protein-2 Promotes Human Mesenchymal Stem Cell Survival and Resultant Bone Formation When Entrapped in Photocrosslinked Alginate Hydrogels. *Advanced healthcare materials* **5**, 2501-2509, doi:10.1002/adhm.201600461 (2016).

277 Manassero, M. *et al.* Comparison of Survival and Osteogenic Ability of Human Mesenchymal Stem Cells in Orthotopic and Ectopic Sites in Mice. *Tissue engineering. Part A* **22**, 534-544, doi:10.1089/ten.TEA.2015.0346 (2016).

278 Lee, S. W., Jeon, T. J. & Biswal, S. Fracture Healing Effects of Locally-Administered Adipose Tissue-Derived Cells. *Yonsei medical journal* **56**, 1106-1113, doi:10.3349/ymj.2015.56.4.1106 (2015).

279 Song, M. *et al.* Dynamic Tracking Human Mesenchymal Stem Cells Tropism following Smoke Inhalation Injury in NOD/SCID Mice. *Stem Cells Int* **2016**, 1691856, doi:10.1155/2016/1691856 (2016).

280 Martinez-Gonzalez, I. *et al.* Human mesenchymal stem cells overexpressing the IL-33 antagonist soluble IL-1 receptor-like-1 attenuate endotoxin-induced acute lung injury. *American journal of respiratory cell and molecular biology* **49**, 552-562, doi:10.1165/rcmb.2012-0406OC (2013).

281 Gálisová, A. *et al.* Multimodal Imaging Reveals Improvement of Blood Supply to an Artificial Cell Transplant Site Induced by Bioluminescent Mesenchymal Stem Cells. *Molecular Imaging and Biology* **19**, 15-23, doi:10.1007/s11307-016-0986-1 (2017).

282 Swart, J. F. *et al.* Mesenchymal stem cell therapy in proteoglycan induced arthritis. *Annals of the rheumatic diseases* **74**, 769-777, doi:10.1136/annrheumdis-2013-204147 (2015).

283 Auletta, J. J. *et al.* Human mesenchymal stromal cells attenuate graft-versus-host disease and maintain graft-versus-leukemia activity following experimental allogeneic bone marrow transplantation. *Stem Cells* **33**, 601-614, doi:10.1002/stem.1867 (2015).

284 Ferreira-Teixeira, M. *et al.* Natural killer cell-based adoptive immunotherapy eradicates and drives differentiation of chemoresistant bladder cancer stem-like cells. *BMC Med* **14**, 163, doi:10.1186/s12916-016-0715-2 (2016).

285 Rong, X. X. *et al.* Recognition and killing of cancer stem-like cell population in hepatocellular carcinoma cells by cytokine-induced killer cells via NKG2d-ligands recognition. *Oncoimmunology* **5**, e1086060, doi:10.1080/2162402x.2015.1086060 (2016).

286 Meleshina, A. V. *et al.* Influence of mesenchymal stem cells on metastasis development in mice in vivo. *Stem Cell Res Ther* **6**, 15, doi:10.1186/s13287-015-0003-7 (2015).

287 Leten, C. *et al.* Controlling and monitoring stem cell safety in vivo in an experimental rodent model. *Stem Cells* **32**, 2833-2844, doi:10.1002/stem.1819 (2014).

288 Vilalta, M. *et al.* Biodistribution, long-term survival, and safety of human adipose tissue-derived mesenchymal stem cells transplanted in nude mice by high sensitivity non-invasive bioluminescence imaging. *Stem cells and development* **17**, 993-1003, doi:10.1089/scd.2007.0201 (2008).

289 Kagawa, T. *et al.* Basic principles of magnetic resonance imaging for beginner oral and maxillofacial radiologists. *Oral Radiology* **33**, 92-100, doi:10.1007/s11282-017-0274-z (2017).

290 van Geuns, R. J. *et al.* Basic principles of magnetic resonance imaging. *Progress in cardiovascular diseases* **42**, 149-156 (1999).

291 Barrow, M. *et al.* Co-precipitation of DEAE-dextran coated SPIONs: how synthesis conditions affect particle properties, stem cell labelling and MR contrast. *Contrast Media and Molecular Imaging* **11**, 362-370, doi:10.1002/cmmi.1700 (2016).

292 Barrow, M., Taylor, A., Murray, P., Rosseinsky, M. J. & Adams, D. J. Design considerations for the synthesis of polymer coated iron oxide nanoparticles for stem cell labelling and tracking using MRI. *Chemical Society reviews* **44**, 6733-6748, doi:10.1039/c5cs00331h (2015).

293 Barrow, M. *et al.* Tailoring the surface charge of dextran-based polymer coated SPIONs for modulated stem cell uptake and MRI contrast. *Biomaterials Science* **3**, 608-616, doi:10.1039/c5bm00011d (2015).

294 Pereira, S. M., Moss, D., Williams, S. R., Murray, P. & Taylor, A. Overexpression of the MRI Reporter Genes Ferritin and Transferrin Receptor Affect Iron Homeostasis and Produce Limited Contrast in Mesenchymal Stem Cells. *International journal of molecular sciences* **16**, 15481-15496, doi:10.3390/ijms160715481 (2015).

295 Yang, C., Tian, R., Liu, T. & Liu, G. MRI Reporter Genes for Noninvasive Molecular Imaging. *Molecules (Basel, Switzerland)* **21**, doi:10.3390/molecules21050580 (2016).

296 Ittrich, H. *et al.* In vivo magnetic resonance imaging of iron oxide–labeled, arterially-injected mesenchymal stem cells in kidneys of rats with acute ischemic kidney injury: Detection and monitoring at 3T. *Journal of Magnetic Resonance Imaging* **25**, 1179-1191, doi:10.1002/jmri.20925 (2007).

297 Lange, C. *et al.* Administered mesenchymal stem cells enhance recovery from ischemia/reperfusion-induced acute renal failure in rats. *Kidney international* **68**, 1613-1617, doi:10.1111/j.1523-1755.2005.00573.x (2005).

298 Lin, B. L. *et al.* Superparamagnetic Iron Oxide Nanoparticles-Complexed Cationic Amylose for In Vivo Magnetic Resonance Imaging Tracking of Transplanted Stem Cells in Stroke. *Nanomaterials (Basel, Switzerland)* **7**, doi:10.3390/nano7050107 (2017).

299 Grudzenski, S. *et al.* The effect of adipose tissue-derived stem cells in a middle cerebral artery occlusion stroke model depends on their engraftment rate. *Stem Cell Research & Therapy* **8**, 96, doi:10.1186/s13287-017-0545-y (2017).

300 Lu, L. *et al.* A novel polymeric micelle used for in vivo MR imaging tracking of neural stem cells in acute ischemic stroke. *RSC Advances* **7**, 15041-15052, doi:10.1039/C7RA00345E (2017).

301 Zhang, F. *et al.* In Vivo Targeted MR Imaging of Endogenous Neural Stem Cells in Ischemic Stroke. *Molecules (Basel, Switzerland)* **21**, doi:10.3390/molecules21091143 (2016).

302 Lamanna, J. J. *et al.* Ferumoxytol Labeling of Human Neural Progenitor Cells for Diagnostic Cellular Tracking in the Porcine Spinal Cord With Magnetic Resonance Imaging. *Stem Cells Transl Med*, doi:10.5966/sctm.2015-0422 (2016).

303 Filippi, M. *et al.* Successful in vivo MRI tracking of MSCs labeled with Gadoteridol in a Spinal Cord Injury experimental model. *Experimental neurology* **282**, 66-77, doi:10.1016/j.expneurol.2016.05.023 (2016).

304 Abramowski, P. *et al.* Mesenchymal Stromal/Stem Cells Do Not Ameliorate Experimental Autoimmune Encephalomyelitis and Are Not Detectable in the Central Nervous System of Transplanted Mice. *Stem cells and development* **25**, 1134-1148, doi:10.1089/scd.2016.0020 (2016).

305 Shmarlouski, A. *et al.* Automatic artifact removal from GFR measurements. *Biomedical Signal Processing and Control* **14**, 30-41, doi:http://dx.doi.org/10.1016/j.bspc.2014.06.010 (2014).

306 Friedemann, J. *et al.* Improved kinetic model for the transcutaneous measurement of glomerular filtration rate in experimental animals. *Kidney international* **90**, 1377-1385, doi:10.1016/j.kint.2016.07.024 (2016).
307 Toora, B. D. & Rajagopal, G. Measurement of creatinine by Jaffe's reaction--determination of concentration of sodium hydroxide required for maximum color development in standard, urine and protein free filtrate of serum. *Indian journal of experimental biology* **40**, 352-354 (2002).
308 Wang, W. *et al.* Endotoxemic acute renal failure is attenuated in caspase-1-deficient mice. *American journal of physiology. Renal physiology* **288**, F997-1004, doi:10.1152/ajprenal.00130.2004 (2005).
309 Fuente Mora, C. *et al.* Differentiation of podocyte and proximal tubule-like cells from a mouse kidney-derived stem cell line. *Stem cells and development* **21**, 296-307, doi:10.1089/scd.2010.0470 (2012).
310 Taylor, A. *et al.* Assessing the efficacy of nano- and micro-sized magnetic particles as contrast agents for MRI cell tracking. *PloS one* **9**, e100259, doi:10.1371/journal.pone.0100259 (2014).
311 Kutner, R. H., Zhang, X. Y. & Reiser, J. Production, concentration and titration of pseudotyped HIV-1-based lentiviral vectors. *Nature protocols* **4**, 495-505, doi:10.1038/nprot.2009.22 (2009).
312 Harari-Steinberg, O. *et al.* Identification of human nephron progenitors capable of generation of kidney structures and functional repair of chronic renal disease. *EMBO molecular medicine* **5**, 1556-1568, doi:10.1002/emmm.201201584 (2013).
313 Lu, J. *et al.* Discrete functions of M2a and M2c macrophage subsets determine their relative efficacy in treating chronic kidney disease. *Kidney international* **84**, 745-755, doi:10.1038/ki.2013.135 (2013).
314 Kitiyakara, C., Eggers, P. & Kopp, J. B. Twenty-one-year trend in ESRD due to focal segmental glomerulosclerosis in the United States. *American journal of kidney diseases : the official journal of the National Kidney Foundation* **44**, 815-825 (2004).
315 Korbet, S. M. Treatment of primary FSGS in adults. *Journal of the American Society of Nephrology : JASN* **23**, 1769-1776, doi:10.1681/asn.2012040389 (2012).
316 Ntziachristos, V. Going deeper than microscopy: the optical imaging frontier in biology. *Nat Meth* **7**, 603-614 (2010).
317 Wang, L. V. & Hu, S. Photoacoustic tomography: in vivo imaging from organelles to organs. *Science (New York, N.Y.)* **335**, 1458-1462, doi:10.1126/science.1216210 (2012).
318 Lasagni, L. *et al.* Notch activation differentially regulates renal progenitors proliferation and differentiation toward the podocyte lineage in glomerular disorders. *Stem Cells* **28**, 1674-1685, doi:10.1002/stem.492 (2010).
319 Preibisch, S., Saalfeld, S. & Tomancak, P. Globally optimal stitching of tiled 3D microscopic image acquisitions. *Bioinformatics* **25**, 1463-1465, doi:10.1093/bioinformatics/btp184 (2009).
320 Licha, K. *et al.* Hydrophilic cyanine dyes as contrast agents for near-infrared tumor imaging: synthesis, photophysical properties and spectroscopic in vivo characterization. *Photochemistry and photobiology* **72**, 392-398 (2000).
321 Hamann, F. M. *et al.* Controlled modulation of serum protein binding and biodistribution of asymmetric cyanine dyes by variation of the number of sulfonate groups. *Molecular imaging* **10**, 258-269, doi:10.2310/7290.2011.00005 (2011).
322 Schock-Kusch, D. *et al.* Transcutaneous measurement of glomerular filtration rate using FITC-sinistrin in rats. *Nephrology, dialysis, transplantation : official publication of the European Dialysis and Transplant Association - European Renal Association* **24**, 2997-3001, doi:10.1093/ndt/gfp225 (2009).

323 Zöllner, F. G. *et al.* Simultaneous Measurement of Kidney Function by Dynamic Contrast Enhanced MRI and FITC-Sinistrin Clearance in Rats at 3 Tesla: Initial Results. *PloS one* **8**, e79992, doi:10.1371/journal.pone.0079992 (2013).

324 Bonventre, J. V., Vaidya, V. S., Schmouder, R., Feig, P. & Dieterle, F. Next-generation biomarkers for detecting kidney toxicity. *Nature biotechnology* **28**, 436-440, doi:10.1038/nbt0510-436 (2010).

325 Dieterle, F. *et al.* Urinary clusterin, cystatin C, beta2-microglobulin and total protein as markers to detect drug-induced kidney injury. *Nature biotechnology* **28**, 463-469, doi:10.1038/nbt.1622 (2010).

326 Zhang, J. *et al.* Sex-related differences in mast cell activity and doxorubicin toxicity: a study in spontaneously hypertensive rats. *Toxicologic pathology* **42**, 361-375, doi:10.1177/0192623313482778 (2014).

327 Tan, R. J., Zhou, L., Zhou, D., Lin, L. & Liu, Y. Endothelin receptor a blockade is an ineffective treatment for adriamycin nephropathy. *PloS one* **8**, e79963, doi:10.1371/journal.pone.0079963 (2013).

328 Yasuda, K. *et al.* Adriamycin nephropathy: a failure of endothelial progenitor cell-induced repair. *The American journal of pathology* **176**, 1685-1695, doi:10.2353/ajpath.2010.091071 (2010).

329 Endre, Z. H., Pickering, J. W. & Walker, R. J. Clearance and beyond: the complementary roles of GFR measurement and injury biomarkers in acute kidney injury (AKI). *American journal of physiology. Renal physiology* **301**, F697-707, doi:10.1152/ajprenal.00448.2010 (2011).

330 Murray, P. T. *et al.* Potential use of biomarkers in acute kidney injury: report and summary of recommendations from the 10th Acute Dialysis Quality Initiative consensus conference. *Kidney international* **85**, 513-521, doi:10.1038/ki.2013.374 (2014).

331 Harrison, T., Jeffery, D., Wiebe, E. & Zemp, R. J. Real-time clinically oriented array-based in vivo combined photoacoustic and power Doppler imaging. *SPIE Proceedings* **8943**, doi:10.1117/12.2040609 (2014).

332 Laufer, J. *et al.* In vivo photoacoustic imaging of mouse embryos. *Journal of biomedical optics* **17**, 061220, doi:10.1117/1.jbo.17.6.061220 (2012).

333 Nam, S. Y., Ricles, L. M., Suggs, L. J. & Emelianov, S. Y. In vivo Ultrasound and Photoacoustic Monitoring of Mesenchymal Stem Cells Labeled with Gold Nanotracers. *PloS one* **7**, e37267, doi:10.1371/journal.pone.0037267 (2012).

334 Dean-Ben, X. L., Buehler, A., Razansky, D. & Ntziachristos, V. Estimation of optoacoustic contrast agent concentration with self-calibration blind logarithmic unmixing. *Physics in medicine and biology* **59**, 4785-4797, doi:10.1088/0031-9155/59/17/4785 (2014).

335 Deliolanis, N. C. *et al.* Deep-tissue reporter-gene imaging with fluorescence and optoacoustic tomography: a performance overview. *Molecular imaging and biology : MIB : the official publication of the Academy of Molecular Imaging* **16**, 652-660, doi:10.1007/s11307-014-0728-1 (2014).

336 Buehler, A. *et al.* High resolution tumor targeting in living mice by means of multispectral optoacoustic tomography. *EJNMMI research* **2**, 14, doi:10.1186/2191-219x-2-14 (2012).

337 Jokerst, J. V., Thangaraj, M., Kempen, P. J., Sinclair, R. & Gambhir, S. S. Photoacoustic Imaging of Mesenchymal Stem Cells in Living Mice via Silica-Coated Gold Nanorods. *ACS nano* **6**, 5920-5930, doi:10.1021/nn302042y (2012).

338 Xiang, L., Ahmad, M., Hu, X., Cheng, Z. & Xing, L. Label-Free Photoacoustic Cell-Tracking In Real-Time. *X-Acoustics: Imaging and Sensing* **1**, doi:10.2478/phto-2014-0002 (2014).

339 Zhang, X. *et al.* Resolvin D1 protects podocytes in adriamycin-induced nephropathy through modulation of 14-3-3beta acetylation. *PloS one* **8**, e67471, doi:10.1371/journal.pone.0067471 (2013).

340 Kairaitis, L. K., Wang, Y., Gassmann, M., Tay, Y.-C. & Harris, D. C. H. HIF-1α expression follows microvascular loss in advanced murine adriamycin nephrosis. *American Journal of Physiology - Renal Physiology* **288**, F198-F206, doi:10.1152/ajprenal.00244.2003 (2005).

341 Egger, C. *et al.* Adriamycin-induced nephropathy in rats: functional and cellular effects characterized by MRI. *Journal of magnetic resonance imaging : JMRI* **41**, 829-840, doi:10.1002/jmri.24603 (2015).

342 Suzuki, E., Fujita, D., Takahashi, M., Oba, S. & Nishimatsu, H. Adult stem cells as a tool for kidney regeneration. *World journal of nephrology* **5**, 43-52, doi:10.5527/wjn.v5.i1.43 (2016).

343 Murray, P. A. & Woolf, A. S. Using stem and progenitor cells to recapitulate kidney development and restore renal function. *Curr Opin Organ Transplant* **19**, 140-144, doi:10.1097/mot.0000000000000052 (2014).

344 Irollo, E. & Pirozzi, G. CD133: to be or not to be, is this the real question? *American Journal of Translational Research* **5**, 563-581 (2013).

345 Grange, C. *et al.* Protective effect and localization by optical imaging of human renal CD133+ progenitor cells in an acute kidney injury model. *Physiological reports* **2**, e12009, doi:10.14814/phy2.12009 (2014).

346 Tögel, F. & Westenfelder, C. Recent advances in the understanding of acute kidney injury. *F1000Prime Reports* **6**, 83, doi:10.12703/P6-83 (2014).

347 Kerr, M., Bray, B., Medcalf, J., O'Donoghue, D. J. & Matthews, B. Estimating the financial cost of chronic kidney disease to the NHS in England. *Nephrology, dialysis, transplantation : official publication of the European Dialysis and Transplant Association - European Renal Association* **27 Suppl 3**, iii73-80, doi:10.1093/ndt/gfs269 (2012).

348 Barai, S., Gambhir, S., Prasad, N., Sharma, R. K. & Ora, M. Functional renal reserve capacity in different stages of chronic kidney disease. *Nephrology (Carlton, Vic.)* **15**, 350-353, doi:10.1111/j.1440-1797.2010.01291.x (2010).

349 Fischer, U. M. *et al.* Pulmonary passage is a major obstacle for intravenous stem cell delivery: the pulmonary first-pass effect. *Stem cells and development* **18**, 683-692, doi:10.1089/scd.2008.0253 (2009).

350 Schrepfer, S. *et al.* Stem Cell Transplantation: The Lung Barrier. *Transplantation Proceedings* **39**, 573-576, doi:10.1016/j.transproceed.2006.12.019 (2007).

351 Eggenhofer, E. *et al.* Mesenchymal stem cells are short-lived and do not migrate beyond the lungs after intravenous infusion. *Frontiers in Immunology* **3**, 297, doi:10.3389/fimmu.2012.00297 (2012).

352 Burst, V. R. *et al.* Poor cell survival limits the beneficial impact of mesenchymal stem cell transplantation on acute kidney injury. *Nephron. Experimental nephrology* **114**, e107-116, doi:10.1159/000262318 (2010).

353 Cao, H. *et al.* Mesenchymal stem cells derived from human umbilical cord ameliorate ischemia/reperfusion-induced acute renal failure in rats. *Biotechnology letters* **32**, 725-732, doi:10.1007/s10529-010-0207-y (2010).

354 Cai, J. *et al.* Maximum efficacy of mesenchymal stem cells in rat model of renal ischemia-reperfusion injury: renal artery administration with optimal numbers. *PloS one* **9**, e92347, doi:10.1371/journal.pone.0092347 (2014).

355 Togel, F. *et al.* Autologous and allogeneic marrow stromal cells are safe and effective for the treatment of acute kidney injury. *Stem cells and development* **18**, 475-485, doi:10.1089/scd.2008.0092 (2009).

356 Sheashaa, H. *et al.* Protective effect of adipose-derived mesenchymal stem cells against acute kidney injury induced by ischemia-reperfusion in Sprague-Dawley rats. *Experimental and therapeutic medicine* **11**, 1573-1580, doi:10.3892/etm.2016.3109 (2016).
357 Toyohara, T. *et al.* Cell therapy using human induced pluripotent stem cell-derived renal progenitors ameliorates acute kidney injury in mice. *Stem Cells Translational Medicine* **4**, 980-992, doi:10.5966/sctm.2014-0219 (2015).
358 Kennedy, S. E. & Erlich, J. H. Murine renal ischaemia-reperfusion injury. *Nephrology (Carlton, Vic.)* **13**, 390-396, doi:10.1111/j.1440-1797.2008.00979.x (2008).
359 Skrypnyk, N. I., Harris, R. C. & de Caestecker, M. P. Ischemia-reperfusion model of acute kidney injury and post injury fibrosis in mice. *Journal of visualized experiments : JoVE*, doi:10.3791/50495 (2013).
360 Wei, Q. & Dong, Z. Mouse model of ischemic acute kidney injury: technical notes and tricks. *American journal of physiology. Renal physiology* **303**, F1487-1494, doi:10.1152/ajprenal.00352.2012 (2012).
361 Hesketh, E. E. *et al.* Renal ischaemia reperfusion injury: a mouse model of injury and regeneration. *Journal of visualized experiments : JoVE*, doi:10.3791/51816 (2014).
362 Le Clef, N., Verhulst, A., D'Haese, P. C. & Vervaet, B. A. Unilateral Renal Ischemia-Reperfusion as a Robust Model for Acute to Chronic Kidney Injury in Mice. *PloS one* **11**, e0152153, doi:10.1371/journal.pone.0152153 (2016).
363 Delbridge, M. S., Shrestha, B. M., Raftery, A. T., El Nahas, A. M. & Haylor, J. L. The effect of body temperature in a rat model of renal ischemia-reperfusion injury. *Transplant Proc* **39**, 2983-2985, doi:10.1016/j.transproceed.2007.04.028 (2007).
364 Lee, H. T., Ota-Setlik, A., Fu, Y., Nasr, S. H. & Emala, C. W. Differential protective effects of volatile anesthetics against renal ischemia-reperfusion injury in vivo. *Anesthesiology* **101**, 1313-1324 (2004).
365 Kusaka, J. *et al.* Age-dependent responses to renal ischemia-reperfusion injury. *The Journal of surgical research* **172**, 153-158, doi:10.1016/j.jss.2010.08.034 (2012).
366 Park, K. M., Kim, J. I., Ahn, Y., Bonventre, A. J. & Bonventre, J. V. Testosterone is responsible for enhanced susceptibility of males to ischemic renal injury. *The Journal of biological chemistry* **279**, 52282-52292, doi:10.1074/jbc.M407629200 (2004).
367 Burne, M. J., Haq, M., Matsuse, H., Mohapatra, S. & Rabb, H. Genetic susceptibility to renal ischemia reperfusion injury revealed in a murine model. *Transplantation* **69**, 1023-1025 (2000).
368 Vaidya, V. S., Ferguson, M. A. & Bonventre, J. V. Biomarkers of Acute Kidney Injury. *Annual review of pharmacology and toxicology* **48**, 463-493, doi:10.1146/annurev.pharmtox.48.113006.094615 (2008).
369 Wang, S. *et al.* Excess Integrins Cause Lung Entrapment of Mesenchymal Stem Cells. *Stem Cells* **33**, 3315-3326, doi:10.1002/stem.2087 (2015).
370 Nystedt, J. *et al.* Cell surface structures influence lung clearance rate of systemically infused mesenchymal stromal cells. *Stem Cells* **31**, 317-326, doi:10.1002/stem.1271 (2013).
371 Lee, R. H. *et al.* Intravenous hMSCs improve myocardial infarction in mice because cells embolized in lung are activated to secrete the anti-inflammatory protein TSG-6. *Cell stem cell* **5**, 54-63, doi:10.1016/j.stem.2009.05.003 (2009).
372 Shiao, C.-C. *et al.* Long-term remote organ consequences following acute kidney injury. *Critical Care* **19**, 438, doi:10.1186/s13054-015-1149-5 (2015).
373 Grams, M. E. & Rabb, H. The distant organ effects of acute kidney injury. *Kidney international* **81**, 942-948, doi:10.1038/ki.2011.241 (2012).

374 Liu, M. *et al.* Acute kidney injury leads to inflammation and functional changes in the brain. *Journal of the American Society of Nephrology : JASN* **19**, 1360-1370, doi:10.1681/asn.2007080901 (2008).
375 Kelly, K. J. Distant effects of experimental renal ischemia/reperfusion injury. *Journal of the American Society of Nephrology : JASN* **14**, 1549-1558 (2003).
376 Faubel, S. & Edelstein, C. L. Mechanisms and mediators of lung injury after acute kidney injury. *Nature reviews. Nephrology* **12**, 48-60, doi:10.1038/nrneph.2015.158 (2016).
377 Chao, C.-T. *et al.* The Impact of Dialysis-Requiring Acute Kidney Injury on Long-Term Prognosis of Patients Requiring Prolonged Mechanical Ventilation: Nationwide Population-Based Study. *PloS one* **7**, e50675, doi:10.1371/journal.pone.0050675 (2012).
378 Walcher, A., Faubel, S., Keniston, A. & Dennen, P. In critically ill patients requiring CRRT, AKI is associated with increased respiratory failure and death versus ESRD. *Ren Fail* **33**, 935-942, doi:10.3109/0886022x.2011.615964 (2011).
379 Balci, M. K., Vayvada, M., Salturk, C., Kutlu, C. A. & Ari, E. Incidence of Early Acute Kidney Injury in Lung Transplant Patients: A Single-Center Experience. *Transplant Proc* **49**, 593-598, doi:10.1016/j.transproceed.2017.01.031 (2017).
380 Peres, L. A., Wandeur, V. & Matsuo, T. Predictors of acute kidney injury and mortality in an Intensive Care Unit. *Jornal brasileiro de nefrologia : 'orgao oficial de Sociedades Brasileira e Latino-Americana de Nefrologia* **37**, 38-46, doi:10.5935/0101-2800.20150007 (2015).
381 Seeley, E. J. Updates in the management of acute lung injury: a focus on the overlap between AKI and ARDS. *Advances in chronic kidney disease* **20**, 14-20, doi:10.1053/j.ackd.2012.10.001 (2013).
382 Feltes, C. M., Hassoun, H. T., Lie, M. L., Cheadle, C. & Rabb, H. Pulmonary endothelial cell activation during experimental acute kidney injury. *Shock (Augusta, Ga.)* **36**, 170-176, doi:10.1097/SHK.0b013e3182169c76 (2011).
383 Hassoun, H. T. *et al.* Kidney ischemia-reperfusion injury induces caspase-dependent pulmonary apoptosis. *American journal of physiology. Renal physiology* **297**, F125-137, doi:10.1152/ajprenal.90666.2008 (2009).
384 Hoke, T. S. *et al.* Acute renal failure after bilateral nephrectomy is associated with cytokine-mediated pulmonary injury. *Journal of the American Society of Nephrology : JASN* **18**, 155-164, doi:10.1681/asn.2006050494 (2007).
385 White, L. E., Santora, R. J., Cui, Y., Moore, F. A. & Hassoun, H. T. TNFR1-dependent pulmonary apoptosis during ischemic acute kidney injury. *American journal of physiology. Lung cellular and molecular physiology* **303**, L449-459, doi:10.1152/ajplung.00301.2011 (2012).
386 Lie, M. L. *et al.* Lung T lymphocyte trafficking and activation during ischemic acute kidney injury. *Journal of immunology (Baltimore, Md. : 1950)* **189**, 2843-2851, doi:10.4049/jimmunol.1103254 (2012).
387 Klein, C. L. *et al.* Interleukin-6 mediates lung injury following ischemic acute kidney injury or bilateral nephrectomy. *Kidney international* **74**, 901-909, doi:10.1038/ki.2008.314 (2008).
388 Kramer, A. A. *et al.* Renal ischemia/reperfusion leads to macrophage-mediated increase in pulmonary vascular permeability. *Kidney international* **55**, 2362-2367, doi:10.1046/j.1523-1755.1999.00460.x (1999).
389 Ahuja, N. *et al.* Circulating IL-6 mediates lung injury via CXCL1 production after acute kidney injury in mice. *American journal of physiology. Renal physiology* **303**, F864-872, doi:10.1152/ajprenal.00025.2012 (2012).

390 Andres-Hernando, A. *et al.* Prolonged acute kidney injury exacerbates lung inflammation at 7 days post-acute kidney injury. *Physiological reports* **2**, e12084, doi:10.14814/phy2.12084 (2014).
391 Elmore, S. Apoptosis: a review of programmed cell death. *Toxicologic pathology* **35**, 495-516, doi:10.1080/01926230701320337 (2007).
392 Gordon, N. *et al.* Corruption of the Fas Pathway Delays the Pulmonary Clearance of Murine Osteosarcoma Cells, Enhances Their Metastatic Potential, and Reduces the Effect of Aerosol Gemcitabine. *Clinical cancer research : an official journal of the American Association for Cancer Research* **13**, 4503-4510, doi:10.1158/1078-0432.CCR-07-0313 (2007).
393 Peter, M. E. *et al.* The role of CD95 and CD95 ligand in cancer. *Cell Death and Differentiation* **22**, 885-886, doi:10.1038/cdd.2015.25 (2015).
394 Thum, T., Bauersachs, J., Poole-Wilson, P. A., Volk, H. D. & Anker, S. D. The dying stem cell hypothesis: immune modulation as a novel mechanism for progenitor cell therapy in cardiac muscle. *Journal of the American College of Cardiology* **46**, 1799-1802, doi:10.1016/j.jacc.2005.07.053 (2005).
395 Morelli, A. E. & Larregina, A. T. Apoptotic cell-based therapies against transplant rejection: role of recipient's dendritic cells. *Apoptosis : an international journal on programmed cell death* **15**, 1083-1097, doi:10.1007/s10495-010-0469-9 (2010).
396 Saas, P., Kaminski, S. & Perruche, S. Prospects of apoptotic cell-based therapies for transplantation and inflammatory diseases. *Immunotherapy* **5**, 1055-1073, doi:10.2217/imt.13.103 (2013).
397 Akyurekli, C. *et al.* A Systematic Review of Preclinical Studies on the Therapeutic Potential of Mesenchymal Stromal Cell-Derived Microvesicles. *Stem Cell Reviews and Reports* **11**, 150-160, doi:10.1007/s12015-014-9545-9 (2015).
398 Bonventre, J. V. Microvesicles from mesenchymal stromal cells protect against acute kidney injury. *Journal of the American Society of Nephrology : JASN* **20**, 927-928, doi:10.1681/asn.2009030322 (2009).
399 Hesketh, E. E., Kluth, D. C. & Hughes, J. Apoptotic cell administration is detrimental in murine renal ischaemia reperfusion injury. *Journal of inflammation (London, England)* **11**, 31, doi:10.1186/s12950-014-0031-6 (2014).
400 Vanikar, A. V., Trivedi, H. L. & Thakkar, U. G. Stem cell therapy emerging as the key player in treating type 1 diabetes mellitus. *Cytotherapy* **18**, 1077-1086, doi:10.1016/j.jcyt.2016.06.006 (2016).
401 Wang, Y., Ji, X., Leak, R. K., Chen, F. & Cao, G. Stem cell therapies in age-related neurodegenerative diseases and stroke. *Ageing research reviews* **34**, 39-50, doi:10.1016/j.arr.2016.11.002 (2017).
402 Doulames, V. M. & Plant, G. W. Induced Pluripotent Stem Cell Therapies for Cervical Spinal Cord Injury. *International journal of molecular sciences* **17**, 530, doi:10.3390/ijms17040530 (2016).
403 Anderson, J. S. & Bauer, G. Fighting HIV with stem cell therapy: one step closer to human trials? *Expert review of anti-infective therapy* **10**, 1071-1073, doi:10.1586/eri.12.105 (2012).
404 Papazova, D. A. *et al.* Cell-based therapies for experimental chronic kidney disease: a systematic review and meta-analysis. *Disease models & mechanisms* **8**, 281-293, doi:10.1242/dmm.017699 (2015).
405 Shiota, G. & Itaba, N. Progress in stem cell-based therapy for liver disease. *Hepatology research : the official journal of the Japan Society of Hepatology*, doi:10.1111/hepr.12747 (2016).
406 Hou, L., Kim, J. J., Woo, Y. J. & Huang, N. F. Stem cell-based therapies to promote angiogenesis in ischemic cardiovascular disease. *American journal of physiology.*

Heart and circulatory physiology **310**, H455-465, doi:10.1152/ajpheart.00726.2015 (2016).

407 Mead, B. *et al.* Stem cell treatment of degenerative eye disease. *Stem cell research* **14**, 243-257, doi:10.1016/j.scr.2015.02.003 (2015).

408 BBC News. *Paolo Macchiarini: A surgeon's downfall*, <http://www.bbc.co.uk/news/magazine-37311038> (2016).

409 Delaere, P. R. & Van Raemdonck, D. The trachea: the first tissue-engineered organ? *The Journal of thoracic and cardiovascular surgery* **147**, 1128-1132, doi:10.1016/j.jtcvs.2013.12.024 (2014).

410 Cyranoski, D. Investigations launched into artificial tracheas. *Nature* **516**, 16-17, doi:10.1038/516016a (2014).

411 Kircher, M. F., Gambhir, S. S. & Grimm, J. Noninvasive cell-tracking methods. *Nat Rev Clin Oncol* **8**, 677-688, doi:10.1038/nrclinonc.2011.141 (2011).

412 Taylor, A., Wilson, K. M., Murray, P., Fernig, D. G. & Levy, R. Long-term tracking of cells using inorganic nanoparticles as contrast agents: are we there yet? *Chemical Society reviews* **41**, 2707-2717, doi:10.1039/c2cs35031a (2012).

413 Terrovitis, J. *et al.* Magnetic resonance imaging overestimates ferumoxide-labeled stem cell survival after transplantation in the heart. *Circulation* **117**, 1555-1562, doi:10.1161/circulationaha.107.732073 (2008).

414 Berman, S. C., Galpoththawela, C., Gilad, A. A., Bulte, J. W. & Walczak, P. Long-term MR cell tracking of neural stem cells grafted in immunocompetent versus immunodeficient mice reveals distinct differences in contrast between live and dead cells. *Magnetic resonance in medicine* **65**, 564-574, doi:10.1002/mrm.22613 (2011).

415 Rehemtulla, A. *et al.* Rapid and Quantitative Assessment of Cancer Treatment Response Using In Vivo Bioluminescence Imaging. *Neoplasia (New York, N.Y.)* **2**, 491-495 (2000).

416 Edinger, M. *et al.* Advancing animal models of neoplasia through in vivo bioluminescence imaging. *European journal of cancer (Oxford, England : 1990)* **38**, 2128-2136 (2002).

417 Paroo, Z. *et al.* Validating bioluminescence imaging as a high-throughput, quantitative modality for assessing tumor burden. *Molecular imaging* **3**, 117-124, doi:10.1162/1535350041464865 (2004).

418 Shih, Y. C. *et al.* Adipose-derived stem cells exhibit antioxidative and antiapoptotic properties to rescue ischemic acute kidney injury in rats. *Plastic and reconstructive surgery* **132**, 940e-951e, doi:10.1097/PRS.0b013e3182a806ce (2013).

419 Campbell, J. P., Merkel, A. R., Masood-Campbell, S. K., Elefteriou, F. & Sterling, J. A. Models of bone metastasis. *Journal of visualized experiments : JoVE*, e4260, doi:10.3791/4260 (2012).

420 Salamon, J. & Peldschus, K. Ultrasound-guided intracardial injection and in vivo magnetic resonance imaging of single cells in mice as a paradigm for hematogenous metastases. *Methods in molecular biology (Clifton, N.J.)* **1070**, 203-211, doi:10.1007/978-1-4614-8244-4_15 (2014).

421 Uluckan, O. *et al.* APT102, a novel adpase, cooperates with aspirin to disrupt bone metastasis in mice. *Journal of cellular biochemistry* **104**, 1311-1323, doi:10.1002/jcb.21709 (2008).

422 Basse, P., Hokland, P., Heron, I. & Hokland, M. Fate of tumor cells injected into left ventricle of heart in BALB/c mice: role of natural killer cells. *Journal of the National Cancer Institute* **80**, 657-665 (1988).

423 Reeves, K. J. *et al.* Prostate cancer cells home to bone using a novel in vivo model: modulation by the integrin antagonist GLPG0187. *International journal of cancer* **136**, 1731-1740, doi:10.1002/ijc.29165 (2015).

424 Arguello, F., Baggs, R. B. & Frantz, C. N. A murine model of experimental metastasis to bone and bone marrow. *Cancer research* **48**, 6876-6881 (1988).

425 Feng, Z. *et al.* Fresh and cryopreserved, uncultured adipose tissue-derived stem and regenerative cells ameliorate ischemia-reperfusion-induced acute kidney injury. *Nephrology, dialysis, transplantation : official publication of the European Dialysis and Transplant Association - European Renal Association* **25**, 3874-3884, doi:10.1093/ndt/gfq603 (2010).

426 Kunter, U. *et al.* Mesenchymal Stem Cells Prevent Progressive Experimental Renal Failure but Maldifferentiate into Glomerular Adipocytes. *Journal of the American Society of Nephrology* **18**, 1754-1764, doi:doi: 10.1681/ASN.2007010044 (2007).

427 Togel, F. *et al.* Administered mesenchymal stem cells protect against ischemic acute renal failure through differentiation-independent mechanisms. *American journal of physiology. Renal physiology* **289**, F31-42, doi:10.1152/ajprenal.00007.2005 (2005).

428 Lee, P. Y. *et al.* Induced pluripotent stem cells without c-Myc attenuate acute kidney injury via downregulating the signaling of oxidative stress and inflammation in ischemia-reperfusion rats. *Cell transplantation* **21**, 2569-2585, doi:10.3727/096368912x636902 (2012).

429 Zonta, S. *et al.* Which is the most suitable and effective route of administration for mesenchymal stem cell-based immunomodulation therapy in experimental kidney transplantation: endovenous or arterial? *Transplant Proc* **42**, 1336-1340, doi:10.1016/j.transproceed.2010.03.081 (2010).

430 Wang, Y., He, J., Pei, X. & Zhao, W. Systematic review and meta-analysis of mesenchymal stem/stromal cells therapy for impaired renal function in small animal models. *Nephrology* **18**, 201-208, doi:10.1111/nep.12018 (2013).

431 Togel, F. *et al.* Vasculotropic, paracrine actions of infused mesenchymal stem cells are important to the recovery from acute kidney injury. *American journal of physiology. Renal physiology* **292**, F1626-1635, doi:10.1152/ajprenal.00339.2006 (2007).

432 Aziz, M. T. A. *et al.* The role of bone marrow derived-mesenchymal stem cells in attenuation of kidney function in rats with diabetic nephropathy. *Diabetology and Metabolic Syndrome* **6**, doi:10.1186/1758-5996-6-34 (2014).

433 Bi, B., Schmitt, R., Israilova, M., Nishio, H. & Cantley, L. G. Stromal cells protect against acute tubular injury via an endocrine effect. *Journal of the American Society of Nephrology : JASN* **18**, 2486-2496, doi:10.1681/asn.2007020140 (2007).

434 Chuah, J. K. C. & Zink, D. Stem cell-derived kidney cells and organoids: Recent breakthroughs and emerging applications. *Biotechnology Advances* **35**, 150-167, doi:http://dx.doi.org/10.1016/j.biotechadv.2016.12.001 (2017).

435 Papadimou, E. *et al.* Direct reprogramming of human bone marrow stromal cells into functional renal cells using cell-free extracts. *Stem cell reports* **4**, 685-698, doi:10.1016/j.stemcr.2015.02.002 (2015).

436 Ben-David, U. & Benvenisty, N. The tumorigenicity of human embryonic and induced pluripotent stem cells. *Nat Rev Cancer* **11**, 268-277 (2011).

437 Kunter, U. *et al.* Transplanted mesenchymal stem cells accelerate glomerular healing in experimental glomerulonephritis. *Journal of the American Society of Nephrology : JASN* **17**, 2202-2212, doi:10.1681/asn.2005080815 (2006).

438 Juffroy, O. *et al.* Subcutaneous graft of D1 mouse mesenchymal stem cells leads to the formation of a bone-like structure. *Differentiation; research in biological diversity* **78**, 223-231, doi:10.1016/j.diff.2009.07.005 (2009).

439 Ngen, E. J. *et al.* Imaging transplanted stem cells in real time using an MRI dual-contrast method. *Scientific Reports* **5**, 13628, doi:10.1038/srep13628 (2015).

440 MediBeacon. *MediBeacon: The Clinical Need*, <http://www.medibeacon.com/products/nephrology/the-clinical-need/> (2017).

441 Burton, N. C. *et al.* Multispectral opto-acoustic tomography (MSOT) of the brain and glioblastoma characterization. *Neuroimage* **65**, 522-528, doi:10.1016/j.neuroimage.2012.09.053 (2013).

442 Comenge, J. *et al.* Preventing Plasmon Coupling between Gold Nanorods Improves the Sensitivity of Photoacoustic Detection of Labeled Stem Cells in Vivo. *ASC Nano* **10**, 7106-7116, doi:10.1021/acsnano.6b03246 (2016).

443 Ricles, L. M., Nam, S. Y., Trevino, E. A., Emelianov, S. Y. & Suggs, L. J. A Dual Gold Nanoparticle System for Mesenchymal Stem Cell Tracking. *Journal of materials chemistry. B, Materials for biology and medicine* **2**, 8220-8230, doi:10.1039/c4tb00975d (2014).

444 Nam, S. Y., Chung, E., Suggs, L. J. & Emelianov, S. Y. Combined ultrasound and photoacoustic imaging to noninvasively assess burn injury and selectively monitor a regenerative tissue-engineered construct. *Tissue engineering. Part C, Methods* **21**, 557-566, doi:10.1089/ten.TEC.2014.0306 (2015).

445 Wang, C. *et al.* Protamine Functionalized Single-Walled Carbon Nanotubes for Stem Cell Labeling and In Vivo Raman/Magnetic Resonance/Photoacoustic Triple-Modal Imaging. *Advanced Functional Materials* **22**, 2363-2375, doi:10.1002/adfm.201200133 (2012).

446 Kanazaki, K. *et al.* Development of human serum albumin conjugated with near-infrared dye for photoacoustic tumor imaging. *Journal of biomedical optics* **19**, 96002, doi:10.1117/1.jbo.19.9.096002 (2014).

447 Copland, J. A. *et al.* Bioconjugated gold nanoparticles as a molecular based contrast agent: implications for imaging of deep tumors using optoacoustic tomography. *Molecular Imaging & Biology* **6**, 341-349, doi:http://dx.doi.org/10.1016/j.mibio.2004.06.002 (2004).

448 Neuschmelting, V. *et al.* Performance of a Multispectral Optoacoustic Tomography (MSOT) System equipped with 2D vs. 3D Handheld Probes for Potential Clinical Translation. *Photoacoustics* **4**, 1-10, doi:http://dx.doi.org/10.1016/j.pacs.2015.12.001 (2016).

449 Eirin, A. & Lerman, L. O. Mesenchymal stem cell treatment for chronic renal failure. *Stem Cell Res Ther* **5**, 83, doi:10.1186/scrt472 (2014).

450 Bates, M. L. *et al.* Hypoxia recruits intrapulmonary arteriovenous pathways in intact rats but not isolated rat lungs. *Journal of applied physiology (Bethesda, Md. : 1985)* **112**, 1915-1920, doi:10.1152/japplphysiol.00985.2011 (2012).

451 Lovering, A. T., Elliott, J. E., Beasley, K. M. & Laurie, S. S. Pulmonary pathways and mechanisms regulating transpulmonary shunting into the general circulation: An update. *Injury* **41**, S16-S23, doi:10.1016/S0020-1383(10)70004-8 (2010).